TECHNISCHE UNIVERSITÄT MÜNCHEN

Lehrstuhl für Physikalische Chemie

Linear and Nonlinear Surface Spectroscopy of Supported Size Selected Metal Clusters and Organic Adsorbates

Martin Georg Thämer

Vollständiger Abdruck der von der Fakultät für Chemie der Technischen Universität München zur Erlangung des akademischen Grades eines

Doktors der Naturwissenschaften

genehmigten Dissertation.

Vorsitzender: Univ.-Prof. Dr. S. Günther

Prüfer der Dissertation:

1. Univ.-Prof. Dr. U. K. Heiz
2. Univ.-Prof. Dr. R. Nießner
3. Univ.-Prof. Dr. M. Moseler, Albert-Ludwigs-Universität Freiburg

Die Dissertation wurde am 16.02.2012 bei der Technischen Universität München eingereicht und durch die Fakultät für Chemie am 08.03.2012 angenommen.

Table of contents

Theoretical section

Experimental section

Results

Summary and outlook

Abstract

The spectroscopic investigation of supported size selected metal clusters over a wide wavelength range plays an important role for understanding their outstanding catalytic properties. The challenge which must be overcome to perform such measurements is the difficult detection of the weak spectroscopic signals from these samples. As a consequence, highly sensitive spectroscopic methods are applied, such as surface Cavity Ringdown Spectroscopy and surface Second Harmonic Generation Spectroscopy. The spectroscopic apparatus developed is shown to have a sensitivity which is high enough to detect sub-monolayer coverages of adsorbates on surfaces. In the measured spectra of small supported silver clusters of the sizes Ag_{42}, Ag_{21}, Ag_9, and Ag atoms a stepwise transition from particles with purely metallic character to particles with molecule-like properties can be observed within this size range.

Zusammenfassung

Die spektroskopische Untersuchung von massenselektierten Metall Clustern auf Oberflächen über einen großen Wellenlängenbereich spielt eine Schlüsselrolle in der Aufklärung ihrer besonderen katalytischen Eigenschaften. Die Herausforderung solcher Messungen liegt in der Detektion der sehr kleinen spektroskopischen Signale solcher Proben. Daher werden hoch sensitive spektroskopische Methoden verwendet, wie die "surface Cavity Rindown Spektroskopie" und die "surface Second Harmonic Generation Spektroskopie". Es wird gezeigt, dass der entwickelte spektroskopische Aufbau sensitiv genug ist, um sub-Monolagen von Oberflächenadsorbaten zu detektieren. Anhand von Messungen von massenselektierten Silber Clustern der Größen Ag_{42}, Ag_{21}, Ag_9 und Ag Atomen auf einer Glasoberfläche kann der schrittweise Übergang von Clustern mit rein metallischen Eigenschaften zu solchen mit molekül-artigen Eigenschaften in diesem Größenbereich beobachtet werden.

1 Introduction

Metals represent 92 of the elements in the periodic table, equivalent to roughly 78 % of all known elements, and thus possess a large variety of physical and chemical properties. These properties have been investigated for centuries, with the result that metals and metal alloys have become one of the most important raw materials for industry. The outstandingly useful mechanical and electrical properties of metals have led to important developments, making a crucial contribution to the success of, for instance, the industrial revolution. The material properties of metals are mainly dominated by the existence of weakly bound electrons in the metal atoms, which when combined in a lattice form an "electron gas" that can move quasi freely inside the entire structure. This electron gas is responsible for the typical characteristics of metals such as electrical conductivity and the mechanical flexibility. However, the physical characteristics of the metallic bulk material are not determined by the intrinsic nature of its building blocks (i.e. the individual atoms), but are developed by the assembly of many metal atoms. As a consequence, the number of metal atoms which a metal particle is composed of, highly influences its physical properties.[1] This opens up the possibility of tuning these properties of a metal by forming small particles (termed metal clusters) and varying their size. Such a tailoring of the physical material characteristics may enable the development of new materials based on small metal clusters for applications in many fields, such as physics, biology, and medicine.[2, 3]

Cluster catalysis

One commonly used chemical application of metals and metal particles is catalysis, which is a field of great importance for the chemical and pharmaceutical industry. In catalysis, a reactant (e.g. an organic molecule) is modified by the electronic interaction with the catalyst (e.g. a Pt metal particle), which accelerates the rate of a chemical reaction. Without the use of specialized catalysts, the chemical synthesis of a large fraction of the today's important organic compounds (medical drugs, synthetic materials etc.) would be either impossible or expensive, achieving only very little yield. However, the enormously growing demand for these products requires the development of new catalysts with an increased selectivity at lower prices. A special area in catalysis is the synthesis of enantiopure compounds, which are of great importance in the pharmaceutical industry because such compounds play an important role in biological systems.[4] Enantio-selective catalysis is, however, an enormous challenge requiring the development of new catalytic materials. These challenges have triggered research into new approaches in catalysis by attempting to selectively tailor the catalytic properties of metal particles. One important step was the more recent discovery of the dependency of the catalytic activity on particle size.[5] This dependency was first observed in experiments using very small, size selected gas phase clusters, consisting of only 1 to 50 atoms[6-11] and was later confirmed by experiments on supported size selected clusters.[12-14] The possibility to tune the catalytic properties of a metal cluster by varying its size could therefore significantly contribute to the development of a completely new generation of catalysts. Furthermore, the possible existence of chiral cluster samples (suggested by theoretical considerations)[15] may even lead to enantio-selective heterogeneous cluster catalysis. These interesting results show that cluster catalysis is an exciting research field with huge potential for future applications. However, in order to tailor the properties of a cluster catalyst towards a specific catalytic application requires the understanding of the influence of several factors on the catalytic activity, such as the cluster size, cluster shape, and the support material. Consequently, systematic studies are necessary. Here, the investigation of the electronic structure of the metal clusters can play a key role.

Electronic properties of clusters

The intrinsic catalytic activity of a catalyst is mainly determined by its electronic properties. One possibility to gain information about the catalytic properties of a metal cluster is consequently the investigation of its electronic structure. As already seen for the catalytic properties, the electronic structure of small metal clusters also varies with cluster size. This effect is particularly pronounced in the size regime of very small clusters (1 - 50 atoms) where every single atom in the cluster has a great influence on the overall electronic properties of the metal particle. In this "non scalable size regime", quantum size effects have a drastic impact on the electronic structure of the cluster.[16-18] The investigation of these electronic size effects can be key for understanding the catalytic properties of small metal clusters and are therefore the subject of many studies in physical chemistry.

For the commercial application of tailor made catalysts based on small metal clusters the particles must, for practical reasons, be supported on a suitable substrate (heterogeneous catalysis). Consequently, in order to understand the properties of supported metal particles, not only must the electronic properties of the clusters themselves be considered, but also their interaction with the substrate and other neighboring clusters, which are each important factors influencing the electronic and therefore catalytic properties of the material. As a result, the investigation of samples with supported metal clusters representing realistic catalytic matter supplies important information about cluster catalysis under conditions which are close to possible applications. However, the study of such clusters is not trivial and necessitates the application, or indeed development of specialist techniques and instrumentation.

Methods for the investigation of the electronic properties of clusters

There are several common techniques that are used to directly investigate the electronic properties of small metal clusters, such as Photoelectron Spectroscopy (UPS/XPS)[19-21], the Electron Energy Loss Spectroscopy (EELS),[22, 23] as well as local techniques such as Atomic Force Microscopy (AFM)[24] and Scanning Tunneling Microscopy (STM),[25, 26] respectively. A second possibility to obtain information about the electronic properties of a cluster is to use an indirect method, where the influence of the cluster on an adsorbed ligand molecule is studied. Here, information about the electronic structure of the metal particle can be gained indirectly, by analyzing several properties of the adsorbed molecules. Such a technique, for example, involves the investigation of the adsobate binding energies to the particle using Temperature Programmed Desorption (TPD) measurements.[27, 28]

Other powerful tools include several optical spectroscopic methods applied in the ultraviolet and visible range of the electromagnetic spectrum, where electronic transitions in the metal clusters can be directly probed.[29, 30] These techniques can, however, be additionally used as an indirect method by analyzing the electronic structure of adsorbate molecules. The electronic transitions in an organic molecule which is adsorbed onto a metal particle are influenced by its electronic interaction with the particle leading to modifications in the UV-Vis spectra of the molecule. A change in the electronic properties of a ligand molecule can additionally lead to shifts in the vibrational resonances of molecules which can be measured in the infrared range.[31, 32] Consequently, a spectroscopic method of investigating metal clusters and adsorbed ligand molecules over a large wavelength range (from the ultraviolet to the infrared) can provide a deep insight into the properties of clusters and their interaction with ligands. This large variety of possible applications included in one single analysis method, makes the optical spectroscopy the favorable technique for the investigation of cluster samples; however, there are a number of challenges.

Challenges

There are several studies on the electronic properties of small metal cluster presented in the literature using optical spectroscopy, which are typically carried out with clusters in either the gas phase[33-35] or embedded in rare gas matrices.[36-39] However, very little is known about the optical properties of small clusters that are supported on substrates (which have more practical applications, such as in heterogeneous catalysis). The reasons for this are the extraordinarily high requirements on the experimental methods, necessary for the production and spectroscopic investigation of such cluster samples. In order to clearly identify cluster size effects, the investigated sample must contain only clusters of one single size. However, to fulfill this condition, two aspects of the experiment must be considered. Firstly, size-selected clusters must be produced and deposited onto a sample and secondly, the agglomeration of clusters on the surface must be avoided. The latter condition can only be achieved by keeping the surface coverage of clusters as low as possible (~1% of a monolayer). However, this low coverage in combination with the small absorption cross sections expected for small metal particles, leads to very weak spectroscopic signals which are beyond the sensitivity of standard spectroscopic methods. Consequently, highly sensitive spectroscopic techniques must be developed to resolve such small spectroscopic features. Furthermore, in order to avoid the contamination of a sample, the experiments must be carried out under ultrahigh vacuum conditions. This is crucial for the production of size selected clusters, as well as for their spectroscopic characterization. Consequently, a specially designed apparatus is needed, so that the entire experimental procedure can be performed within a vacuum chamber, which necessitates the adaption of the desired highly sensitive spectroscopic methods.

Topic of this thesis

The central aim of this thesis is to investigate the electronic properties of small, size selected metal clusters (1 - 50 atoms) that are supported on a substrate, using highly sensitive optical spectroscopy. The applied spectral range should therefore cover the wavelength regions from the ultraviolet to the infrared, allowing for the investigation of the electronic transitions in metal clusters and adsorbed molecules (UV-Vis range) as well as the study of vibrational transitions in the latter (IR range). These wavelength regions of interest, required to investigate the various electronic (UV-Vis) and vibrational transitions (IR) of the supported metal clusters and organic ligands are summarized pictorially in figure 1-*01*.

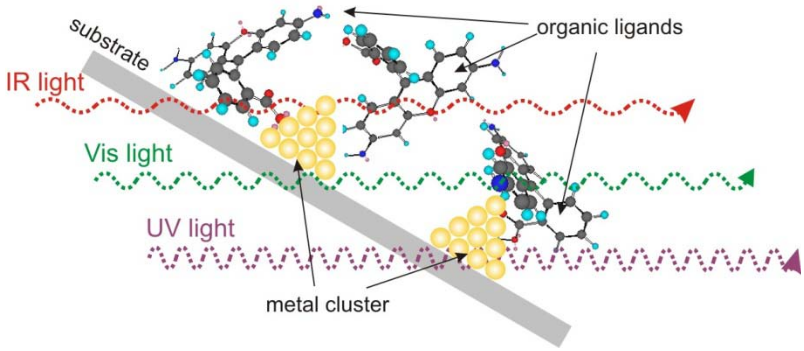

Fig. 1-*01*. Spectroscopic investigation of a cluster sample with organic absorbates.

In order to perform these measurements, an instrument must first be developed and characterized, which allows the preparation and spectroscopic investigation of such samples under UHV conditions, using an already existing cluster source. Here, the main challenge consists of the installation of a suitable spectroscopic setup and its adaptation for the use in combination with an UHV chamber. The second step is then the spectroscopic investigation of the cluster samples using the installed apparatus, where the evolution of the optical (electronic) properties of size selected clusters with the cluster size is of central interest. The results should contribute towards a better understanding of the role of those clusters in catalytic reactions.

Spectroscopic methods used in this thesis

Due to the weak spectroscopic signals of the cluster samples mentioned previously, highly sensitive spectroscopic methods must be employed. In order to cover the broad wavelength range from the ultraviolet to the infrared two different types of spectroscopic techniques are used, the highly sensitive Surface Cavity Ringdown Spectroscopy (s-CRDS) and Surface Second Harmonic Generation Spectroscopy (s-SHG), the latter of which is a nonlinear method. s-CRDS can be applied in both the visible and the infrared wavelength range, whereas s-SHG spectroscopy covers the ultraviolet range. Both techniques are laser based methods which allow the measurement of low surface coverages of adsorbates and are thus used in this thesis.

Outline of this thesis

The presented thesis is divided into three main parts. In the beginning (chapter 2), the theoretical aspects of the spectroscopic methods are discussed, followed by a presentation of the basic theoretical concepts describing the optical properties of small metal particles (chapter 3). In the experimental section, the apparatus for the sample preparation is shown (chapter 4) and the implementation of the different spectroscopic methods (s-Vis-CRD, s-IR-CRD, s-SHG) into one single experimental setup, which is furthermore adapted for the use in a vacuum chamber is described in detail (chapter 5). The challenge here was to design a setup which allows fast switching between different spectroscopic methods, and enables their application in the study of the very same sample. In the third part of the thesis, the results from different measurements are shown and discussed. Starting from chapter 6, which concerns the spectroscopic properties of different substrate materials and discusses the adequacy for the different spectroscopic methods, measurements of different organic molecules coated onto substrates are subsequently presented (chapter 7). The results obtained here are used in order to demonstrate the reliability and the high sensitivity of the spectroscopic setup. In the last results chapter (chapter 8), measurements of supported metal clusters are shown. The most detailed characterization is carried out with supported silver clusters of different sizes. Here, the evolution of the spectroscopic properties with decreasing cluster size and with varying cluster shape is particularly investigated and compared to both, theoretical predictions and other measurements which are present in the literature.

2. Linear and Nonlinear Spectroscopic Methods

In the following sub-chapters, the theoretical aspects of the spectroscopic methods which are used in this thesis are presented. In the beginning, the principles of the linear technique, surface Cavity Ringdown Spectroscopy (s-CRDS), are shown and its sensitivity is discussed. Furthermore, a technique is presented (transversal mode matching) which allows for improving the sensitivity of the spectroscopy, in particular, if solid samples are investigated. In the second part, the theoretical aspects of the nonlinear spectroscopic technique, surface Second Harmonic Generation Spectroscopy (s-SHG), are explained in detail, in combination with the discussion of the type of information it can yield.

2.1. Surface Cavity Ringdown Spectroscopy (s-CRDS)

Cavity Ringdown spectroscopy is a highly sensitive linear absorption technique. It is widely used in gas phase studies, e.g. for the detection of trace materials in the ppb range[40-42] or the measurement of very week absorption bands in several species[43-46], such as the weak $b^1\Sigma_g \rightarrow X^3\Sigma_g$ bands of molecular oxygen[47]. The application of CRDS to solid samples (s-CRDS) is more demanding, however, in some experimental systems the potential of this technique has already been demonstrated[48-56]. In general, a Cavity Ringdown apparatus consists of a laser source, an external optical resonator (cavity), and a detection unit. The working principle of CRDS is presented in the following sections.

2.1.1 Theory of s-CRDS

A single laser pulse is injected into an optical resonator (cavity) consisting of two highly reflective dielectric mirrors (reflectivity > 99.98 %), and is reflected back and forth while a small fraction of the light leaks out of the cavity in each reflection. This causes a decrease in the total intensity of light inside the cavity, diminishing in form of an exponential decay function. By detecting the light that leaks from the cavity, the ringdown signal can be measured in order to determine the ringdown time, and subsequently the loss of photons within the cavity. In figure *2-01*, a schematic of the external resonator for surface Cavity Ringdown measurements is shown.

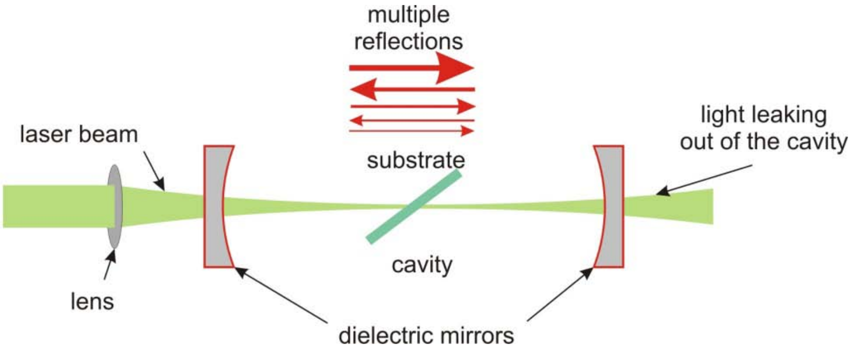

Fig. 2-*01*. Optical resonator for s-CRD measurements. A laser pulse is reflected back and forth between the two mirrors, while a small fraction of the light leaks from the resonator.

For an empty cavity (note that between the two mirrors there is only vacuum), the time evolution of the light intensity behind the resonator, I_t, can be described using equation 2-01.

$$I_t = I_0 \cdot e^{t \cdot \frac{c}{d} \ln(R)} \quad \textit{(eq.2-01)}$$

where, I_0, is the light intensity at $t = 0$ (behind the resonator), R, the reflectivity of the dielectric mirrors, c, the speed of light in vacuum, and d, the distance between the two CRD mirrors. The value I_0 is proportional to the light intensity of the laser pulse, I_{laser}, and can be expressed as:

$$I_0 = I_{\text{laser}} \cdot (1 - R)^2 \quad \textit{(eq.2-02)}$$

Equation 2-01 describes the exponentially decaying time evolution of the intensity of a laser pulse behind the cavity. This function is measured using a photomultiplier. The resulting data points are fitted using the function:

$$f_{(t)} = A \cdot e^{-\frac{t}{\tau}} + B \quad \textit{(eq.2-03)}$$

where, A, B, and τ are the fit parameters (the parameter B is introduced to account for any linear offsets). The time constant, τ, is called "ringdown time". Comparing equations 2-01 and 2-03, the following expression for the ringdown time in an empty cavity can be found:

$$\tau = -\frac{d}{c \cdot \ln(R)} \quad \textit{(eq.2-04)}$$

From the ringdown time, the fraction of extinguished photons inside the cavity per path of the laser beam (Λ) can be calculated. Considering that the travelling time per path is $\Delta t = d/c$, the relative photon loss per path is given by:

$$\Lambda = \frac{I_t - I_{t+\Delta t}}{I_t} = 1 - e^{-\frac{d}{c\cdot\tau}} \approx \frac{d}{c\cdot\tau} \quad \text{for } c\cdot\tau \gg d \qquad \textit{(eq.2-05)}$$

Equation 2-05, however, is only valid for small losses Λ. In the case of the empty cavity, the loss can be calculated by:

$$\Lambda^{(\text{empty cavity})} = 1 - R \qquad \textit{(eq.2-06)}$$

which is intuitively correct, because all photons that are extinguished inside the cavity are the photons which are not reflected by the CRD mirrors. If a sample is introduced into the cavity, additional photon losses originating from absorption and scattering processes are generated. In order to account for these losses, equation 2-01 is extended to equation 2-07.

$$I_t = I_0 \cdot e^{t\frac{c}{d}\ln(R)} \cdot e^{-t\frac{c}{d}\cdot\alpha_{ext}} = I_0 \cdot e^{t\frac{c}{d}(\ln(R)-\alpha_{ext})} \qquad \textit{(eq.2-07)}$$

here, α_{ext}, represents the extinction coefficient of the sample. From this equation, the ringdown time is then calculated using:

$$\tau = -\frac{d}{c\cdot\ln(R)} + \frac{d}{c\cdot\alpha_{ext}} \qquad \textit{(eq.2-08)}$$

and the corresponding relative photon loss is consequently given by:

$$\Lambda \approx (1-R) + \alpha_{ext} = \Lambda^{(\text{empty cavity})} + \alpha_{ext} \qquad \textit{(eq.2-09)}$$

Equation 2-09 shows that the different sources of photon losses inside the cavity are additively connected and that those losses directly represent the extinction coefficients. An important consequence of this is, that the losses obtained from the measurement of the empty cavity can be simply subtracted to determine the extinction coefficients of the sample. In order to measure an entire spectrum, the ringdown signals are recorded as a function of the laser wavelength. Using the fit function in equation 2-03, the ringdown times for each wavelength and subsequently the photon losses can be extracted. By subtracting a reference measurement and plotting the relative photon losses as a function of the wavelength, the linear absorption spectrum of a sample is obtained. The advantage of the CRD technique over more common linear absorption techniques (i.e. a commercial UV-Vis spectrometer instrument) is its superior sensitivity, as demonstrated in ref[57, 58].

2.1.2 Sensitivity of s-CRDS

With the Cavity Ringdown technique it is possible to measure relative photon losses which are smaller than one extinguished photon (part) per million (1 ppm). This high sensitivity has two main origins. Firstly, from equation 2-03 it can be seen, that the ringdown time is independent of the initial laser intensity, I_0, which avoids any fluctuations in the laser intensity from disturbing the measurement. In an s-CRD experiment there is consequently no noise arising from the laser source (this is strictly valid only in theory). The second origin is based on the application of the fit function on the ringdown signal. The signal itself represents thousands of absorption processes because the light travels through the sample at each path of the laser light inside the cavity. By fitting the exponential function to the ringdown signal, the resulting value of the ringdown time is already an average over all of these absorption incidences. In other words, the extracted ringdown time of one single laser pulse has the accuracy of the average of thousands of single transmission experiments. As a consequence, the larger the ringdown time is, the higher is the sensitivity of the technique. This leads to the necessity to keep all losses as small as possible. In order to achieve this, special dielectric cavity mirrors must be used with a reflectivity of more than 99.98 %. Such mirrors do not exist as broadband mirrors and consequently, the applicable wavelength range where the reflectivity is above this value is limited. By combining some sets of mirrors which have the maximum of reflectivity centred at different wavelengths, this range can be extended. However, to cover e.g. the entire visible range (400 nm-650 nm) at least five mirror pairs are needed.

In order to study adsorbates on surfaces using s-CRD spectroscopy, a solid sample must be introduced into the cavity. As a result, the photon loss is highly increased. In order to limit this additional photon loss, all possible sources of light extinction must be minimized. Consequently, one fundamental condition for a suitable substrate is a very high transparency over the entire wavelength range of interest. Using Brewster´s angle configuration, reflection losses from the substrate are minimised and the main source of light extinction which is left is light scattering at the surfaces (front and rear) of the substrate. Its surfaces should therefore be as smooth as possible in order to minimize the scattering.

The scattering of light, however, is wavelength dependent. If the diameter, d, of the scattering centres is small compared to the wavelength of the light, the wavelength dependency of the scattering cross section, $\sigma_{(sca)}$, follows the Rayleigh law:

$$\sigma_{(sca.)} = \frac{2\pi^5}{3}\frac{d^6}{\lambda^4}\left(\frac{n^2-1}{n^2+2}\right)^2 \qquad \textit{(eq.2-10)}$$

where, λ, is the wavelength of the light, and n, the refractive index of the particle material. Equation 2-10 shows that the scattering cross section is proportional to $1/\lambda^4$. This means that for decreasing wavelengths the amount of scattered light increases drastically. As a consequence, the sensitivity of the CRD technique with solid samples strongly diminishes towards the ultraviolet region.

Light scattering occurs at any material and consequently, it also occurs at the surfaces of the CRD mirrors. This explains the observation that the reflectivities of CRD mirrors for the ultraviolet region are smaller than for the visible region (see chapter 6.4.1) leading to a further decrease in the sensitivity of CRD in the UV region. The scattering problem thus limits the reasonably applicable range of the Cavity Ringdown spectroscopy to the visible and the infrared wavelength range.

2.1.3 Transversal Mode Matching

The mathematical descriptions given in chapter 2.1.1 are only valid if one single mode of the resonator is excited. In reality, this is hardly possible to achieve and the light beam oscillating between the two mirrors consists of the superposition of several different resonator modes. Firstly, there is a superposition of longitudinal modes inside the cavity originating from the spectral width of the laser pulse. Each longitudinal mode has a slightly different ringdown time and consequently, the measured value represents an averaged ringdown time. However, as long as the measured absorption bands of the sample are broader than the spectral width (this is usually the case for electronic transitions in the visible range and vibrational transitions in the infrared range), this does not lead to a distortion of the spectrum. A different situation, however, is present for the superposition of different transversal electromagnetic resonator modes (TEM modes) inside the cavity. Each TEM mode has a different intensity distribution in the plane orthogonal to the propagation direction of the light. This is the case at the position of the cavity mirrors as well as in the middle of the cavity where the sample is placed. The losses at different positions on the sample can vary hugely, which leads to very different ringdown times for each TEM mode. Furthermore, the homogeneity of the mirrors is also far from being perfect. As a consequence, the measured ringdown signal consists of several contributions of highly different ringdown times which are averaged by the exponential fit. However, if the beam profile of the used laser source is not stable from pulse to pulse or the position of the cavity changes e.g. due to vibrations, the composition of the different TEM modes changes from laser pulse to laser pulse. As a result, a rather large noise in the measured spectrum can be observed which diminishes the signal to noise ratio. In order to circumvent this problem, it must be ensured that only the fundamental TEM_{00} resonator mode is excited. This mode has a Gaussian intensity distribution and is that one with the smallest waist in the middle of the cavity. Therefore, two conditions must be fulfilled. The laser beam itself must have a Gaussian beam profile and the beam must be guided via lenses in the cavity in such a way, that its beam parameters (curvature of the wave front and the beam diameter) match those of the TEM_{00} resonator mode (the latter are defined by the curvature of the CRD mirrors and their distance). The shaping of the laser beam to form a Gaussian beam profile can be performed by focussing the laser beam through a small pinhole (spatial filtering). In order to perform the mode matching, several focusing lenses must be placed at exactly defined positions in the beam path in front of the cavity. The positions can be calculated using the formalism of the ray transfer matrix analysis for Gaussian beams[59]. It could be shown that, using these techniques, the signal to noise ratio is considerably enhanced (noise reduction of 50 %)[60]. More details about the calculations for the transversal mode matching can be found in a previous dissertation[61].

2.2 Surface Second Harmonic Generation Spectroscopy (s-SHG)

Surface Second Harmonic Generation Spectroscopy (s-SHG) is a surface sensitive technique which makes use of the nonlinear effects that occur at interfaces when illuminated by strong laser pulses[62]. "Nonlinear" means here that these effects do not depend linearly on the intensity of the fundamental light pulse. s-SHG spectroscopy allows for the very precise measurement of resonances at the interface regions between two different media, such as air-liquid, liquid-liquid, solid-liquid, solid-air interfaces[63]. Due to the special symmetry rules for the SHG process, the technique gives information about orientations of the probed species with respect to the interface[64-67]. In the following, the basic theory of the generation of the second harmonic and its application as surface sensitive spectroscopic method is shown.

2.2.1 The Generation of the Second Harmonic

In classical linear optics, the polarization density of matter, $\vec{P}_{(t)}$, which is irradiated by an electromagnetic wave is described by equation 2-11.

$$\vec{P}_{(t)} = \varepsilon_0 \cdot \vec{\chi} \cdot \vec{E}_{(t)} \quad \textit{(eq.2-11)}$$

where, $\vec{E}_{(t)}$, is the electric field component of the electromagnetic wave, ε_0, the electric permittivity of vacuum, and $\vec{\chi}$, the electric susceptibility tensor. Equation 2-11 connects the oscillation of the electric field of light and the induced oscillation of charges in the matter in a linear relation. This is valid under the assumption, that the charges in the material are confined in a harmonic potential, which is a good approximation for small displacements of the charges during the oscillation induced by weak electric fields. However, for strong electric fields, for example, in short laser pulses, the harmonic potential approximation is no longer suitable because new, nonlinear effects occur which cannot be described by equation 2-11. In order to account for the anharmonicity of the potential, the susceptibility tensor must be replaced by a parameter which is dependent on the electric field $\vec{E}_{(t)}$. This parameter can be expressed as a Taylor series of the susceptibility tensor as a function of the electric field.

$$\vec{\chi} = \vec{\chi}^{(1)} + \underbrace{\frac{d\vec{\chi}}{d\vec{E}_{(t)}}}_{\vec{\chi}^{(2)}} E_{(t)} + \underbrace{\frac{d^2\vec{\chi}}{d\vec{E}^2_{(t)}}}_{\vec{\chi}^{(3)}} E^2{}_{(t)} + \ldots \quad \textit{(eq.2-12)}$$

where, $\vec{\chi}^{(1)}, \vec{\chi}^{(2)}, \vec{\chi}^{(3)}$ are the first, second, and third order susceptibilities. Inserting equation 2-12 into equation 2-11 yields:

$$\vec{P}_{(t)} = \varepsilon_0 \cdot \left(\vec{\chi}^{(1)} \vec{E}_{(t)} + \vec{\chi}^{(2)} \vec{E}^2_{(t)} + \vec{\chi}^{(3)} \vec{E}^3_{(t)} + \ldots \right) \quad \textit{(eq.2-13)}$$

Equation 2-13 shows that the polarization density for the model of the anharmonic potential is a superposition of a linear term (described by the first order susceptibility) and additional nonlinear terms. If a monochromatic electromagnetic wave of the form $E_{(t)} = E_0 \cos(\omega t)$ is inserted in equation 2-13, the polarization density is derived to give:

$$P_{(t)} = \varepsilon_0\left(\chi^{(1)}\cdot E_0\cos(\omega t) + \chi^{(2)}\cdot E_0^{\;2}\cos^2(\omega t) + \chi^{(3)}\cdot E_0^{\;3}\cos^3(\omega t) + \ldots\right)$$

$$= \varepsilon_0(\chi^{(1)}\cdot E_0\cos(\omega t) + \frac{1}{2}\chi^{(2)}E_0^{\;2} + \frac{1}{2}\chi^{(2)}E_0^{\;2}\cdot\cos(2\omega t) +$$

$$+\frac{3}{4}\chi^{(3)}E_0^{\;3}\cdot\cos(\omega t) + \frac{1}{4}\chi^{(3)}E_0^{\;3}\cdot\cos(3\omega t) + \ldots) \quad \textit{(eq.2-14)}$$

The linear part of the polarization oscillates at the fundamental frequency; however, the nonlinear terms lead to contributions to the oscillation at the second (shown in red) and third harmonic frequency (blue). Since the contribution of the nonlinear terms highly depends on the amplitude of the electromagnetic wave, they can be neglected for low power electromagnetic waves but must be considered for high power waves, such as those in short laser pulses. In figure 2-*02*, the polarization is plotted as function of time for the low power and the high power case. The latter clearly shows the contribution of an oscillation at the second harmonic frequency.

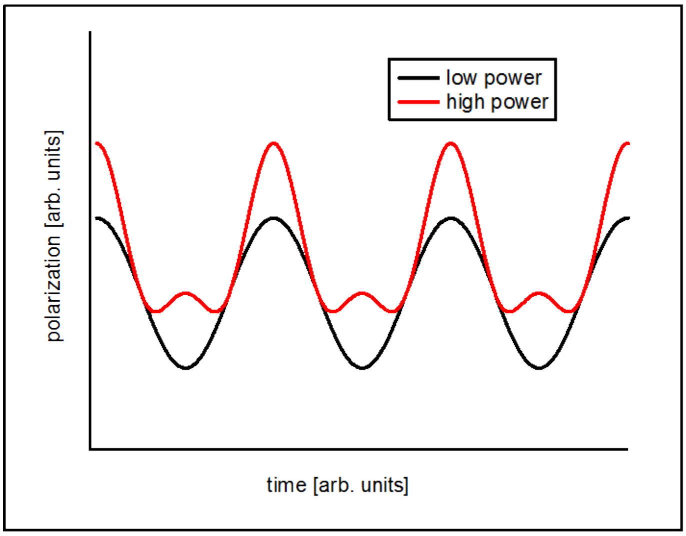

Fig. 2-*02*. Polarization of matter as function of time for low power irradiation (black line) and high power irradiation (red line). In the high power case, a contribution of an oscillation at the second harmonic frequency can be observed.

Following equation 2-14, the polarization can be expressed as superposition of a linear $(\vec{P}^{(1)}{}_{(t)})$ and nonlinear polarizations $(\vec{P}^{(n)}{}_{(t)})$.

$$\vec{P}_{(t)} = \vec{P}^{(1)}{}_{(t)} + \vec{P}^{(2)}{}_{(t)} + \vec{P}^{(3)}{}_{(t)}\ldots \quad \textit{(eq.2-15)}$$

In the following, we concentrate on the second order nonlinear effect and neglect higher order contributions. The second order polarization can be consequently written as:

$$P^{(2)}{}_{(t)} = \varepsilon_0 \cdot \left(\frac{1}{2}\chi^{(2)} E_0{}^2 + \frac{1}{2}\chi^{(2)} E_0{}^2 \cdot \cos(2\omega t) \right) \quad \textit{(eq.2-16)}.$$

The oscillation of the polarization at the second harmonic frequency is the source for the generation of an electromagnetic wave at this frequency. If the light source is a coherent laser source, the generated second harmonic beam is also a coherent, laser-like beam. This facilitates the detection of the generated photons because standard laser optics can be used. Following from equation 2-16, the electric field of the generated SH beam can be expressed as:

$$E_{(2\omega)(t)} \sim \chi^{(2)} E_0{}^2 \cdot \cos(2\omega \mathrm{t}) \quad \textit{(eq.2-17)}$$

and its intensity, $I_{(2\omega)}$, is consequently:

$$I_{(2\omega)} \sim \left|\chi^{(2)}\right|^2 \cdot I_{(\omega)}{}^2 \quad \textit{(eq.2-18)}.$$

Equation 2-18 shows a fundamental characteristic of the SHG process: The intensity of the generated second harmonic beam increases with the square of the intensity of the fundamental beam $(I_{(\omega)})$.

The equations shown in this section represent the fundamental classical description of nonlinear processes. Equivalent quantum mechanical formalisms lead to the same results.[68, 69]

2.2.2 Second Harmonic Generation in a Nonlinear Crystal

If the second harmonic is generated in a nonlinear crystal, interferences between the SH components that are generated at different positions in the crystal occur, which drastically diminish the intensity of the resulting SH beam. The reason for the interferences is the fact that in any dispersive material, the phase velocities of electromagnetic waves with different frequencies differ from each other. This leads to a different travelling speed of the fundamental and the second harmonic beams through the crystal, the result of which is that the SH beams generated at different positions in the crystal possess a different phase. A complete constructive interference of the SH beams can consequently only be achieved in a material where the refractive indices (the refractive index is defined by the phase velocity) at the fundamental and the second harmonic frequency are equal. The most common possibility to realize this is the use of birefringent crystals. If a light beam travels through a birefringent crystal, the beam is split into two components, an ordinary wave which follows the Snell's law of refraction and an extraordinary wave with different properties. One of these properties is the anisotropy of the phase velocity of the extraordinary wave in the crystal. The propagation speed of the extraordinary wave consequently depends on the polarization of the incident light wave and the angle of incidence with respect to the crystal planes. As a result, there are two refractive indices correlated to birefringent materials, an isotropic ordinary, n_o, and an anisotropic extraordinary, n_{eo}. By turning the crystal n_{eo} can be modified, whereas n_o remains constant. This can be used to achieve complete constructive interference in an SHG process since an angle of incidence can be found were the ordinary refractive index at the fundamental frequency matches the extraordinary refractive index at the second harmonic frequency $n_o{}^{(\omega)} = n_{eo}{}^{(2\omega)}$. This procedure is called "phase matching" and the specific angel "phase matching angle". For each fundamental frequency, a different phase matching angle must be adjusted. Under phase matching conditions transformation efficiencies from the fundamental to the second harmonic beam of up to 60 % can be reached[70].

2.2.3 Symmetry Considerations and Surface Sensitivity

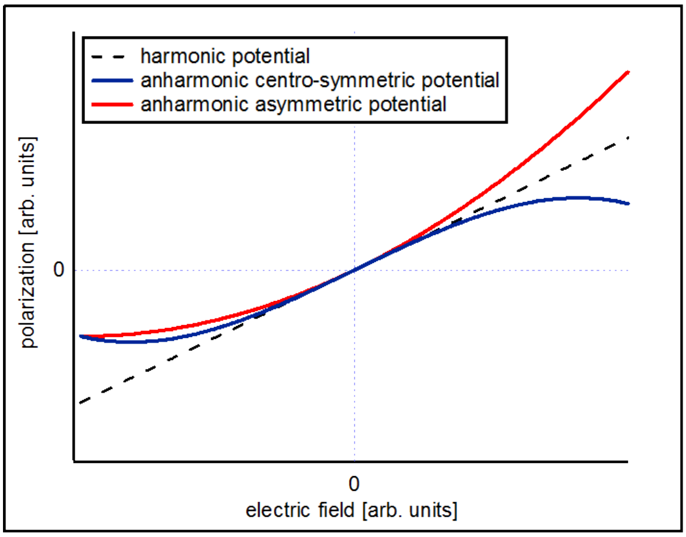

Fig. 2-*03*. Polarization of matter plotted as a function of the electric field for three different potentials.

The second order susceptibility possesses some distinct symmetry properties[62, 68, 69] which are discussed in the following. The most important property of $\chi^{(2)}$ is that in a centro-symmetric electric environment the second order susceptibility is zero. This can be illustrated using figure 2-*03*. Here, the polarization of the matter is shown as a function of the electric field for different electric potentials in which the charges are confined. The black dotted line represents the harmonic potential, the blue line an anharmonic centro-symmetric potential, and the red line an anharmonic asymmetric potential. As discussed in chapter 2.2.1, in a harmonic potential the second harmonic frequency is not generated. From the curve for the anharmonic centro-symmetric potential, the following relation can be extracted:

$$-P_{(t),(E)} = P_{(t),(-E)} \quad \textit{(eq.2-19)}$$

Inserting equation 2-13 into equation 2-19 yields:

$$-\varepsilon_0\left(\chi^{(1)}E_{(t)} + \chi^{(2)}E^2_{(t)} + \chi^{(3)}E^3_{(t)} + \ldots\right) = \varepsilon_0\left(\chi^{(1)}(-E_{(t)}) + \chi^{(2)}(-E_{(t)})^2 + \chi^{(3)}(-E_{(t)})^3 + \ldots\right)$$

$$\Rightarrow \chi^{(2)} = -\chi^{(2)} \quad \textit{(eq.2-20)}$$

Equation 2-20 can only be fulfilled if $\chi^{(2)} = 0$ and consequently, no oscillation at the second harmonic frequency can be induced in such materials. This is the case, for example, in all materials which have a centro-symmetric crystal structure (the electric potential is here also centro-symmetric). However, for the case of the anharmonic asymmetric potential the second order susceptibility can have any value. Examples for this case are materials, which do not have a centro-symmetric crystal structure (e.g. frequency doubling crystals in laser systems). A special case are randomly ordered systems, for example, amorphous structures, liquids or gases. Even if each subunit of these systems does not have a centro-symmetric structure, the overall potential is centro-symmetric and no second harmonic light is generated. This can be explained by the random orientation of the subunits towards each other which can be combined to a centro-symmetric superstructure. This rule holds, whenever the distances between the subunits are small compared to the wavelength of the used fundamental light[71, 72].

The fact, that in centro-symmetric and randomly ordered systems no second harmonic light is generated can be used in order to achieve an interface sensitivity. At the interface of two different centro-symmetric media, the symmetry is broken and SH photons are consequently generated, whereas inside the bulk of the two media the SHG process is forbidden. As a result, all of the generated photons in such an experiment must originate from the interface region, which allows for investigating this region with a very high sensitivity. By using a solid sample with a centro-symmetric or an amorphous crystal structure, this surface sensitivity of the s-SHG technique is ensured.

2.2.4 Resonance Enhancement of the SHG Process

In order to gain spectral information using s-SHG spectroscopy, the intensity of the generated second harmonic beam is recorded as a function of the wavelength. By dividing the SH intensity spectrum by the square of the intensity spectrum of the fundamental beam, the square of the second order susceptibility as a function of the wavelength is obtained (see equation 2-18).

$$\frac{I_{(2\omega)}}{I^2_{(\omega)}} \sim \left|\chi^{(2)}\right|^2 \quad \textit{(eq.2-21)}$$

For the interpretation of the spectrum of the second order susceptibility, its properties must first be understood, especially in wavelength regions with resonance transitions in the investigated system. The dispersion relation of the second order susceptibility can be derived using a classical description of the oscillation of electrons induced by an external field, $E_{(t)}$, where the electrons are confined in an anharmonic potential[68]. This potential, $U_{(x)}$, expressed as a function of the displacement, x, from the equilibrium is given as:

$$U_{(x)} = \frac{1}{2}kx^2 + \frac{1}{3}\alpha x^3 + \frac{1}{4}\beta x^4 + \ldots \quad \textit{(eq.2-22)}$$

where, k, α and β, are parameters. The restoring force, F, acting on the electron is consequently given by:

$$F = -\frac{dU_{(x)}}{dx} = -\left(kx + \alpha x^2 + \beta x^3 + \ldots\right) \quad \textit{(eq.2-23)}$$

In the following, only the first two summands are used because they are responsible for all first and second order effects. With a damping of the oscillation of γ, the motion of one electron can be described by the following differential equation:

$$\frac{d^2x_{(t)}}{dt^2} + \gamma\frac{dx_{(t)}}{dt} + \omega_0{}^2 \cdot x_{(t)} + \frac{\alpha}{m} \cdot x^2{}_{(t)} = -\frac{e}{m}E_{(t)} \quad \textit{(eq.2-24)}$$

where, $x_{(t)}$, represents the position of the electron as function of time, e, is the charge, and m, the mass, and finally ω_0, is the resonance frequency of the corresponding harmonic oscillator $\left(\omega_0 = \sqrt{k/m}\right)$. The term $\omega_0^{\,2} \cdot x_{(t)} + \frac{\alpha}{m} \cdot x^2_{(t)}$ describes the restoring force acting on the electron in the anharmonic potential according to equation 2-23. Equation 2-24 can be solved for a monochromatic excitation wave, $E_{(t)}$, using the perturbation theory. With the perturbation parameter α/m the solution has the form:

$$x_{(t)} = x^{(1)}{}_{(t)} + \frac{\alpha}{m} \cdot x^{(2)}{}_{(t)} \qquad \textit{(eq.2-25)}$$

where, $x^{(1)}{}_{(t)}$, is the motion of the electron for the harmonic limit. Equation 2-25 describes a superposition of two different oscillations, one is linear and the other nonlinear. With an excitation wave, $E_{(t)}$, of the form:

$$E_{(t)} = E_0 \cdot \left(\frac{e^{i\omega t} + e^{-i\omega t}}{2} \right) \qquad \textit{(eq.2-26)}$$

the solutions for $x^{(1)}{}_{(t)}$ and $x^{(2)}{}_{(t)}$ are given by:

$$x^{(1)}{}_{(t)} = -\frac{e}{m} \cdot \frac{E_0}{\left[\omega_0^{\,2} - \omega^2 - i\gamma\omega\right]} \cdot \left[\frac{e^{i\omega t} + e^{-i\omega t}}{2} \right] \qquad \textit{(eq.2-27)}$$

$$\frac{\alpha}{m} \cdot x^{(2)}{}_{(t)} = -\frac{\alpha \cdot e^2}{4m^3} \cdot \frac{E_0^{\,2}}{\left[\omega_0^{\,2} - \omega^2 - i\gamma\omega\right]^2 \cdot \left[\omega_0^{\,2} - 4\omega^2 - 2i\gamma\omega\right]} \cdot \left[1 + \frac{e^{i2\omega t} + e^{-i2\omega t}}{2} \right] \qquad \textit{(eq.2-28)}$$

where, $x^{(1)}{}_{(t)}$, describes an oscillation at the fundamental frequency ω of the excitation wave. However, $x^{(2)}{}_{(t)}$ possesses an oscillatory part with a frequency of 2ω which is responsible for the generation of the second harmonic, and a second part describing a time independent static displacement of the electron. The latter could already be observed in equation 2-16. From the displacement of the electron, $x_{(t)}$, the polarization, $P_{(t)}$, can be derived using equation 2-29.

$$P_{(t)} = -e \cdot x_{(t)} = -e \cdot x^{(1)}{}_{(t)} - e \cdot \frac{\alpha}{m} \cdot x^{(2)}{}_{(t)} = P^{(1)}{}_{(t)} + P^{(2)}{}_{(t)} \qquad \textit{(eq.2-29)}$$

In combination with equation 2-13, the first and second order susceptibilities can be extracted:

$$\chi^{(1)} = \frac{e^2}{\varepsilon_0 \cdot m} \cdot \frac{1}{\left[\omega_0^2 - \omega^2 - i\gamma\omega\right]} \qquad (eq.2\text{-}30)$$

$$\chi^{(2)} = \frac{\alpha \cdot e^3}{2\varepsilon_0 \cdot m^3} \cdot \frac{1}{\left[\omega_0^2 - \omega^2 - i\gamma\omega\right]^2 \cdot \left[\omega_0^2 - 4\omega^2 - 2i\gamma\omega\right]} \qquad (eq.2\text{-}31)$$

The susceptibilities in equations 2-30 and 2-31 are complex quantities and describe the amplitude and the phase shift of the oscillating polarization with respect to the excitation wave. In an s-SHG experiment, the square of the second order susceptibility is measured according to equation 2-21. In equation 2-32 this quantity is calculated.

$$\left|\chi^{(2)}\right|^2 = \left[\frac{\alpha \cdot e^3}{2\varepsilon_0 \cdot m^3}\right]^2 \cdot \frac{1}{\left[\left(\omega_0^2 - \omega^2\right)^2 + \gamma^2\omega^2\right]^2 \cdot \left[\left(\omega_0^2 - 4\omega^2\right)^2 + 4\gamma^2\omega^2\right]} \qquad (eq.2\text{-}32)$$

In figure 2-*04*, the square of the second order susceptibility is shown as a function of the photon energy (with a damping constant of $\gamma = 1/8\,\omega_0$).

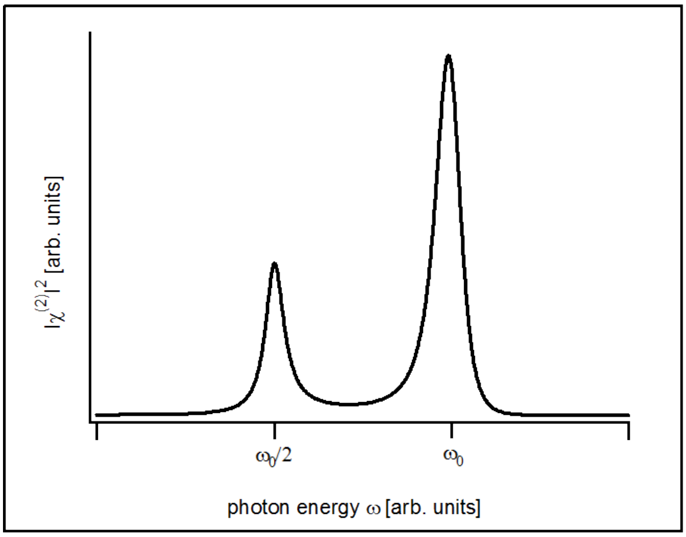

Fig. 2-*04*. Square of the second order susceptibility plotted as a function of the photon energy. Two peaks can be observed in the spectrum, one at ω_0 and the second at $\omega_0/2$.

In the spectrum, two peaks can be observed although there is only one resonance frequency of the oscillator (at ω_0). This observation can be explained by analyzing the product of the denominator in equation 2-32. The spectrum of the susceptibility shows a maximum, whenever the denominator reaches a minimum. This is the case for the first factor at $\omega = \omega_0$ and for the second at $\omega = 1/2\,\omega_0$. There are consequently two maxima for $\left|\chi^{(2)}\right|^2$. Using a photonic picture, the origin of these two different resonance enhancements can be illustrated. In the SHG process, the frequency of the fundamental wave is doubled. This corresponds to the coalescence of two fundamental photons to one single photon with double the energy (SH photon). In figure 2-*05*, three different types of this photon coalescence are shown schematically.

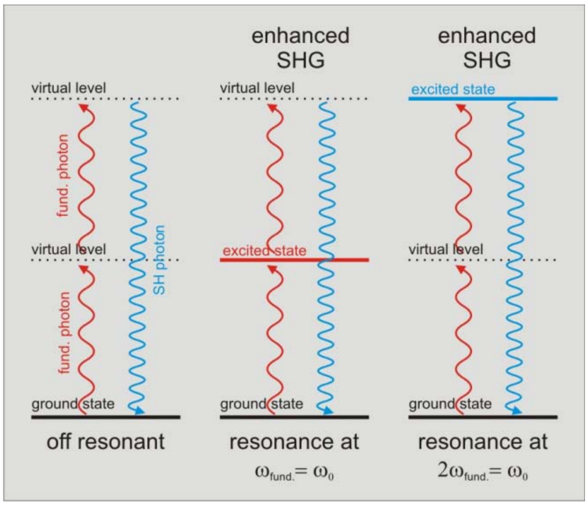

Fig. 2-*05*. Schematic for the illustration of the resonance enhancement of the SHG process using a photonic picture. If the fundamental or the SH photon energy is in resonance with a transition in the material, the SHG transition probability is enhanced.

The first transition type on the left side in the figure starts from the ground state and occurs over two virtual energy levels, whereas for the second and third transition type there is an excited state located at the fundamental and the SH photon energy, respectively. The frequency dependent part of the transition probability for this three photon process is the product of the transition probabilities for each photon. In the second and the third case shown in the figure, the SHG transition probability is consequently enhanced. This is expressed in equation 2-32 by the product in the denominator. The frequency dependent part of the transition probability of each of the two fundamental photons is represented by the expression $\frac{1}{\left[\left(\omega_0^2 - \omega^2\right)^2 + \gamma^2\omega^2\right]}$ and for the SH photon by $\frac{1}{\left[\left(\omega_0^2 - 4\omega^2\right)^2 + 4\gamma^2\omega^2\right]}$. The geometric part of the transition probability (transition dipole moment) corresponds to the expression

$\left[\frac{\alpha \cdot e^3}{2\varepsilon_0 \cdot m^3}\right]^2$, where the parameter α describes the shape of the potential and contains consequently the selection rules for the SHG process derived earlier in chapter 2.2.3. The product of the geometric and the three frequency dependent parts (one for each involved photon) yields the transition probability of the SHG process and is equivalent to the expression in equation 2-32. This demonstrates that the mathematical descriptions of the SHG process derived from classical mechanics is in a good agreement with quantum mechanical considerations.

As shown above, the peaks in the spectrum of $\left|\chi^{(2)}\right|^2$ represent resonances in the measured sample. For the interpretation of the nonlinear spectrum, however, it is necessary to distinguish between the two cases of resonance enhancement to determine the spectral position of the resonance. By applying an additional, complementary highly sensitive linear technique, such as the s-CRD spectroscopy, this crucial information can be obtained. As shown earlier in this chapter, s-CRD spectroscopy is not applicable in the UV range; however, the range of study can be extended towards the UV with s-SHG spectroscopy by using a fundamental laser frequency in the visible range and probing the resonances at the second harmonic frequency (which is consequently in the UV range).

2.2.5 Comparison between Linear and Nonlinear Spectra

Since the measurements which are carried out in this thesis combine linear (s-CRD) and nonlinear spectra (s-SHG), it is necessary to quantify the differences between the two spectra obtained from the same sample. One important aim of this investigation is to verify if the equations derived for the linear spectrum of a sample are also applicable to describe its nonlinear properties. As an example, the model of the anharmonic oscillator (shown previously) is used. The nonlinear spectrum is given by equation 2-32 and the linear absorption spectrum can be calculated from the first order susceptibility given by equation 2-30. The absorption cross section, $\sigma_{abs.}$, of a particle which is small compared to the wavelength is given by equation 2-33:

$$\sigma_{abs.} = \frac{\omega}{c}\operatorname{Im}\left\{\chi^{(1)}\right\} \quad \textit{(eq.2-33)}$$

where, c, is the speed of light in vacuum, and $\mathrm{Im}\left\{\chi^{(1)}\right\}$, is the imaginary part of the first order susceptibility which can be derived from equation 2-30. The absorption cross section of the anharmonic oscillator is then given by:

$$\sigma_{abs.} = \frac{\omega \cdot e^2}{c \cdot \varepsilon_0 \cdot m} \cdot \frac{\gamma \cdot \omega}{\left[\left(\omega_0^2 - \omega^2\right)^2 + \gamma^2 \omega^2\right]} \qquad (eq.2\text{-}34)$$

In figure 2-*06* the spectra of $\sigma_{abs.}$ and $\left|\chi^{(2)}\right|^2$ are shown as function of the fundamental photon energy.

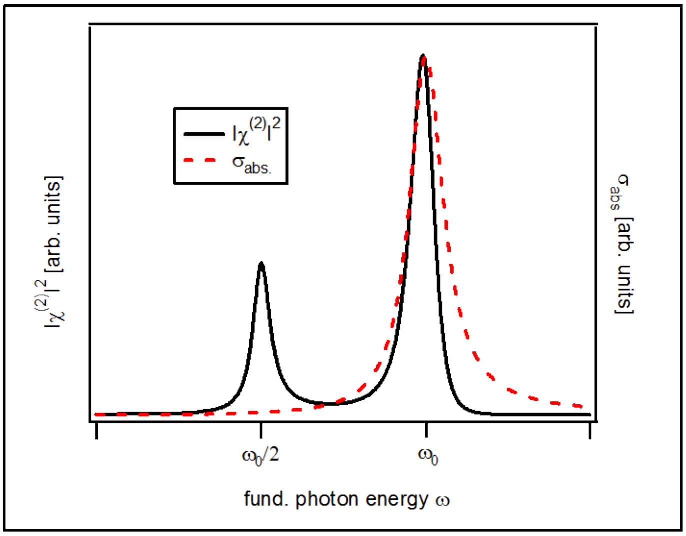

Fig. 2-*06*. Comparison between a linear absorption spectrum and the nonlinear s-SHG spectrum. Both spectra are plotted as function of the fundamental photon energy. The width of the peak at ω_0 in the nonlinear spectrum is reduced and slightly red shifted with respect to the linear spectrum.

The linear spectrum shows one peak at the resonance frequency of the oscillator (ω_0) and in the nonlinear spectrum two peaks (as discussed in the previous section) can be observed. By comparing the linear absorption peak with the nonlinear peak located at the fundamental resonance frequency, ω_0, some differences in the shape can be observed. The nonlinear peak is narrower and slightly red shifted with respect to the linear spectrum. This discrepancy highly complicates the direct comparison of the two spectra, and especially the estimation of the damping constant of the oscillator (responsible for the peak width) from the nonlinear spectrum is difficult. The interpretation of a peak in the nonlinear spectrum originating from the resonance at the fundamental frequency using the equations describing the linear spectrum is consequently not very accurate. However, the much lower complexity of the linear description compared to the nonlinear one makes the use of the former favourable.

In figure 2-*07*, the nonlinear spectrum is plotted as function of the second harmonic photon energy (2ω) and compared to the linear absorption spectrum (the latter is plotted as function of the fundamental photon energy). Using this method, the peak located at $\omega_0/2$ (fund. frequency) of the nonlinear spectrum is superimposed with the linear absorption peak. In the figure, it can be observed that those two peaks match each other almost perfectly (in position as well as in peak width). In this case, the use of the linear description for the interpretation of the peak in the s-SHG spectrum (at $\omega_0/2$) is consequently justified in a good approximation. However, in order to perform, for example, a fit of the nonlinear spectrum using the function for the linear spectrum, the s-SHG spectrum must be plotted as function of the SH photon energy and the peak must originate from a resonance at the SH frequency in order to obtain an accurate result. In chapter 8, most of the s-SHG measurements of supported metal clusters are fitted using the equations for the linear absorption of small metal particles. Using the procedure shown above, the extracted fit parameters should be reliable.

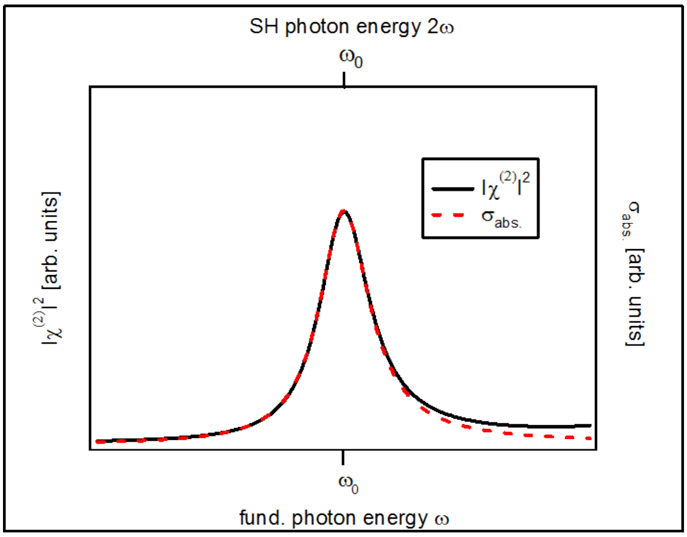

Fig. 2-*07*. Comparison between a linear absorption spectrum and the nonlinear s-SHG spectrum. The linear spectrum is plotted as function of the fundamental photon energy and the nonlinear spectrum as function of the SH photon energy.

2.2.6 From the One Oscillator Model to Real Systems

The anharmonic oscillator is a good model system in order to understand the principles of linear and nonlinear responses of matter. However, in real materials more than one resonance frequency is generally present. These resonances originate from different transition processes in the material. If the excitations of the different resonances are independent from each other, the overall susceptibility of such a system can be described by a superposition of multiple anharmonic oscillators[73]. The first order susceptibility in such a system is consequently given by:

$$\chi^{(1)} = \sum_n \frac{q_n^{\;2}}{\varepsilon_0 \cdot m_n} \cdot \frac{1}{\left[\omega_n^{\;2} - \omega^2 - i\gamma_n\omega\right]} \qquad \textit{(eq.2-35)}$$

where, q_n, are the effective charges of the oscillating species, m_n, their masses, ω_n, the oscillator resonance frequencies, and γ_n, the damping constants. Similarly derived is the second order susceptibility:

$$\chi^{(2)} = \sum_n \frac{\alpha_n \cdot q_n^{\;3}}{2\varepsilon_0 \cdot m_n^{\;3}} \cdot \frac{1}{\left[\omega_n^{\;2} - \omega^2 - i\gamma_n\omega\right]^2 \cdot \left[\omega_n^{\;2} - 4\omega^2 - 2i\gamma_n\omega\right]} \qquad \textit{(eq.2-36)}$$

The parameter α_n varies for different excitations because of its dependency on the symmetry of the transition (selection rules). For some transitions it could be, for example, zero, and these transitions would consequently not contribute to the second order susceptibility. However, such transitions can contribute to the first order susceptibility (different selection rules) which leads to a difference between the nonlinear spectrum and the linear one. In general, it can be pointed out that the composition of different oscillators in the susceptibilities is not necessarily equal for the linear and the nonlinear case. In such a case, the accuracy of the interpretation of the nonlinear spectrum using the equations for the linear spectrum (as shown in the previous section) can be highly reduced.

2.2.7 Nonlinear Properties of Non-Absorbing Dielectric Samples

The complex second order susceptibility becomes real in lossless media when all resonances are far from the wavelength of the illuminating light.[68] Examples of such materials are those that are dielectric, such as glasses or metal oxides. This effect can be illustrated using equation 2-31 in combination with the condition $\omega_0^2 - \omega^2 \gg \gamma\omega$.

$$\chi^{(2)} = \frac{\alpha \cdot e^3}{2\varepsilon_0 \cdot m^3} \cdot \frac{1}{\left[\omega_0^2 - \omega^2 - i\gamma\omega\right]^2 \cdot \left[\omega_0^2 - 4\omega^2 - 2i\gamma\omega\right]} \xrightarrow{\omega_0^2 - \omega^2 \gg \gamma\omega}$$

$$\chi^{(2)} = \frac{\alpha \cdot e^3}{2\varepsilon_0 \cdot m^3} \cdot \frac{1}{\left[\omega_0^2 - \omega^2\right]^2 \cdot \left[\omega_0^2 - 4\omega^2\right]} \qquad \textit{(eq.2-37)}$$

Furthermore, from equation 2-37 it can be derived that the second order susceptibility in such media can be approximated as being constant over a wide range of photon energy because the denominator in equation 2-37 hardly changes with ω for $\omega_0 \gg \omega$. Dielectrics are consequently good reference substrates for calibrating the s-SHG setup because their SH conversion efficiency is in first approximation constant over the measured range.

2.3 Summary Chapter 2

In chapter 2, the theoretical aspects of the s-CRD spectroscopy were presented and discussed in detail. Furthermore, the parameters influencing the sensitivity of the method were shown and the necessity of the transversal mode matching procedure for the investigation of solid samples using s-CRDS was justified, which can reduce the noise in the obtained spectrum by up to 50 %.

In the second part of the chapter, several principles of nonlinear optics were presented in order to explain the origin of the second harmonic generation (SHG) at the surfaces of substrates. In the following sections, the use of this nonlinear effect to perform surface sensitive spectroscopic measurements (s-SHG) was shown and basic selection rules for second order nonlinear processes were derived. Finally, the different properties of linear (s-CRD) and nonlinear (s-SHG) spectra were discussed using as model system the anharmonic oscillator. It could be shown that the existence of one single resonance in the investigated system results in the presence of two peaks in the s-SHG spectrum; the first peak is located where the fundamental frequency is in resonance with the transition and the second, where the SH frequency is resonant. Based on these considerations, a procedure could be found allowing for the direct comparison of the two different types of spectra which will be used in the following chapters for the interpretation of s-SHG spectra.

3. Optical Properties of Metal Clusters and Adsorbed Molecules

In the present chapter, the optical properties of metal clusters both, with and without organic ligands are discussed and some principles of the theoretical description are shown. In the first part, the fundamental linear optical properties of metal particles e.g. the excitation of collective oscillations of the conduction electrons (plasmons) are derived from bulk optical constants using the classical Mie theory. Furthermore, a formalism describing the particle size and shape dependency of the optical constants is presented and the effects occurring for metal clusters supported on substrates are discussed. The second part of this chapter concerns the influence of organic adsorbates on the optical properties of the clusters followed by the third part, where the nonlinear optical properties of supported metal particles are described. Here, a brief introduction of this wide field is given, focusing on the nonlinear plasmonic properties of the particles.

3.1 Linear Optical Properties of Metal Clusters

The linear optical properties of metal particles are dominated by the presence of conducting electrons, which can be described in a first approximation as a free electron gas dispersed in the lattice of metal cores inside the particle. The extraordinarily high mobility of these electrons leads to a strong coupling between themselves and incoming electromagnetic waves. In the following section, the plasmonic oscillation of these electrons are characterized using the bulk optical constants of the metal in combination with the Mie theory. This simplified description is precise enough to give sufficient insight into the fundamental optical properties of metal particles, especially in terms of the effect of size and shape. However, this model is limited since it is based on the existence of an electronic band structure inside the particles, as is the case for the bulk material but not necessarily for small particles. Below a certain particle size (which is so far undetermined for supported metal clusters) the electronic band structure must be replaced by discrete energy levels, leading to a failure of the classical model.

3.1.1 Optical Constants of Bulk Metal

The optical properties of bulk metal can be described by its dispersive dielectric function, $\varepsilon(\omega)$, which is related to the electric susceptibility of the material, $\chi(\omega)$, as shown by equation 3-01:

$$\varepsilon(\omega) = 1 + \chi(\omega) \quad \textit{(eq.3-01)}$$

Taking the model of the harmonic oscillator to describe the susceptibility of the conducting electrons in bulk metals leads to the following expression of the susceptibility (see chapter 2.2.4):

$$\chi(\omega) = \frac{N \cdot e^2}{\varepsilon_0 \cdot m} \cdot \frac{1}{\left[\omega_0^{\;2} - \omega^2 - i\gamma\omega\right]} \quad \textit{(eq.3-02)}$$

where, N , is the number of oscillators per unit volume, e, the elementary electric charge, m, the effective electron mass, ε_0, the dielectric constant, ω_0, the resonance frequency of the oscillator, and γ, the damping constant of the oscillation. The factors in front of the frequency dependent term can be combined to give the plasma frequency, ω_p, which is material dependent:

$$\frac{N \cdot e^2}{\varepsilon_0 \cdot m} = \omega_p^{\;2} \quad \textit{(eq.3-03)}$$

The dielectric function is then derived to give:

$$\varepsilon(\omega) = 1 + \frac{\omega_p^{\;2}}{\left[\omega_0^{\;2} - \omega^2 - i\gamma\omega\right]} \quad \textit{(eq.3-04)}$$

Equation 3-04 is the Lorentz model of the dielectric function of matter. From this equation, it can be concluded that the dielectric function is a complex quantity which can be divided into its real and imaginary parts, $\varepsilon_1(\omega)$ and $\varepsilon_2(\omega)$:

$$\varepsilon(\omega) = \varepsilon_1(\omega) + i\varepsilon_2(\omega) \quad \textit{(eq.3-05)}$$

In bulk metals, the conducting electrons can be considered as "free" electrons which are not acted upon b y restoring forces when they perform oscillations. Within the model of the harmonic oscillator this corresponds to a system with a vanishing resonance frequency

$\omega_0 \to 0$. This can be illustrated by a simple spring model. An oscillation without any restoring forces corresponds to a vibrating spring with the spring constant $k = 0$. Since the resonance frequency in the harmonic oscillator is defined as $\omega_0 = \sqrt{k/m}$, it can be replaced by the value zero $(\omega_0 = 0)$. Inserting this condition into equation 3-04 gives the Drude model of the dielectric function of bulk metals:

$$\varepsilon(\omega) = 1 - \frac{\omega_p^{\ 2}}{\omega^2 + i\gamma\omega} \qquad \textit{(eq.3-06)}$$

with its real and imaginary parts given by:

$$\varepsilon_1(\omega) = 1 - \frac{\omega_p^{\ 2}}{\omega^2 + \gamma^2}$$

$$\varepsilon_2(\omega) = \frac{\omega_p^{\ 2}\gamma}{\omega\left(\omega^2 + \gamma^2\right)} \qquad \textit{(eq.3-07)}$$

Equation 3-06 describes the dielectric function of a perfect free electron metal. This is an especially good approximation for alkaline and alkaline earth metals.[74, 75] However, for many other metals such as noble metals, additional effects have to be considered. In figures 3-*01* and 3-*02*, the real and imaginary parts of the experimentally determined dielectric function of bulk silver[76] is shown and compared to the functions derived from equations 3-07.

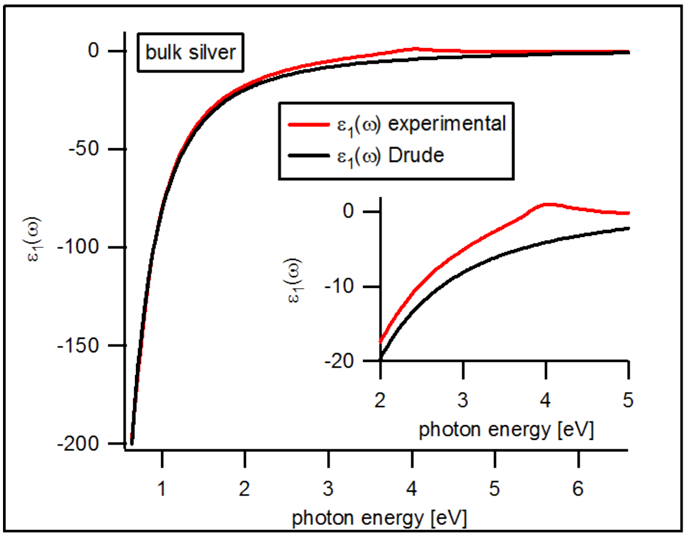

Fig. 3-*01*. Real part of the dielectric function for bulk silver calculated with the Drude model (black line) and determined experimentally (red line). The inset shows an enlarged fraction of the spectrum.

For the plasma frequency the value $\omega_p = 9.08 \text{ eV}$ is used and as damping constant for bulk silver the value $\gamma = 0.018 \text{ eV}$. These values are derived experimentally from measurements of a thin silver film.[76] For small photon energies the Drude dielectric function matches well with the measured curves; however, for larger energies strong deviations can be observed. The imaginary part of the measured dielectric function (figure 3-*02*) in particular, shows an onset to higher values at about 3.8 eV, whereas the Drude function remains close to zero. The Drude dielectric function only treats the conducting electrons and neglects all other lower lying electrons. These electrons, however, can perform transitions to higher energy bands known as interband transitions[77, 78] which leads to additional photon absorption processes. For silver, the onset of these interband transitions is located at 3.8 eV which explains the deviation of the measured curves from the Drude function.[79] In the spectrum of the imaginary part of the dielectric function, the onset of the interband transition is marked.

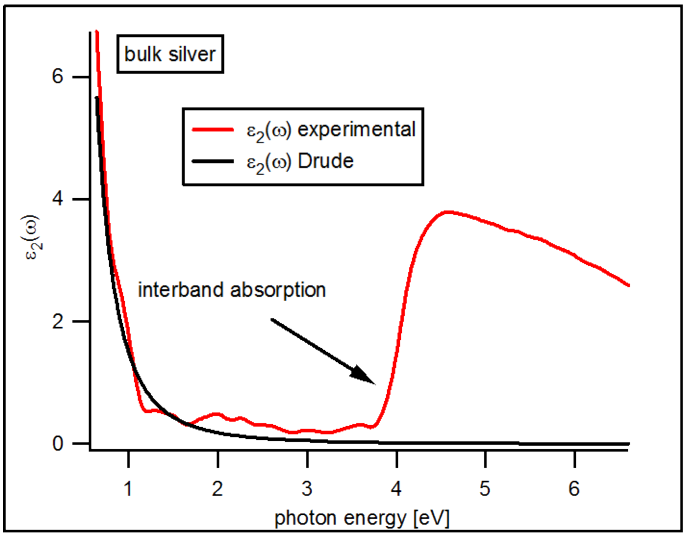

Fig. 3-*02*. Imaginary part of the dielectric function for bulk silver calculated with the Drude model (black line) and determined experimentally (red line). In the spectrum the onset of the interband transition is marked.

As a consequence of this observation, the dielectric function must be extended in order to account for possible interband transitions. The overall susceptibility of a realistic metal can be expressed as a sum of a Drude part, χ^D, and a part for the interband transitions, χ^{IB}.[80] Using equation 3-01 the dielectric function is then given by:

$$\varepsilon(\omega) = 1 + \chi^D + \chi^{IB} \quad \textit{(eq.3-08)}$$

Inserting the Drude part from equation 3-06 yields:

$$\varepsilon(\omega) = 1 - \frac{\omega_p^{\,2}}{\omega^2 + i\gamma\omega} + \chi^{IB} \quad (eq.3\text{-}09)$$

Since the interband susceptibility is a complex quantity, it can be divided in its real and its imaginary parts, χ_1^{IB} and χ_2^{IB}, resulting in the following expressions for the real and imaginary parts of the dielectric function:

$$\varepsilon_1(\omega) = 1 - \frac{\omega_p^{\,2}}{\omega^2 + \gamma^2} + \chi_1^{IB} \quad (eq.3\text{-}10)$$

$$\varepsilon_2(\omega) = \frac{\omega_p^{\,2}\gamma}{\omega\left(\omega^2 + \gamma^2\right)} + \chi_2^{IB} \quad (eq.3\text{-}11)$$

Equations 3-10 and 3-11 can be used in order to describe the dielectric function and thus the optical properties of a realistic metal. For an exact description of the interband susceptibilities, however, concrete quantum mechanical calculations must be carried out.[81]

3.1.2 Optical Properties of Small Metal Particles (Plasmons)

The optical properties of metal particles can differ strongly from those of the corresponding bulk metal. In a particle, the conducting electrons are confined within the particle volume, whereas in the bulk they can move freely inside the entire lattice. This leads to electrostatic restoring forces when the electrons perform oscillations, holding the electrons inside the particle. As a consequence, the oscillations of electrons in metal particles have distinct resonance frequencies called plasmon resonances. These effects are treated within the classical Mie theory. In his theory, Mie derives the exact solution for the adsorption and scattering of light by a spherical particle which is embedded in a homogeneous medium (for a given dielectric function of the particle material) by solving Maxwell's equations for the electromagnetic fields inside and outside the particle.[82] Later, the theory was extended in order to include non-spherical particle shapes and interface effects, such as the influence of adsorbates at the particle surface.[73, 83-85] For spherical particles which are small compared to the wavelength of the light used (dipole approximation), the extinction cross section derived from Mie theory is given by:

$$\sigma_{ext} = 9\frac{\omega}{c_0}\varepsilon_m^{3/2}\cdot V_0\frac{\varepsilon_2(\omega)}{\left[\varepsilon_1(\omega)+2\varepsilon_m\right]^2+\varepsilon_2(\omega)^2} \qquad \textit{(eq.3-12)}$$

where, c_0, is the speed of light in vacuum, ε_m, the dielectric constant of the surrounding medium, V_0, the particle volume, and finally $\varepsilon_1(\omega)$ and $\varepsilon_2(\omega)$, the real and the imaginary parts of the dielectric function of the particle, respectively. In this approximation, the phase retardation effects and the excitation of higher multipoles are neglected and only dipole oscillations are described. Equation 3-12 is considered to be a good approximation, whenever the particle radius is small compared to the wavelength of the probing light $(R \ll \lambda)$. For the spectral range investigated in the present thesis (UV-Vis), this condition can be considered as fulfilled for particle radii smaller than 10 nm (this is the case for all cluster samples investigated in the present thesis).[73] Furthermore, the scattering cross section of particles of such small sizes is orders of magnitude smaller than the absorption cross section.[73] Consequently, the extinction cross section approximately equals the absorption cross section $\sigma_{ext} = \sigma_{abs}$ leading to a highly reduced complexity for the interpretation of the measured spectra. The extinction cross section in equation 3-12 possesses a maximum, whenever the denominator in the frequency dependent part is at a minimum. Provided that the imaginary part of the dielectric function of the particle, $\varepsilon_2(\omega)$, is small, the denominator possesses a minimum where:

$$\varepsilon_1(\omega) = -2\cdot\varepsilon_m \qquad \textit{(eq.3-13)}$$

The frequency where equation 3-13 is fulfilled is called the Fröhlich frequency, ω_F. Obviously, the Fröhlich frequency depends on the dielectric constant of the surrounding medium (which is assumed to be non absorbing) and can be influenced by the choice of the medium in which the particle is embedded. The absorption spectrum shows a peak at ω_F called the plasmon peak. However, the shape of the plasmon peak is highly dependent on the evolution of the imaginary part of the dielectric function of the particle in the region of ω_F. This can be illustrated by comparing the noble metals silver, gold, and copper. In figure 3-*03*, the imaginary parts of the experimentally derived dielectric functions of the three noble metals are shown.[76] Additionally, the Fröhlich frequencies are marked for each metal, calculated for a vacuum $(\varepsilon_m = 1)$ as surrounding medium.

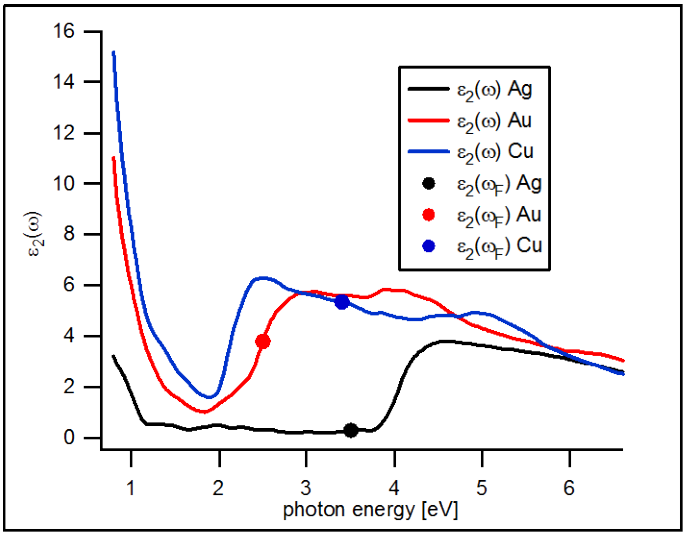

Fig. 3-*03*. Imaginary parts of the dielectric functions for silver (black line), gold (red line), and copper (blue line). Additionally, the Fröhlich frequencies for particles of these metals are marked, calculated with $\varepsilon_m = 1$.

For silver the value of $\varepsilon_2(\omega)$ at the Fröhlich frequency is small, whereas for gold and copper ω_F is in the region of the interband transitions for these metals and $\varepsilon_2(\omega)$ thus has much higher values. Consequently, silver particles should possess the most pronounced plasmon peak in the absorption spectrum. Inserting the experimentally derived dielectric functions of silver, gold, and copper[76] into equation 3-12, the absorption spectra of small particles of these metals can be calculated. The resulting spectra are depicted in figure 3-*04*. Note, that a vacuum is considered as surrounding medium $(\varepsilon_m = 1)$.

As predicted, the most pronounced plasmon peak is present in the spectrum of the silver particles at the Fröhlich frequency of $\omega_F = 3.5$ eV. Note that this spectrum is scaled to 1/10 with respect to the spectra of the gold and copper particles (i.e. in reality, the peak in the silver spectrum is 10 t imes higher than depicted). The plasmon peak of the gold particles is broadened compared to that of silver and located at the onset of the interband transition of gold. Furthermore, the absorption maximum at 2.43 eV is slightly shifted compared to the Fröhlich frequency $\omega_F = 2.5$ eV. In the spectrum of the copper particles, the plasmon peak has almost completely vanished and is highly broadened (the plasmon resonance should not be mistaken with the small peak at 2.1 eV, originating from the interband transition in copper). Here, the Fröhlich frequency $(\omega_F = 3.4$ eV$)$ represents not even the maximum in the absorption spectrum.

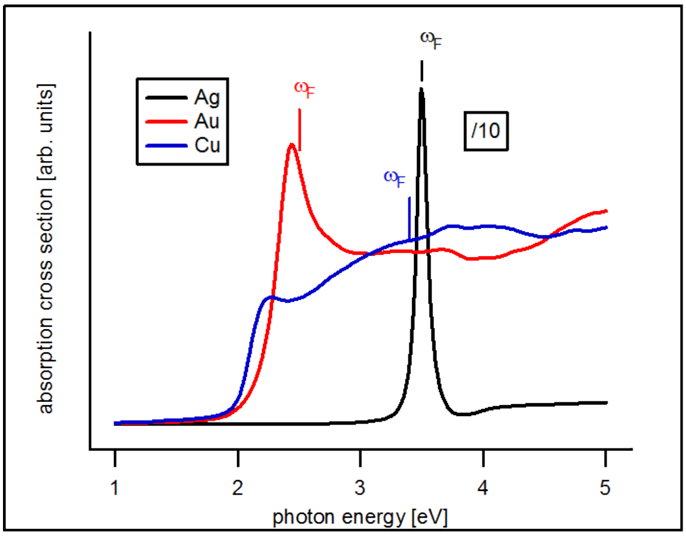

Fig. 3-*04*. Calculated absorption spectra of silver, gold, and copper particles. The Fröhlich frequencies for the particles of each metal are marked in the spectra.

In summary, it can be concluded that the existence of a plasmon resonance (Fröhlich frequency) for a metal particle does not necessarily coincide with the existence of a visible plasmon peak in the absorption spectrum. However, the plasmon peak can be made visible by shifting the Fröhlich frequency to a value where $\varepsilon_2(\omega)$ of the measured metal particle is small. This can be achieved by choosing a suitable embedding medium. In general, silver particles are considered the best candidates for plasmon studies among the noble metals because of their sharp pronounced plasmon peak in the spectrum.

3.1.3 Particle-Shape Effects[73]

So far, only the optical properties of spherical particles have been treated. However, for supported metal particles deviations from spherical shape have been observed.[86-88] Such deviations can have enormous influence on the plasmonic properties of the metal particles and consequently, some basic principles of the optical properties of non-spherical particles are presented in the following. Here, the theoretical description focuses on spheroid shaped particles which is a good approximation of the real shape of supported metal clusters.

From Mie theory (its extension), the polarizability, α_i, of small spheroid particles $(R \ll \lambda)$ can be calculated as follows:

$$\alpha_i = V_0 \cdot \frac{\varepsilon(\omega)-\varepsilon_m}{\varepsilon_m + \left[\varepsilon(\omega)-\varepsilon_m\right]\cdot L_i} \quad \textit{(eq.3-14)}$$

(The quantities used here follow the notation in the previous chapters) The parameter L_i is a shape parameter and the index, i, represents the $i-\mathrm{th}$ principal axis of the particle. α_i, is consequently the polarizability of the particle along its $i-\mathrm{th}$ principal axis. A general relation between the different shape parameters of an arbitrary particle is given by equation 3-15:

$$\sum_i L_i = 1 \quad \textit{(eq.3-15)}$$

The formula to calculate the different values of L_i depends on the symmetry of the particle. Here, the case of an oblate shaped particle is presented. An oblate spheroid is defined by the radii of its three principal axis, $a, b,$ and c, with the relations $a = b$ and $c < a$. The shape parameter for such an object can be derived using equation 3-16:

$$L_a = L_b = \frac{R_{c/a}}{2\left(1-R_{c/a}{}^2\right)^{3/2}}\left[\frac{\pi}{2} - \tan^{-1}\left(\frac{R_{c/a}}{\sqrt{1-R_{c/a}{}^2}}\right)\right] - \frac{R_{c/a}{}^2}{2\left(1-R_{c/a}{}^2\right)} \quad \textit{(eq.3-16)}$$

where the axis ratio is given by $R_{c/a} = \frac{c}{a}$. The shape parameter of the short axis, c, can be derived on basis of equation 3-15:

$$L_c = 1 - 2\cdot L_a \quad \textit{(eq.3-17)}$$

The extinction cross section of a particle can be calculated from the polarizability using the relation:

$$\sigma_{i,ext} = \frac{\omega}{c_0}\cdot\sqrt{\varepsilon_m}\cdot \mathrm{Im}\left\{\alpha_i\right\} \quad \textit{(eq.3-18)}$$

where, $\mathrm{Im}\left\{\alpha_i\right\}$, represents the imaginary part of the $i-\mathrm{th}$ polarizability. Inserting equation 3-14 yields:

$$\sigma_{i,ext} = \frac{\omega}{c_0}\varepsilon_m{}^{3/2}\cdot V_0 \cdot \frac{\varepsilon_2(\omega)}{\left[\left(\varepsilon_1(\omega)-\varepsilon_m\right)L_i + \varepsilon_m\right]^2 + \varepsilon_2(\omega)^2\cdot L_i^2} \quad \textit{(eq.3-19)}$$

Using equation 3-19, the different extinction cross sections, $\sigma_{i,ext}$, along the different principal axes, i, of the particle can be derived. For an oblate shape the relation $\sigma_{a,ext} = \sigma_{b,ext} \neq \sigma_{c.ext}$ is valid. In the special case of a sphere the shape parameters are $L_a = L_b = L_c = 1/3$. Inserting this into equation 3-19 yields equation 3-12 presented in the previous section, which describes the absorption cross section of a sphere. Note that equation 3-12 is obviously a special case of the more general description given by equation 3-19. From equation 3-19, it can be concluded that the absorption properties of an arbitrary particle change with respect to its orientation towards the exciting light wave. For an oblate particle two different spectra can be obtained, one from the excitation of an oscillation along the long axis of the particle and the other along the short axis. In figure 3-*05*, the absorption spectra of an oblate and a spherical silver particle are depicted.

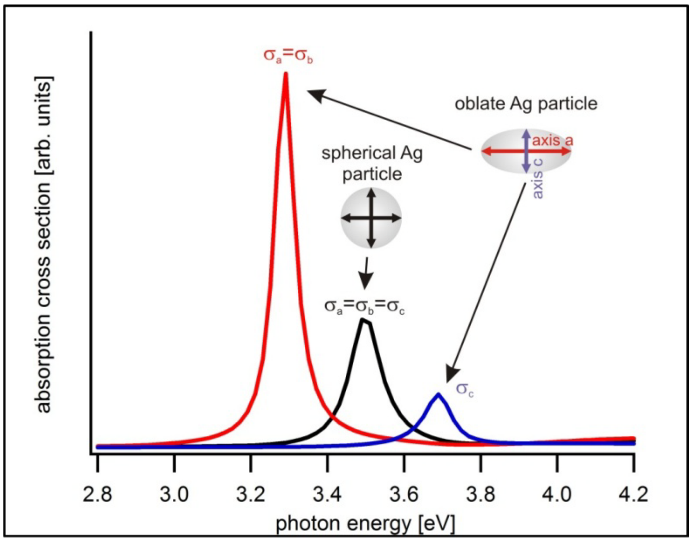

Fig. 3-*05*. Calculated absorption spectra of a spherical silver particle (black line) and an oblate silver particle. In the latter spectra the plasmon resonance peak is split into two plasmon peaks (red and blue line).

The spectra are calculated using equation 3-19 and the dielectric function of bulk silver from the previous sections. For the oblate particle the axis ratio $R_{c/a} = 0.5$ is taken yielding shape parameters of $L_a = L_b = 0.2364$ and $L_c = 0.5272$. Consequently, for the oblate particle two spectra are obtained, one for $\sigma_{a,ext}$ and one for $\sigma_{c,ext}$. For the dielectric constant of the surrounding medium, ε_m, the value for vacuum is again used. By comparing the spectrum obtained for the spherical silver particle with the spectra of the oblate particle, it can be observed that in the latter case the plasmon peaks are both shifted. However, the resonance peak for the oscillation parallel to the short axis is blue shifted $(\omega_{\max} = 3.69 \text{ eV})$, whereas the peak corresponding to the oscillation parallel to the long axis of the particle is red shifted $(\omega_{\max} = 3.29 \text{ eV})$ with respect to the spherical case with $\omega_{\max} = 3.5 \text{ eV}$. In a realistic absorption measurement of oblate silver particles, a somehow weighted superposition of the two peaks would be measured depending on the orientations of the particles with respect to the polarization of the light wave. In general, it should be pointed out that any deviation of the particle shape from a sphere leads to a splitting of the single plasmon resonance peak into several plasmon peaks, in case of an oblate particle the plasmon peak is split into two peaks. The magnitude of the shifts of the plasmon peaks for an oblate particle obviously depends on the axis ratio $R_{c/a}$. In figure 3-*06*, the peak positions of the two plasmon peaks for oblate silver particles are depicted as a function of the axis ratio.

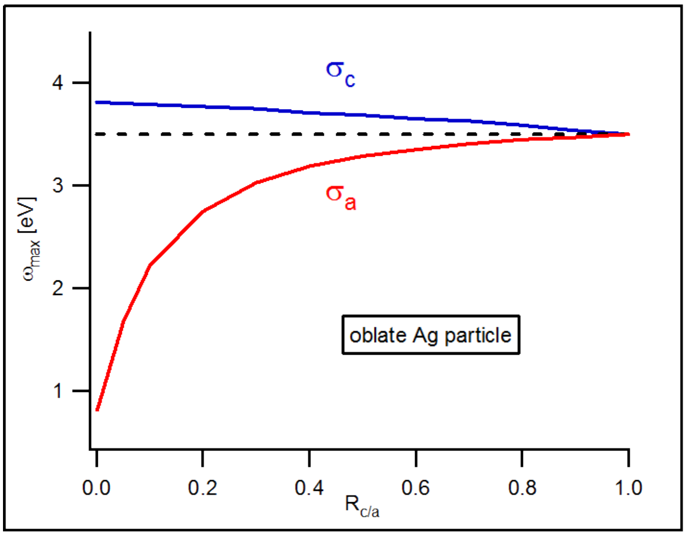

Fig. 3-*06*. Plasmon peak positions of the two resonance peaks (σ_c = short axis and σ_a = long axis) for oblate silver particles as function of the axis ratio. The axis ratio of $R_{c/a} = 1$ corresponds to a spherical particle. The splitting of the plasmon peaks increases with a decreasing axis ratio.

In the figure, it can be observed that the smaller the axis ratio (i.e. the flatter the particle) the larger the distance between the resonance peak of the oscillation parallel to the short axis and the resonance peak of the oscillation along the long axis. The axis ratio of $R_{c/a} = 1$ corresponds to a spherical particle with one single plasmon peak at 3.5 eV. Using this plot the axis ratio of a measured particle can be derived from the positions of the two plasmon resonances.

3.1.4 Cluster Matter

In the previous sections, the optical properties of metal particles embedded in an homogeneous medium were described. However, the cluster samples investigated in the framework of this thesis are metal particles dispersed on a substrate. Here, the surrounding medium of the particle is inhomogeneous. Furthermore, the local electric field in which the particle is exposed is influenced by image charges induced in the substrate and the presence of other metal particles in the closer neighborhood. The quantity of the latter depends on the particle sizes and the surface coverage of particles on the sample. The influence of all these effects on the shape of the absorption spectrum is described mathematically in the following sections.

3.1.4.1 Choice of ε_m

For an inhomogeneous surrounding medium of the particle the correct choice of the value for the dielectric constant, ε_m, is not obvious. When dispersed on the surface of a substrate, one fraction of the particle surface is in contact with the substrate material, whereas the rest of its surface is exposed to vacuum. Consequently, the true "effective" dielectric constant, ε_m, lies somewhere between the value of the substrate material and that of the vacuum. A possible way of estimating ε_m is described in the literature.[89] Here, the mean value of the two media is taken and simply weighted by the fraction of the particle surface exposed to each media, as given by the following equation:

$$\varepsilon_m = x \cdot \varepsilon_s + (1-x) \cdot \varepsilon_{vac} \quad (eq.3\text{-}20)$$

where, ε_s, is the dielectric constant of the substrate, ε_{vac}, the dielectric constant of vacuum $(\varepsilon_{vac} = 1)$, and x, is the fraction of the particle surface in contact with the substrate. The quantity of x obviously depends on the geometry of the supported particle. However, if the surface of the substrate is assumed to be perfectly flat, the value for x can range between 0 and 0.5. The different geometries corresponding to these values are depicted in figure 3-*07*.

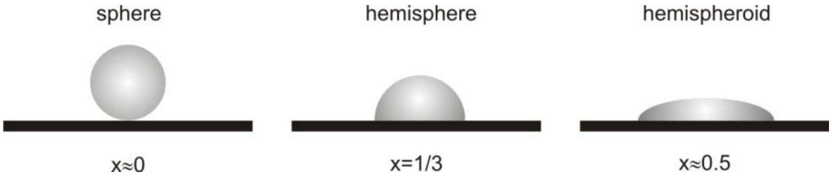

Fig. 3-*07*. Left: Sphere on a substrate. The fraction of the particle surface in contact with the substrate is approximately zero. Middle: Hemisphere on a substrate. x is exactly 1/3. Right: Very flat hemispheroid. Here the fraction x has nearly the value 0.5.

On the left side, a spherical metal particle supported on a substrate is shown which leads to a value for x of approximately zero. For the case of a hemisphere depicted in the middle of the figure, an exact value of $x = 1/3$ can be derived. Finally, on the right side, the extreme example of a very flat hemispheroid particle, whereby almost half of the particle surface is in contact with the substrate is given, which thus yields a value of $x \approx 0.5$.

Overall, the shape of the particle on the surface and thus the value of x after deposition depends on many factors, such as the particle material, the substrate material, and the kinetic energy of the particle before the collision with the substrate during the deposition. Since the binding energy of the particle depends amongst other parameters on the particle size, the latter is an additional factor which can influence the final shape. Consequently, it is difficult to precisely predict the x value, which instead must be determined experimentally.

3.1.4.2 Local Field Correction

The local electric field, which metal particles dispersed on a surface of a substrate are exposed to is influenced by the image charge induced in the substrate and the electric fields generated by the neighboring particles. The change of the local field with respect to the electric field of the incoming light wave influences the shape of the absorption spectrum of the particles. The local field correction can be performed by replacing the polarizability of the particle, α_i, by a modified polarizability, $\alpha^{\beta}{}_i$, accounting for the changes in the local field. The $\alpha^{\beta}{}_i$ term can be calculated from α_i using the local field correction parameter, β_i:[86, 90]

$$\alpha^{\beta}{}_i = \frac{\alpha_i}{1 + \frac{\alpha_i}{V_0}\beta_i} \qquad (eq.3\text{-}21)$$

Inserting the expression for the polarizability of an spheroid particle (equation 3-14) into equation 3-21 yields:

$$\alpha^{\beta}{}_{i} = V_0 \frac{\varepsilon(\omega) - \varepsilon_m}{\varepsilon_m + \left[\varepsilon(\omega) - \varepsilon_m\right]\left(L_i + \beta_i\right)} \qquad \textit{(eq.3-22)}$$

Using equation 3-18, the local field corrected extinction cross section, $\sigma^{\beta}{}_{i,ext}$, is then given by:

$$\sigma^{\beta}{}_{i,ext} = \frac{\omega}{c_0} \varepsilon_m{}^{3/2} \cdot V_0 \cdot \frac{\varepsilon_2(\omega)}{\left[\left(\varepsilon_1(\omega) - \varepsilon_m\right)\left(L_i + \beta_i\right) + \varepsilon_m\right]^2 + \varepsilon_2(\omega)^2 \cdot \left(L_i + \beta_i\right)^2} \qquad \textit{(eq.3-23)}$$

Equation 3-23 is very similar to equation 3-19 representing the extinction cross section of a spheroid particle without any local field correction. In equation 3-23, the shape parameter, L_i, is simply replaced by the expression $\left(L_i + \beta_i\right)$. As a consequence, the fundamental properties of the absorption spectrum do not change (if local field effects are considered) but the parameter β_i leads to an additional shift of the plasmon resonance peak. The calculation of β_i for a spheroid particle supported on a substrate is presented in the following paragraphs.

The local field correction parameter, β_i, corrects the polarizability for the change in the local field at the position of the particle. Its calculation, shown here, is based on the assumption that spheroid particles are uniformly dispersed on a substrate. Uniformly means, that the short axis of all particles are oriented parallel to each other. This assumption is reasonable since the origin of the deformation of the particles is the presence of the substrate surface. For the change in the local field two contributions are considered, the first is the field generated by the induced image dipole in the substrate and the second is the field generated by the neighboring particles. In figure 3-*08*, these interactions are shown in a sketch for the two different oscillation directions inside the particles. From the figure it can be concluded that the interaction between the oscillating field of the particle and its image dipole leads to a weakening of the local field for both oscillation directions. However, the interaction between the generated fields of different particles leads to an enhanced local field for the oscillation direction depicted on the left side, whereas this interaction in the case shown on the right side attenuates the local field. Consequently, there are two different values for β_i for the two different oscillation directions. Following the notation of the two different extinction cross sections of an oblate particle, σ_a and σ_c (representing the oscillations parallel to the a- and the c-axis of the particle), the different β_i are labeled β_a and β_c.

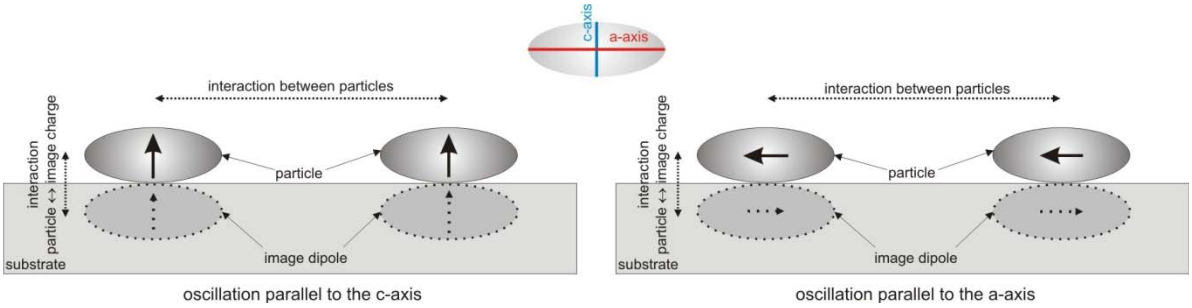

Fig. 3-*08*. Local field effects for small supported metal particles. On the left side, the dipole-dipole interactions for an oscillation parallel to the c-axis of the particle is shown. On the right side, the oscillation is parallel to the a-axis of the particle. The different directions of the oscillations lead to different interactions and thus different local fields.

The parameter β_i can be divided into its two contributions, β_i^{ID}, representing the particle-image dipole interaction and β_i^*, representing the particle-particle interaction:

$$\beta_i = \beta_i^{ID} + \beta_i^* \quad (eq.3\text{-}24)$$

whereby the values for β_a^{ID} and β_c^{ID} can be derived from equations 3-25 and 3-26, respectively:

$$\beta_a^{ID} = -\frac{V_0}{4\pi l^3} \cdot \frac{\varepsilon_s - 1}{\varepsilon_s + 1} \quad (eq.3\text{-}25)$$

$$\beta_c^{ID} = -\frac{2V_0}{4\pi l^3} \cdot \frac{\varepsilon_s - 1}{\varepsilon_s + 1} \quad (eq.3\text{-}26)$$

where, V_0, is the particle volume, l, the distance between the center of the particle and the center of the image dipole, and ε_s, is the dielectric constant of the substrate. The volume of an oblate particle can be expressed by:

$$V_0 = \frac{1}{6}\pi \cdot \frac{c^3}{R_{c/a}} \quad (eq.3\text{-}27)$$

where, c, is the length of the short axis of the particle, and $R_{c/a}$, the axis ratio introduced in the previous sections. The distance between the center of the image dipole and the center of the particle, l, can be replaced in good approximation by the length of the short axis of the particle, c, if an oblate shape is assumed and the short axis is perpendicular to the surface. Inserting into equations 3-25 and 3-26 yields:

$$\beta_a^{ID} = -\frac{1}{24 \cdot R_{c/a}^{\ 2}} \cdot \frac{\varepsilon_s - 1}{\varepsilon_s + 1} \quad \text{(eq.3-28)}$$

$$\beta_c^{ID} = -\frac{1}{12 \cdot R_{c/a}^{\ 2}} \cdot \frac{\varepsilon_s - 1}{\varepsilon_s + 1} \quad \text{(eq.3-29)}$$

Both, β_a^{ID} and β_c^{ID} have negative values leading to a red shift of the plasmon resonance peak in the absorption spectrum. The value for β_i^*, describing the interaction between the particles, obviously depends on the mean distance of the particles and thus on their spatial distribution on the surface. The latter can be approximated by a simple model.[90] Here, the particles are assumed to be placed on lattice points of a quadratic lattice with the lattice constant g. Furthermore, an effective particle layer thickness is defined as: $d_{eff} = 1.21 \cdot F \cdot R_{particle}$ where, $R_{particle}$, is the particle radius, and F, the fraction of a monolayer of deposited particles (a monolayer of particles corresponds to the value $F = 1$).[87, 91] The parameter β_i^* can then be derived for the two oscillation directions from equations 3-30 and 3-31:

$$\beta_a^* = -\frac{2}{\varepsilon_s + 1} \cdot 0.716 \frac{d_{eff}}{2g} \quad \text{(eq.3-30)}$$

$$\beta_c^* = \frac{2\varepsilon_s}{\varepsilon_s + 1} \cdot 0.716 \frac{d_{eff}}{g} \quad \text{(eq.3-31)}$$

The lattice constant, g, is given by:

$$g = \sqrt{\frac{V_0}{d_{eff}}} \quad \text{(eq.3-32)}$$

where, V_0, is the particle volume. The fraction parameter, F, can be approximated by equation 3-33:

$$F \approx \rho \cdot \pi R^2_{particle} \quad \textit{(eq.3-33)}$$

where, ρ, is the surface coverage of the particles. Equations 3-30 and 3-31 are then derived to give:

$$\beta_a^* = -\frac{2}{\varepsilon_s + 1} \cdot 0.2327 \cdot R^3_{particle} \cdot [\pi \cdot \rho]^{3/2} \quad \textit{(eq.3-34)}$$

$$\beta_c^* = \frac{2\varepsilon_s}{\varepsilon_s + 1} \cdot 0.4654 \cdot R^3_{particle} \cdot [\pi \cdot \rho]^{3/2} \quad \textit{(eq.3-35)}$$

The value for β_i^{ID} depends on the particle axis ratio and the dielectric constant of the substrate, whereas the value for β_i^* depends on the coverage, the particle size, and ε_s. Combining these two contributions yields β_i (equation 3-24). Equations 3-34 and 3-35 show that the interaction between the particles leads to a negative contribution to β_i for the dipole oscillation parallel to the surface (red shift of the plasmon resonance peak) and to a positive contribution for the oscillation perpendicular to the surface (blue shift of the plasmon peak). By measuring the plasmon resonance peak, the value for the expression $(L_i + \beta_i)$ can be derived from a fit of the spectrum using equation 3-23. From these values, particle parameters such as the axis ratio are accessible.

3.1.5 Particle-Size Effects

All descriptions of the optical properties of metal particles presented so far are thoroughly valid for all metal particles which are small compared to the wavelength of the light illuminating the particles. However, the dielectric function of the particles which is inserted into the equations must be correctly determined. So far, the dielectric function of the bulk material is used, but it obviously depends on the particle size. The smaller the particles are, the more the electronic properties of a metal particle deviate from those of the bulk. One extreme example is a metal atom lacking of most of the typical metallic properties (e.g. the existence of a plasmon). Consequently, a mathematical description of the dielectric function is needed in order to account for particle-size effects. The major difference between a small and a large particle is the ratio, $R_{\text{surface/bulk}}$, between atoms located at the particle surface and atoms inside the particle. This ratio increases with decreasing particle radius, $R_{partcle}$, and can be expressed by the relation: $R_{\text{surface/bulk}} \sim 1/R_{particle}$. This leads to a size dependency of the electronic environment of the electrons inside the particle and thus the dielectric function. Obviously, the conducting electrons which can move "freely" inside the particle are influenced the most by a change of $R_{\text{surface/bulk}}$ (all other electrons are bound to their metal cores and have a strongly limited freedom of motion). Since the excitation of a plasmon is a property of the conducting electrons, a change in $R_{\text{surface/bulk}}$ influences the shape of the plasmon peak.

The impact of the particle-size on the dielectric function of metal particles has been studied by several groups.[92-96] It could be found that the main effect of reducing the particle-size is a broadening of the plasmon peak originating from an increasing damping constant, γ, in the free electron part of the dielectric function. In order to explain this effect a simple model has been proposed.[97, 98] According to the classical model describing the plasmon oscillation, the damping is caused by the scattering processes of the oscillating electrons. Scattering occurs between the electrons, between the electrons and the lattice, and between the electrons and the particle surface. As a consequence of the particle-size dependency of the ratio $R_{\text{surface/bulk}}$, the contribution of electron-surface scattering increases for decreasing particle-size. This contribution becomes significant if the particle diameter drops below the free mean path of the conducting electrons inside the particle which is limited by the electron-electron and the electron-lattice scattering. This effect of additional damping of the plasmon oscillation is known as "free mean path effect".[92] For the free electrons in silver e.g. the free mean path was determined to approximately 52 nm at room temperature.[80] A mathematical description of the damping constant is given in the following paragraphs.

The bulk damping constant, γ_{bulk}, can be determined by equation 3-36:

$$\gamma_{bulk} = \frac{v_F}{l_{bulk}} \quad \text{(eq.3-36)}$$

where, v_F, is the Fermi velocity of the electrons, and l_{bulk}, their free mean path inside the bulk. For small particles the additional damping can be expressed as:

$$\Delta\gamma_{(R)} = A\frac{v_F}{R_{particle}} \quad \textit{(eq.3-37)}$$

where, A, is the damping parameter, and $R_{particle}$, the particle radius. The size dependent overall damping constant, $\gamma_{(R)}$, is the sum of the two contributions:

$$\gamma_{(R)} = \gamma_{bulk} + A\frac{v_F}{R_{particle}} \quad \textit{(eq.3-38)}$$

As mentioned before, the additional damping mainly affects the free electron part of the dielectric function and the interband contribution remains in first approximation unchanged. In order to correct the bulk dielectric function for the free mean path effect, the free electron part of the function must be replaced by a modified term containing the corrected damping constant $\gamma_{(R)}$ instead of the bulk damping constant, γ_{bulk}. As shown in chapter 3.1.1, the dielectric function of a metal consists of the free electron- (χ^D) and the interband contribution (χ^{IB}) of the form:

$$\varepsilon(\omega) = 1 + \chi^D + \chi^{IB} \quad \textit{(eq.3-39)}.$$

Since the dielectric function is usually derived from bulk measurements, its free electron part (Drude part) contains the bulk damping constant. In order to replace this part by the Drude part $\chi^D{}_{(R)}$ containing the particle-size corrected damping constant, equation 3-40 is used:

$$\varepsilon_{(R)}(\omega) = \varepsilon_{bulk}(\omega) - \chi^D + \chi^D{}_{(R)} \quad \textit{(eq.3-40)}$$

Inserting equations 3-10 and 3-11 yields the corrected real and imaginary parts of the dielectric function, given by:[80]

$$\varepsilon_{1,(R)}(\omega) = \varepsilon_{1,bulk}(\omega) + \frac{\omega_p{}^2}{\omega^2 + \gamma^2{}_{bulk}} - \frac{\omega_p{}^2}{\omega^2 + \gamma^2{}_{(R)}} \quad \textit{(eq.3-41)}$$

$$\varepsilon_{2,(R)}(\omega) = \varepsilon_{2,bulk}(\omega) + \frac{\omega_p{}^2\gamma_{(R)}}{\omega\left(\omega^2 + \gamma^2{}_{(R)}\right)} - \frac{\omega_p{}^2\gamma_{bulk}}{\omega\left(\omega^2 + \gamma^2{}_{bulk}\right)} \quad \textit{(eq.3-42)}.$$

The effect of the increased damping constant for decreasing particle size on the absorption spectrum is shown in figure 3-*09* using the example of spherical silver particles in vacuum.

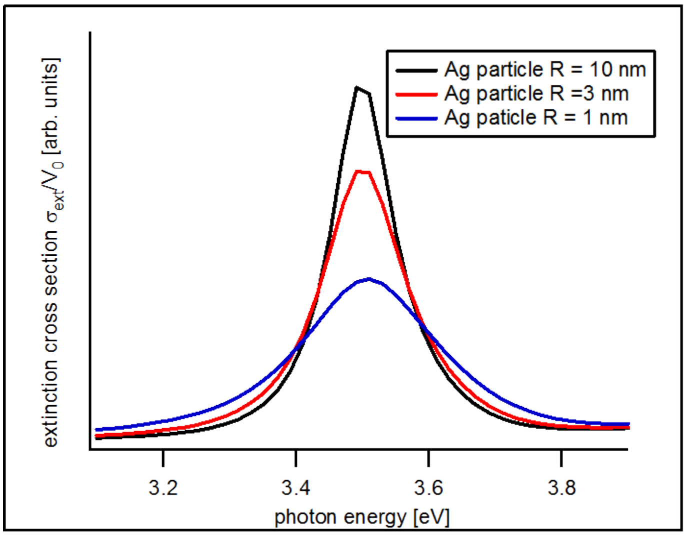

Fig. 3-*09*. Calculated absorption spectra of spherical silver particles in vacuum for different particle sizes. The spectra are all normalized to the same particle volume, V_0, (see equation 3-12) for a better comparability. A clear tendency can be observed: the smaller the particle the broader the plasmon resonance peak.

The three spectra are calculated using equation 3-12 and normalized to the same particle volume, V_0, for a better comparability. The correction of the bulk dielectric function is performed using equations 3-41 and 3-42. The different size dependent damping constants are derived from equation 3-38 with a value for the A parameter of 0.25 and the Fermi velocity of the electrons in bulk silver of $v_F = 0.922 \text{ eV} \cdot \text{nm}$. For the bulk damping constant of silver the value $\gamma = 0.018 \text{ eV}$ is used.[76] In the figure, an increasing width of the plasmon resonance peak with decreasing particle size can be observed, however, the position of the peak maximum remains almost unchanged.

For metal particles which are embedded in a medium (not in vacuum), an increased damping of the plasmon resonance compared to the damping for the same particle size in vacuum can be observed. This type of additional damping of the oscillation is known as chemical interface damping.[99] The origin of this effect is the possibility of a tunneling of the conducting electrons from the metal particle into the surrounding material during the oscillation. This process involves inelastic scattering and diminishes the plasmon lifetime, leading to an increased damping constant. Within this model, the effect is also known as "electron-spill-out effect". Its magnitude depends on the energetic location of electronic states in the surrounding medium. If an occupied electronic state in the particle coincides in its energy with an electronic state of the surrounding, electrons can completely be transferred from the particle into the surrounding material. In this case, the plasmon peak of the particle completely vanishes. A detailed description of these processes can be found in the literature.[100] Since the chemical interface damping occurs at the particle surface, its contribution to the overall damping constant shows the same particle-size dependency as the mean free path effect. Consequently, equation 3-38 can be modified in the following way:

$$\gamma_{(R)} = \gamma_{bulk} + \left(A_{size} + A_{\text{interface}}\right)\frac{v_F}{R_{particle}} \qquad (eq.3\text{-}43)$$

where, A_{size}, describes the additional damping originating from the free mean path effect, and $A_{\text{interface}}$, represents the contribution of the chemical interface damping. Theoretical calculations of the A parameter yield for A_{size} a value of 0.25 (if the units eV and nm are used in equation 3-43). The magnitude of $A_{\text{interface}}$ obviously depends on the surrounding material. A special case is, however, particles that are dispersed on a substrate. In this case, only a fraction of the particle surface area is in contact with the substrate, leading to a more complex description of the $A_{\text{interface}}$ parameter.[100, 101]

3.1.6 Very Small Metal Clusters

The theoretical descriptions of the optical properties of metal particles carried out in the previous sections are in good agreement with the observations in measurements of small particles, down to a size of approximately 1 nm particle radius.[102] However, the question arises, to what extent these concepts apply for very small particles consisting of only a few atoms. This question can be divided into two parts, the validity of the electrodynamic calculations based on Mie theory and the validity of the calculation of the dielectric function presented previously. The Mie theory is conceptually independent of the physical properties of the particles which are described by the dielectric function. It simply connects the intrinsic physical properties of a material with the extinction spectra of the corresponding particle of a certain size and shape. As a consequence, it is valid for all sizes of particles. The theoretical description of the dielectric function and also its correction for the additional damping effects (see previous sections), however, is based on the assumption that an electronic band structure, including a populated conduction band exists in the metal particle. The concept of band structures originates from solid state physics describing the electronic properties of metallic bulk materials with an infinite lattice size. Here, this model is appropriate since the infinite number of energy levels in such systems join to form continuous energy bands in which the collective oscillations of electrons can be induced. With a decreasing number of metal atoms in a particle, however, the number of energy levels forming the energy band diminishes, leading to a band splitting into discrete energy levels. In this case, a collective electron transition is not possible resulting in a superposition of single electron transition events. Consequently, the extinction spectrum should show several sharp absorption lines instead of a single plasmon peak. This plasmon peak splitting could be observed for several small metal clusters in vacuum[103, 104] and embedded in rare gas matrixes[36-39]. To our knowledge, the effect has not yet been observed for metal clusters dispersed on a substrate.

The failure of the energy band model for very small clusters makes the classical descriptions of the dielectric function for such small particle sizes inappropriate. Instead, its calculation must be based on quantum mechanical considerations. However, the great number of electrons involved leads to a high complexity of the calculations even for clusters consisting of only a few atoms. The presence of a substrate further complicates the prediction of the extinction spectra of very small supported metal clusters.

3.2 Ligand Stabilized Clusters

A wide field in cluster science is the investigation of the optical properties of ligand stabilized clusters.[105-107] These cluster systems, mostly synthesized chemically in solution, consist of a metal cluster in the center surrounded by organic (or inorganic) ligands. Such systems are of great interest because they allow the study of the interactions between metal particles and organic molecules. These interactions are key towards understanding the catalytic properties of supported metal clusters.[108, 109] For an interpretation of the measured extinction spectra, the influence of ligands on the optical properties of the metal core must be known. Some of these influences are discussed in the following paragraph.

There are two types of ligand stabilized clusters one, where the ligands are physisorbed on the metal surface and another with chemisorbed ligands. In the first case, the presence of the ligands shifts the resonance position of the plasmon peak by the change of the dielectric constant of the surrounding medium, ε_m. In most cases this will lead to a red shift of the plasmon peak with respect to the peak position for clusters in vacuum because the dielectric constant of any material is larger than 1 (in absence of absorption bands in the medium in the wavelength range of interest). A second effect that occurs is the additional chemical interface damping leading to a broadening of the plasmon peak. In the case of chemisorbed ligands, the electronic properties of the metal clusters are changed more drastically by the presence of a chemical bond between the ligand and the cluster. For most ligands the cluster will be oxidized, which leads to a reduction of the electron density, N, in the metal. According to equation 3-03, the plasma frequency, ω_p, of the conducting electrons is proportional to the electron density. Consequently, a reduction of N reduces ω_p leading to a red shift of the plasmon resonance. For either very small clusters or a high oxidation state, the reduction of conducting electrons can even lead to a vanishing of the plasmon peak or to its splitting in several transition peaks (see previous section). Furthermore, the damping constant will be highly increased in the presence of chemisorbed ligands due to a large enhancement of the electron-spill-out effect. Here, the oscillating electrons in the cluster can be transferred over the existing chemical bond into the ligand, leading to a reduced plasmon lifetime.

In addition to the afore mentioned influences of the ligands on the plasmonic properties of the metal cluster, the cluster also influences the electronic transitions in the ligand which can be observed using spectroscopy. Caused by this interaction, not only the change in the electronic properties of the ligand may be observed, but also other effects such as shifts in the resonance positions of its vibrational transitions. The latter can be determined using spectroscopy in the infrared wavelength range. The investigation of plasmonic properties of the cluster in combination with spectra showing electronic and vibrational transitions of the ligands provides a large quantity of information for the characterization of the cluster-ligand interactions.

3.3 Nonlinear Optical Properties of Metal Clusters

Metal clusters show strong nonlinear effects, such as the generation of the second harmonic frequency due to the large amplitudes of the plasmonic excitations.[110-115] However, as seen in chapter 2.2.3, a condition which must be fulfilled in order to allow for the generation of the second harmonic is the absence of centro-symmetry for the measured species. One possible method to create a sample with non-centro-symmetric metal particles, is electron beam lithography (EBL). Lamprecht *et al.* fabricated two samples with non-centro-symmetric silver particles on a substrate for SHG studies.[116] In figure 3-*10*, the arrangements of their particles on the surface are illustrated.

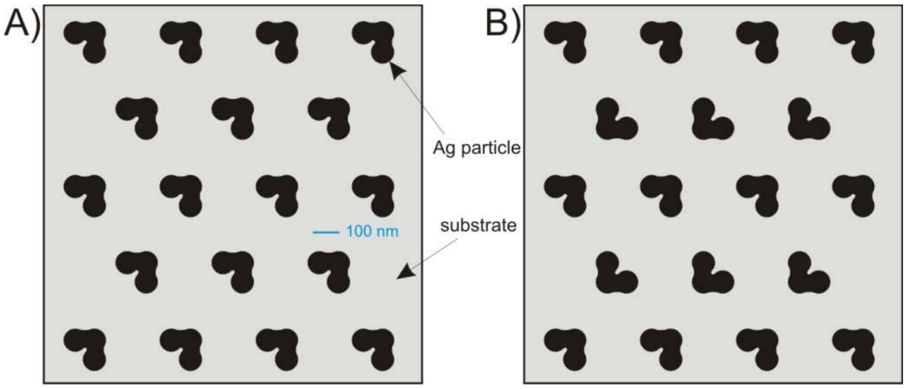

Fig. 3-*10*. Silver particles on a substrate created by electron beam lithography by Lamprecht *et al.* The particles have non-centro-symmetric shape and are arranged A), in a non-cetro-symmetric pattern and B), in a centro-symmetric pattern.

The L-shaped (non-centro-symmetric) particles are arranged in A), in a non-centro-symmetric- and in B), in a centro-symmetric pattern. SHG measurements were performed using these samples at normal incidence, probing only the SH component parallel to the surface. Sample A) showed a large second harmonic signal, whereas for sample B) no signal at the second harmonic frequency could be observed. The negative result of the second measurement could be explained by the destructive interference between the generated SH waves originating from the different metal particles due to their arrangement. This experiment shows, that the condition of the absence of centro-symmetry in a sample for the generation of the second harmonic is not only valid for single particles, but also for the overall arrangement of the particles. The same result as for the sample B) would be observed for non-centro-symmetric particles which are randomly distributed on the substrate. The reason for this is, that randomly ordered systems possess an overall centro-symmetry. This can be illustrated by considering that the average long distance composition of the material is equal for all directions. This result has an important consequence for the SHG measurements of metal particles in gas phase or dispersed in a liquid. Even if the shape of the particles is non-centro-symmetric, no second harmonic light is generated due to their random distribution.

The symmetry condition for samples used for the generation of the second harmonic discussed above is strictly valid under electric dipole approximation. However, if higher multipoles are excited, the generation of the second harmonic is possible even in centro-symmetric systems. The contribution of higher multipole oscillations in metal particles strongly depends on the particle size with respect to the wavelength of the excitation light and becomes significant for particle diameters which are in the same order of magnitude as the wavelength. The particle sizes of the clusters which are investigated in the framework of this thesis are smaller than 2 nm in diameter and thus contributions of higher multipoles can be neglected. A more detailed description of nonlinear multipole excitations in metal particles can be found in the literature.[117, 118]

A special symmetry situation is present for small supported metal particles. As seen above, the oscillation inside the particles parallel to the surface is for randomly ordered particles SHG inactive even if the particles themselves have non-centro-symmetric shape. However, the oscillation perpendicular to the substrate surface is SHG active because the centro-symmetry is broken by the presence of the surface. The lack of centro-symmetry, in this case, is independent of the shape or the distribution of the particles and thus always given. In figure 3-*11*, this situation is illustrated in a sketch using as an example a supported rotationally symmetric particle.

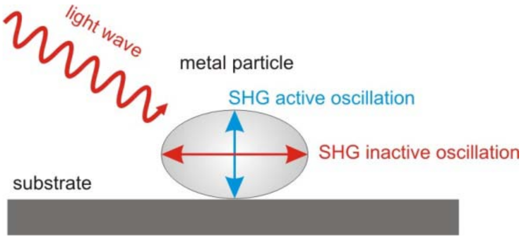

Fig. 3-*11*. Supported rotationally symmetric particle excited by a light wave. From the two depicted oscillation directions (parallel to the surface, red; perpendicular to the surface, blue) only the perpendicular oscillation is SHG active since the centro-symmetry of the particle is broken by the surface in this direction.

The parameter quantifying this symmetry breaking is the asymmetry parameter a, which was introduced in chapter 2.2.4. It describes the asymmetry of the electric potential in which the oscillating charges are confined. From equation 2-31 it can be deduced, that the second order susceptibility is proportional to the quantity of a. For a centro-symmetric particle the asymmetry parameter is zero; however, in the case of supported particles the presence of the substrate leads to deviations of the potential at the interface region between the particle and the substrate, leading to $a \neq 0$. The quantity of a obviously depends on the strength of the perturbation of the electric potential inside the metal particle induced by the substrate and thus on the electric interaction between the particle and the substrate. As a consequence, the intensity of the generated second harmonic beam from such samples can be influenced by the choice of the substrate material.

Due to resonance enhancement of the SHG process (see chapter 2.2.4), plasmon resonances of small supported metal clusters can be probed using s-SHG spectroscopy. However, for particles which are either distributed randomly on the surface or possess a cento-symmetric shape, only plasmonic oscillations which are perpendicular to the surface give rise to an SH signal. Consequently, the s-SHG spectroscopy only probes the plasmonic properties along the height of the particles of such samples. Several s-SHG experiments of small supported metal particles have been reported in the literature confirming the considerations presented above.[115, 119] For the interpretation of the measured s-SHG spectra of supported metal particles, a theoretical description is necessary. In chapter 2.2.5 it could be shown, that for the model of the anharmonic oscillator the calculated s-SHG spectrum matches the calculated linear spectrum in the region of the resonance peak in good approximation (if the s-SHG spectrum is plotted as function of the SH photon energy). Here, the question arises, whether the description of the plasmon resonance shown in the previous sections (equation 3-19) is equivalent to the model of the anharmonic oscillator. This would open the possibility to also use the formulas derived for the linear absorption spectrum for the interpretation of the s-SHG spectra. The equivalence can be tested by only considering the free electron part of the dielectric function of the metal (for simplification), and inserting the latter into equation 3-19. The real and imaginary parts of the free electron part are given in equation 3-07. The resulting cross section of the metal particle is obtained after some algebraic transformations:

$$\sigma_{i,ext} = \frac{\omega}{c_0}\varepsilon_m^{3/2} \cdot V_0 \frac{\omega_p^2}{f} \cdot \frac{\gamma \cdot \omega}{\left[\frac{\omega_p^2}{f} - \omega^2\right]^2 + \gamma^2\omega^2} \qquad (eq.3\text{-}44)$$

where, $f = L_i + (1 - L_i)\varepsilon_m$. Equation 3-44 has the form (the frequency dependent part) of the linear absorption cross section derived for the model of the anharmonic oscillator (equation 2-34) with the resonance frequency $\omega_0 = \omega_p^2 / f$. From this observation it can be concluded, that the mathematical description of the plasmon resonance given by the Mie theory is equivalent to the equations derived on basis of the model of the anharmonic oscillator (if only the free electron part is considered). The consequence of this observation is that equation 3-19 can be used in order to describe the shape and resonance position of a plasmon peak measured in a s-SHG experiment (using the procedure presented in chapter 2.2.5). This is not necessarily correct for parts of the spectrum where interband transitions appear since only the free electron part of the dielectric function is considered here. However, in first approximation the use of the linear description is reasonable.

Plasmon field enhancement

The large amplitude of the plasmon oscillation in metal particles leads to a strong enhancement of the local field close to the particle surface. The enhancement can thereby reach up to factors of 10^4 or higher, depending on the particle sizes and shapes.[120] This effect plays an important role in many nonlinear spectroscopic techniques, such as surface enhanced Raman spectroscopy and is known as plasmon field enhancement (PFE).[121, 122] A strong influence of the PFE can also be observed for the generation of the second harmonic at the surface of cluster samples.[123] The local field at the position of a certain metal particle in such samples is enhanced by the particle itself and by the neighboring particles. Since the amplitude of the generated second harmonic wave depends on the square of the amplitude of the local field (see chapter 2.2.1), its enhancement can have drastic effects on the nonlinear process. The enhancement factor obviously depends on the frequency of the fundamental beam which can even lead to shifts of the plasmon resonance position in the s-SHG spectrum. Such shifts are described in the context of the local field correction in chapter 3.1.4.2 for the linear case. However, since a change in the local field affects second order processes in a different manner (quadratic relation) than it affects linear processes (linear relation), the validity of the derived equations for the local field correction in s-SHG measurements is questionable. Furthermore, a significant difference between the linear and the nonlinear excitations appears in the case of the s-SHG measurement of a particle plasmon, where the plasmon transition is in resonance with the second harmonic frequency. Here, the local field is enhanced by the oscillation of the conducting electrons at the fundamental frequency which is far from the plasmon resonance at 2ω. In a linear experiment, the absorption maximum of a plasmon always roughly coincides with maximum in the local field enhancement. This discrepancy can lead to large differences between the local field parameters for linear and nonlinear plasmon excitations. A more detailed description of the plasmon field enhancement effect on nonlinear processes can be found in the literature.[124, 125]

3.4 Summary Chapter 3

In chapter 3, the mathematical description of the optical properties of metal particles based on Mie theory was presented. It could be shown that the conducting electrons in metal particles can perform collective oscillations with a distinct resonance frequency (plasmon resonance), leading to an intense absorption peak in the linear spectrum. Furthermore, several factors influencing the properties of the plasmon resonance were presented, such as the particle shape, the particle size, and the presence of a substrate. It was found that the deviation of the particle shape from a sphere necessarily leads to the splitting of the plasmon resonance into several modes, for spheroid particles into two plasmon modes. In a separated section the limits of the theoretical description towards very small clusters were pointed out followed by a discussion of the impact of organic ligands on the optical properties of the metal particles.

In the last part of the chapter, several principles of the nonlinear properties of supported metal particles were shown. From symmetry considerations it could be extracted, that only the plasmon oscillation parallel to the particle height can give rise to the generation of the second harmonic frequency if supported particles are investigated using s-SHG spectroscopy. Furthermore, it could be shown that the mathematical description of plasmon excitations derived from Mie theory is equivalent to the model of the anharmonic oscillator. This result justifies the use of the theoretical descriptions of the linear cluster spectra for the interpretation of the nonlinear s-SHG spectra (as proposed in chapter 2).

4. Cluster Sample Preparation Setup

In this chapter, the experimental setup required for the cluster sample preparation is described. In the first subsection, a general overview of the cluster source design and its characteristics are presented and briefly discussed; further details may also be found in ref.[61] The chapter then focuses on the working principles of a number of enhancements made to the original cluster source setup, namely the substrate sample holder, the low energy electron source (used to neutralize deposited clusters), and the sample transfer chamber, which were each developed as part of this thesis (the latter was primarily developed by Dr. Aras Kartouzian). Overall, the enhanced cluster sample preparation setup allows the precise, clean and reliable preparation of supported metal clusters on various substrate materials (including non conducting materials), necessary for spectroscopic analysis.

4.1 Cluster Source

In order to produce size selected metal clusters, a so-called laser evaporation cluster source is used. The cluster source in the surface spectroscopy laboratory is constructed using as antetype design the cluster source presented by Heiz *et al.*[126] A schematic of the cluster source, including the analysis chamber where the spectroscopic measurements are carried out is depicted in figure 4-*01*. The clusters are formed in the source chamber via evaporating the metal atoms of a rotating target (using a laser), which collide with He atoms (introduced via a gas pulse) to form a mixture of sizes of charged clusters. The metal cluster gas mixture then expands into the vacuum of the octopole chamber which guides the clusters to the deflection chamber, where the metal clusters are deflected 90° out of the principle axis of the laser beam, and toward a quadrupole mass filter located at the entrance of the analysis chamber. A specific cluster size may then be selected by the quadrupole mass filter, guided and subsequently deposited onto a suitable sample substrate. In the following paragraph the setup, the cluster formation process, and the propagation of the cluster beam are described in greater detail.

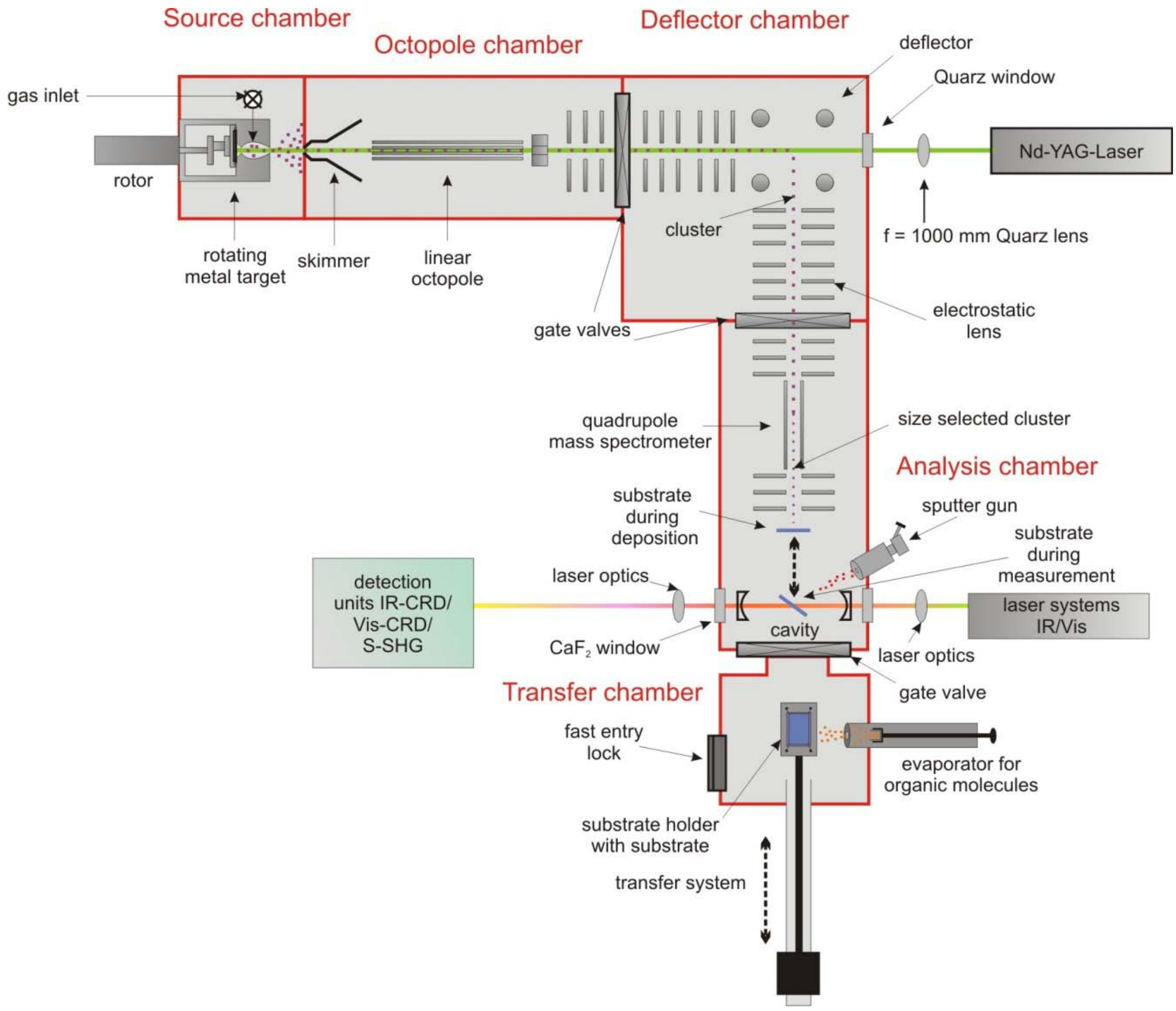

Fig. 4-*01*. Schematic of the experimental setup. The red lines mark the different vacuum chambers of the setup (source chamber, octopole chamber, deflector chamber, analysis chamber and transfer chamber). The dotted line (violet) shows the cluster beam path through the different ion guiding elements. The deposition and the spectroscopic measurements are carried out in the analysis chamber, which is additionally equipped with an argon ion sputter gun for the cleaning of the substrate surface. In the transfer chamber, a sample transfer system is installed. This, in combination with a fast entry lock allows for changing substrates without breaking the vacuum of the analysis chamber. For the deposition of organic molecules, there is an evaporator connected to the transfer chamber.

The clusters are formed in the source chamber where a laser pulse of the second harmonic beam of a NdYAG laser (Innolas, Spitlight DPSS, 100 Hz) evaporates metal atoms and ions from a rotating metal target. Using a piezo valve, a triggered He gas pulse is injected into a nozzle which is placed in front of the metal target. Due to collisions of the metal atoms and ions with the gas molecules, larger clusters are formed which leave the nozzle together with the seed gas in a supersonic expansion into the vacuum chamber. Passing through a skimmer, the clusters are guided inside a next vacuum chamber (octopole chamber) in a linear octopole which is driven by a radio frequency (RF) transceiver (Kenwood, TS-570S). Behind the octopole, the cluster beam is guided into the deflector chamber using electrostatic lenses. Here, a electrostatic deflector bends the cluster beam by 90° into a second set of electrostatic lenses which guide the beam into a quadropole mass filter (Extrel, 5500 series) which is mounted in a third vacuum chamber (analysis chamber). Inside the quadropole mass filter, the mass selection of the clusters takes place. A superposition of a DC with a RF electric field on the four rods of the quadropole defines the mass of a charged particle which possesses a stable trajectory through the quadrupole. These particles are transmitted, whereas all particles with different masses do not reach the exit of the quadropole. By tuning the DC and the RF field, the selected mass can be changed. This can be done using an automated software (Extrel, Merlin 3.0) from the manufacturer of the quadropole. At the exit of the mass filter, a set of three electrostatic lenses allows for focusing the cluster beam onto the substrate which is mounted on a sample holder (see chapter 4.2). The sample holder is connected to a rotatable x,y,z manipulator and thus movable inside the analysis chamber. Since the mass selection in the quadropole mass filter only works for charged particles, all electrostatic elements are optimized to guide positively charged clusters. All four vacuum chambers (source chamber, octopole chamber, deflector chamber and analysis chamber) are differentially pumped by three turbo pumps and the source chamber is additionally pumped by a rootspump. The latter is required due to the high gas pressures in this part of the cluster source. Between the octopole and the deflector chamber, as well as between the latter and the analysis chamber, there are gate valves which allow the separation of the different chambers.

The analysis chamber is (in addition to the turbo pump mentioned above) equipped with an ion getter, and a titanium sublimation pump to give a base vacuum pressure of $< 310^{-10}$ mbar. The amount of water and oxygen under these conditions are below the detection limit of a commercial quadrupole mass spectrometer for trace gas analysis. This is crucial, since at already very low partial pressures the presence of water and oxygen can lead to the oxidation of the deposited clusters. During the deposition, the pressure increases to the range between 10^{-7} and 10^{-6} mbar due to the injection of the helium gas. Consequently, the helium gas is a potential source of impurities which can enter the analysis chamber. In order to avoid contamination, highly pure helium gas is used (He 6.0, Air Liquid). Before the deposition of clusters onto a substrate is performed, its surface is cleaned by sputtering. Therefore, an argon ion sputter gun (Thermo VG Scientific, EX 03) is connected to the analysis chamber. The cleaning by sputtering is crucial because any substrate which is transferred from ambient conditions into the vacuum chamber (using the sample transfer system) is covered by water, which can only be removed by either heating or sputtering. After the cleaning step, the sample holder can be moved in front of the electrostatic lenses which are mounted at the exit of the quadropole mass filter, and clusters can subsequently be deposited on the clean substrate.

The cluster current can be measured by introducing a metal plate into the cluster beam which is connected to a picoamperemeter (Keithley, 6517A). The metal plate can be moved by a linear feedthrough which is mounted orthogonal to the cluster beam in the analysis chamber. The performance of the cluster source can be demonstrated by recording a mass spectrum using the picoamperemeter. Such a mass spectrum of platinum clusters is shown in figure 4-*02*.

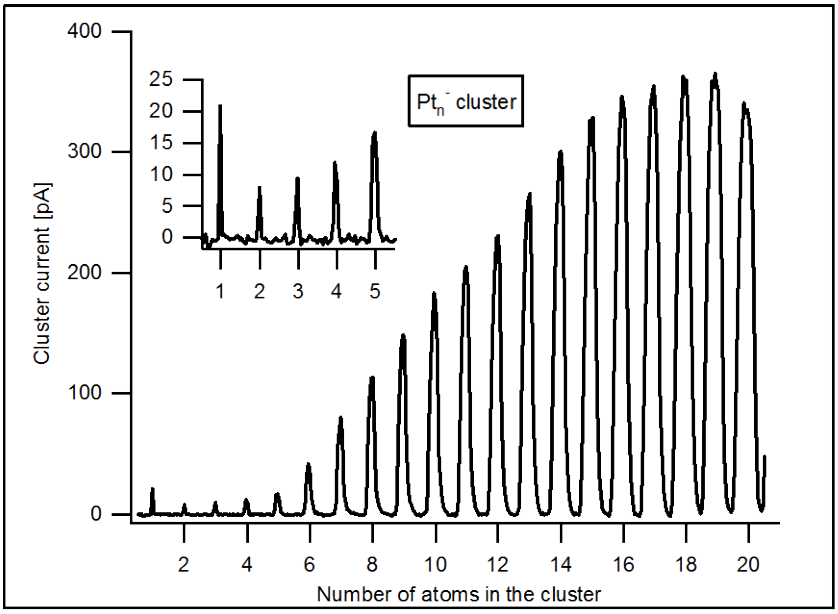

Fig. 4-*02*. Mass spectrum of Pt clusters produced by the cluster source. All sizes between atoms and Pt_{20} clusters are present. The maximal mass which can be selected by the quadrupole mass filter is 1600 amu.

All sizes between Pd atoms and Pt_{20} clusters are present with cluster currents up to 350 pA, however, the cluster current strongly varies for different cluster sizes. There are two main factors controlling the size distribution of clusters in the mass spectrum. Firstly, the pressure conditions in the source chamber have a strong influence on the size of the produced clusters. The sizes formed can be influenced by tuning the time delay between the helium gas pulse and the laser pulse, as well as by tuning the voltage which is applied at the piezo valve. Furthermore, the opening time of the piezo and the back pressure of the helium gas behind the valve are important parameters. The second factor, concerns the voltages at the electrostatic elements along the cluster beam path. In order to optimize the cluster current of a certain cluster size, all these parameters must be adjusted. In the case presented here, the cluster source is optimized for Pt_{19} clusters which explains the maximum in the mass spectrum for this size. The maximum cluster current which can be achieved with this cluster source strongly depends on the metal which is used. For example, silver is a metal which does not form clusters easily. The highest currents which were reached for silver clusters are in the range of 40 pA at comparatively high helium pressures.

The kinetic energy of the clusters is in the range between 0.2 and 0.8 eV per atom.[61] This is smaller than the typical binding energy of metal clusters with $E_{\text{bind}} > 1\text{eV}$ per atom.[127, 128] The low kinetic energy allows the deposition of the clusters on surfaces without risking to destroy the clusters via the collision of the clusters with the surface. This type of deposition is called "soft landing".

The choice of a suitable substrate material is limited due to the very distinct requirements that are defined by the applied spectroscopic techniques (see chapter 6). One requirement is a very high transparency of the substrate which makes the use of electrically conducting materials impossible. This leads to a charging problem on the surface because the clusters deposited on the surface are positively charged. If the substrate is an insulator, the charges from the clusters accumulate on the surface and the so generated electric field repels further clusters. The deposition is consequently impossible. One possible way to avoid this situation is to neutralize the surface by supplying electrons. This can be done, using an electron source which produces an electron shower in front of the substrate. The kinetic energy of the electrons should be low to avoid a large negative charge being generated on the substrate. This would lead to an acceleration of the clusters which could result in their destruction when hitting the surface of the substrate. In order to fulfill all these requirements, a homemade electron source is mounted to a specially designed sample holder. The sample holder and the electron source are described in detail in the following section.

4.2 Sample Holder

A special sample holder was designed in order to account for the special requirements of the spectroscopic techniques and the cluster deposition. The sample holder carries both, the substrate and the electron source, and is mounted on the end of a long stainless steel tube with manipulator located inside the analysis chamber. The mounting of the electron source onto the sample holder has one major advantage compared to installing it somewhere else in the analysis chamber. The electron source is not only needed for the neutralization of deposited clusters, but also for the substrate sputtering process which is performed using positively charged argon ions. Since the sputter gun is installed at a different location inside the vacuum chamber, the substrate has to be moved using the manipulator for sputtering. Using the sample holder presented here, the electron source remains at the same position with respect to the substrate and no further alignment is required. In order to allow for the samples to be changed easily using the transfer system, the substrate is placed on a substrate holder and fixed with four springs, as illustrated in figure 4-*03*.

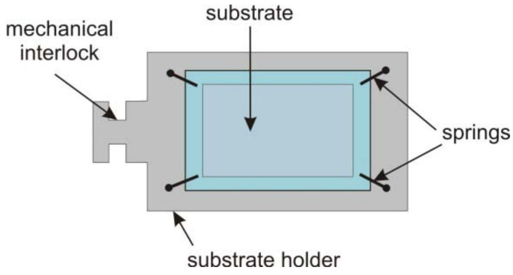

Fig. 4-*03*. Sketch of the substrate holder with substrate. The substrate is placed in the middle of the holder and fixed with four springs. Behind the substrate, there is a window in the substrate holder allowing the laser beam to pass through the sample. The mechanical interlock is part of the sample transfer system and serves as connection point to the transfer rod of the system.

The mechanical interlock located on the left side of the substrate holder is for connecting the tip of the transfer rod of the transfer system to the substrate holder. The substrate can be placed in the sample holder by sliding the substrate holder into a slit, with the body of the sample holder on one side and two clips on the other. Inside this slit, the substrate holder is fixed and the transfer rod can be removed. Above the substrate holder the electron source is mounted (see figure 4-*04*). Between the substrate and the electron source, a round shield blocks the heat radiation which is produced from the hot filament of the electron source in order to avoid heating the substrate. A small slit in the shield guides the electrons towards the substrate. Using this sample holder, electron currents in the range of 20 nA can be measured in front of the substrate. The entire sample holder is made of copper to ensure good thermal conductivity. This is necessary, since the substrate is cooled from outside via the tube of the manipulator using liquid nitrogen. If the sample holder is cooled to 77 K (liquid nitrogen), the substrate reaches a temperature of about 120 K.[61] The discrepancy can be explained by the low thermal conductivities of the insulating substrates and their large absorption of heat radiation. Even if the radiation from the electron source (it heats up to several hundred degrees during operation) is blocked, there is still a large amount of heat radiation coming from the walls of the chamber which remain at room temperature. To block as much of this radiation as possible, there is also a second round copper shield installed at the lower end of the sample holder. The equatorial area cannot be shielded, since this area must remain free in order to perform the spectroscopic measurements. A concept for a more efficient shielding has already been developed and can be found in ref.[61] The cooling of the substrate fulfills two purposes. Firstly, without the necessary cooling the electron source would heat the entire sample holder including the substrate, which in turn could lead to the agglomeration of the clusters. Here, the temperature of the sample holder can reach up to 100° C within one hour of running electron source. If the sample holder is cooled, the heat of the electron source is fully compensated. A second reason for cooling the substrate is attributed to the fact that the agglomeration of clusters may already take place at room temperature. In principle, the colder the substrate is the more stable are the clusters on its surface. In figure 4-*04*, a three dimensional image of the sample holder is shown.

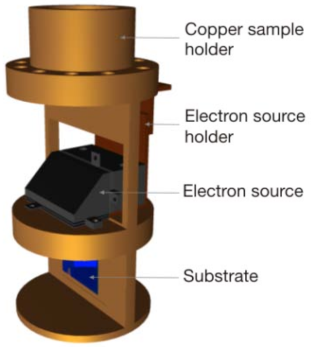

Fig. 4-*04*. 3D image of the sample holder showing the electron source and the position of the substrate. Note that in order to simplify the alignment of the s-SHG setup (see chapter 5.2.1), a thin (1 mm) BBO crystal is mounted under the copper shield located at the lower end of the sample holder (which is not depicted here).

4.3 Electron Source

In figure 4-*05*, the electron source is depicted in detail. The electrons are produced by a hot tantalum filament which is wound around a ceramic rod. The filament and ceramic rod are mounted inside a tantalum housing which is open on one side. There, the electrons are guided through an electrically isolated metal mesh, followed by a 90° bending downwards in a second part of the tantalum housing. At the end of this part, a second metal mesh and an end plate with a window of the size of the mesh are installed. Here, the electrons leave the source in downwards direction.

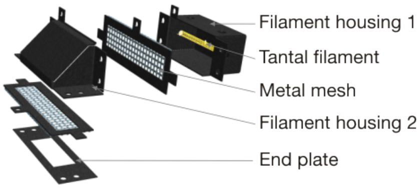

Fig. 4-*05*. 3D image of the electron source shown in its fragments. It consists of a filament housing carrying the Ta filament, two electrically isolated metal meshes for the electron guiding, a second housing part for bending the electron beam, and a metal end plate.

At the filament, a voltage of ~13 V is applied, whereby the positive pole is grounded (potential: 0 V). The entire housing and the end plate are set to the same potential as the negative pole of the filament (-13 V) and the metal meshes are grounded. In this configuration the electrons which leave the filament have a potential ranging from 0 V to -13 V, depending on the position at the filament from which they are emitted. Due to these potentials, all electrons are repelled by the housing and attracted by the metal meshes which ensures the electrostatic guiding of the electrons to the exit of the electron source housing. Arriving at the substrate, the kinetic energy of the electrons is consequently between 0 eV and 13 eV considering a potential of the substrate of 0 V. The geometry of the electron source is chosen to avoid that Ta atoms or ions which are evaporated from the hot filament leave the source and lead to the contamination of the substrate. Neutral particles cannot reach the substrate because there is no directly straight path from the filament to the outside of the electron source housing. The Ta ions produced are almost exclusively cations which cannot penetrate the metal mesh due to its potential, but are instead attracted by the housing where they are trapped. Using this electron source, a production of low energy electrons is possible without contaminating the substrate with the material of the filament.

4.4 Transfer chamber

A transfer chamber is connected via a gate valve to the analysis chamber in order to enable the replacement of the sample without breaking the vacuum. The transfer system consists of a long transfer rod with a special tip which can be connected to the substrate holder (via the mechanical interlock, see figure 4-*03*). The rod is connected to a handle at the outside of the transfer chamber via strong magnets and can be moved in and out by moving the handle (see figure 4-*01*). A fast entry lock is installed which is used to introduce the sample into the transfer chamber. Therefore, a special docking station for the substrate holder is present. The transfer chamber is pumped by a turbo pump and the transfer is carried out as soon as the pressure in the chamber underruns the value of $1 \cdot 10^{-7}\,\text{mbar}$ after starting the turbo pump. This is necessary in order to avoid the contamination of the analysis chamber with water when opening the gate valve. For the deposition of organic molecules on t he substrate via evaporation, the transfer chamber is additionally equipped with a molecule evaporator of in-house design.

More detailed information about the experimental setup can be found in ref.[61] All experiments in this thesis are carried out using the presented experimental setup.

5. Spectroscopic Setup

In this chapter, the spectroscopic setup for the investigation of supported metal clusters and organic adsorbates under UHV conditions is described and characterized. A key aim of this thesis was to construct a spectroscopic setup which is capable of readily switching between the three spectroscopic methods (i.e. s-Vis-CRD, s-IR-CRD, and s-SHG) with a minimum of alignment needed (when switching techniques), in order to enable the full characterization of a single cluster sample. In the beginning, the different laser sources are described and characterized, followed by a detailed description of the spectroscopic setup. To finish, the characterization and calibration of the photodiode that is used to measure the pulse energy of the fundamental beam is shown.

5.1 Laser Sources

For the three spectroscopic techniques tunable laser sources are required for the visible and the infrared range. However, there is no commercially available laser source which covers the entire wavelength range from the visible to the infrared (around 3000 cm^{-1}), and therefore two different laser systems are used. For the visible range, a laser system consisting of an optical parametric oscillator (OPO) which is pumped by the third harmonic of a NdYAG laser is used and tunable IR laser light is generated by difference frequency mixing (DFM) of the output of a dye laser with the fundamental of a NdYAG laser. The performance of the laser systems is shown in the following section.

5.1.1 Performance OPO Laser System

A midband optical parametric oscillator (OPO) (GWU, premiScan ULD/400) pumped by the third harmonic of a pulsed NdYAG laser (Innolas, Spitlight 1200, 20 Hz) is used as the tunable laser source for the visible range. The laser system generates pulsed laser light in the wavelength range between 420 and 900 nm and a pulse length of 7 ns. An OPO laser splits the pump photon into two photons (signal and idler) following the relation:

$$\omega_{\text{pump}} = \omega_{\text{signal}} + \omega_{\text{idler}} \qquad (eq.5\text{-}01)$$

Equation 5-01 describes the optical parametric process which can be seen as reverse sum frequency mixing.[129] The frequencies, ω_{signal}, and ω_{idler}, of the signal and the idler wave can be tuned by rotating the nonlinear crystal (BBO) inside the OPO (in this crystal the OPO process takes place). The reason for this is that for every crystal angle the phase matching conditions must be fulfilled for the two generated waves (see chapter 2.2.2).[130] The two resulting laser beams are separated by a rotatable Pellin-Broca prism inside the OPO housing and by a dielectric mirror which is highly reflecting for the signal wave and highly transparent for the idler. In order to cover the wavelength range from 420 to 900 nm, two different BBO crystals can be introduced in the OPO resonator which are each cut in different angles with respect to the crystal planes. With the first crystal (blue crystal) the wavelength of the signal wave can be tuned between 420 and 515 nm and for the second crystal the signal wave covers the range from 505 to 710 nm, where the frequency of the signal matches the frequency of the idler wave. At this point, the efficiency of the optical parametric process is nearly zero, resulting in a very low generated laser power. In order to obtain laser radiation between 710 and 900 nm, the idler wave of the red crystal is coupled out. Signal and idler waves are polarized orthogonally to each other and consequently, the polarization of one of the two must be turned by 90° to ensure one single polarisation direction of the laser beam over the entire wavelength range. This is achieved using two different beam paths as shown in figure 5-*01*.

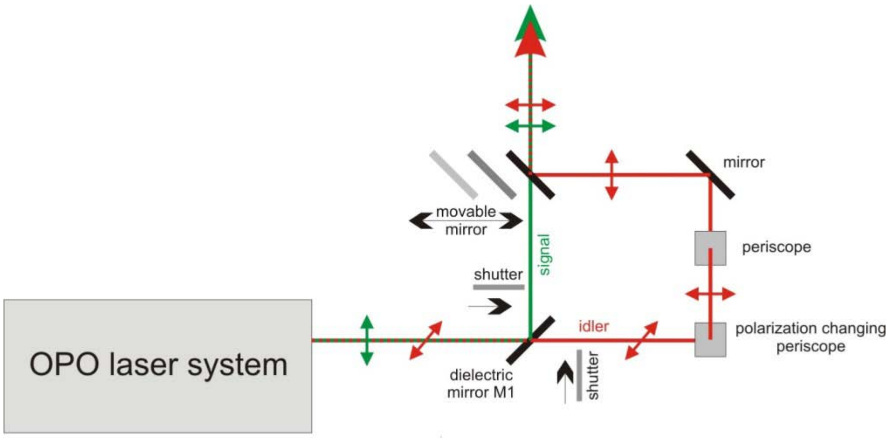

Fig. 5-*01*. Setup for switching between signal and idler wave of the OPO laser system without changing the polarization. The idler beam (red line) is coupled out using the dielectric mirror M1 and its polarization is turned by 90° in the first periscope. Using a movable mirror the idler is reinjected in the beam path of the signal wave (green line).

Behind the separation of the signal and the idler beam inside the OPO laser system by the Pellin-Broca prism, the dielectric mirror M1 is positioned inside the beam path. This mirror is highly reflecting in the wavelength range of the signal wave, but highly transparent in the IR range of the idler. From this point on, the beam paths of the two waves differ from each other. In contrast to the path of the signal beam, the branch of the idler is equipped with a polarization changing periscope. A second periscope readjusts the original height of the beam over the laser table. Using a mirror which is mounted on a linear micrometer translation stage, the idler beam can be re-injected into the beam path of the signal wave. Here, the polarization of the two beams is equal. Two shutters allow the blocking of one or the other branch of the beam path. Using this system, it can be easily switched between signal and idler wave by changing the position of the movable mirror and blocking one of the branches without changing the polarization. Since the beam profile of the laser beams generated by the OPO system is rather triangular (with three intensity maxima) than circular, irises are introduced in each branch to form a better intensity profile. However, because the beam profile of this type of OPO laser changes for different wavelengths (see figure 5-*02*), a perfect positioning of the irises is impossible. Figure 5-*02* shows the beam profiles obtained after positioning the irises for three different wavelengths.

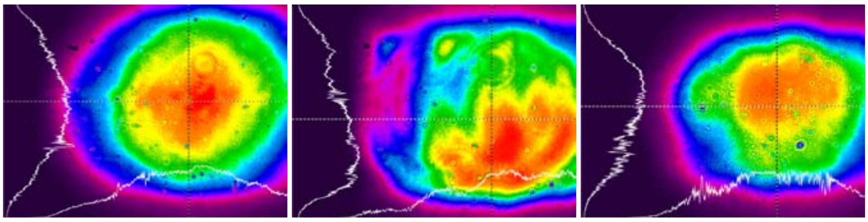

Fig 5-*02*. Beam profiles for 470 nm (signal wave, blue crystal) (left), 660 nm (signal wave, red crystal) (middle) and 830 nm (idler wave, red crystal) (right).

The beam profile of the signal wave from the blue crystal at 470 nm has a nearly Gaussian shape, which is not the case for the beam profile of the signal wave from the red crystal at 660 nm. Here, the light intensity forms several hot spots and has an oval shape. The beam profile of the idler wave at 830 nm is acceptable although it is not round, either. These profiles are the result of the best alignment of the irises which could be obtained. The poor quality of the beam profiles of the output from the OPO laser system inhibits a better alignment which is definitively a huge drawback for the use in highly sensitive spectroscopic techniques. However, a different tunable laser source would be necessary in order to improve the beam profile.

In figure 5-*03*, the measured pulse energy of the OPO laser system (including the setup shown in figure 5-*01*) is shown as a function of the wavelength. The energy ranges from 2 mJ to approximately 10 mJ with a huge drop to almost zero at 710 nm. This is the wavelength (mentioned above) where the frequency of the signal matches the frequency of the idler beam. Due to the low laser intensity, it is not possible to carry out spectroscopic measurements in this region. Consequently, all the measured spectra using this laser system show a gap between 700 nm and 720 nm.

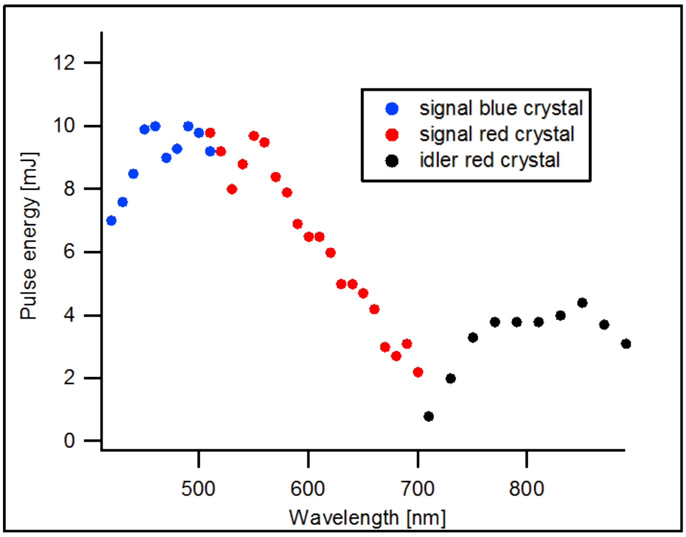

Fig. 5-*03*. Pulse energy of the OPO laser system shown as a function of the wavelength. Pulse energies ranging from 2 to 10 mJ are available with a drop around 710 nm.

5.1.2 IR Laser System

Tunable IR laser light is produced by difference frequency mixing of the fundamental beam of a NdYAG laser (Lummonics, HY 750, 20 Hz) and the output beam of a dye laser (Lambda Physik, Scanmate 2) in a nonlinear crystal ($LiNbO_3$). The dye laser is pumped with the second harmonic beam of the NdYAG laser and produces tunable laser light in the range between 760 nm and 830 nm using the laser dye *styryl 11*. The resulting IR beam covers a frequency range between 2800 cm^{-1} and 3600 cm^{-1}. The setup of the IR laser source is depicted in figure 5-*04*. Inside the difference frequency mixing unit (DFM-unit), the fundamental beam of the NdYAG laser passes after a delay line a half wave plate that turns its polarization by 90°. The delay line is necessary to ensure that the two laser pulses arrive at the same time in the nonlinear crystal. The laser light from the dye laser is widened by passing through a telescope and its polarization can be adjusted using a rotatable Fresnel rhomb. In the nonlinear crystal the two beams are superimposed, generating the sum- and the difference frequency. The horizontal displacement of the beams originating from the $LiNbO_3$ crystal is compensated by a CaF_2 crystal which is always oriented in the opposite direction with respect to the optical axis. Behind the crystals, the fundamental frequency of the NdYAG laser is blocked by a dielectric mirror (S1) which is highly reflective at a wavelength of 1064 nm and guides the beam into a beam dump. A second dielectric mirror (S2) blocks the beams from the dye laser and the generated sum frequency which are reflected to a second beam dump. Both mirrors are highly transparent in the wavelength range of the generated difference frequency beam. Consequently, the resulting laser light behind the mirrors only consists of the generated difference frequency and can be used for the s-IR-CRD experiments. The wavelength is tuned by changing the output wavelength of the dye laser and the angle of the nonlinear crystal in the DFM-unit. The compensator is mechanically connected to the nonlinear crystal and thus turns automatically. Using a calibration table, the tuning of the wavelength is fully automated and driven by a LabView based program.

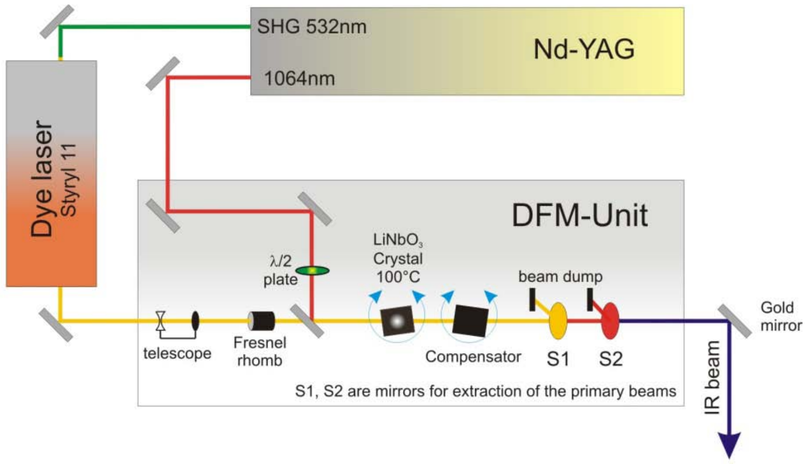

Fig. 5-*04*. Setup of the IR laser source. A NdYAG laser is used to pump a dye laser with the laser dye *Styryl 11*. The resulting laser beam is mixed with the fundamental beam of the NdYAG laser in a nonlinear crystal, generating the sum and the difference frequency. With the mirrors S1 and S2 the beam with the difference frequency is coupled out.

In figure 5-*05*, the pulse energies generated by the presented setup are shown as a function of the photon energy. The pulse energies range from 0.25 mJ up to almost 2 mJ per pulse. At around 3500 cm^{-1} the pulse energy is highly reduced which can be explained by absorption bands of water molecules inside the $LiNbO_3$ crystal in this region. The presence of water in the nonlinear crystal is caused by its hygroscopic properties. In order to keep it as dry as possible, the crystal is heated to 100°C.

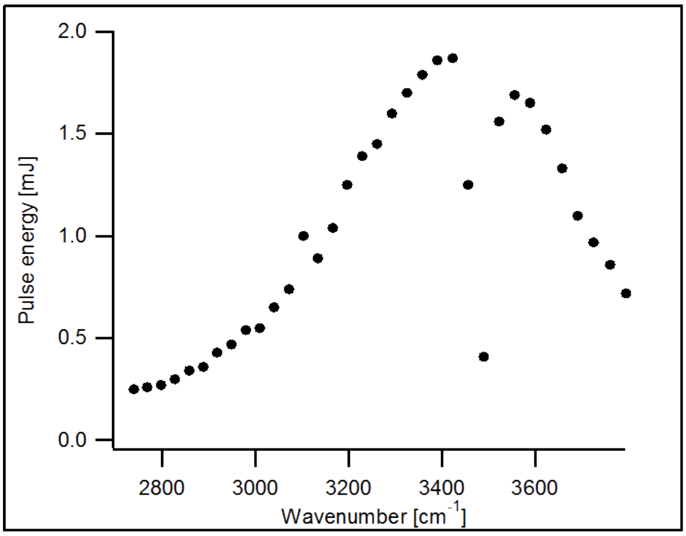

Fig. 5-*05*. Pulse energy of the laser beam generated by difference frequency mixing in the setup presented as a function of the photon energy. The strong decrease in energy around 3500 cm^{-1} originates from absorption bands of water molecules inside the nonlinear crystal.

5.2 Setup of the Spectroscopic Methods

The entire spectroscopic setup is depicted schematically in figure 5-*06*. It consists of three different beam paths for the three spectroscopic methods, marked in different colors (s-SHG, s-Vis-CRD, s-IR-CRD). Each laser path is described in detail in the following.

Setup s-SHG

The OPO laser system serves as the laser source for the s-SHG measurements. In order to ensure the clarity of the schematic, the part of the setup which is depicted in figure 5-*01* is left out of figure 5-*06*. The laser beam from the OPO laser system is focussed onto a 0.8 mm^2 spot on the sample (calculated for normal incidence) where the second harmonic frequency is generated. In order to eliminate any possible components of light oscillating at the second harmonic frequency from the fundamental laser beam, a UV filter (Schott, GG 435) is introduced in the beam path in front of the first focussing lens (components of SH light might be generated inside the OPO system and at each optical element of the setup). The sample is mounted onto a rotatable x,y,z manipulator in an UHV chamber. CaF_2 windows are used for the injection of the laser beam into the chamber. They are placed 26 cm from the focus; this geometry avoids any second harmonic generation at their surfaces. In fact, the diameter of the beam is about 3 mm at the position of the window. After passing the sample and the UHV chamber, the beam is re-collimated and separated into its fundamental and second harmonic parts by a rotatable dispersive Pellin-Broca prism. The fundamental beam is blocked by a beam dump, whereas the SH beam is cleaned from any residual contributions of the fundamental by a second Pellin-Broca prism. Further wavelength selection (suppressing of scattered fundamental light) is achieved using a monochromator (LOT-Oriel, Omni-λ 300). A photomultiplier (Hamamatsu, H9305-03) located at the exit of the monochromator detects the SH signal, which is recorded by a digital 4 channel oscilloscope (LeCroy, Waverunner 6051). The monochromator, the two prisms, and the OPO crystals are synchronized and driven by step motors (PI, M-222.20). A LabView based program of in-house design drives the step motors and allows for fully automated wavelength scans.

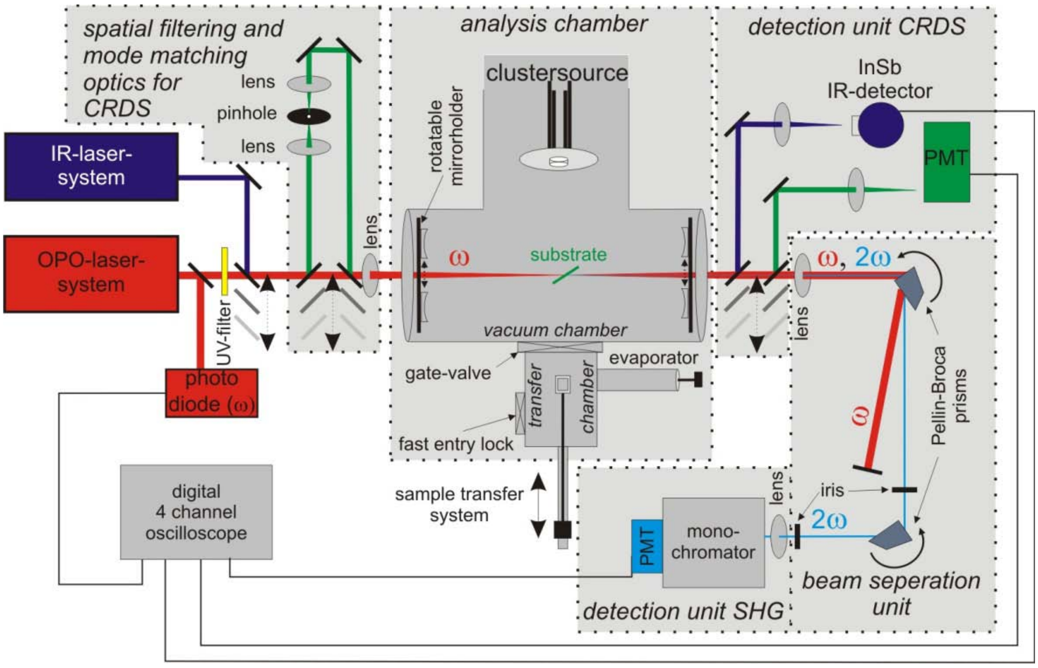

Fig. 5-*06*. Schematic of the spectroscopic setup. The beam paths for the different spectroscopic techniques are depicted in different colours (red: s-SHG, green: s-Vis-CRD, dark blue: s-IR-CRD). The double arrows indicate movable mirrors which are mounted onto micrometer translation stages.

For measuring the intensity of the fundamental beam, a small part is reflected out of the beam path into a photodiode (Thorlabs, 201/579-7227) using a quartz window as beam splitter. The signal of the photodiode is recorded simultaneously with the SH signal by the oscilloscope. For measuring a spectrum 200 pulses are recorded and averaged at every wavelength in order to reduce noise.

Setup s-Vis-CRD

For the s-Vis-CRD measurements, the OPO laser source is used in the same way as for the s-SHG measurements. However, the laser path is rerouted behind the OPO system by introducing two broadband dielectric mirrors mounted onto a linear micrometer translation stage. This optical branch contains two lenses and a 35 μm pinhole for spatial filtering and mode matching. The spatial filtering forms the laser beam from the OPO system to a beam with an intensity profile of perfect Gaussian shape which is crucial in order to achieve good mode matching.[60] At the end of this deviation the beam joins the original laser path in front of the focussing lens which is placed in front of the UHV chamber. All three lenses in front of the chamber are part of the mode matching optics. Inside the vacuum chamber behind the CaF_2 windows, two rotatable UHV-compatible mirror exchangers are mounted containing six Cavity Ringdown mirrors each (five for s-Vis-CRD and one for s-IR-CRD) and an empty slot (for s-SHG measurements). Each mirror can be placed and adjusted in the beam path without breaking the UHV. Behind the cavity, outside the chamber, the CRD signal is coupled out by introducing another movable mirror and focussed onto a photomultiplier (Hamamatsu, H 7732-10). The signal is then recorded by the oscilloscope. The pulse energies generated by the OPO laser source varies strongly with the wavelength (see figure 5-*03*). This, in combination with the wavelength dependency of the reflectivity of the CRD mirrors in the measured range, leads to huge variations in the intensity of the light beam which is detected by the photomultiplier. In order to avoid saturating the measured signal, the amplification of the photomultiplier is controlled by a LabView based program which uses a calibration curve to keep the signal output at a constant level. The amplification control is included in the main processing program which allows for fully automated wavelength scans.

Setup s-IR-CRD

The IR laser source presented in chapter 5.1.2 is used for the s-IR-CRD experiments. The IR light is coupled into the measurement beam path by a gold mirror which is mounted onto a linear micrometer translation stage. Behind the chamber, the IR beam is coupled out by a foldable gold mirror and focussed onto a liquid nitrogen cooled InSb detector (InfraRed associates Inc., IS-10) by a CaF_2 lens. The signal from the detector is monitored by the oscilloscope. Since the InSb detector is a passive detection unit, it is not possible to control its amplification as it is done for the photomultiplier in the s-Vis-CRD experiments. As a consequence, the IR light beam is attenuated before entering the vacuum chamber using a filter wheel. A wavelength scan is then devided into wavelength regions, in which the intensity of the light beam behind the cavity is inside a certain range of acceptance. For each part of the scan, the filter wheel is readjusted. In order to decrease the noise in the spectra, 100 pulses are recorded and averaged for all s-CRD measurements (Vis- and IR-).

By introducing and removing the five movable mirrors, the setup can easily be switched between s-Vis-CRD, s-IR-CRD and s-SHG spectroscopy.

5.2.1 Alignment of the s-SHG Setup

In order to align the Pellin-Broca prisms for the s-SHG spectroscopy, a small BBO crystal is mounted under the sample holder in the UHV chamber (see chapter 4.2). The crystal has a thickness of 1 mm. Using the manipulator, the crystal can be first placed in the focus of the laser beam and then (by tuning the azimuth angle) a position can be found where the phase matching conditions for the SHG process are fulfilled. The ultraviolet laser beam generated is separated from the fundamental beam in the first Pellin-Broca prism and can be made visible by blocking the beam using, for example, a white business card. The brightener in the white paper transforms the UV into blue-violet light via fluorescence processes, and consequently a weak blue spot can be observed on the card. Repeating this procedure for other wavelengths, the motor positions of the first Pellin-Broca prism can be adjusted to match the positions of the SH spots for different wavelengths. In a second step, the SH beam is guided through the entire setup including the second Pellin-Broca prism at a fixed wavelength. The calibration of the motor positions of the second Pellin-Broca prism is subsequently achieved by optimizing the SH signal intensity detected by the photomultiplier. Here, the SH beam generated by a real sample should be used (and not the BBO crystal) to avoid a possible misalignment caused by the horizontal beam displacement induced by the BBO crystal which is much thicker than the substrates which are used for the s-SHG experiments. The weak SH signal from the samples can be highly enhanced by the deposition of gold or silver clusters on the back side of the substrate simplifying the alignment of the setup.

5.3 Calibration of the Photodiode

The fundamental pulse energy of the OPO laser system is measured using a photodiode (see figure 5-*06*). In order to verify its linearity, the pulse energy is simultaneously recorded at a fixed wavelength by the photodiode and a laser powermeter. This measurement is repeated for different attenuations of the laser pulses which is achieved by changing the delay of the Pockels cell inside the pump laser. The resulting data points are shown in figure 5-*07*.

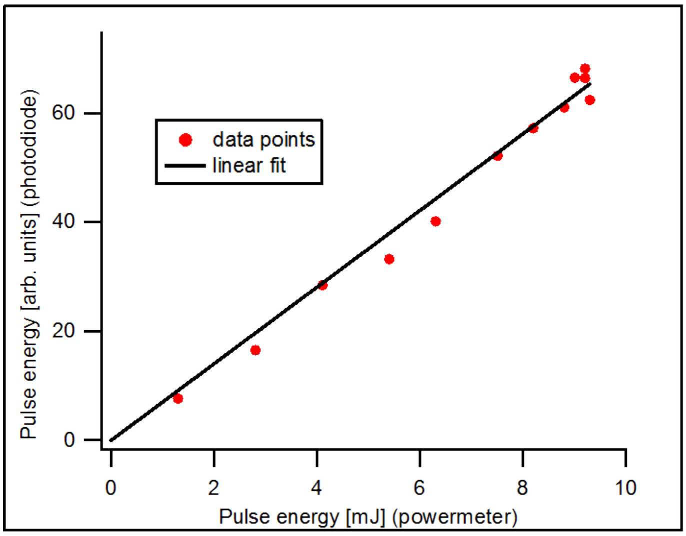

Fig. 5-*07*. Laser intensity measured by the photodiode and a laser powermeter to verify the linearity of the diode. Included in the figure is a linear fit (black line).

A linear dependency between the values measured with the photodiode and the powermeter can be clearly observed, confirming the linearity of the photodiode. By taking the slope of the linear fit, the actual pulse energy can be calculated from the value obtained by the photodiode. The slope is given by the sensitivity of the diode which is wavelength dependent. Consequently, the sensitivity of the photodiode as a function of the wavelength must be determined. This is demonstrated in a next experiment by performing a wavelength scan and recording the pulse energy with the photodiode and a calibrated laser powermeter simultaneously. The resulting sensitivity curve is depicted in figure 5-*08*.

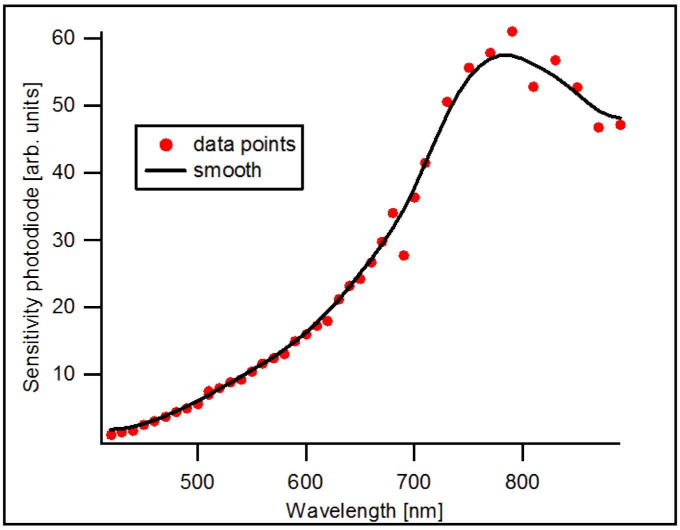

Fig. 5-*08*. Measurement of the sensitivity curve of the photodiode.

The sensitivity curve shows a strong wavelength dependency with maximum at a wavelength of approximately 800 nm. This sensitivity curve is used as calibration curve in order to derive the pulse energies from the response of the photodiode in all s-SHG measurements carried out in this thesis.

5.4 UV-Vis and FT-IR Measurements

In the framework of this thesis, UV-Vis and FT-IR measurements are performed using commercial spectrometer. For these experiments the spectrometer, Analytik Jena; *Specord* (UV-Vis), and Thermo scientific; *Nicolet 380* (FT-IR) are used.

6. Support Material

In this chapter, the required properties of a suitable support material for the spectroscopic investigations are defined and discussed. The choice of the substrate material is crucial for the reliability and sensitivity of the measurements carried out in this thesis and is consequently described in the following in detail. A surface analysis technique is presented which allows for testing the substrates for their adequacy for the experiments and its performance is demonstrated. Based on these considerations and measurements two suitable substrate materials are chosen and their linear and nonlinear spectroscopic properties are determined. The exact characterization of the spectroscopic properties of the used substrates is important in order to distinguish between substrate contributions and the contribution of the adsorbates (e.g. clusters) in the measured spectra of samples (e.g. cluster samples) presented in the following chapters. Furthermore, procedures for the cleaning of the substrates are developed and characterized using the spectroscopic techniques of the presented setup.

6.1 Requirements

The substrate which is used as support material for the cluster deposition must fulfill several very distinct requirements to be suitable for the applied spectroscopic methods (s-Vis-CRDS, s-SHG, s-IR-CRDS). The most demanding technique here is surface Cavity Ringdown spectroscopy. One condition for its high sensitivity is that the overall photon-loss must be as low as possible. However, a substrate introduced in an optical cavity disturbs the flux of photons either by absorption or by deflection out of its direction. The latter can be caused by scattering and reflection at the surface or linear displacement of the beam while travelling through the substrate. All these effects increase the overall photon-loss and reduce the sensitivity. To minimize these effects, the choice of a suitable substrate is crucial.

The most important requirement is that the substrate must be highly transparent over the entire used wavelength range (400 nm - 3600 nm) to avoid absorption losses. This is typically the case for metal oxides or glasses. Especially in the visible wavelength range only insulators are highly transparent which leads to the necessity of neutralization of the clusters during their deposition. Reflections of the beam at the surfaces can be avoided by placing the substrate at Brewster's angle inside the resonator if only p-polarized light is used. As a consequence, no birefringent material can be used because in this case for each pass of the light pulse through the substrate an s-polarized component is generated, which does not fulfill the Brewster's angle condition and is reflected. This reduces the choice of substrates to materials with either a cubic or an amorphous crystal structure. An additional consideration is that mechanical stress can also lead to birefringence, and consequently care must be taken when mounting the substrate on the sample holder e.g. the screws of the springs which hold the substrate should be tightened as softly as possible (see chapter 4.2).

The scattering of light occurs at any material; however, the amount is highly dependent on the size of the scattering centers. Consequently, most of the light is scattered via dust particles and rough structures present on surfaces, whereas in the bulk of a material the scattering takes place on the atomic scale and is thus orders of magnitude smaller. A substrate where both surfaces (back and front) are atomically flat, and which is fabricated under dust free conditions is therefore needed. Alternatively, the substrate can be carefully cleaned to remove the dust. Another important parameter is the thickness of the substrate. A light beam undergoes a linear displacement when it travels through a material with a different refractive index with respect to the surrounding medium; in case the surface normal is not parallel to the optical axis (e.g. at Brewster's angle). This displacement is proportional to the thickness of the substrate and can therefore be minimized by using very thin plates. Additionally, it must be ensured that the two surfaces are perfectly parallel; otherwise the angle of the outgoing beam does not match that of the incoming. In this case, a linear configuration of the cavity would not be possible.

For the s-SHG spectroscopy a suitable substrate should be in the first instance centro-symmetric in its crystal structure because this is the condition for the surface sensitivity of the method. Amorphous structures as in glasses also fulfill this condition because potential differences for different directions are averaged out by the random orientation (which leads to an overall symmetric potential). Furthermore, the sample must be transparent at least for the wavelength of the fundamental beam. Both conditions for the s-SHG spectroscopy are automatically fulfilled by substrates which are suitable for s-CRD spectroscopy.

In this work, almost all measurements were carried out using one of two types of substrates which were found to be the most suitable: (i) Borosilicate glass slides (BK7) which are produced as cover glass for microscopy applications were used for most of the s-Vis-CRDS and s-SHG measurements, and (ii) Yttrium doped Zirconia (ZrO_2:Y) substrates for s-IR-CRDS. The thickness is 130 μm for BK7 and 150 μm for the ZrO_2:Y slides, respectively. The BK7 glass slides possessed among all tested substrates (MgO, NaCl, quartz glass, ZrO_2:Y) the best optical properties for s-Vis-CRD and s-SHG measurements. It was found that the fabrication of a very thin, atomically flat substrate whose two surfaces are perfectly parallel is a huge challenge for the manufacturing companies, especially for single crystals like MgO, NaCl and ZrO_2:Y. As a consequence, those substrates (despite their high cost) possessed rather poor optical quality, in particular, the deformation of the surface led to difficulties in aligning the cavity. A drawback of the BK7 slides, however, is that they are non-transparent in the IR range. Here ZrO_2:Y showed the best performance. The doping with Yttrium is necessary because it transforms the structure of ZrO_2 into a cubic crystal structure. A substrate, which can be used for all three spectroscopic methods is one of the major future challenges to be faced.

6.2 Surface Topography Analysis

Due to the problems associated with the surface deformation of certain substrates (as was discussed in the preceding section), a powerful method is developed in order to characterize the substrate surface. The principle idea is to map the sample using a HeNe laser and to extract the substrates topography from the angle of reflection of the surface. A schematic of the setup is shown in figure 6-*01*.

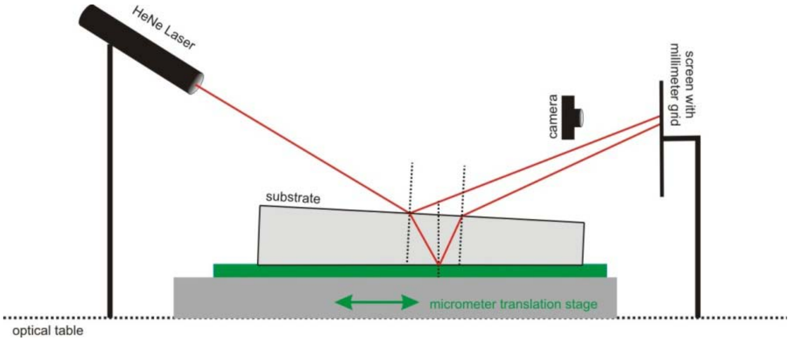

Fig. 6-*01*. Surface topography analysis setup. The topography is mapped by recording the positions of the reflected laser beams on the screen as a function of the substrate position.

The advantage of using a HeNe laser is its low divergence and small beam diameter (0.8 mm) which ensures high accuracy of the measurement. The laser is positioned in a way that the beam hits the surface of the sample in a rather low angle. In this setup, an angle of 15 degrees between the laser and the optical table is chosen. On a screen with a millimeter grid which is placed about two meters away from the sample two spots appear, one from the beam reflected at the upper surface and one from the lower. For substrates with perfectly parallel surfaces and a thickness of 130 µm (BK7) the distance between the spots is calculated to be around 60 µm. In this case it is hardly possible to distinguish between the two spots. However, already small angular mismatches between the two surfaces lead to a separation of the two spots. Figure 6-*02* shows an example of this effect. Moving the substrate on a micrometer translation stage, changes of the local surface angle for both surfaces can be calculated from the different spot positions in a single measurement. The angular resolution which can be easily achieved with this apparatus is approximately 1.5 arc seconds ($\approx 4.3\cdot10^{-4}$ degrees). In front of the screen, a camera is mounted to record the spot positions.

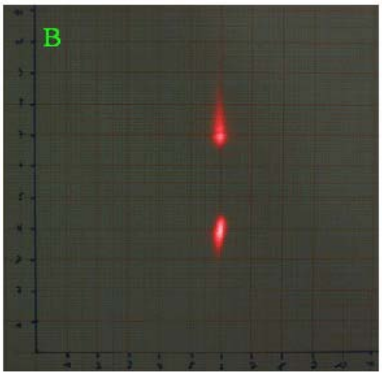

Fig. 6-*02*. Photo of the millimeter grid with the two reflection spots.

6.2.1 Calculation of the Topography

In figure 6-*03*, a detailed sketch of the different reflections is given.

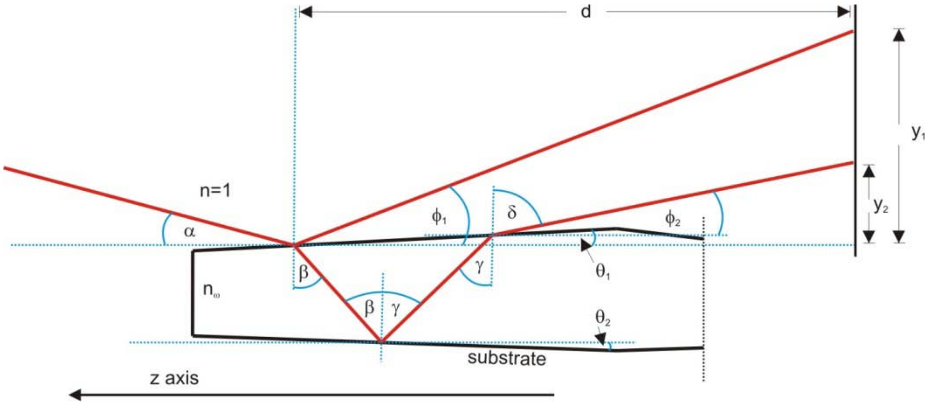

Fig. 6-*03*. Sketch of the two reflections. The positions of the reflected beams on the screen (y_1, y_2) are influenced by the local surface angle.

The angle between the upper surface and the optical table (θ_1) can be calculated as follows:

$$\theta_1 = \frac{1}{2}(\phi_1 - \alpha) \text{ with } \phi_1 = \arctan\left[\frac{y_1}{d}\right] \quad \textit{(eq.6-01)}$$

where, y_1, is the position of the laser spot on the screen, and d, is the distance between the screen and the point of reflection. The angle of incidence, α, is determined by taking the mean value of all measured ϕ_1 angles at different positions on the sample. By moving the substrate along the z-axis, θ_1 can be calculated as a function of z. The angle, θ_2, is determined using Snell's law of refraction. For all indicated angles in figure 6-*03*, the z-axis (not the surface) is used as reference axis which transforms Snell's law to:

$$\frac{\cos(\alpha+\theta_1)}{\sin(\beta-\theta_1)} = n_\omega \text{ and } \frac{\cos(\phi_2-\theta_1)}{\sin(\gamma+\theta_1)} = n_\omega \quad \textit{(eq.6-02)}$$

whereby, n_ω, is the refractive index of the substrate. The relation between β and γ is given by:

$$\gamma = \beta - 2\theta_2 \quad \textit{(eq.6-03)}$$

Combining these equations gives:

$$\cos(\phi_2-\theta_1) = n_\omega \cdot \sin\left[2(\theta_1-\theta_2) + \arcsin\left(\frac{\cos(\alpha+\theta_1)}{n_\omega}\right)\right] \quad \textit{(eq.6-04)}$$

Applying the addition theorems of trigonometry and the small angle approximations $\sin(x) \approx x$; $\cos(x) \approx 1$ for $x \ll 1$ the angle θ_2 can be calculated to give:

$$\theta_2 = \theta_1 - \frac{\cos(\phi_2-\theta_1) - \cos(\alpha+\theta_1)}{2\sqrt{n_\omega{}^2 - \cos^2(\alpha+\theta_1)}} \quad \textit{(eq.6-05)}$$

where, ϕ_2, can be approximated by $\phi_2 = \arctan\left[\frac{y_2}{d}\right]$ because d is much larger than the distance between the two reflected laser beams at the surface. After a z-scan (in 0.5 mm steps), the derived angles for θ_1 and θ_2 are transformed into a function of z using a polynomial fit. To obtain the height profile of the substrate, these functions are simply integrated over z (the integral of the slope gives the height. The slope is $\tan(\theta) \approx \theta$ for $\theta \ll 1$). All these calculations are included in an automated procedure developed in the program *IgorPro*, which allows for fast data treatment. Using this method, the height profile along the z-axis of any transparent substrate can be determined within minutes.

The reproducibility of the method was tested via two experiments with the same sample where the substrate was turned upside down between the measurements. As result, the calculated profile of the lower surface of the second experiment matches that of the upper from the first measurement and vice versa. The deviations in height are found to be smaller than 1 µm.

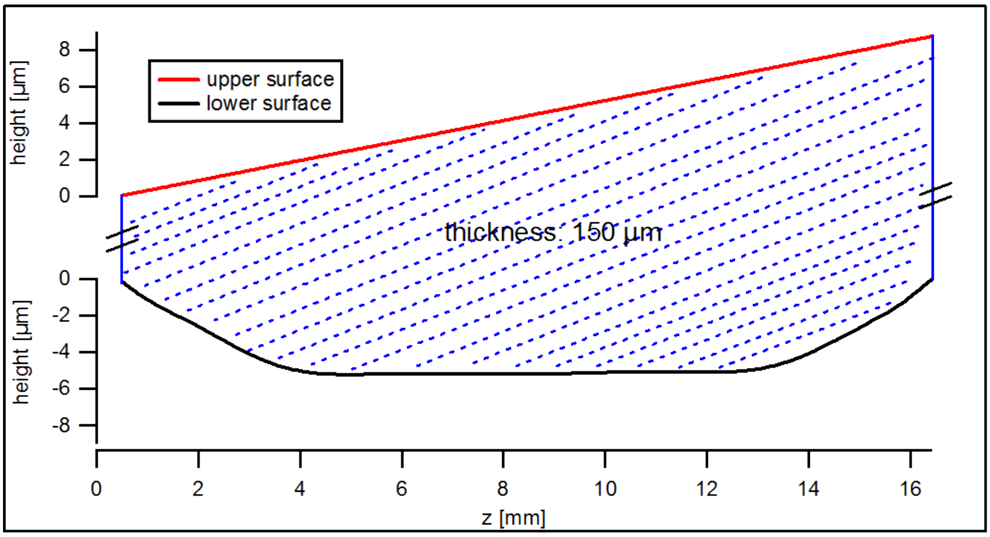

Fig. 6-*04*. Measured topography of both surfaces of the quartz glass substrate. The upper surface is flat, whereas the lower surface shows a deformation. The two surfaces are clearly not parallel.

Figure 6-*04* shows an example of the surface analysis of a quartz glass substrate where both sides are polished. The upper surface is extremely flat whereas the lower surface shows a deformation of about 5 µm. Also an angular mismatch between the two sides of roughly 0.029 degree is present, and consequently the substrate is not suitable for s-CRD spectroscopy. The deformation of the lower surface seems to come from the fabrication process. In order to polish the first surface, the substrate is glued to a holder on its reverse surface. After that, the glue is dissolved and the sample is turned around to polish the other side. The upper surface in figure 6-*04* was probably polished at the end and by demounting the sample the surface, which was fixed to the holder, became deformed. Most of the tested substrates possessed comparably poor quality and where consequently not used in the experiments. However, both the relatively low priced BK7 microscopy glass slides (which

possessed deformations below the detection limit of the surface topography analysis method) and ZrO_2:Y possessed acceptable surface quality.

6.3 Cleaning of the Substrates

To remove dust and other impurities from the surface, the substrates must first be carefully cleaned. It was therefore important to evaluate substrate cleaning procedures and choose the most appropriate, reliable method. Such cleaning is especially crucial for s-CRD spectroscopy because it is highly sensitive to all kinds of impurities, in particular dust which increases the loss through the sample.

The best results were achieved using special lens cleaning tissues (*Thorr Labs*). In this method, the tissues are folded and moistened with four drops (two on each side) of spectroscopy grade acetone. The substrate is subsequently wiped until the tissue has almost dried; however, the cleaning technique in terms of compression and the wiping speed are important factors. A high compression leads to scratches on the surface and must be avoided. When the tissue becomes too dry, fibers from the tissue may be deposited on the surfaces again whereas a tissue with too much acetone leaves traces of impurities on the substrate. For a really clean sample 5 to 10 circles of wiping are necessary, each time with a new tissue. After each circle, the result can be uncovered by using a strong torch light where even the smallest dust particles appear as bright spots. Using a black background, the contrast is highly increased.

The substrates of all experiments were cleaned using this same procedure. Further cleaning steps are performed in vacuum (such as the sputtering of the substrate) and are discussed later in this chapter.

6.4 Linear Spectroscopic Properties of the BK7 Glass Substrate

At first, different spectroscopic properties of the BK7 glass substrate are investigated. Following the above mentioned requirements of a substrate for s-CRD spectroscopy, the surface should be as flat as possible. Amorphous structures such as glasses are known to have rather rough surfaces and consequently, as first step, the flatness of the surface of a BK7 glass slide is determined using the Atomic Force Microscopy (AFM) technique. These measurements were carried out in Marseille in the group of Prof. C. Henry at the CINaM-CNRS in the framework of the "Deutsch Französische Hochschule". The samples are characterized using a standard AFM apparatus under ambient conditions. Figure 6-*05* shows an AFM image of a clean BK7 glass surface which is found to be surprisingly smooth. The height difference between the highest and the lowest areas of the surface is below $1.8\ \mathrm{nm}$. This is the reason for the small scattering losses observed for this substrate.

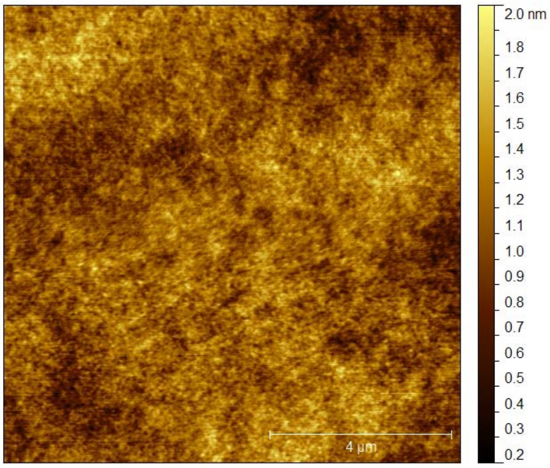

Fig. 6-*05*. AFM image of the surface of a BK7 glass substrate. The maximal height difference on the surface is below 1.8 nm.

6.4.1 s-Vis-CRD Measurements

For the s-CRD measurements a BK7 glass substrate is cleaned and mounted to the sample holder. Using the transfer chamber, the sample is brought into the main vacuum chamber with a base pressure of $2 \cdot 10^{-10}\,\mathrm{mbar}$. Using the x,y,z manipulator, the sample can then be positioned at the Brewster's angle in the middle of the cavity. In order to determine the extinction spectrum of the substrate, the point in the middle of the sample and the empty cavity are measured for each set of mirrors. The difference between both gives in approximation the extinction spectrum of the substrate. For BK7 the accuracy of this method is rather good because of its good optical quality and the fact that it is very thin. However, in principle this method only works if the properties of the resonator are almost unchanged when introducing a substrate. The total Loss of the resonator, $\Lambda_{(\omega)}$, can be expressed as follows:

$$\Lambda_{(\omega)} = \Lambda_{(\omega)}^{(\mathrm{cavity})} + \Lambda_{(\omega)}^{(\mathrm{substrate})} \qquad (eq.6\text{-}06)$$

and the difference between the measurement with the sample and the empty cavity is consequently:

$$\Delta\Lambda_{(\omega)} = \Lambda_{(\omega)}^{(\text{substrate})} + \Delta\Lambda_{(\omega)}^{(\text{cavity})} \qquad (eq.6\text{-}07)$$

where, $\Delta\Lambda_{(\omega)}^{(\text{cavity})}$, is the change in the optical properties of the resonator caused by a change in the optical path of the light beam introduced by the sample. Depending on the quality of the substrate it can reach up to several 100 ppm and is wavelength dependent. That means that the difference between the two measurements will not be necessarily equal to the extinction spectrum of the substrate. However, for the BK7 substrate $\Delta\Lambda_{(\omega)}^{(\text{cavity})}$ should be small enough so that the linear optical properties of the sample can be characterized.

In figure 6-*06*, an s-CRD measurement of a BK7 glass substrate (P1) and the associated empty cavities are shown. One measurement consists of five different cavities (plotted in different colors). The cavity centered at 480 nm had to be split into two regions due to a big change in intensity of the laser source in this wavelength region. Taking the difference between P1 and the empty cavity for each wavelength region gives the curve shown in figure 6-*07*.

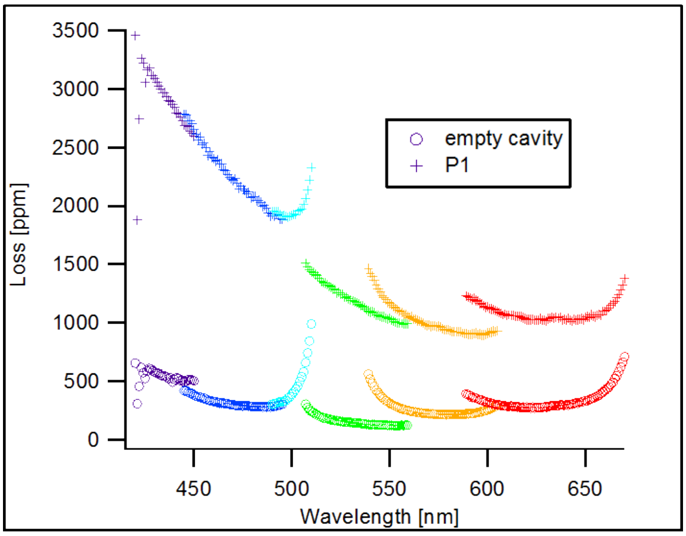

Fig. 6-*06*. s-CRD measurement of the empty cavity and the BK7 glass substrate. The different colors represent the different measured wavelength ranges covered by the different sets of CRD mirrors.

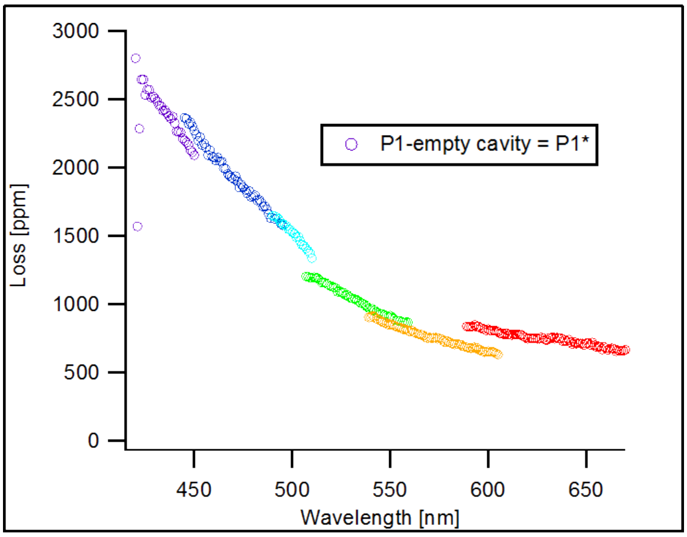

Fig. 6-*07*. Difference s-CRD spectrum of the BK7 glass substrate. Small offsets in the overlapping regions of the different sections (plotted in different colors) are present.

The difference s-CRD spectrum shows small offsets in the overlapping regions of the different sections of the spectrum (plotted in different colors). This discontinuity in the spectrum can be attributed to a change in $\Delta\Lambda_{(\omega)}^{\text{(cavity)}}$ for the different cavities because it is sensitive to the alignment of the cavity. It is not obvious how these offsets must be corrected because there are many factors which contribute to $\Delta\Lambda_{(\omega)}^{\text{(cavity)}}$ (e.g. the homogeneity of the reflecting layers of the CRD mirrors and the beam size inside the cavity which depends on the alignment etc.). It has, however, been shown previously[51] that a correction by simply shifting each section of the spectrum (corresponding to each cavity) so that they overlap each other does not distort the spectrum within an acceptable limit. Consequently, this method of obtaining a continuous spectrum is used for all s-CRD experiments carried out in this thesis.

Figure 6-*08* shows the corrected extinction spectrum of the BK7 glass substrate. The spectrum is dominated by scattering losses which can be seen by the strong increase in the loss towards shorter wavelengths, rather than the absorption of the sample itself which is nearly zero (the absorption edge of BK7 is around 300 nm). The same effect plays an important role for the reflectivity of the CRD mirrors because scattering also occurs at their surfaces. This can be seen in figure 6-*06*, whereby the loss also increases for the empty cavity towards shorter wavelengths. This is not ideal for s-CRD spectroscopy because high losses decrease the sensitivity of the technique, and consequently the method is limited to a wavelength range where the scattering is small. Here, the lower wavelength limit was chosen to be around

420 nm. To measure the optical responses in the ultraviolet range, another spectroscopic method should instead be applied. An exact mathematical description of the scattering curve of the substrate is not possible because the wavelength dependency of the scattering highly depends on the size of the scattering centers (Mie scattering). On the surface of the sample, there is a large distribution of sizes for the scattering centers which leads to a superposition of many different scattering curves with different contributions, making a precise analysis very difficult.

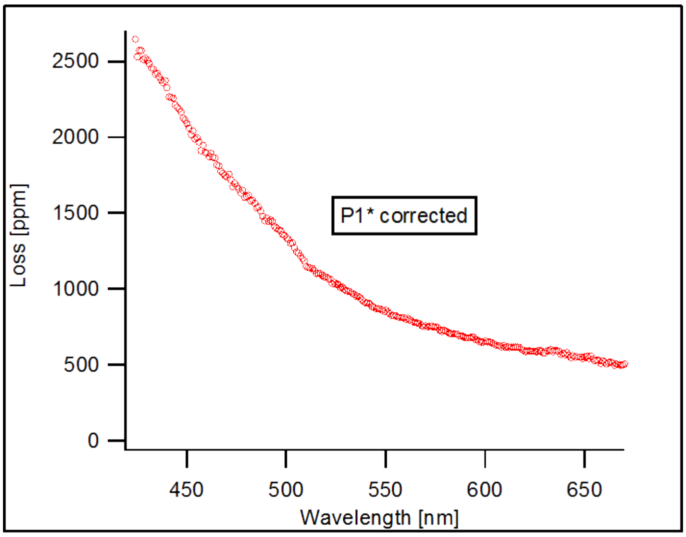

Fig. 6-*08*. Corrected difference s-CRD spectrum of the BK7glass spectrum. The increase in loss towards shorter wavelengths originates from light scattering at the surfaces.

6.4.2 Effect of Sputtering on the s-CRD Spectrum

Despite the first cleaning step (described in section 6.3) and subsequent transfer of the substrate into vacuum, there are still substances present on the surface, such as water molecules or acetone etc. To guarantee an atomically clean surface for the deposition of clusters it is necessary to perform a second cleaning step in vacuum. Using a sputter gun, Argon ions are created and accelerated to bombard the substrate surface. These high energy ions are able to displace surface atoms and remove impurities. However, care should be taken because sputtering also leads to a roughening of the surface which increases the scattering of light. As a consequence, low energy sputtering conditions should be used. Systematic studies of the impact of sputtering on the s-CRD spectra of BK7 glass using different parameters were carried out and the most convenient results were achieved using Ar^+ ions with a kinetic energy of between 300 and 1000 eV for a sputtering time of 5 to 10 minutes. Figure 6-*09* shows an s-CRD loss surface map of a BK7 glass substrate before and after sputtering for 5 minutes at a kinetic energy of 1 keV. The loss at a fixed wavelength (550 nm) is recorded as a function of the substrate position. It can be observed that the loss increases homogeneously by approximately 250 ppm, whereas the structures on the surface remain unchanged.

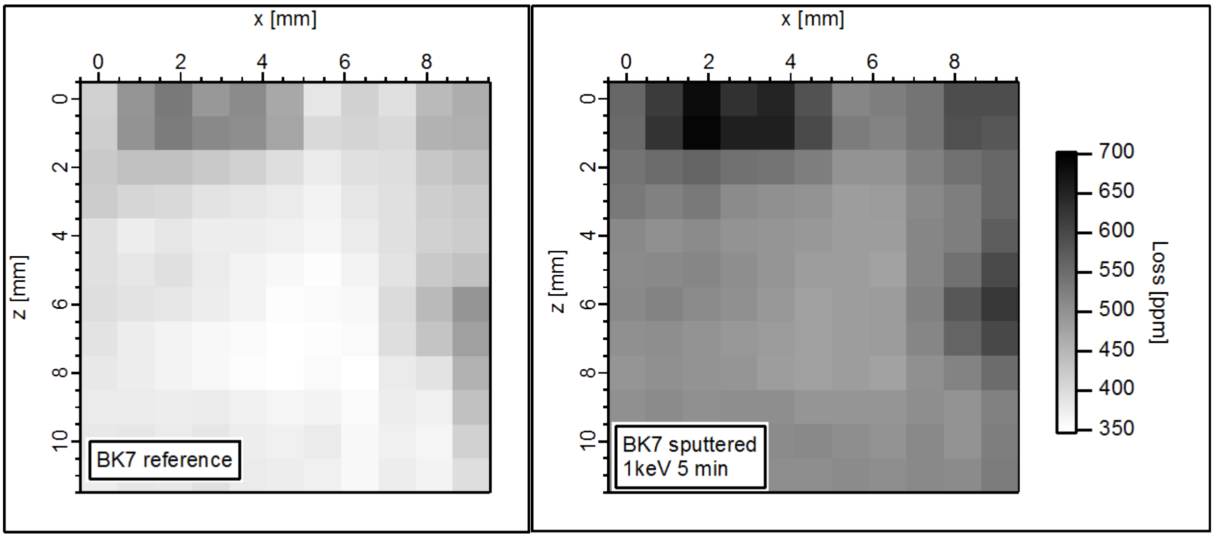

Fig. 6-*09*. s-CRD loss surface map of the unsputtered (left) and the sputtered (right) sample. After sputtering the overall loss is increased, whereas the structures on the surface remain unchanged.

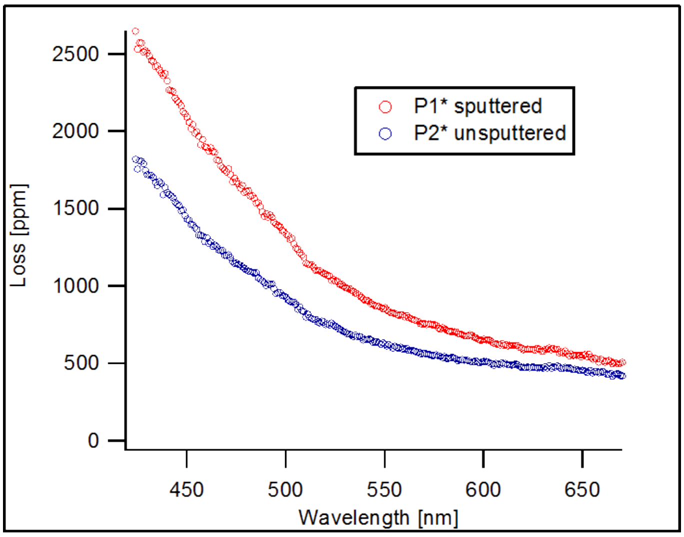

Fig. 6-*10*. Corrected s-CRD difference spectra of an unsputtered (blue circles) and a sputtered (red circles) spot on the sample. The s-CRD spectrum of the sputtered spot shows an increased scattering (loss).

In figure 6-*10*, s-CRD spectra of an unsputtered and a sputtered location (300 eV, 10 min.) of a BK7 substrate are shown. The loss of the sputtered location is increased, the degree of which is dependent on wavelength. The increased scattering of the sputtered location and the wavelength dependence can be explained by considering that roughening the surface increases the number of scattering centers. The scattering cross section of one scattering center which is small compared to the wavelength can be expressed in the following way (this assumption is justified since the roughening takes place on the atomic scale):

$$\sigma_{(sca.)} = \frac{2\pi^5}{3}\frac{d^6}{\lambda^4}\left(\frac{n^2-1}{n^2+2}\right)^2 \qquad \textit{(eq.6-08)}$$

whereby, *d*, is the diameter of the scattering center, *n*, the refractive index, and λ, the wavelength. The cross section shows a $1/\lambda^4$ dependency. The overall scattering loss of a surface is the summation over the cross sections of all scattering centers in the considered area and thus proportional to $\sigma_{(sca)}$. Consequently, the difference between the spectra of the two points (figure 6-*10*) must show the same wavelength dependency, if the additional scattering originates exclusively from a roughening of the surface on the atomic scale (which is the case for sputtering). In figure 6-*11*, the difference between the two spectra of figure 6-*10* is plotted including a fit using the function $\Lambda_{(\lambda)} = A/\lambda^4$ where, A, is the fit parameter. The fit matches well the data points confirming that the increased loss does originate from surface roughening.

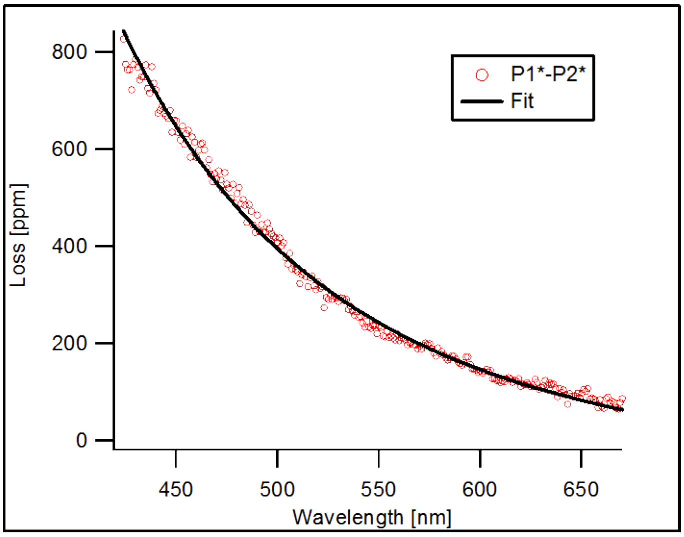

Fig. 6-*11*. Effect of sputtering on the s-CRD spectrum. The difference between the s-CRD spectra of a sputtered and an unsputtered location of the substrate shows a $1/\lambda^4$ dependency (see fit) confirming that the increased loss originates from surface roughening.

The accuracy of the difference spectrum of two different locations on the same substrate is much higher than that of the difference spectrum of one point and the empty cavity. The reason for this is that for a homogeneous substrate, $\Delta\Lambda_{(\omega)}^{(\text{cavity})}$ is zero comparing two locations on the same sample because the change in the light path inside the cavity which is induced by the substrate remains the same when moving the substrate from one location to the other.

By measuring the time evolution of the loss after sputtering the sample, an exponentially decaying decrease of the loss with time can be observed. This effect can be attributed to a healing process of the surface. During sputtering many surface defects such as vacancies are created which can be removed by diffusion processes. Because defects are scattering centers, a decreasing number of defects leads to a decreasing cavity loss. This shows that s-CRD spectroscopy can be used to study diffusion processes and defect formations on surfaces, which could prove to be a promising application of this technique. A consequence of this observation is, that after sputtering one must wait until the loss of the substrate is stabilized before reliable s-CRD measurements can be performed. This is usually the case after approximately one hour (depending on the sputtering conditions).

6.5 Surface Second Harmonic Generation Spectroscopy of BK7 Glass

Using a BK7 glass substrate, s-SHG spectroscopy can be considered to be a surface sensitive technique. This means that all SH photons, which are measured are generated at the surface region of the substrate where the electric potential is asymmetric due to the presence of the interface (see chapter 2.2.3). However, not all oscillations of charges at the surface are SHG active, instead only the oscillations that are perpendicular to the surface take place in an asymmetric electric potential and consequently give rise to an SH signal. This leads to an angular and polarization dependency of the SH intensity. Additionally, oscillations in the s-SHG spectrum may be observed for wavelengths where the substrate is transparent to their second harmonic frequencies because of the constructive/destructive interferences between the generated SH beams of the two substrate surfaces (front and back). Consequently, an understanding of the nonlinear optical properties of the substrate is crucial before an understanding of the spectra of supported metal clusters can be gained. Therefore, different s-SHG experiments with the BK7 glass substrate are carried out and their results are interpreted in the following sections.

6.5.1 Angular Dependency of the SH Signal for BK7

In order to calculate the angular dependency of the intensity of the generated SH beam, several effects that occur using thin substrates must be considered. First of all, the polarization of the fundamental beam with respect to the sample plays an important role. As mentioned above, only oscillations which are perpendicular to the surface contribute to the SH light, which explains why only p-polarized laser light gives rise to a measurable SH signal (s-polarized light does not have a component perpendicular to the surface). Another important point is that multiple reflections of the fundamental laser beam take place inside the sample, which leads to a modulation of its intensity while changing the angle of incidence. This effect has a drastic influence on the SH intensity, which can be seen in the following.

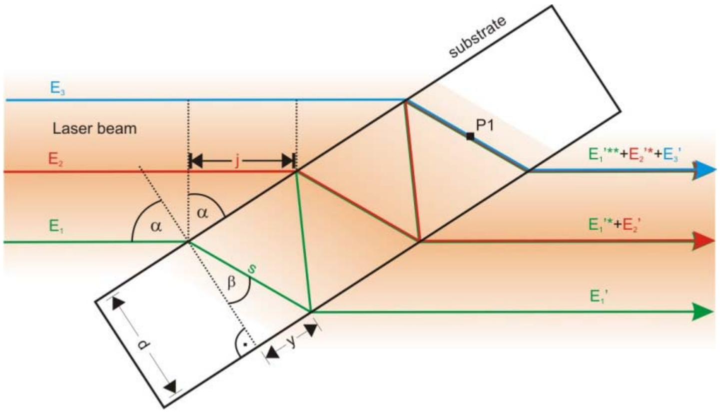

Fig. 6-*12*. Sketch of the multiple reflections of the fundamental beam inside a thin substrate. The interferences lead to modulations in the fundamental intensity as function of the angle of incidence.

Figure 6-*12* shows a sketch of a light beam traveling through a thin substrate where multiple internal reflections occur. In order to calculate the intensity at point P1 in the sketch, the transmitted and the reflected waves must be superimposed to give a resulting wave from which the intensity can be derived. The intensity at P1 ($I_{(P1)}$) can be written as:

$$I_{(P1)} = \phi_{(P1)} \cdot \phi^{*}_{(P1)} \text{ where } \phi_{(P1)} = \sum_{n=0}^{\infty} \phi_n \quad (eq.6\text{-}09)$$

where, ϕ_n, are the wave functions of the light beams, E_n, and ϕ^*, is the conjugate-complex function of ϕ. From figure 6-*12* the following equations can be formulated:

$$s = \frac{d \cdot n_{(\omega)}}{\sqrt{n^2_{(\omega)} - \sin^2 \alpha}} \; ; \; j = \frac{2d \cdot \sin^2 \alpha}{\sqrt{n^2_{(\omega)} - \sin^2 \alpha}} \quad (eq.6\text{-}10)$$

where, $n_{(\omega)}$, is the refractive index of the sample. To superimpose the different light beams, the phase shifts between them must be considered. We take, as an example, the waves E_3 and E_2 from figure 6-*12*. Up to the point P1, both waves have traveled a certain path together, and additionally each of them has traveled some way alone (for E_2 it is twice the distance s and for E_3 it is j). The traveling times for the latter (Δ for E_2 and δ for E_3) are given by:

$$\Delta = \frac{2d \cdot n^2_{(\omega)}}{c \cdot \sqrt{n^2_{(\omega)} - \sin^2 \alpha}} \; ; \; \delta = \frac{2d \cdot \sin^2 \alpha}{c \cdot \sqrt{n^2_{(\omega)} - \sin^2 \alpha}} \quad (eq.6\text{-}11)$$

where, *c*, is the speed of light in vacuum. Further considerations are also the different amplitudes of E_3 and E_2 at point P1. E_3 is directly transmitted, whereas E_2 is both transmitted and reflected twice (see Fresnel formulas). By taking the general time dependent wave function of light, $\phi = Ae^{i\omega t}$, the resulting wave $\phi_{(P1)}$ for multiple reflections can be written as:

$$\phi_{(P1)} = t_p \cdot A \cdot \sum_{n=0}^{m} r_p^{\,2n} e^{i\omega[t+(m-n)\delta+n\Delta]} \quad (eq.6\text{-}12)$$

where, t_p and r_p, are the Fresnel factors for p-polarized light for transmission and reflection, respectively. The intensity is then given by:

$$I_{(P1)} = (1 - R_p^{\,*}) \cdot A^2 \cdot \left[\sum_{n=0}^{m} R_p^{\,n} e^{i\omega[t+(m-n)\delta+n\Delta]} \right] \cdot \left[\sum_{n=0}^{m} R_p^{\,n} e^{-i\omega[t+(m-n)\delta+n\Delta]} \right] \quad (eq.6\text{-}13)$$

using the relations $r_p^{\,2} = R_p$ and $t_p^{\,2} = 1 - R_p^{\,*}$, where, R_p, is the reflectance inside the substrate, and $R_p^{\,*}$, the reflectance at the surface from the beam entering the sample. These reflectances can be derived from the Fresnel formulas, and can be written as:

$$R_p^{\,*} = \left[\frac{n^2_{(\omega)} \cos\alpha - \sqrt{n^2_{(\omega)} - \sin^2 \alpha}}{n^2_{(\omega)} \cos\alpha + \sqrt{n^2_{(\omega)} - \sin^2 \alpha}} \right]^2 \; ; \; R_p = \left[\frac{-n^2_{(\omega)} \cos\alpha + \sqrt{n^2_{(\omega)} - \sin^2 \alpha}}{n^2_{(\omega)} \cos\alpha + \sqrt{n^2_{(\omega)} - \sin^2 \alpha}} \right]^2 \quad (eq.6\text{-}14)$$

With these formulas the intensity of the fundamental beam at point P1 can be calculated. The effect of multiple reflections is also treated by the Airy formula describing the multiple reflections in a Fabry-Pérot interferometer. This formula is much more compact, but its main disadvantage is that it uses the approximation $j \to 0$ and is consequently only valid for small angles α. However, here the exact solution is needed as the effect of multiple reflections of the fundamental beam arises in the s-SHG measurements only for angles of α which are close to 90°. On the other hand, an exact calculation here is not possible either because the sum over the interfering beams consists of an infinite number of additions. Using the fact that the contribution of every addition decreases with increasing n ($R < 1 \Rightarrow \lim_{n\to\infty} R^n = 0$), the sum can be approximated by taking $m = 10$.

The so calculated fundamental beam now generates the second harmonic at the surfaces of the substrate. At first, we reduce the problem to the SHG originating from the second surface and neglect the contribution of the first one. This describes the case for such wavelengths where the substrate is not transparent in the region of their second harmonic frequency. Using the electric dipole approximation, the polarization at the second harmonic frequency at the surface, $P_{(2\omega)}$, can be written as (see chapter 2.2.1):

$$\vec{P}_{(2\omega)} \sim \vec{\chi}^{(2)} \cdot \vec{E}^{2}_{(\omega)} \quad \textit{(eq.6-15)}$$

where, $\vec{\chi}^{(2)}$, is the second order susceptibility tensor, and $\vec{E}_{(\omega)}$, the electric field. As mentioned above, only the component of the polarization which is perpendicular to the surface, $P^{(p)}{}_{(2\omega)}$, is SHG active. From this condition, the nature of the susceptibility tensor can be derived and equation 6-15 can be rewritten as:

$$P^{(p)}{}_{(2\omega)} \sim E^{2}{}_{(\omega)} \sin\alpha \quad \textit{(eq.6-16)}$$

In figure 6-*13*, a sketch of the described process is shown. Here, the generation of the second harmonic takes place at the point P2. The oscillation at the second harmonic frequency at point P2 generates a new electromagnetic wave, from which one part is reflected at the surface back into the substrate and another part radiates into the vacuum. The transmission efficiency is given by the Fresnel coefficient $t_{(p,2\omega)}$. The angle at which the SH beam leaves the sample is the same as that of the fundamental beam although their frequencies are different. The reason for this is that the refractive index of the vacuum is not wavelength dependent. As a consequence, the amplitude of the transmitted SH beam is reduced by the factor $\sin\alpha$ compared to the amplitude of the oscillation. Here, a simple projection of the oscillation vector to the electric field vector of the SH beam is used. The combination of the

Fresnel coefficient and the projection factor is, however, only an approximation. An exact solution would instead have to be derived by solving the nonlinear Maxwell equations at the substrate vacuum interface. However, the approximation is good enough to give a qualitative picture of the angular dependency of the SH signal for BK7.

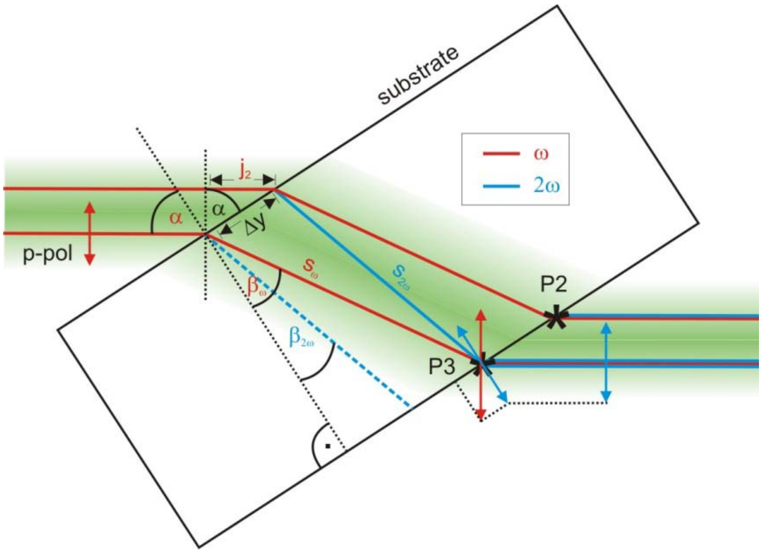

Fig. 6-*13*. Sketch of the generation of the second harmonic at the surfaces of a thin substrate. In point P3 only the generation at the backside of the substrate is considered. Point P2 represents the case where an interference between the SH beams generated at both surfaces occurs.

Considering all mentioned effects, the electric field component of the generated SH beam can be approximated as:

$$E_{(2\omega)} \sim t_{(p,2\omega)} \cdot E^2_{(\omega)} \cdot \sin^2 \alpha \qquad (eq.6\text{-}17)$$

Following this equation the intensity is then given by:

$$I_{(2\omega)} \sim (1 - R_{(2\omega)}) \cdot I^2_{(\omega)} \cdot \sin^4 \alpha \qquad (eq.6\text{-}18)$$

Here again, the relation between the Fresnel coefficient and the reflectivity, $t_p{}^2 = 1 - R_p$, is used. As already seen before, the reflectivity can be derived from the Fresnel formulas:

$$R_{(2\omega)} = \left[\frac{-n^2_{(2\omega)} \cos\alpha + \sqrt{n^2_{(2\omega)} - \sin^2\alpha}}{n^2_{(2\omega)} \cos\alpha + \sqrt{n^2_{(2\omega)} - \sin^2\alpha}} \right]^2 \qquad (eq.6\text{-}19)$$

where, $n_{(2\omega)}$, is the refractive index of BK7 at the second harmonic frequency. Considering that $I_{(\omega)}$ is just the above calculated intensity of the fundamental beam inside the substrate, $I_{(P1)}$, the intensity of the generated SH beam can be calculated as a function of the incident angle.

In figure 6-*14*, an angular dependent s-SHG measurement of a BK7 glass substrate is shown (red line). At a fundamental wavelength of 520 nm the SH intensity is recorded as function of α. Additionally, the result of the calculated curve derived from the above relations is plotted for comparison (blue line). Qualitatively, the calculation is in good agreement with the measurement data. This shows that the main factors influencing the shape of the s-SHG measurement are well understood. In the inset on the upper left side of the plot, the right part of the measurement is enlarged.

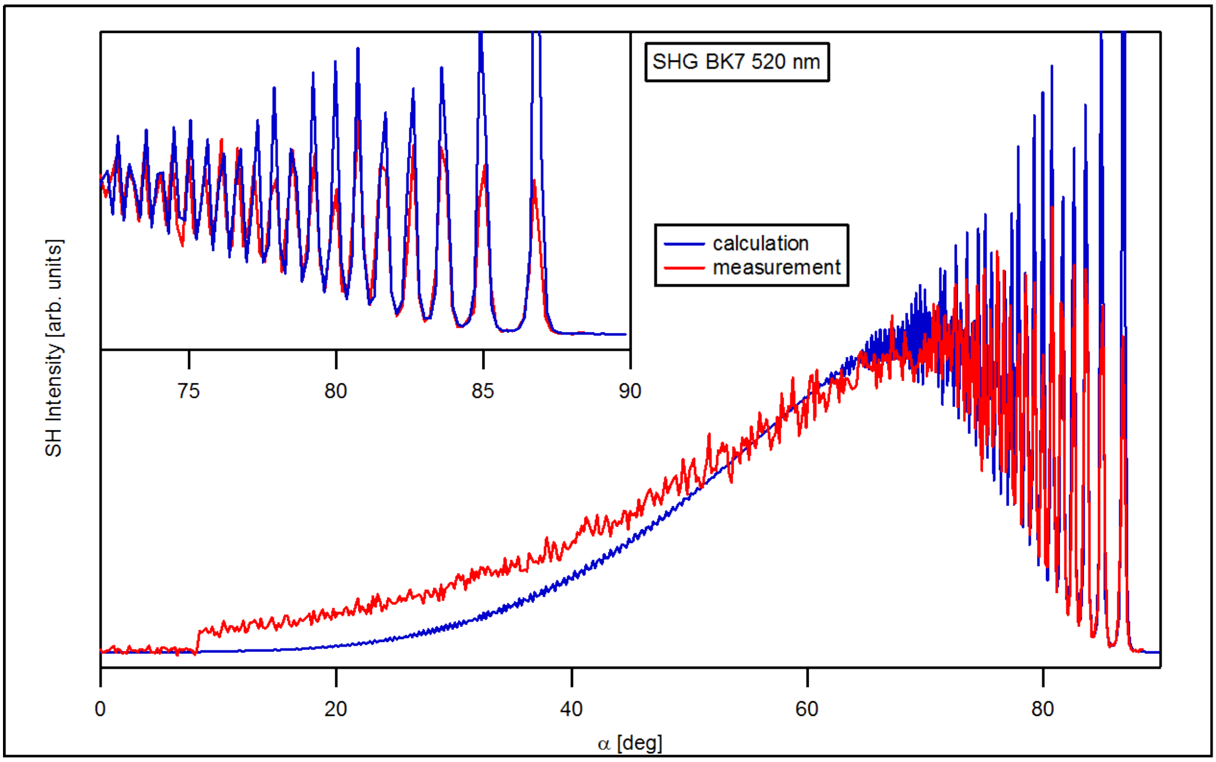

Fig. 6-*14*. Measurement of the angular dependence of SH signal for the BK7 substrate (red line). Included, calculated curve from the above relations (blue line). Parameter used in the calculation: d = 135 µm, n_ω= 1.52, $n_{2\omega}$ = 1.565, λ = 520 nm. The intense sharp peaks on the right side of the plot originate from multiple reflections of the fundamental beam inside the substrate. The plotted blue curve consists of the same number of data points as the measured curve. Consequently, sampling problems can be observed in both spectra in the region of large angles.

In the measured and the calculated curves, a structure with sharp, highly intense peaks dominates the region towards larger angles. The calculated curve fits the peak positions almost exactly. This structure is caused by the multiple reflections of the fundamental beam inside the substrate, whereas in the rest of the measurement those interferences do not show any pronounced peaks. One important consequence of this observation is that s-SHG spectra should be recorded with the substrate at the Brewster's angle. At this angle (for BK7 ca. 56 deg.), there are no internal reflections and the SH intensities are relatively high. This avoids interference patterns in the s-SHG spectrum and ensures good background spectra.

In a next step, we consider a fundamental wavelength where the substrate is transparent to its second harmonic frequency. Figure 6-*15* shows a UV-Vis spectrum of the BK7 glass substrate. The absorption edge is located approximately at 300 nm. This means that for fundamental wavelengths above 600 nm interferences between the generated SH beams of the two surfaces come into play.

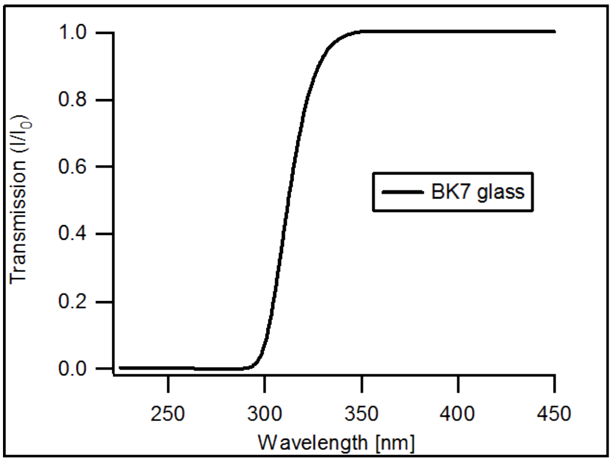

Fig. 6-*15*. Transmission measurement of the BK7 glass substrate. The absorption edge is located approximately at 300 nm.

The resulting intensity I_{int} after the interference of the two beams can be expressed as follows:

$$I_{\text{int}} = \left[A_1 \cdot e^{i2\omega(t+\zeta)} + A_2 \cdot e^{i2\omega t}\right] \cdot \left[A_1 \cdot e^{-i2\omega(t+\zeta)} + A_2 \cdot e^{-i2\omega t}\right] \quad (eq.6\text{-}20)$$

where, A$_1$ and A$_2$, are the amplitudes of the two SH beams, and ζ, is the time delay between the first and the second SH beam. This time delay is a result of the different phase velocities of the fundamental and the SH beam when traveling through the sample. If the substrate is totally transparent at the second harmonic frequency, A_1 and A_2 are nearly equal and can be replaced by A. Expansion of the equation then gives:

$$I_{\text{int}} = 2A^2 \cdot [1+\cos(2\omega \cdot \zeta)] \quad \textit{(eq.6 - 21)}$$

The square of the amplitude is the intensity of a light beam and the intensity of the SH beam is just the intensity, $I_{(2\omega)}$, calculated above. The equation transforms to:

$$I_{\text{int}} = 2I_{(2\omega)} \cdot \left[1+\cos(2\omega \cdot \zeta)\right] \quad \textit{(eq.6 - 22)}$$

The time delay, ζ, can be calculated from figure 6-*13*. The interference takes place in point P3 (fig. 6-*13*). Considering the different traveling paths and the different velocities of the two beams (ω, 2ω), following equation is found:

$$\zeta = \frac{d}{c}\left[\sqrt{n^2_{(2\omega)} - \sin^2\alpha} - \sqrt{n^2_{(\omega)} - \sin^2\alpha}\right] \quad \textit{(eq.6 - 23)}$$

where, *c*, is the speed of light in vacuum, and *d*, the thickness of the substrate.

The mathematical difference between the SH beam intensities $I_{(2\omega)}$ and I_{int} (the first without SH interference and the latter with interference) is the factor $\left[1+\cos(2\omega \cdot \zeta)\right]$ which describes an additional modulation of the signal compared to the case shown in figure 6-*14*. A measurement of the SH intensity as function of the incident angle at a fundamental wavelength of 640 nm is shown in figure 6-*16*. The additional modulation can be clearly observed, leading to an oscillation of the SH signal as function of the incident angle with an increasing amplitude towards larger angles. The calculated curve (blue line) is qualitatively in a good agreement with the measured data.

To summarize, there are three effects which dominate the measurement of the angular dependency of the SH intensity for the BK7 glass substrate. Firstly, the increase of SH intensity towards larger angles, α, due to the symmetry of $\chi^{(2)}$, secondly, at angles, α, close to 90 degrees there are pronounced peaks which can be attributed to interferences of the fundamental beam via multiple reflections inside the substrate, and finally, for fundamental wavelengths above 600 nm interferences between the SH beams generated at the two surfaces show a modulation of the signal. The latter contains phase information of the generated SH light and could be used to study resonance induced nonlinear phase shifts in experiments with samples containing surface adsorbates.

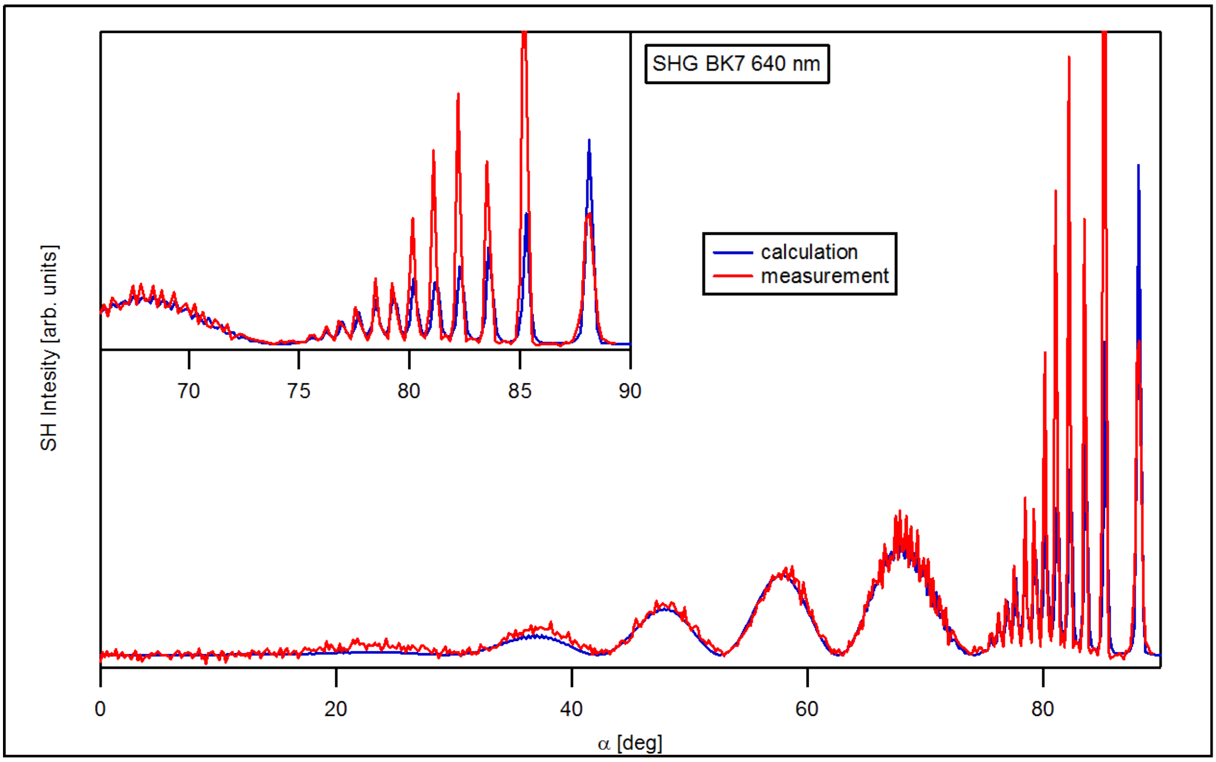

Fig. 6-*16*. Measurement of the angular dependency of SH signal for the BK7 substrate (red line). Included, calculated curve from the above relations considering the interferences between the two SH beams generated at the two surfaces of the substrate (blue line). Parameter used in the calculation: d = 135.2 µm, n_ω= 1.515, $n_{2\omega}$= 1.5565, λ = 640 nm. The additional modulation of the signal leads to an oscillation of the SH intensity as function of the incident angle with an increasing amplitude towards larger angles. A sampling problem due to the limited number of data points is also present in this measurement.

6.5.2 s-SHG Spectrum of BK7 Glass

For the measurement of a s-SHG spectrum, a BK7 glass substrate is positioned at Brewster's angle in the focus of the fundamental beam and a wavelength scan is then carried out. The resulting spectrum is power corrected by dividing the SH intensity by the square of the measured fundamental laser power at each wavelength. In figure 6-*17*, the resulting spectrum is shown (red line). It can be observed that above a fundamental wavelength of ~600 nm the interference between the two SH beams generated at the two surfaces of the substrate leads to an oscillation of the measured SH signal. The dotted blue line shows the transparency spectrum of the sample (from fig. 6-*15*) and is plotted versus the SH wavelength axis. In agreement with the theoretical considerations (see last section), the onset of the measured oscillation is located at the same position as the adsorption edge of the transparency spectrum.

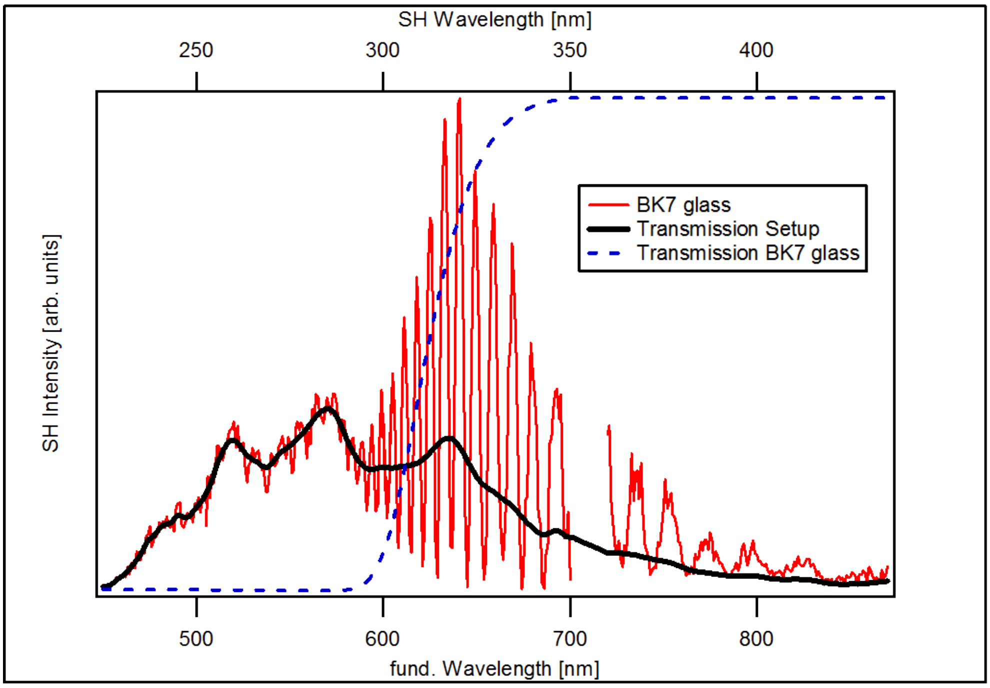

Fig. 6-*17*. s-SHG spectrum of the BK7 glass substrate (red line). The oscillations of the signal above a wavelength of 600 nm originate from the interference between the two SH beams generated at the two surfaces of the substrate. The dotted blue curve shows the transparency spectrum of the substrate plotted versus the SH wavelength axis. The black solid line is the spectrometer function, calculated from the s-SHG spectrum (transmission function of the setup).

In order to understand the form of the spectrum, its main features can be described mathematically. Considering the interference, the wavelength dependent SH intensity measured in the detector, $I_{(\lambda)}{}^{(SHG)}$, can be expressed as:

$$I_{(\lambda)}{}^{(SHG)} = Y_{(\lambda)} \cdot \left[A_{(\lambda)} \cdot e^{i2\omega t} + T_{(\lambda)} \cdot A_{(\lambda)} \cdot e^{i2\omega(t+\zeta)} \right] \cdot \left[A_{(\lambda)} \cdot e^{-i2\omega t} + T_{(\lambda)} \cdot A_{(\lambda)} \cdot e^{-i2\omega(t+\zeta)} \right]$$

$$\Rightarrow I_{(\lambda)}{}^{(SHG)} = Y_{(\lambda)} \cdot A^2{}_{(\lambda)} \left[1 + T^2{}_{(\lambda)} + 2T_{(\lambda)} \cdot \cos(2\omega \cdot \zeta) \right] \quad \textit{(eq.6-24)}$$

where, $T^2{}_{(\lambda)}$, is the measured transparency curve of the substrate, $A^2{}_{(\lambda)}$, the wavelength dependent SH conversion efficiency of one surface ($A^2{}_{(\lambda)} \sim \chi^{(2)}$), and $Y_{(\lambda)}$, the spectrometer function. The latter describes effects, such as the transmission of the optical components in the setup as well as the sensitivity of the photomultiplier, for instance. To extract from the measurement the product $Y_{(\lambda)} \cdot A^2{}_{(\lambda)}$, the oscillation described by the term $2T_{(\lambda)} \cdot \cos(2\omega \cdot \zeta)$ must be removed from the spectrum. The most practical way to do this is to use a smoothing procedure, which averages the cosine to zero. The result is consequently given by:

$$I_{smooth} = Y_{(\lambda)} \cdot A^2_{(\lambda)} \cdot \left[1 + T^2_{(\lambda)}\right] \quad (eq.6\text{-}25)$$

Dividing this expression by the function $1+T^2_{(\lambda)}$ (which can be derived from the transmission spectrum of the substrate) gives the function $Y_{(\lambda)} \cdot A^2_{(\lambda)}$. The latter is plotted in figure 6-*17* (black line). This function must be derived from the measurement because the factor $Y_{(\lambda)}$ cannot be calculated. However, the oscillatory part of the spectrum $I_{(\lambda)}^{(SHG)}$ can be described theoretically, and the theoretical spectrum can subsequently be obtained by multiplying the measured function $Y_{(\lambda)} \cdot A^2_{(\lambda)}$ by the term $\left[1+T^2_{(\lambda)} + 2T_{(\lambda)} \cdot \cos(2\omega \cdot \zeta)\right]$. The time delay, ζ, follows the relation (as seen in the previous section):

$$\zeta = \frac{d}{c}\left[\sqrt{n^2_{(2\omega)} - \sin^2\alpha} - \sqrt{n^2_{(\omega)} - \sin^2\alpha}\right] \quad (eq.6\text{-}26)$$

The variable here (in contrast to section 6.5.1) are not the α terms but instead the wavelength dependent refractive indices: $n_{(\omega)}$ and $n_{(2\omega)}$, of the substrate. In figure 6-*18*, the measured (red line) and the calculated spectrum (black line) are shown.

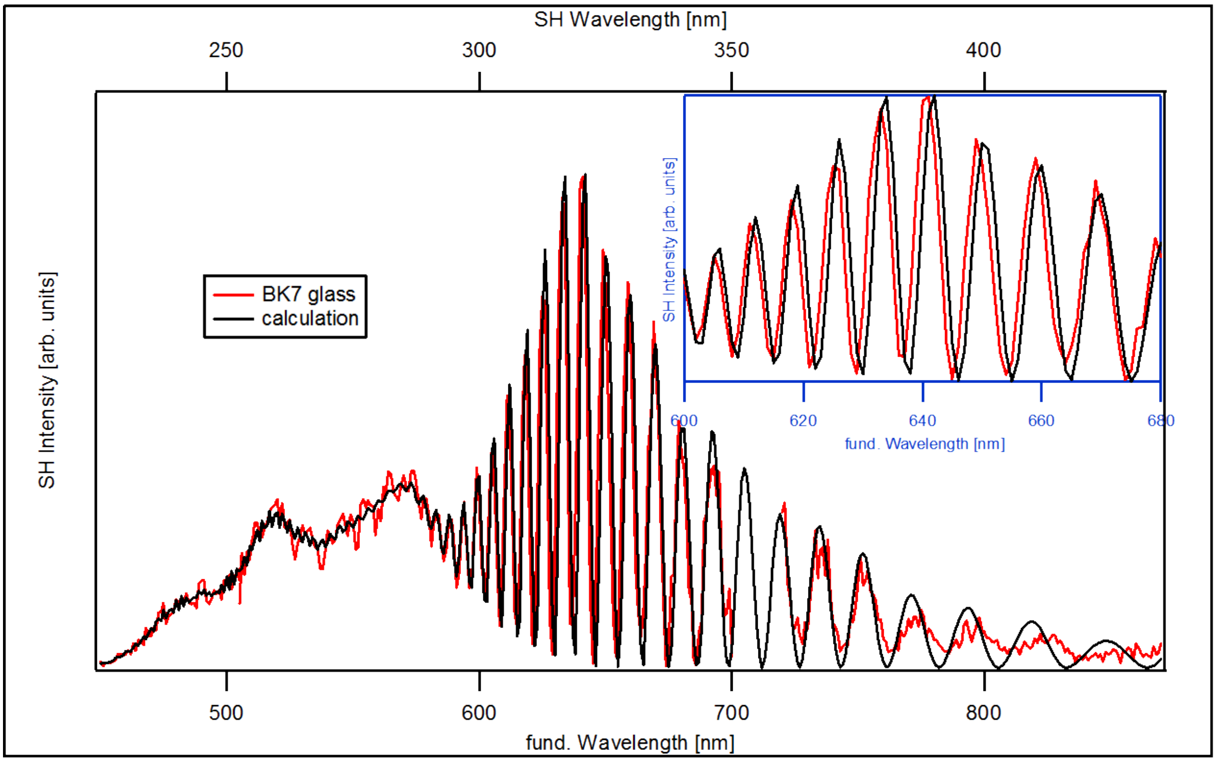

Fig. 6-*18*. s-SHG spectrum of the BK7 glass substrate (red line) and calculated s-SHG spectrum (black line). The calculated curve matches well the measured spectrum. In the oscillatory part the peak positions as well as the amplitudes show a good agreement with the theoretically derived curve. In the inset on the upper right side, the oscillatory part of the spectrum is enlarged.

The interferences are well matched, not only by the peak positions but also the calculated intensities. This shows that all effects contributing to the form of the spectrum are well understood. The peak positions of the oscillations are obviously very sensitive to the refractive indices, $n_{(\omega)}$ and $n_{(2\omega)}$ (n represents the real part of the complex refractive index N). This fact can be used to derive a very precise function $n_{(\omega)}$ of the substrate.

Of particular note is, that values of $n_{(\omega)}$ in the wavelength range close to the absorption edge can be extracted. In order to describe the wavelength dependency of the refractive index, a simple Taylor series of the form:

$$n_{(\lambda)} = a + \frac{b}{\lambda^2} + \frac{c}{\lambda^4} + \frac{d}{\lambda^6} \quad (eq.6\text{-}27)$$

also known as Cauchy's equation is used. In the standard model, only the parameters a and b are used for a rough approximation. For BK7, typical textbook values for the parameters are: $a = 1.5046$ and $b = 4.2 \cdot 10^{-3}\ \mu m^2$. By performing the fit of the measured spectrum, the following values are found: $a = 1.5046$; $b = 4.2 \cdot 10^{-3}\ \mu m^2$; $c = 7.5 \cdot 10^{-5}\ \mu m^4$; $d = 3.8 \cdot 10^{-6}\ \mu m^6$. The resulting curve for $n_{(\lambda)}$ (red line) is plotted in figure 6-*19*. Additionally, the function using only the standard values *a* and *b* is shown. Comparing the two curves, one can see that there are deviations especially towards the absorption edge (300 nm). The fitted curve tends to produce larger values than the standard model. However, the good agreement between the calculated curve and the measured data in figure 6-*18* shows that the derived function of the refractive index is much more accurate.

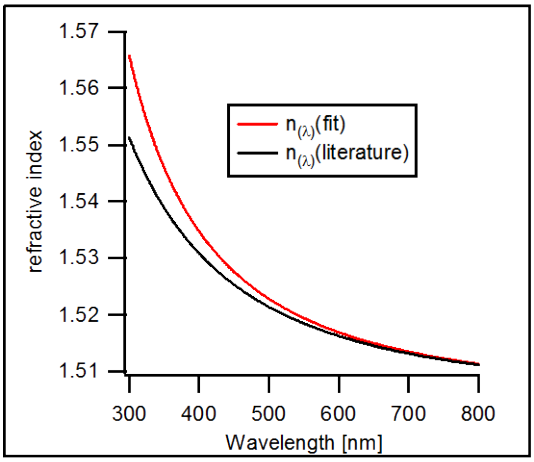

Fig. 6-*19*. Wavelength dependency of $n_{(\omega)}$ for BK7. Red curve: $n_{(\omega)}$ obtained from the fit of the s-SHG spectrum; black curve: $n_{(\omega)}$ calculated from textbook values using equation 6-27. The former tends to produce larger values for $n_{(\omega)}$ towards the absorption edge (300 nm) than the standard model.

One of the big challenges of nonlinear spectroscopy is to determine the spectrometer function, $Y_{(\lambda)}$. Because s-SHG is not a transmission spectroscopy, $Y_{(\lambda)}$ is not automatically cancelled out by subtracting the measured spectrum from that of a reference sample. Instead, the contribution of the spectrometer function to the measured spectrum must be removed by dividing the spectrum through by $Y_{(\lambda)}$, which must therefore be pre-determined. As shown before, it is easily possible to extract the function $Y_{(\lambda)} \cdot A^2{}_{(\lambda)}$ from the spectrum, the question is only, which factor dominates this product. In chapter 2.2.7, it was shown that the SH intensity does not show a large wavelength dependency as long as there is no resonance at either the fundamental or the second harmonic frequency. Because the BK7 glass substrate is not transparent below 300 nm, this could be interpreted as resonant absorption which would enhance the SH signal. Nevertheless, there is no drastic change in SH intensity in the measured spectrum which suggests that the absorption is not due to an SHG active resonance at the substrate surface. It could instead be a bulk property or a resonance with a very high damping constant. In order to investigate this phenomenon, an s-SHG spectrum of MgO is measured (see figure 6-*20*).

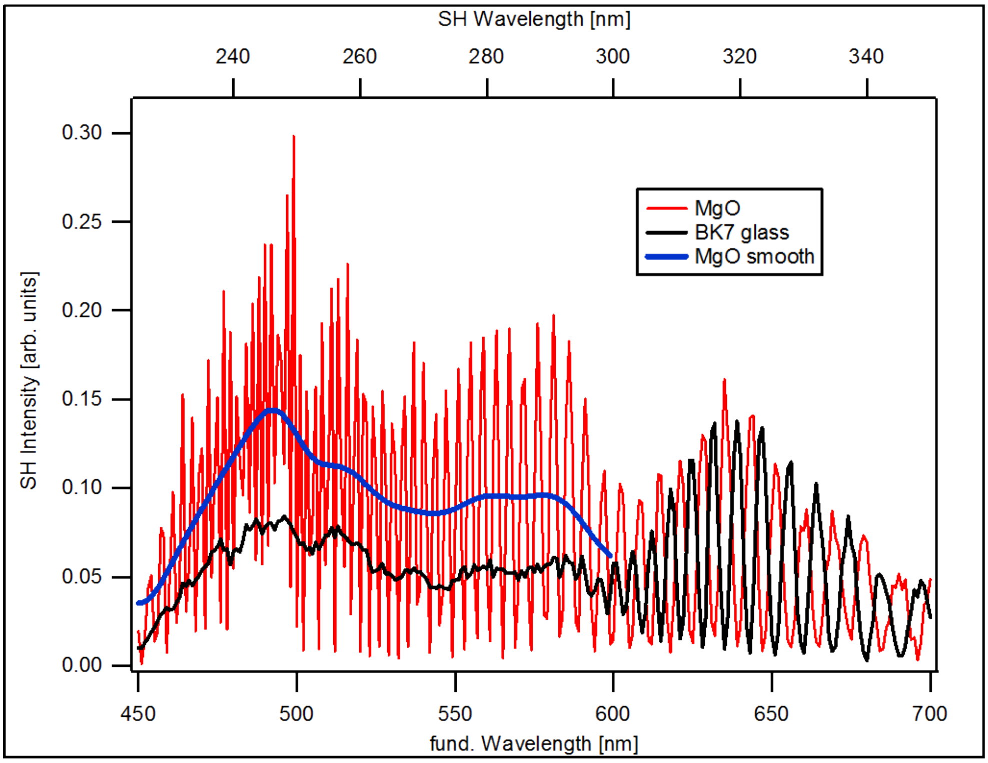

Fig. 6-*20*. Comparison between the s-SHG spectra of a MgO (red line) and a BK7 substrate (black line). MgO is transparent in the UV range down to 200 nm and consequently, interferences between the SH beams generated at its two surfaces are present in the entire measured wavelength range. The smoothed curve (blue line) of the MgO spectrum shows the same spectral structure as the BK7 spectrum.

MgO is transparent in the UV range down to 200 nm (and thus $A^2_{(\lambda)}$ is nearly constant). Consequently, the interference patterns are present in the entire measured range. In the region below 500 nm of the fundamental, the oscillation frequency is so high that it cannot be sufficiently sampled by the spectroscopy, which subsequently slightly distorts the appearance of the spectrum. However, it can be seen that all main features of the MgO spectrum (red line) are also present in the spectrum of the BK7 glass substrate (black line). This becomes even more obvious by smoothing the MgO spectrum (blue line). If the two curves show the same intensity in the region of the oscillation in the BK7 spectrum - which is the case - the smoothed line of MgO should be twice as high as the data points of BK7 in the low wavelength range. This is due to the fact, that the smoothed line of MgO shows the contribution of two surfaces (MgO is transparent in the entire wavelength range), whereas in the case of BK7 only the SH light of the second surface is measured (below 300 nm the SH contribution of the first surface is absorbed while traveling through the BK7 substrate). In the figure, it can be observed that the above mentioned relation is given in a precise manner. From this observation it can be concluded that the influence of the absorption edge of the BK7 substrate on the second order susceptibility is negligible. Furthermore, it is found that the second order susceptibilities of MgO and BK7 are nearly identical. This means that for BK7, $A^2_{(\lambda)}$ also does not show any strong wavelength dependency. A very important consequence of this is, that the product $Y_{(\lambda)} \cdot A^2_{(\lambda)}$ is highly dominated by the spectrometer function $Y_{(\lambda)}$. Hence, it can be written in a good approximation:

$$Y_{(\lambda)} \sim Y_{(\lambda)} \cdot A^2_{(\lambda)} \quad \textit{(eq.6 - 28)}$$

This result can be used in the following to correct the measured s-SHG spectra since the spectrometer function can be extracted from a reference spectrum of the BK7 glass substrate. In a further experiment, the impact of sputtering on the s-SHG spectrum was investigated. No measurable effect could be observed.

In these sections, the nonlinear properties of the BK7 glass substrate were characterized and all important features of the measured s-SHG spectrum could be explained. One of the most pronounced spectral features which is observed is the oscillation of the SH signal due to the interference of the two SH beams. Although it contains phase information which could help in characterizing measured spectra, it leads to a rather complicated data treatment procedure and decreases the signal to noise ratio. The interference could be suppressed by taking a substrate, which is wedge-shaped. Using such a substrate, the SH beams of the two surfaces leave the substrate at different angles. There are, however, several drawbacks which must be considered when using such substrates. Firstly, the beam path would not be straight which makes an alignment of the s-SHG setup much more challenging. For example, it would no longer be possible to adjust the Pellin-Broca prisms using the BBO crystal, because the beam path would be different to that with the introduced sample. Secondly, the angle at which the SH beam leaves the substrate would be dependent on the angle of incidence which makes a very precise adjustment of the sample necessary. Finally, all angles would be wavelength dependent which limits the applicable frequency range without readjusting the setup. New solutions to cope with these challenges will need to be developed.

6.6 Spectroscopic Properties of ZrO_2:Y

In this section, the spectroscopic properties of the second substrate, a ZrO_2:Y crystal, which is used in this thesis are investigated. In the following sections, s-IR-CRD and s-Vis-CRD measurements of the substrate are shown and interpreted.

6.6.1 s-IR-CRD Spectroscopy

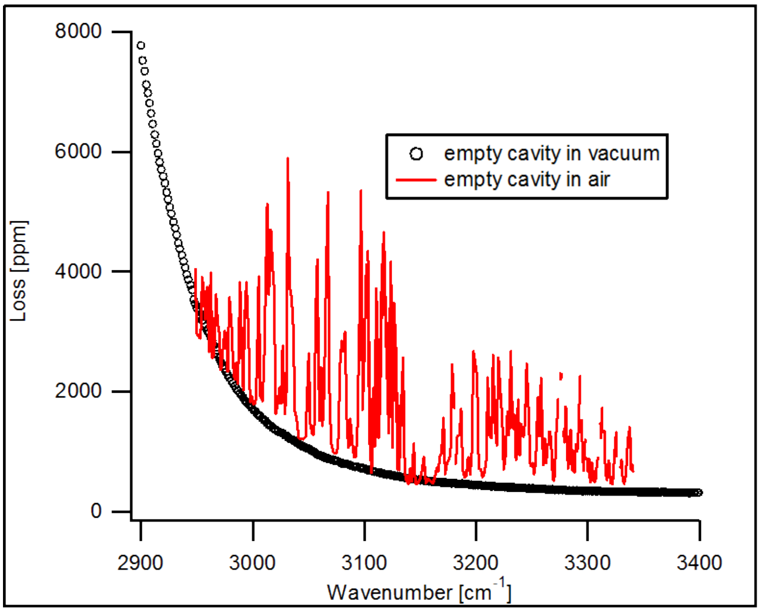

Fig. 6-*21*. s-IR-CRD spectrum of the empty cavity measured in air (red line) and under UHV conditions (black circles). In the spectrum of air, sharp absorption peaks are present originating from absorption bands of water molecules. Under UHV conditions no absorption bands are observed.

The BK7 glass substrate is not transparent in the infrared region, which leads to the necessity of a suitable substrate for the s-IR-CRD experiments. Here, the wavelength range of interest is between 2500 nm and 3600 nm (4000 cm^{-1} to 2800 cm^{-1}), because in this region the vibrational transitions of the C-H group are located. The measurement of those vibrational transitions are part of the aim of this thesis. In order to cover the entire wavelength range, only one or a maximum of two sets of CRD mirrors are needed. A crucial condition for the s-IR-CRDS is that the experiments must be carried out under UHV conditions. The reason for this is, that many of the substances which are found in the air (especially water and traces of volatile organic molecules) possess sharp absorption bands in the IR region which leads to a very noisy background spectrum. To illustrate this, a s-IR-CRD spectrum of the empty cavity recorded in air (red line) and in vacuum (black line) is shown in figure 6-*21*. Absorption peaks that are even higher than 4000 ppm can be observed in the spectrum of air, whereas the vacuum spectrum is approximately as smooth as that of the s-Vis-CRD measurements. This way the noise can be reduced to about 4 ppm. The InSb detector, which is used to measure the IR signal is a passive detector, and therefore it is not possible to adjust the intensity of the detector output by changing its amplification. However, an adjustment is necessary because the intensity of the light leaving the cavity shows drastic changes over the applied wavelength range. The only possibility is to weaken the laser beam before it enters the detector using an optical density filter. As a consequence, the spectrum must be divided in several regions and a suitable filter needs to be introduced for each of them.

6.6.2 s-IR-CRD Measurement of ZrO_2:Y

The most suitable for the s-IR-CRDS of all tested substrates proved to be a ZrO_2:Y substrate (single crystal). In figure 6-*22*, the s-IR-CRD difference spectrum (the spectrum of the empty cavity is subtracted) of the sample is shown. In order to perform the measurement, a cleaned ZrO_2:Y substrate is transferred into vacuum and placed at Brewster's angle inside the cavity. In the spectrum, it can be seen that the optical quality of this substrate is already much worse than that of the BK7 substrate, because the loss over the entire wavelength range is above 1500 ppm. Scattering cannot be the main reason for the high loss because the surfaces of the substrate are highly polished. In general, scattering losses in the IR region should be orders of magnitude smaller than in the visible range because the scattering cross section scales with $1/\lambda^4$ (see chapter 6.4.2). Using the surface topography analysis method (see chapter 6.2), small deformations at both surfaces could be observed, which probably cause these high losses. Care should be taken when interpreting the obtained spectrum because these deformations lead to high values of $\Delta\Lambda_{(\omega)}^{(\text{cavity})}$ (see section 6.4.1), which distorts the form of the difference spectrum. This could, for example, be the reason for the increase of the loss towards smaller wavenumbers, because it is noticeable that the spectrum of the empty cavity shows a similar increase (indicating that the increase might be an effigy of the empty cavity). However, two interesting features can be observed in figure 6-*22*. One is the very broad band, which is centered around 3330 cm^{-1} and the other is the double peak between 2900 cm^{-1} and 2960 cm^{-1}. The first can be attributed to an O-H absorption band of water (which is present in trace amounts inside the substrate), whereas the latter probably originates from C-H absorption bands; however, their exact origins are unknown (although it might be organic impurities). Despite the poor optical quality the ZrO_2:Y substrate can be used as support for s-IR-CRD spectroscopy.

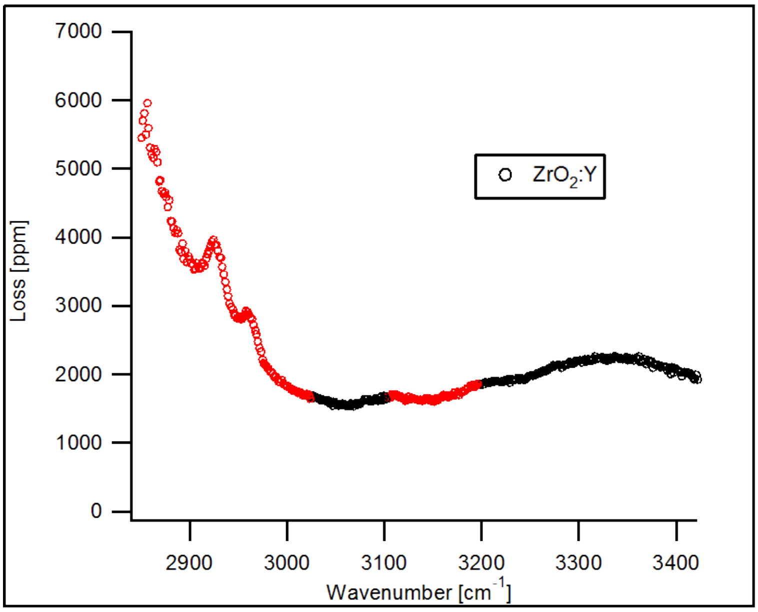

Fig. 6-*22*. s-IR-CRD spectrum of the ZrO_2:Y substrate (the spectrum of the empty cavity is subtracted). The different colors represent the different sections in which the measurement is divided.

6.6.3 s-Vis-CRD Measurement of ZrO_2:Y

The s-Vis-CRD measurement of the ZrO_2:Y substrate shows a surprising spectrum (see figure 6-*23*). There are very distinct and sharp peaks between 500 nm and 600 nm present. The substrate material itself does not show any absorption patterns, however, the peaks can be attributed to electronic transitions in Nd^{3+} ions.[60, 131-133] Nd is a typical impurity in Yttrium salts and was probably introduced in traces with the dopant in the substrate. The sharp peaks observed are typical for f-f transitions which can be found in most of the f-metals. However, such a structured background is not a good reference for the s-Vis-CRD spectroscopy and this substrate is consequently not used for measurements in the visible region.

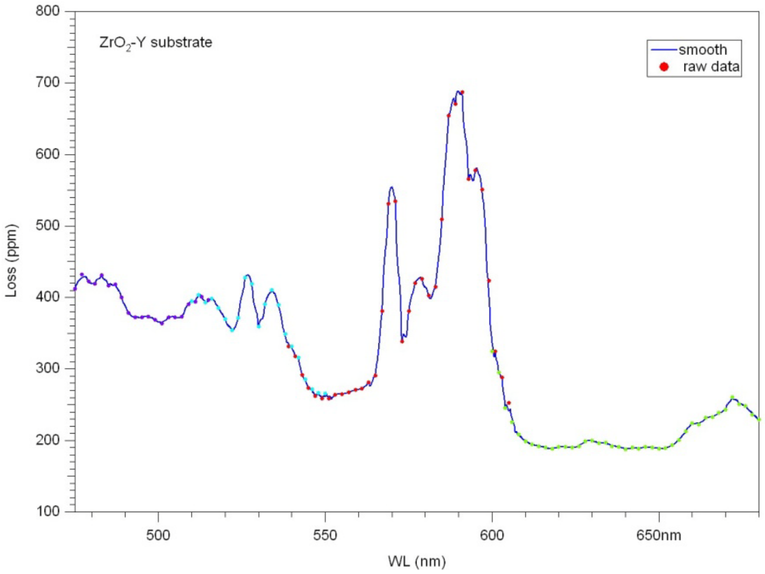

Fig. 6-*23*. s-Vis-CRD spectrum of the ZrO_2:Y substrate. The sharp absorption bands in the spectrum can be attributed to electronic f-f transitions in the Nd^{3+} ion. Nd is in traces present in the substrate (as impurity).

6.7 Summary Chapter 6

In this chapter, two substrate materials were presented, BK7 glass and ZrO_2:Y, which have been shown to be suitable for the use in experiments with the described spectroscopic methods (s-Vis-CRDS, s-IR-CRDS, and s-SHG spectroscopy). All relevant linear and nonlinear spectroscopic properties of the two types of substrates were determined and characterized. Furthermore, a theoretical description of the s-SHG spectra of the BK7 substrate could be developed which explains the origin of the spectral features obtained by the measurements. Based on these results, it was possible to extract the spectrometer function of the setup from the measurement, which is a crucial achievement in order to extract spectral information from measured raw data using s-SHG spectroscopy. Additionally, experimental routines for s-CRD and s-SHG measurements could be defined and justified using the results of the measurements in this chapter. In all following experiments in this thesis, these results are consequently used as basis for the interpretation of the obtained data.

7. Surface Spectroscopy of Organic Molecules

In this chapter, measurements of samples containing thin layers of organic adsorbates coated onto a substrate are presented. The spectroscopic investigations of these samples are carried out for two purposes: Firstly, the characterization of the spectroscopic setup presented in chapter 5 (determination of the reliability and sensitivity of the spectroscopic methods) and secondly, the spectroscopic characterization of organic molecules representing possible ligands for the preparation of ligand stabilized clusters. The investigation of the latter is one of the important future projects, because by studying the spectroscopic properties of ligand stabilized clusters the cluster-ligand interaction can be characterized which provides important information about the cluster reactivity.

For the characterization of the spectroscopic setup in the first part of the chapter, measurements of the laser dye Rhodamine 110 coated onto a substrate are performed using all the three spectroscopic methods of the setup (s-Vis-CRD, s-IR-CRD, and s-SHG spectroscopy). The resulting spectra are used in order to demonstrate the reliability and the high sensitivity of the spectroscopic methods. In the second part, measurements of the organic molecules Binol, BiBuQ, and {5}Helicene coated onto a substrate are presented and the resulting spectra are discussed in detail. This part focuses on the sustainability of the measured molecules for the use as ligand molecule by discussing the obtained spectroscopic properties.

7.1 Rhodamine 110

In order to characterize the reliability and sensitivity of the three spectroscopic methods (s-Vis-CRD, s-IR-CRD and s-SHG), a reference sample with well known optical properties is needed. It must be an organic substance (important for the s-IR-CRD) with a strong absorption in the visible range (s-Vis-CRD) and distinct nonlinear optical properties (s-SHG). In the s-SHG spectroscopy, high laser pulse energies are used (1-10 mJ per pulse) which can lead to photo damage or the evaporation of the molecules from the surface with the consequence of destruction of the sample. This problem arises in particular, if the fundamental laser frequency is in resonance with an electronic transition inside the molecule. However, as shown in chapter 2.2.4, the s-SHG spectroscopy can probe resonances at the fundamental as well as at the second harmonic frequency. In the latter case, the destructive impact of the laser pulses on the molecules is much smaller, provided that the fundamental frequency is far from any absorption band in the adsorbate. As a consequence, the ideal substance should have two absorption peaks, one in the ultraviolet, and one in the visible range with the additional condition that half the frequency of the UV band should be far from the resonance in the visible.

All of these requirements are fulfilled for the laser dye Rhodamine 110. In figure 7-*01*, a UV-Vis spectrum of the dye dissolved in methanol is shown. A very intense absorption band is located at around 510 nm along with a second band in the UV range at 334 nm with much smaller intensity. An important observation is that the absorption of the molecules at 668 nm (half the frequency of the peak at 334 nm) is nearly zero, which makes it possible to measure the latter peak in an s-SHG experiment without the risk of destroying the sample.

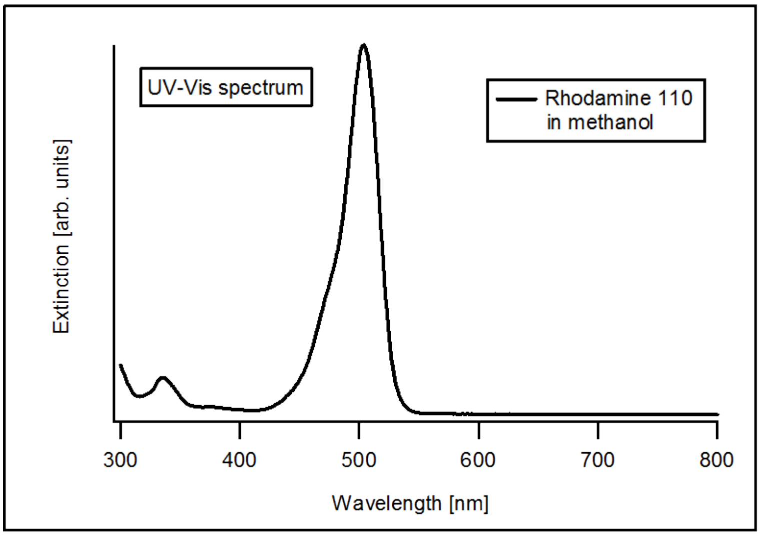

Fig. 7-*01*. UV-Vis spectrum of Rhodamine 110 in methanol. Two absorption peaks are present, one at 510 nm, and a second at 334 nm.

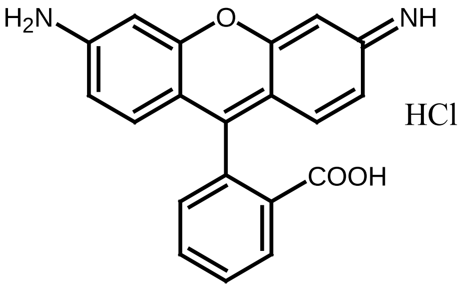

Fig. 7-*02*. Chemical structure of Rhodamine 110.

The structure of Rhodamine 110 is depicted in figure 7-*02*. A large aromatic π-electron system is present which is responsible for its intense absorption bands at low transition energies. In the literature[134], the two peaks were attributed to the electronic $S_1 \leftarrow S_0$ (510 nm) and the $S_2 \leftarrow S_0$ transitions (334 nm) in the molecular orbitals of the Rhodamine 110 molecule. In order to measure the IR spectrum of the dye, a few drops of a highly concentrated solution of Rhodamine 110 in methanol are dried on a KBr window and subsequently measured in an FT-IR spectrometer. The obtained spectrum is shown in figure 7-*03*. The strong absorption band at 3180 cm^{-1} can be attributed to the C-H stretch vibrational mode of the molecule. Considering the chemical structure of Rhodamine 110, it is obvious that all C-H groups belong to carbon atoms which are sp^2 hybridized. This gives rise to one single C-H absorption peak in the spectrum without any significant splitting. Furthermore, the resonance position of 3180 cm^{-1} is typical for C-H stretching modes in aromatic systems as present in the molecule investigated here. The two peaks at 3320 cm^{-1} and 3400 cm^{-1} belong to the symmetric and antisymmetric stretch vibrational modes of the NH_2 group (the antisymmetric mode is located at higher wave-numbers). These three absorption bands lie within the spectral range, which is accessible using the s-IR-CRD setup.

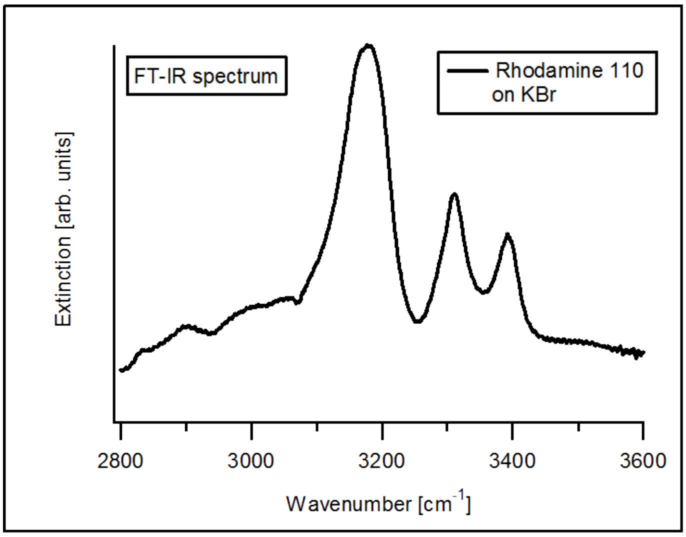

Fig. 7-*03*. FT-IR spectrum of Rhodamine 110 on KBr. The intense peak at 3180 cm^{1} is the C-H stretch vibrational mode and the double peak at 3320 cm^{-1} and 3400 cm^{-1} belongs to the symmetric and antisymmetric stretch vibrational mode of the NH_2 group, respectively.

In order to perform measurements of Rhodamine 110 using the three surface spectroscopic techniques, the dye must be coated onto a surface. As substrate for the s-Vis-CRD and the s-SHG measurements the BK7 glass substrate is used, whereas the ZrO_2:Y crystal is chosen for the s-IR-CRD measurements (see chapter 6). Different coating methods were tested, such as spin- and dip-coating, but the best results were achieved by simply wetting a lens cleaning tissue with the dye solution and wiping the dye on the surface. Using this technique, a sample with a quite homogeneous film of Rhodamine 110 can be prepared. For the two Cavity Ringdown experiments (Vis- and IR-) the dye is coated onto both sides of the substrate, whereas for the s-SHG measurement only the back side is coated. The reason for this is that interferences between the SH contributions of the dye from the two surfaces should be avoided in order to obtain a clear spectrum.

7.1.1 s-Vis-CRD Measurement of Rhodamine 110

Figure 7-*04* shows the s-Vis-CRD spectrum of Rhodamine 110 coated onto BK7. The electronic $S_1 \leftarrow S_0$ transition at 510 nm is clearly resolved. The spectrum is obtained by subtraction of a reference BK7 spectrum from the spectrum of the sample with the dye. The resulting data points are corrected using the method shown in chapter 6.4.1.

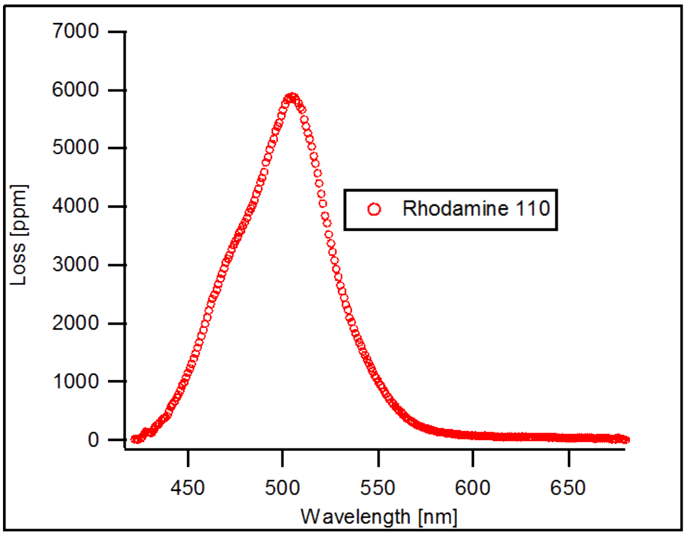

Fig. 7-*04*. s-Vis-CRD spectrum of Rhodamine 110. The intense absorption peak at 510 nm (see figure 7-*01*) is clearly resolved.

From the spectrum, the coverage of the dye molecules on the surface can be estimated as shown in the following. The intensity, *I*, of a light beam traveling through an absorbing substance follows the Beer-Lambert law:

$$\frac{I}{I_0} = 10^{-\varepsilon_\lambda \cdot c \cdot l} = e^{-\ln(10)\cdot\varepsilon_\lambda \cdot c \cdot l} \quad \textit{(eq.7-01)}$$

where, ε_λ, is the decadal extinction coefficient, *c*, the concentration of the absorber, and *l*, the length of the optical path through the absorbing substance. In the case of a very thin layer of molecules ($l \ll 1$) it can be written approximatively:

$$e^{-\ln(10)\cdot\varepsilon_\lambda \cdot c \cdot l} \approx 1 - \ln(10)\cdot\varepsilon_\lambda \cdot c \cdot l \quad \textit{(eq.7-02)}$$

The expression, $c \cdot l$, can be replaced by the coverage, ρ, and $\ln(10)\cdot\varepsilon_\lambda$ can be transformed to the extinction cross section, σ_{ex}. The photon loss per pass, Λ, in an s-CRD experiment is nothing other than the ratio of extinguished photons to initial photons, which is: $1 - I/I_0$. Consequently, the photon loss can be expressed as:

$$\Lambda = \sigma_{\mathrm{ex}} \cdot \rho \quad \textit{(eq.7-03)}$$

If the extinction cross section of the molecules on the surface is known, the coverage can be calculated from the s-Vis-CRD spectrum. In the literature, the value of $\varepsilon_\lambda = 9 \cdot 10^4 \frac{\mathrm{L}}{\mathrm{mol} \cdot \mathrm{cm}}$ can be found for the decadal extinction coefficient of Rhodamine 110 in ethanol at the peak wavelength.[135] Based on this value, the extinction cross section for the dye in solution is calculated to be $3.44 \cdot 10^{-16}\,\mathrm{cm}^2$. In general, the extinction cross section of a molecule is dependent on its orientation with respect to the optical axis of the light beam and its environment. For molecules in solution, the measured value gives the cross section averaged over all possible rotational positions of the molecules because they are usually randomly orientated. On a surface, however, this is not necessarily the case. Here, processes such as the self organization of organic molecules on surfaces can lead to well defined molecular orientations. However, for the estimation of the coverage these effects are neglected owing to the fact that the real configuration is not known. The second effect influencing the absorption cross section is the presence of the surface. Typically, this leads to a broadening of the resonance peak in the spectrum. This peak broadening diminishes absorption at the maximum of the resonance peak, whereas the peak area remains the same and consequently it can be written:

$$\int_{\text{peak}} \sigma_{ex}^{\ solution} d\lambda = \int_{\text{peak}} \sigma_{ex}^{\ \text{surface}} d\lambda \quad (eq.7\text{-}04)$$

Using this relation, the extinction cross section of Rhodamine 110 coated on a surface, $\sigma_{ex}^{\ \text{surface}}$, at $\lambda_{\max}$ can be calculated. The UV-Vis spectrum of the dye in methanol is therefore scaled so that its maximum equals the above calculated value of $3.44\cdot10^{-16}\text{cm}^2$ for the cross section in solution. In a second step, the s-Vis-CRD spectrum is overlaid and scaled in such a way that the peak areas equal each other, representing now the absolute values of the extinction cross section for the dye coated onto a surface. Figure 7-*05* shows the two curves. The maximal value of $\sigma_{ex}^{\ \text{surface}} = 2.18\cdot10^{-16}\text{cm}^2$ can now be derived from the plot.

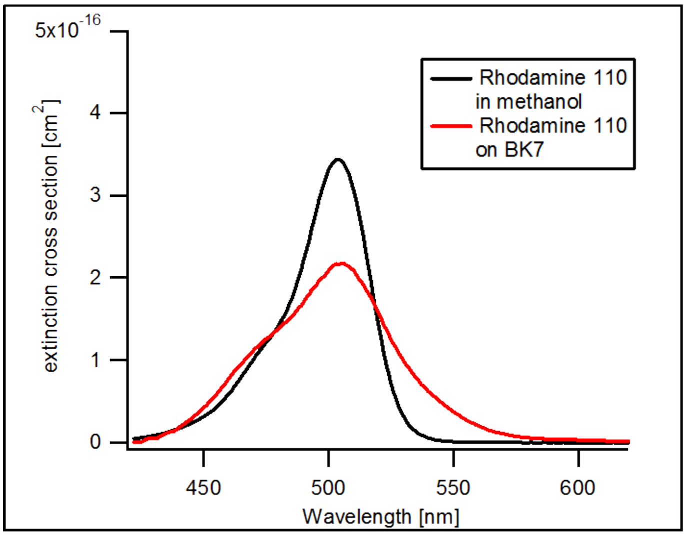

Fig. 7-*05*. Plot of the extinction cross sections of Rhodamine 110 in methanol (black line) and coated onto a BK7 substrate (red line). The curves are scaled so that the peak areas equal each other.

By taking the measured maximal loss from figure 7-*04* of 5886 ppm, the surface coverage of the Rhodamine 110 molecules is calculated to be $2.7\cdot10^{13}\text{cm}^{-2}$. One dye molecule covers approximately 0.5 nm^2 of the surface (for random orientation), leading to a surface coverage in the presented experiment of 13.5% of a monolayer. However, because both sides of the substrate are coated in this experiment, each surface is actually covered with 6.75% of a monolayer of the dye.

By considering the noise of the s-Vis-CRD apparatus (< 4 ppm), absorption peaks down to approximately 20 ppm in height can be detected. This corresponds to surface coverages of Rhodamine 110 which are below 0.1% of a monolayer. This sensitivity is far beyond the sensitivities which can be achieved using standard spectroscopic methods.

7.1.2 s-IR-CRD Measurement of Rhodamine 110

For the s-IR-CRD measurement a ZrO_2:Y substrate is coated with Rhodamine 110 using the technique described in the previous section and transferred into the vacuum chamber. A clean ZrO_2:Y substrate serves as reference sample. The measured spectrum is shown in figure 7-*06*.

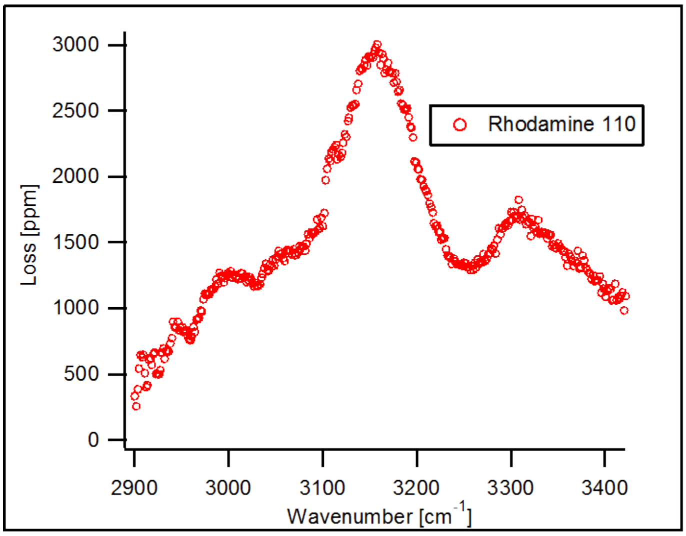

Fig. 7-*06*. s-IR-CRD spectrum of Rhodamine 110 coated onto a ZrO_2:Y substrate. The absorption peak corresponding to the C-H stretch vibrational mode at 3180 cm^{-1} is clearly resolved. The second absorption peak at 3320 cm^{-1} can be attributed to the symmetric stretch vibrational mode of the NH_2 group.

The absorption band of the C-H stretch vibrational mode at 3180 cm^{-1} is well resolved and a second absorption peak is located at 3320 cm^{-1}, which can be attributed to the symmetric NH_2 stretch vibrational mode. In contrast to the FT-IR spectrum of Rhodamine 110 (fig. 7-*03*), however, the second peak of the NH_2 group at 3400 cm^{-1} has disappeared. A possible reason for the lack of the antisymmetric contribution is the presence of the surface. One of the hydrogen atoms of the NH_2 group might be bound to the surface leading to a confinement of its freedom of motion and a shift of its vibrational transition frequency. As a consequence, the symmetric and antisymmetric vibrational modes of the NH_2 group transform into a free and a bound N-H vibrational mode. The free N-H mode corresponds in frequency approximately to that in secondary amines (3310 cm^{-1}), whereas the bound N-H mode can be drastically shifted (it might be shifted out of the measured range). Similar effects have been observed in weakly bound complexes consisting of a heavy bound atom and a molecule involving bound and free carbon hydrogen stretching vibrations. Although the dye is also coated onto a surface for the FT-IR measurement presented here, the coverage in these experiments is much higher and thus molecules in contact with the surface represent only a very small percentage. Therefore, surface effects do not influence the N-H stretching modes in the measurements using the conventional FT-IR spectrometer. However, to investigate this effect in detail further measurements would be necessary.

In order to calculate the sensitivity of the s-IR-CRDS apparatus, the coverage of dye on the surface must be determined. Since the absorption cross section of the C-H stretch vibrational mode on a surface is not known, it cannot be derived from the s-IR-CRD spectrum. Furthermore, the ZrO_2:Y substrate is not suitable for the s-Vis-CRD spectroscopy, so that it is hardly possible to determine the coverage by measuring the intensity of the electronic $S_0 \rightarrow S_1$ transition on the sample. Because the dye is highly soluble in ethanol, however, it can be washed off the sample using a defined volume of the solvent. From the resulting solution a UV-Vis spectrum is measured (using a UV-Vis spectrometer), from which the concentration of dye in the solution can be extracted. Assuming a homogeneous dispersion of the molecules on the sample, the coverage is subsequently calculated.

In figure 7-*07*, the obtained UV-Vis spectrum of the Rhodamine 110 dissolved in 8.4 mL ethanol is depicted. Using the Beer Lambert law and the decadal extinction coefficient of the dye, $\varepsilon_\lambda = 9 \cdot 10^4 \frac{\mathrm{L}}{\mathrm{mol} \cdot \mathrm{cm}}$, the concentration of the dye is calculated to be $c = 7.29 \cdot 10^{-7} \frac{\mathrm{mol}}{\mathrm{L}}$. The total amount of molecules in the solution is consequently $n = 6.12\ \mathrm{nmol}$. Assuming this is dispersed homogeneously on the substrate with a surface area of 12.5 cm^2 (back and front side), the coverage is calculated to be $\rho = 2.95 \cdot 10^{14}\,\mathrm{cm}^{-2}$. This corresponds roughly to 1.5 monolayers of the dye on each side of the substrate. Since the absorption of both surfaces is measured in the s-IR-CRDS experiment, the maximal value of the loss in the spectrum of ~3000 ppm corresponds to the absorption of 3 monolayers of Rhodamine 110. From the determined coverage and the observed loss in the s-IR-CRD spectrum, the absorption cross section of the C-H stretch vibrational mode can be derived. Considering that there are ten C-H groups per dye molecule, the cross section per C-H group is $5.1 \cdot 10^{-19}\,\mathrm{cm}^2$ which is in a good agreement with typical textbook values for C-H groups in aromatic systems. The noise of the s-IR-CRD apparatus is approximately 4 ppm and consequently coverages of Rhodamine 110 down to 1% of a monolayer can be detected. That means that the sensitivity of the s-CRD technique in the IR range is much smaller than in the visible (detection limit below a surface coverage of 0.1 % of a monolayer). The reason for the lower sensitivity is due to the fact that the absorption cross sections of vibrational transitions are approximately two orders of magnitude smaller than those of electronic transitions in dyes.

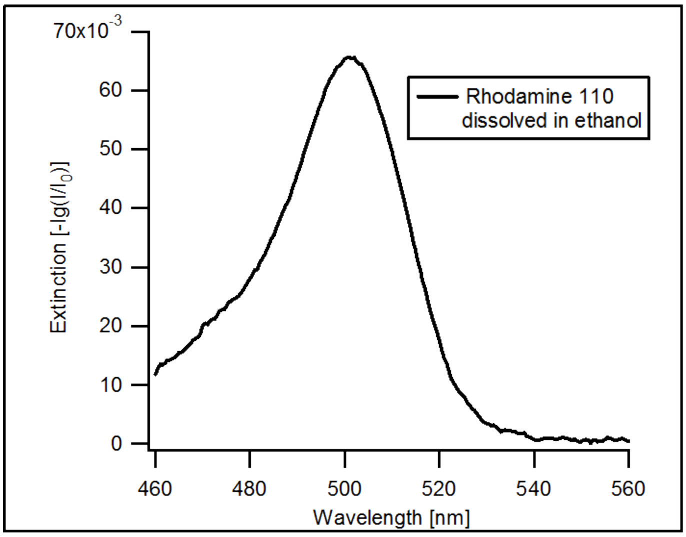

Fig. 7-*07*. UV-Vis spectrum of Rhodamine 110 in solution. The dye is washed off the sample with ethanol.

In order to test the reliability of the method to determine the coverage of Rhodamine 110 in the IR experiment presented above, a BK7 glass substrate is coated with the dye and its transmission is measured in the UV-Vis spectrometer. After that, the dye is washed off with 7.8 mL ethanol and a second UV-Vis spectrum (of the solution) is measured. These two spectra are shown in figure 7-*08*. By taking the surface area of both sides of the BK7 substrate (15.36 cm^2) and the decadal extinction coefficient, $\varepsilon_\lambda = 9 \cdot 10^4 \dfrac{\mathrm{L}}{\mathrm{mol} \cdot \mathrm{cm}}$, a surface coverage of $1.53 \cdot 10^{14}\,\mathrm{cm}^{-2}$ can be calculated from the spectrum of the dye in ethanol. Similarly, by taking the spectrum of the dye coated on BK7 and the surface corrected value of the extinction cross section of $\sigma_{ex}^{\mathrm{surface}} = 2.18 \cdot 10^{-16}\,\mathrm{cm}^2$, the calculation of the coverage per side of the substrate gives the value of $1.42 \cdot 10^{14}\,\mathrm{cm}^{-2}$. The deviation from the first value is approximately 7%. One possible reason for this deviation is that the coverage at the edges of the substrate is higher than in the middle, which is a result of the substrate coating process. Consequently, the surface coverage of Rhodamine 110 determined for the IR experiment is most likely slightly overestimated (in this case the sensitivity of the s-IR-CRD setup is even higher). However, this experiment confirms the reliability of the method used here, and the high accuracy of the derived values.

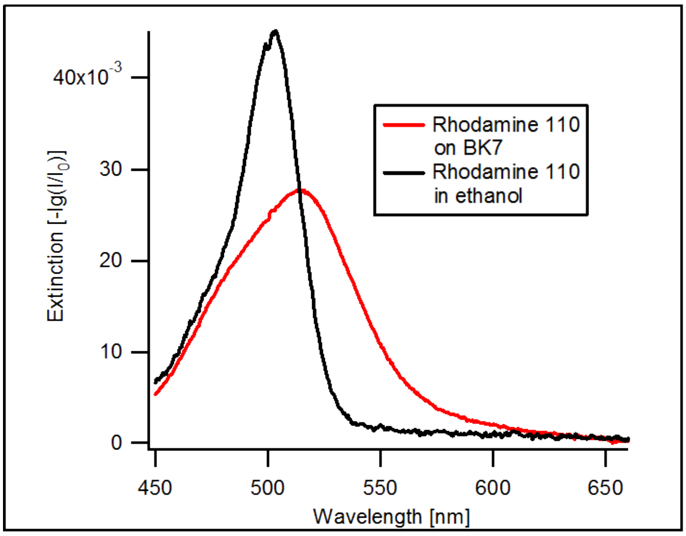

Fig. 7-*08*. UV-Vis spectra of Rhodamine 110 in ethanol (black line) and coated onto a BK7 substrate (red line).

7.1.3 s-SHG Measurement of Rhodamine 110

For the s-SHG measurement, Rhodamine 110 is coated on the backside of a BK7 glass substrate. All s-SHG measurements, which are presented in chapter 7 were carried out using a less sophisticated version of the s-SHG apparatus, where the experiments were carried out under ambient conditions (i.e. UHV conditions were not required). In contrast to the setup described in chapter 5, the beam separation unit (for the separation of the fundamental and the SH beam) consisted of a four prism Pellin-Broca device and the fundamental pulse energy was measured using a photomultiplier. The resulting spectra from the s-SHG measurements are only corrected by the fundamental power and not by the spectrometer function (see chapter 6). This can lead to a slight distortion of the spectra; however, all important spectroscopic features can be resolved. In figure 7-*09*, the s-SHG spectrum of Rhodamine 110 coated onto a BK7 substrate is presented. The red line shows the raw data and the black line the smoothed curve. The peak at 668 nm of the fundamental wavelength which can be observed in the spectrum originates from the electronic $S_2 \leftarrow S_0$ transition in the dye. In the linear UV-Vis spectrum (fig. 7-*01*) this transition is located at 334 nm, which means that the peak in the s-SHG spectrum originates from the resonance enhancement of the SHG process at second harmonic frequency. This s-SHG spectrum is in a very good agreement with the s-SHG measurement of the same dye coated onto a quartz glass substrate performed by the group of Shen.[136]

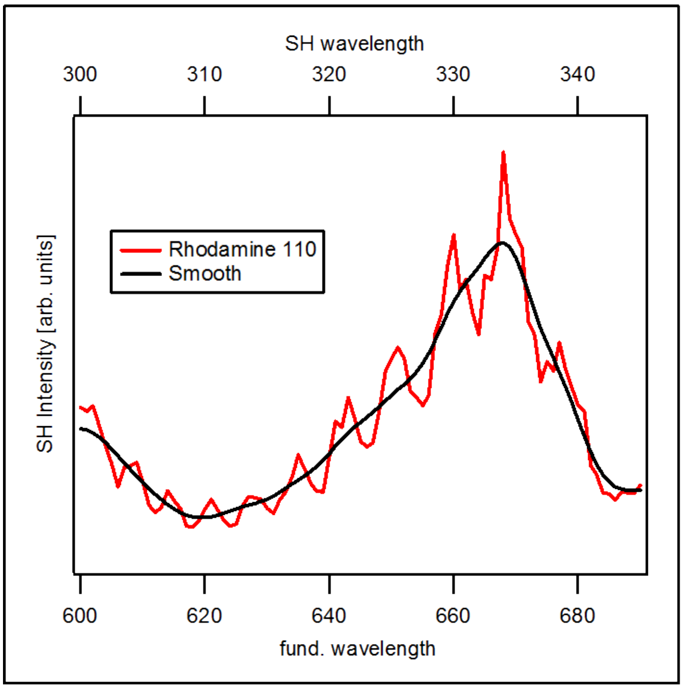

Fig. 7-*09*. s-SHG spectrum of Rhodamine 110 on BK7. The peak in the spectrum can be attributed to the electronic $S_2 \leftarrow S_0$ transition in the dye via resonance enhancement at the SH frequency. The oscillations which are present in the raw data originate from the interference between the SH contributions of the two sides of the substrate (see chapter 6).

From the measured s-SHG spectrum, information about the orientation of the molecules on the substrate can be gained. The transition dipole moment of the $S_2 \leftarrow S_0$ transition lies in the molecular plane of the Rhodamine 110 m olecule. Due to the symmetry considerations presented in chapter 3.3, the presence of the resonance peak in the s-SHG spectrum indicates that the molecules do not lie flat on the surface. If this was the case there would be no component of the transition dipole moment perpendicular to the surface and the transition would be SHG inactive. From their measurements, Shen and co-workers estimated the angle between the surface plane of the substrate and the molecular plane of the Rhodamine molecules to be 34° under the assumption that all molecules are tilted in the same angle. This discussion illustrates the potential of the s-SHG technique in studying molecular orientations of surface adsorbates.

An accurate determination of the surface coverage of the dye for the estimation of the sensitivity of the s-SHG setup was not possible, due to a strong inhomogeneity of the coated dye layer in the presented experiment. However, due to the selection rules of s-SHG only molecules, which are located at the interface region where the substrate has an influence on the electric potential in the adsorbates, are detected. Consequently, the second harmonic signal intensity already reaches its maximum at a single monolayer of the dye molecules. This effect has been shown by Kikteva *et al.* for the laser dye Rhodamine 6G on a fused silica substrate. The observation shows that the s-SHG spectroscopy is sensitive enough to detect sub-monolayer coverages of molecules coated onto a surface. Shen and co-workers measured in their experiment coverages of Rodamine110 molecules corresponding to about 25 % of a monolayer.

7.1.4 Performance of the Spectroscopic Setup

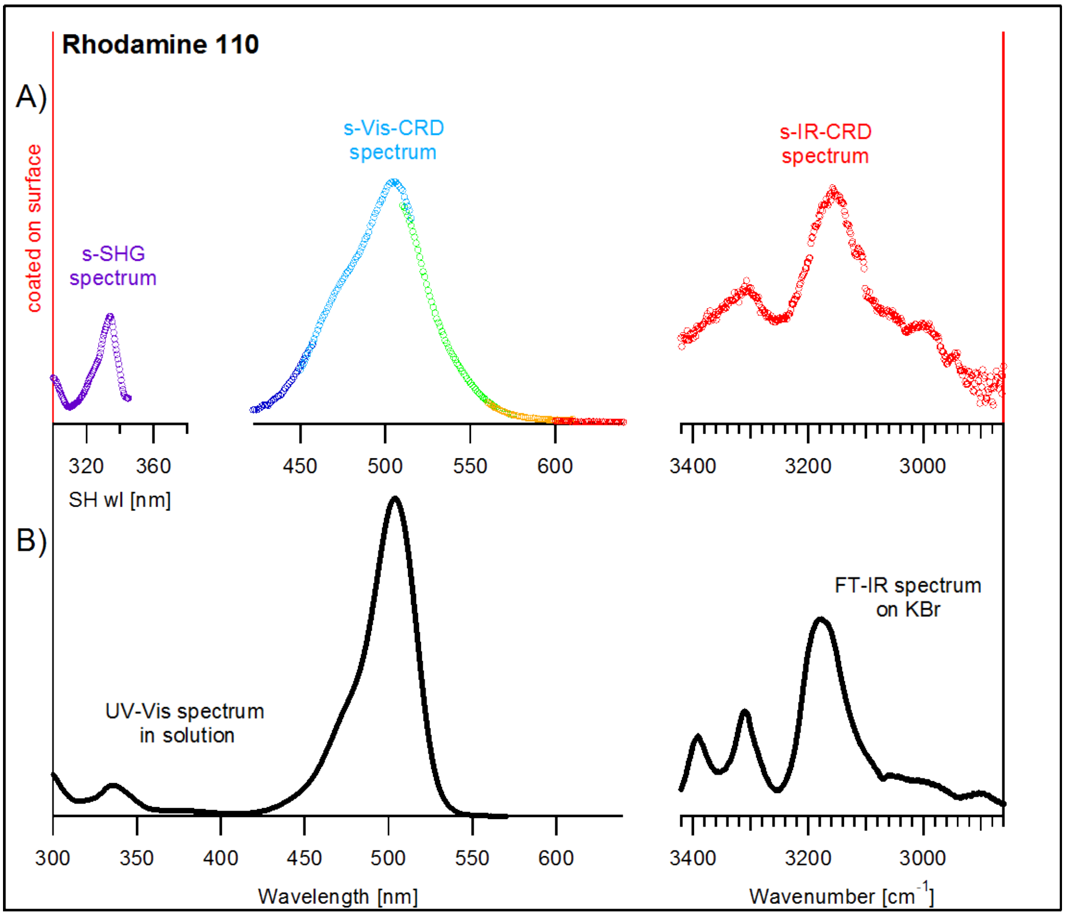

Fig. 7-*10*. Overview plot of Rhodamine 110 spectra. A): Measured spectra of the dye coated on a surface using the three spectroscopic methods of the presented setup. B) Measured spectra using standard techniques.

The measurements of Rhodamine 110 using the three different spectroscopic methods of the presented apparatus give a good overview over the performance of the setup. The laser dye Rhodamine 110 coated onto a surface proved to be an excellent reference sample for the characterization of the entire apparatus. All three spectroscopic methods of the setup are shown to have a sensitivity high enough to detect sub-monolayer coverages of adsorbates on surfaces. Additionally to that, the reliability of the methods could be demonstrated by comparing the obtained spectra with reference spectra using standard spectroscopic methods. All of these results are summarized in figure 7-*10*, where especially the large frequency range is pointed out, in which spectra from the very same sample can be measured.[137]

7.2 Surface Spectroscopy of Binol (1,1'-Bi-2-naphthol)

In order to investigate the sustainability of Binol for the use as ligand molecule in ligand stabilized clusters, its linear and nonlinear spectroscopic properties are investigated using the presented spectroscopic setup. In figure 7-*11*, the chemical structure of Binol is depicted.

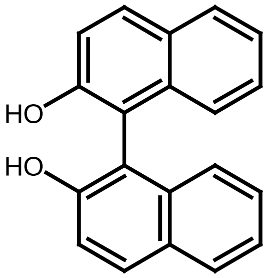

Fig. 7-*11*. Chemical structure of Binol

The organic molecule Binas which is chemically related to Binol (in the former the OH groups are simply replaced by SH groups) has successfully been used as ligand molecule for ligand stabilized clusters in the group of T. Bürgi. In their experiments the chiral properties of Binas were used in order to prepare chiral cluster-ligand complexes which were subsequently characterized using spectroscopic methods.[138-140] In addition to this, Binol was successfully used as coating for the investigation of the nonlinear circular dichroism (CD-s-SHG) using s-SHG spectroscopy.[141] The chirality of Binol (even if no chiral carbon atom is present) originates from the repulsion of the two OH groups leading to a twisted configuration of the molecule. This explains the CD activity of Binol (in Binas a similar situation is present). The extension of the present s-SHG setup in order to perform CD-s-SHG measurements is one of the future projects (see chapter 10.5). All these properties mentioned above make the Binol molecule a good candidate of a suitable ligand molecule for future experiments and is therefore chosen and investigated.

7.2.1 s-IR-CRD Measurement of Binol

For the s-IR-CRD experiment, Binol is evaporated in the transfer chamber on a clean ZrO_2:Y substrate using the installed molecule evaporator (see chapter 4.4). The sample is subsequently transferred into the analysis chamber (under UHV conditions) where the s-IR-CRD measurements are carried out. In figure 7-*12*, the derived spectrum of Binol is shown.

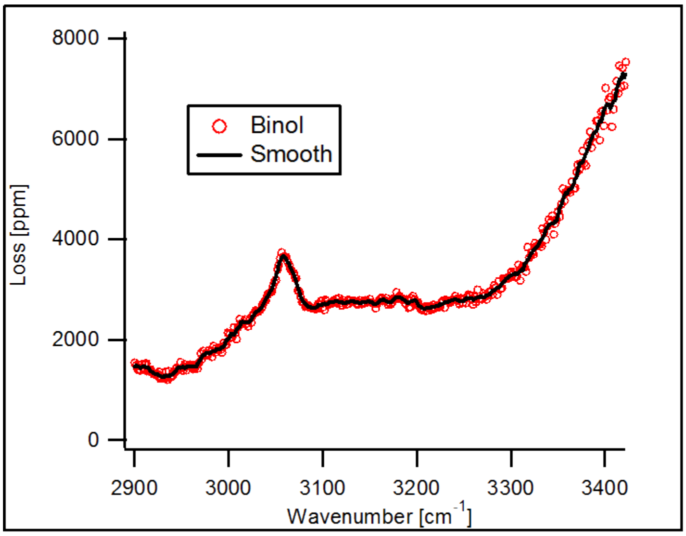

Fig. 7-*12*. s-IR-CRD spectrum of Binol. The absorption band at 3058 cm^{-1} can be attributed to the C-H stretch vibrational mode of the molecule. The increase of the loss towards larger wavenumbers indicates the onset of the O-H vibrational band.

In the spectrum, two features can be observed. The strong increase in loss towards larger wavenumbers can be attributed to the typical broad O-H absorption band located at 3500 cm^{-1}, originating from the two OH groups which are present in the Binol molecule. The second feature is the absorption band of the C-H stretch vibrational mode at 3058 cm^{-1}. For the experiment the sample is cooled to a temperature of 200 K. The reason for this is, that Binol was found not to be stable on the substrate under UHV conditions at room temperature. It evaporates constantly from the sample which can be observed in the results of an additional experiment depicted in figure 7-*13*.

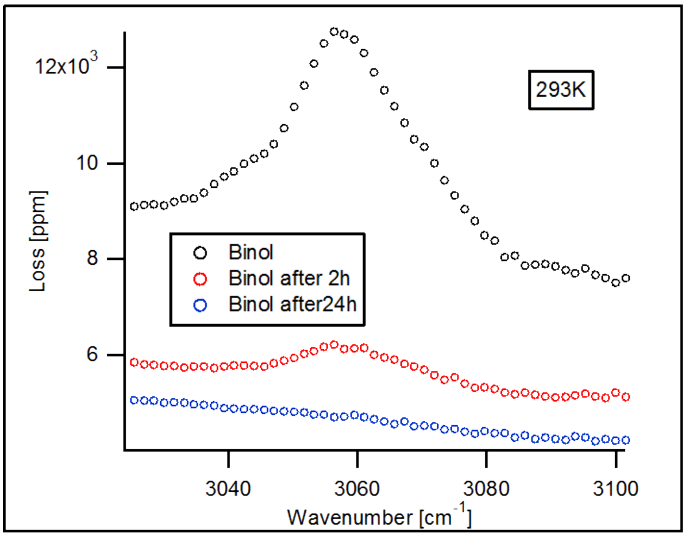

Fig. 7-*13*. s-IR-CRD spectra of Binol measured immediately after the preparation of the sample (black circles), after 2h (red circles), and after 24h (blue circles). It can be clearly observed that Binol evaporates from the substrate within hours if stored at room temperature under UHV conditions.

This measurement is carried out with a freshly prepared Binol sample using s-IR-CRD spectroscopy in the spectral region of the C-H vibrational transition band. Subsequently, the measurement is repeated after two hours and after 24 hours, respectively. After two hours, the absorption peak has already drastically decreased and after 24 hours it is below the detection limit of the spectroscopic setup. The same experiment carried out at a substrate temperature of 200 K shows a much smaller decrease of the peak height with time. In order to investigate this effect in detail, the time evolution of the loss at the peak position is measured. A clean ZrO_2:Y substrate is therefore coated with several monolayers of Binol in vacuum (using the evaporator) and subsequently transferred into the analysis chamber. Here, the height of the C-H peak is measured as function of time using s-IR-CRD spectroscopy, by recording the loss of the sample at 3058 cm^{-1} in defined time intervals. From all measured losses, the loss of the bare substrate is subtracted (for background correction) and the resulting curve is normalized to its initial value. Figure 7-*14* shows the results of the measurement carried out at room temperature (red circles) and at a substrate temperature of 200 K (black circles). In the beginning of the experiments (between 0 m in and 40 m in) an approximately constant evaporation rate of Binol (expressed by the slope of the data points) is measured. This observation can be explained by considering that the number of molecules which are located at the interface to the vacuum remains constant during the evaporation process, as long as there is more than one monolayer of Binol left on the surface. From the slope of the data points in the experiment carried out at room temperature, it can be concluded that the evaporation rate slightly decreases as more time elapses. Here, probably the influence of the substrate can be observed. When the thickness of the Binol layer approaches one monolayer, the energy barrier which has to be overcome by the molecules to evaporate increases due to a stronger binding of the molecule to the substrate. The measurement carried out at 200 K shows that the evaporation rate is highly reduced for the cooled sample. Here, after two hours only 20 % of the Binol has evaporated.

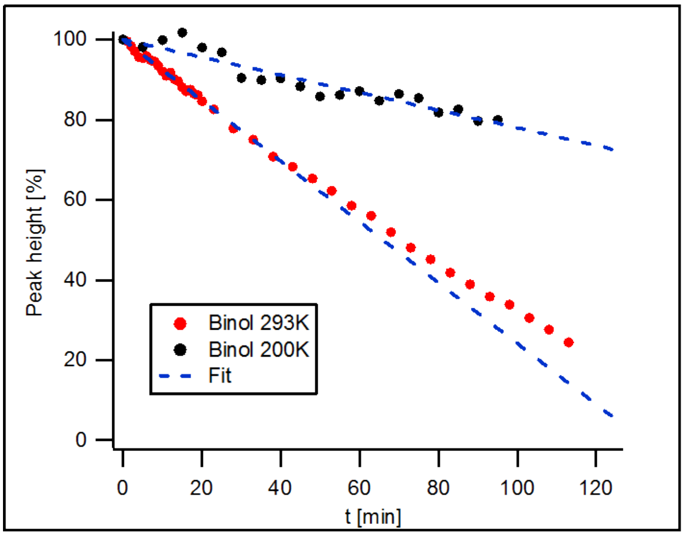

Fig. 7-*14*. Evaporation rates of Binol at room temperature (red circles) and at 200 K (black circles). In the latter case the evaporation rate is reduced.

From the measurements shown in figure 7-*14*, the intermolecular binding energy can be estimated. The relation between the rate constant, *k*, and the temperature, *T*, is described by the Arrhenius law:

$$k = A \cdot e^{-\frac{E_a}{RT}} \quad (eq.7\text{-}05)$$

where, *R*, is the universal gas constant, E_a, the activation energy, and *A*, the prefactor. In the case of an evaporation process, the activation energy equals the intermolecular binding energy. Taking the logarithm of equation 7-05 yields:

$$\ln(k) = \ln(A) - \frac{E_a}{RT} \quad (eq.7\text{-}06)$$

By plotting ln(k) versus *1/RT*, the intermolecular binding energy can be derived from the slope of the resulting curve. This plot is depicted in figure 7-*15*. From the slope, the intermolecular binding energy is calculated to be 6.5 kJ/mol. Because there are only two data points from the measurements available, the result represents just a rough approximation of the real value; however, for Binol where the intermolecular forces consist of dipole-dipole, hydrogen bond, and Van der Waals interactions, this value seems reasonable.

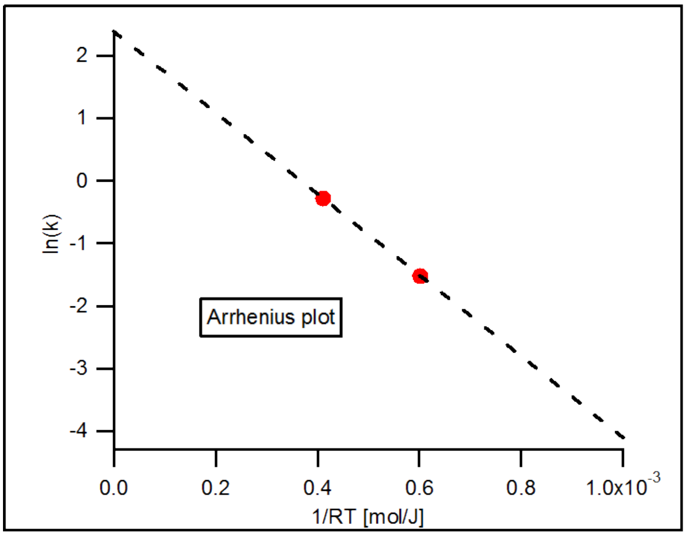

Fig. 7-*15*. Arrhenius plot for the evaporation of Binol from the ZrO_2:Y substrate. From the plot the intermolecular binding energy is calculated to be 6.5 kJ/mol.

By determining the absorption cross section of the C-H stretch vibrational mode for Binol coated on ZrO_2:Y using the method shown in chapter 7.1.2, the coverage of Binol at each point of the evaporation measurement could be determined. Subsequently, these results could be used in order to calculate the binding energy of Binol on the surface as function of coverage. This would give a greater insight into the interactions between Binol and the substrate. However, more detailed experiments would therefore be necessary. The results presented in this section show that Binol can be stabilized on the surface by cooling the sample. Furthermore, it could be shown that by studying the evaporation process using s-IR-CRD spectroscopy, information about binding energies can be gained. The latter could be used in order to determine the binding energies between Binol and supported metal clusters in future experiments.

7.2.2 s-SHG Measurement of Binol

For the s-SHG experiment, Binol is coated onto a BK7 glass substrate and measured under ambient conditions (see chapter 7.3.1). The obtained spectrum is shown in figure 7-*16*. There are two dominant peaks present, which are located at 643 nm and 672 nm of the fundamental frequency, respectively. Furthermore, small features can be observed around 580 nm.

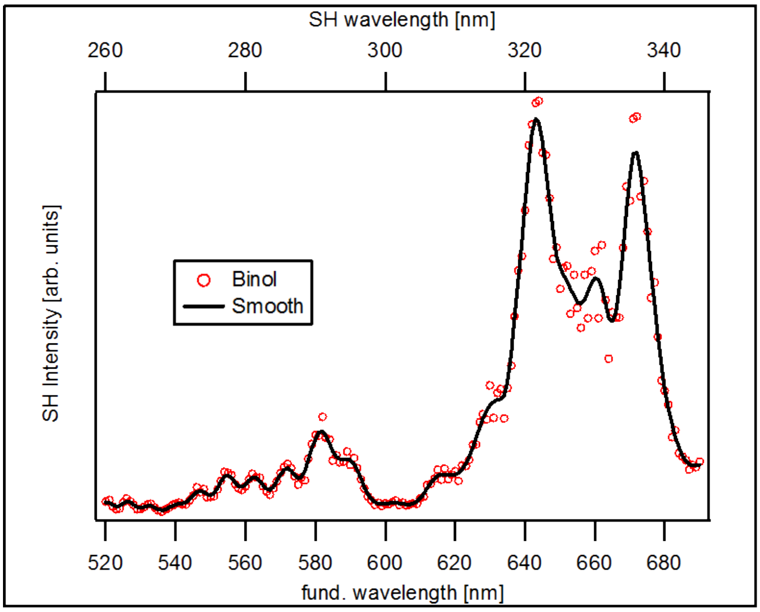

Fig. 7-*16*. s-SHG measurement of Binol on BK7.Two dominant peaks located at 643 nm and 672 nm can be observed. The peaks originate from a resonance at the SH frequency.

Since Binol is fully transparent in the visible range, these s-SHG peaks must originate from resonances at the second harmonic frequency. In order to compare the obtained spectrum with linear spectra, UV-Vis measurements of Binol in different solvents and coated on quartz glass are carried out. The obtained spectra are shown in figure 7-*17*. It can be observed, that all features that are present in the s-SHG spectrum can also be observed in the linear spectra. However, compared to the linear spectrum (especially the spectrum of Binol on quartz glass) the s-SHG spectrum shows much more pronounced peaks. Comparing the spectra of Binol measured in different solvents, it can be observed that the best resolution of the optical features is achieved using the nonpolar solvent cyclohexane. In this spectrum, even the small peak at 327 nm is resolved which suggests that also the corresponding band in the s-SHG spectrum at 330 nm is real (despite the high noise level in the s-SHG raw data in this region).

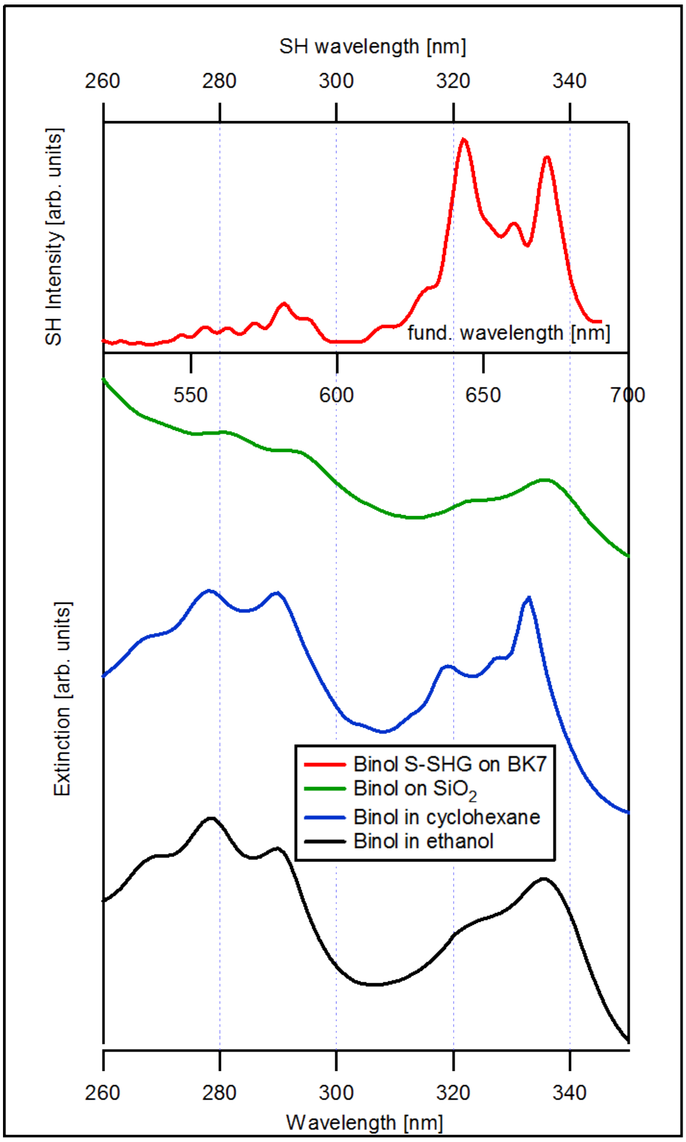

Fig. 7-*17*. Comparison between linear and nonlinear spectra of Binol. In the top part of the figure the s-SHG spectrum of Binol coated on BK7 is shown. The three spectra in the lower part are UV-Vis spectra of Binol in different solvents. The main spectral features can be observed in all measured spectra.

The high accuracy and the good resolution of the peaks in the s-SHG spectra demonstrate the potential of the presented spectroscopic setup to measure even small changes in the nonlinear optical response of organic surface adsorbates. Furthermore, Binol has proven to be an excellent coating reagent for the investigation of surface processes using linear and nonlinear spectroscopic techniques. Consequently, Binol (Binas) is a promising ligand molecule for the preparation and the spectroscopic characterization of ligand stabilized clusters using the presented setup.

7.3 s-SHG Measurement of 4,4'''-Bis-(2-butyloctyloxi)-p-quaterphenyl (BiBuQ)

In order to further investigate the nonlinear optical properties of organic surface adsorbates, a next s-SHG measurement is carried out with a second laser dye (BiBuQ) coated onto a BK7 glass substrate. The purpose of this measurement is to verify, if the generation of the second harmonic in surface adsorbates is restricted to molecules which possess a non centro-symmetric molecule structure (which is the case for Rhodamine 110 and Binol). According to the theory (see chapter 3.3), the presence of the substrate surface should be sufficient to generate a non centro-symmetric electric potential perpendicular to the substrate surface and thus SHG activity, even in molecules with a centro-symmetric molecule structure. Consequently, such a molecule is chosen for the experiment. In figure 7-*18*, the chemical structure of BiBuQ is depicted.

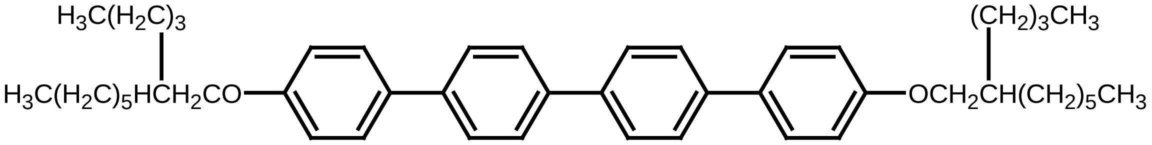

Fig. 7-*18*. Chemical structure of BiBuQ

The dye possesses a very symmetric molecule structure e.g. a center of inversion on the molecular axis. This symmetry leads to a centro-symmetric electric potential in which the π-electros are confined. Any oscillation inside this π-electron system is consequently not SHG active (for the molecule without any external influences). However, in figure 7-*19*, the s-SHG measurement of BiBuQ coated on a BK7 glass substrate is shown and a clear resonance peak can be observed. For comparison, a UV-Vis spectrum of the dye in solution is included in the figure, showing an absorption peak located at the same wavelength. From the resonance position (close to the visible range), it can be concluded that the peak originates from an electronic transition in the π-electron system. Consequently, the observed resonance peak in the s-SHG spectrum corresponds to an oscillation of the π-electrons. From this result it can be concluded, that the centro-symmetry of the electric potential inside the molecule is sufficiently broken by the presence of the surface in order to allow for the generation of the second harmonic frequency. This observation suggests a rather strong impact of the substrate on the π-electron system of the molecule. The s-SHG experiment with the BiBuQ molecule confirms, that in principle any molecule which is coated onto a surface can be investigated using s-SHG spectroscopy. The only condition is, that the transition dipole moment of the measured resonance must have a contribution that is perpendicular to the substrate surface.

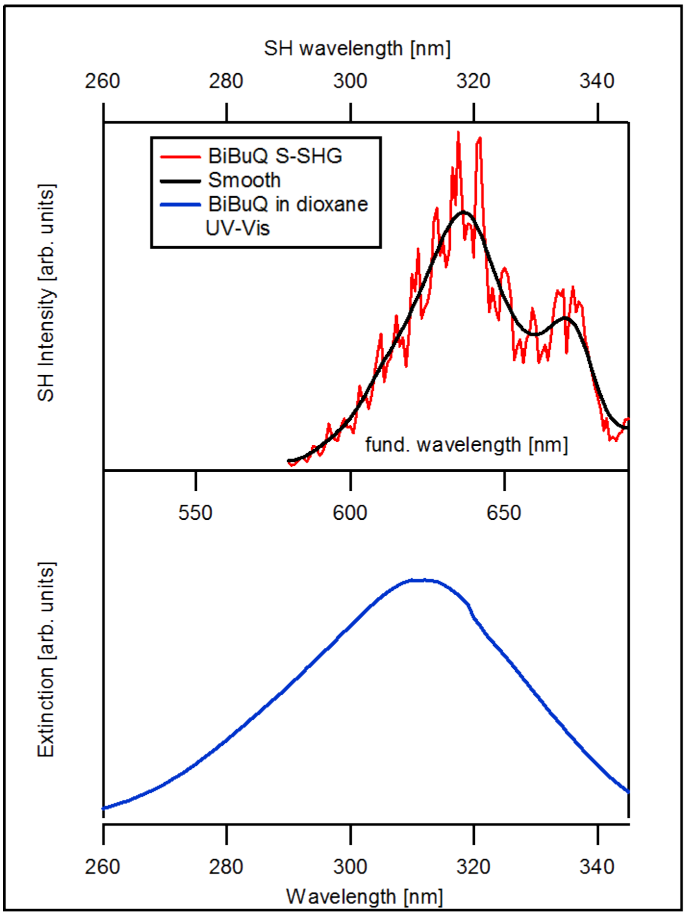

Fig. 7-*19*. In the upper part of the figure the s-SHG spectrum of BiBuQ on BK7 is depicted. In the lower part a UV-Vis spectrum of the dye is shown for comparison. A clear resonance peak can be observed in both spectra.

By comparing the two spectra in figure 7-*19*, a shoulder at approximately 670 nm of the fundamental frequency can be observed in the s-SHG spectrum which is not present in the UV-Vis spectrum. The distance between the main peak and its shoulder corresponds to ~1600 cm^{-1}, which is in the range of the transition energies of vibrational modes in organic molecules. This observation suggests that the shoulder is formed by a combined transition of an electronic and vibrational contribution. Since this spectral feature is not present in the UV-Vis measurement (BiBuQ measured in solution), it is likely that the appearance of the shoulder is caused by surface effects.

7.4 Surface Spectroscopy of {5}Helicene

In a last experiment in this chapter, the spectroscopic properties of {5}Helicene are investigated. Helicenes are polycyclic organic compounds with benzene rings that are connected in the ortho position. It can be synthesized starting from Binol. The chemical structure of {5}Helicene is shown in figure 7-*20*. {5}Helicene molecules are chiral, even if they lack chiral carbon atoms. The chirality is caused by sterical effects, which lead to the formation of a helix structure. Consequently, there are two different enantiomers, Δ and Λ. From X-ray studies of the crystal structure of {5}Helicene, the screw axis was determined to have a pitch of 3.05 Å.[142] This corresponds to a tilt angle of approximately 12 degrees. However, coated on a substrate these values can change due to surface-molecule interactions.

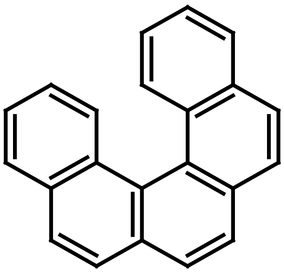

Fig. 7-*20*. Chemical structure of {5}Helicene

In a first step, a UV-Vis measurement of {5}Helicene dissolved in dichloromethane (DCM) is performed. The obtained spectrum is depicted in figure 7-*21*.

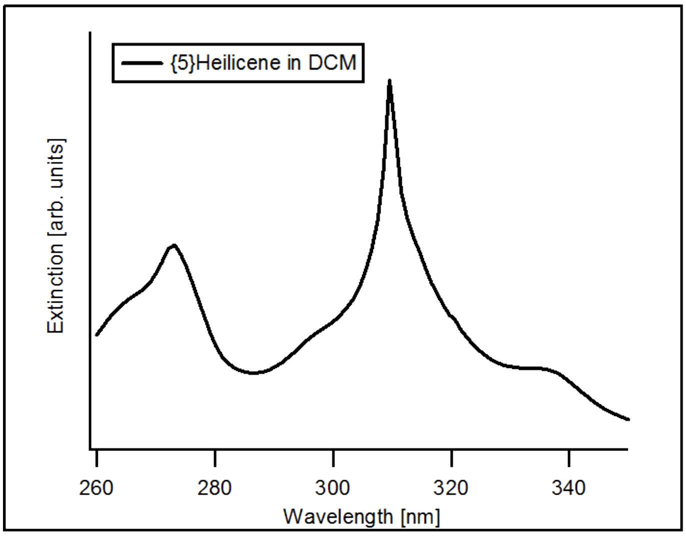

Fig. 7-*21*. UV-Vis spectrum of {5}Helicene in DCM. Two pronounced peaks can be observed at 310 nm and 274 nm, respectively.

Two pronounced peaks can be observed in the spectrum, one at a wavelength of 310 nm, and the second at 274 nm. In a second step, {5}Helicene is coated onto a BK7 substrate and subsequently, an s-SHG spectrum of the sample is measured under ambient conditions. The obtained spectrum does not show any nonlinear activity of the coated molecules. The resonance peaks observed in the UV-Vis spectrum correspond consequently to SHG inactive electron oscillations. This result suggests, that the transition dipole moment of the coated Helicene molecules is parallel to the substrate surface (see previous section). Since the transition dipole moment for transitions in the π- electron system is parallel to the molecular plane, this means that the Helicene molecules must lie flat on the surface of the BK7 substrate. However, this configuration is impossible for helical molecules, unless they are highly flattened by the surface-molecule interactions. As a consequence, we assume the {5}Helicene molecules to be almost planar when coated onto the BK7 substrate. This experiment demonstrates the potential of s-SHG measurements to investigate orientations of molecules on surfaces.

In order to exclude the possibility that {5}Helicene is not stable on the surface, an s-IR-CRD measurement of the molecules coated on ZrO_2:Y is carried out under UHV conditions. The instability of {5}Helicene on the surface could be another reason for the lack of nonlinear activity of the sample. The obtained spectrum is shown in figure 7-*22*. The peak at 3060 cm^{-1} corresponds to the C-H stretch vibrational mode in the Helicene molecule. This confirms, that the Helicene molecules are stable on the substrate even under UHV conditions.

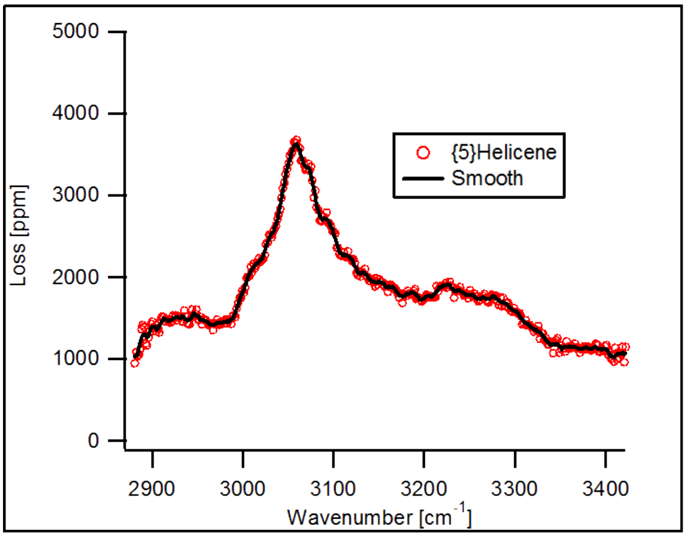

Fig. 7-*22*. s-IR-CRD spectrum of {5}Helicene on ZrO_2:Y. The observed resonance peak (originating from the C-H stretch vibrational mode) confirms the stability of {5}Helicene on a surface.

7.5 Summary Chapter 7

In this chapter, measurements of different organic molecules coated on surfaces were presented. In the first part of the chapter, the reliability and the high sensitivity of the three spectroscopic methods (s-Vis-CRD, s-IR-CRD and s-SHG) could be demonstrated. Therefore, spectra of the laser dye Rhodamine 110 coated onto the surface of a substrate were measured using all the three spectroscopic methods of the presented setup. The obtained results were subsequently compared to spectra which were measured using standard spectroscopic techniques with the result, that the reliability of the methods could be confirmed. Small but significant differences in the obtained spectra could be attributed to surface effects, such as surface-adsorbate interactions. In the following sections, the sensitivity of the three spectroscopic methods was determined using the measured spectra in combination with additional techniques. It could be shown that all three spectroscopic techniques in the presented setup are sensitive enough to study coverages of adsorbates which are far below one monolayer.[137]

In the second part of the chapter, the linear and nonlinear optical properties of the molecules Binol, BiBuQ, and {5}Helicene coated onto a substrate were investigated. The purpose of these measurements were to test their sustainability for the use as ligand molecule for the preparation and spectroscopic characterization of ligand stabilized clusters. It could be shown, that Binol (and/or Binas) is a suitable candidate for such experiments, in particular due to its excellent linear and nonlinear spectroscopic properties when coated onto a surface (well resolved spectra could be obtained using s-IR-CRD and s-SHG spectroscopy). From s-SHG experiments carried out with BiBuQ coated on BK7 it could be learned, that in principle any organic adsorbate molecule can be measured using s-SHG spectroscopy, as long as the orientation of the molecule on the surface allows for the generation of the second harmonic frequency. This dependency of the SHG activity on the molecule orientation could be finally illustrated by measurements with {5}Helicene molecules on BK7. With the measurements carried out in this chapter the potential in surface science could be demonstrated when combining the three highly sensitive spectroscopic methods to investigate surface processes.

8. Supported Clusters

In this chapter, the linear and nonlinear spectra of supported metal clusters are shown and discussed. In the first part of the chapter, it is demonstrated using both, AFM and spectroscopic surface mapping techniques, that clusters can be successfully deposited on substrates that are insulators, that they are generally stable, and that the plasmonic excitations in small non-size-selected clusters (< 2 nm) can be measured using s-SHG spectroscopy. In the second part, the optical properties of silver clusters (non-size-selected and size-selected) are then investigated using both, s-CRD and s-SHG spectroscopy, with the resulting observations compared to a model based on Mie theory. The experiments show a splitting of the plasmon resonance peak which can be attributed to a non-spherical shape of the supported silver clusters. Using s-CRD spectroscopy, the onset of the p-mode plasmon excitation resonance (parallel to the substrate surface) can be observed up to ~2.9 eV for the supported silver clusters, whereas s-SHG spectroscopy is capable of selectively resolving the s-mode plasmon excitation (perpendicular to the substrate surface) at ~3.7 eV. Based on the observations for size-selected silver clusters (Ag_{42}, Ag_{21}, Ag_9, and Ag_1) it will be revealed that by using s-SHG spectroscopy, it is possible to distinguish between supported metal clusters with 3 and 2 dimensional metallic properties.

8.1 Deposition of Metal Clusters on Non-Conducting Substrates

In order to test if the deposition and neutralization of metal clusters on a BK7 glass substrate can be performed using the presented cluster source and neutralization unit, a number of experiments are first carried out for clarification. For detecting the clusters on the surface, three analysis techniques are applied, the Atomic Force Microscopy (AFM), the surface loss mapping using s-Vis-CRD spectroscopy, and an s-SHG intensity surface mapping.

For the first experiment, Rhodium nano-particles are deposited onto a BK7 glass substrate. The deposition is carried out using the RF-only mode (i.e. no single size selection) of the quadrupole mass filter of the cluster source, which is set at a mass of 2000 atomic mass units (amu). In this mode, only clusters with masses above 7/9ths of the chosen value (here 2000 amu) are guided through the filter. The sizes of the deposited clusters using this setting vary between approximately 1 and 3 nm in diameter. The precise size distribution is mainly defined by the settings of the electrostatic elements and the pressure conditions in the cluster source. The total number of deposited Rh clusters amounts to $6 \cdot 10^{13}$. With a spot-size of about 0.1 cm^2 this corresponds to a coverage of few monolayers for the given cluster sizes. In figure 8-*01*, two example AFM images depicting sample/surface roughness are shown, which are measured under ambient conditions. The image on the left side is that of a bare BK7 glass substrate, whereas the image on the right shows the BK7 glass substrate supporting Rhodium nano-particles. By comparing the two images, an increase in the graining of the right AFM image can be observed, indicating that the surface is covered with clusters. This result confirms the successful deposition of Rh clusters. From the height profile of the AFM measurement an average size of roughly 1.6 nm can be extracted.

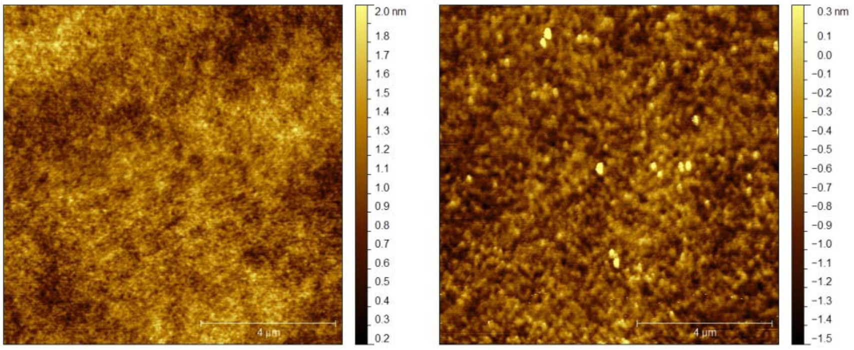

Fig. 8-*01*. AFM images of a bare BK7 glass substrate (left) and supported Rhodium nano-particles (right). The coverage is above one monolayer. The increase in the graining of the right AFM image shows that the surface is covered by clusters with a height of approximately 1.6 nm.

For a second experiment using the s-Vis-CRD surface loss mapping technique, gold nano-particles are deposited under UHV conditions on a BK7 substrate using again the RF-only mode of the quadrupole mass filter of the cluster source at 2000 amu. Here, the surface coverage of clusters is about one monolayer. A surface loss mapping of the substrate is carried out at a wavelength of 520 nm before and after the deposition. In a further step, the clusters are removed from the surface by sputtering with Ar ions (see chapter 6.4.2) for 10 minutes at an ion energy of 500 eV, followed by a third s-Vis-CRD surface loss mapping. The results are shown in figure 8-*02*. In image (A), the surface loss mapping of the bare substrate before cluster deposition is depicted. Images (B) and (C) are taken after the deposition and after the removal of the particles by sputtering, respectively. In images (D) and (E), the differences (B) - (A), and (C) - (A) are plotted. The cluster spot is well resolved and shows an increased loss of approximately 500 ppm (image (D)). After sputtering, the clusters are completely removed from the surface and even the characteristic features of the sample in picture (A) can be found in (C). This shows that the removal of the clusters leaves the substrate almost unchanged, and only a slight increase in overall loss is observed, which is attributed to the roughening of the surface induced by the ion sputtering. These results are published in.[60]

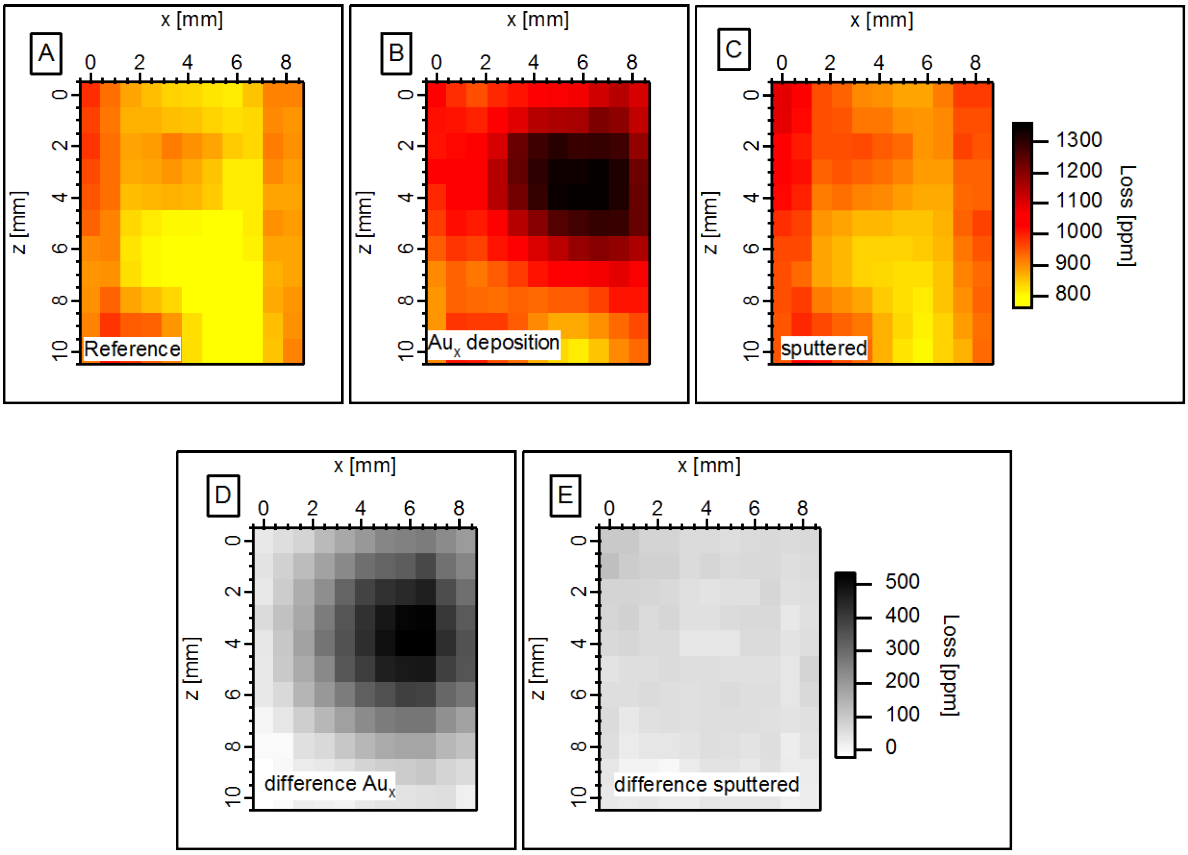

Fig. 8-*02*. s-Vis-CRD surface loss mapping of the bare BK7 glass substrate (A), after deposition of gold nano-particles (B) and after the removal of the particles by sputtering (C). In image (D) and (E), the differences (B) - (A) and (C) - (A) are depicted.

An s-SHG intensity surface mapping of a similar sample with a comparable coverage of gold nano-particles is shown in figure 8-*03*. Here, the intensity of the second harmonic signal at a fundamental wavelength of 560 nm is recorded as a function of the substrate position. In this experiment p-polarized laser light is used with an azimuth substrate angle of 45°. For all s-SHG experiments it is crucial that the clusters are deposited on the backside of the substrate, because the sample would otherwise absorb the SH contribution of the clusters in the wavelength region where the substrate is not transparent to the SH frequency. Figure 8-*03* shows that also in the s-SHG intensity surface mapping the cluster spot can be clearly identified from the strong increase of SH intensity at its position. Due to the huge intensity difference between the regions with and without gold nano-particles, the s-SHG intensity surface mapping technique is nearly background free and is a highly precise tool for mapping the spatial distribution of metal particles on surfaces. At the coordinates, x = 7.5; z = 7, in the plot a drop in SH intensity compared to the intensity at the surrounding pixels can be observed. This is the position at which a s-SHG spectrum was recorded before, suggesting that the clusters are partly evaporated from the surface at this position, which is likely to be induced by the strong laser radiation. However, considering that the fundamental laser wavelength of 560 nm lies close to the position of the surface plasmon resonance of gold nano-particles, the clusters are surprisingly stable.

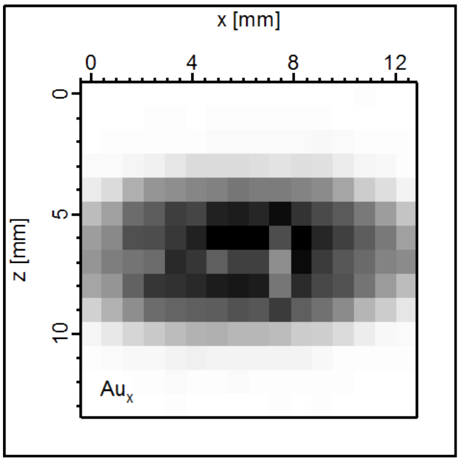

Fig. 8-*03*. s-SHG intensity surface mapping of gold nano-particles deposited on a BK7 glass substrate. The cluster spot in the middle of the substrate is well resolved.

All these three experiments clearly show a successful deposition of metal clusters on the BK7 glass substrate, either by means of an increase in surface roughness (AFM), the increase of the absorption loss (s-Vis-CRD), or the enhancement of the SH signal (s-SHG). Furthermore, the surface mapping techniques (s-Vis-CRD and s-SHG) proved to be a powerful tool in order to measure the spatial distribution of clusters deposited on a substrate. The determination of the spatial distribution of clusters on a surface is necessary in order to calculate the surface coverage of the clusters. The latter is needed for any kind of calculation of cluster-cluster interaction, which influences their electronic properties.

8.2 Supported Coinage-Metal Clusters

Following the theoretical formulation of the nonlinear optical properties of deposited metal nano-particles in chapter 3.3, it should be possible to measure the plasmon excitation of coinage metal clusters using s-SHG spectroscopy. For particles that are small compared to the wavelength of the laser light, the only SHG active oscillation mode is the dipole oscillation of the particle which is perpendicular to the surface. Only the p-polarized fundamental laser light, therefore, can give rise to an enhanced SH signal. The positions of the plasmon frequencies can be approximated from the calculation of the linear optical spectra for spherical gold, silver and copper clusters using the Mie theory for small particles (for details see chapter 3.1.2). The absorption cross section, σ_{abs}, can be expressed as:

$$\sigma_{abs} = 9\frac{\omega}{c_0}\varepsilon_m^{3/2}V_0\frac{\varepsilon_2(\omega)}{[\varepsilon_1(\omega)+2\varepsilon_m]^2+\varepsilon_2(\omega)^2} \qquad (eq.8\text{-}01)$$

whereby, V_0, is the particle volume, and c_0, is the speed of light in vacuum. The dielectric functions of the metals $(\varepsilon_1(\omega), \varepsilon_2(\omega))$ for the calculations, meanwhile, are taken from the measured bulk data obtained by Johnson and Christy.[76] For the dielectric constant of the surrounding medium, the value $\varepsilon_m = 1.63$ is used, representing the mean value between vacuum ($\varepsilon_v = 1$) and the BK7 glass substrate $(\varepsilon_s = 2.25)$.

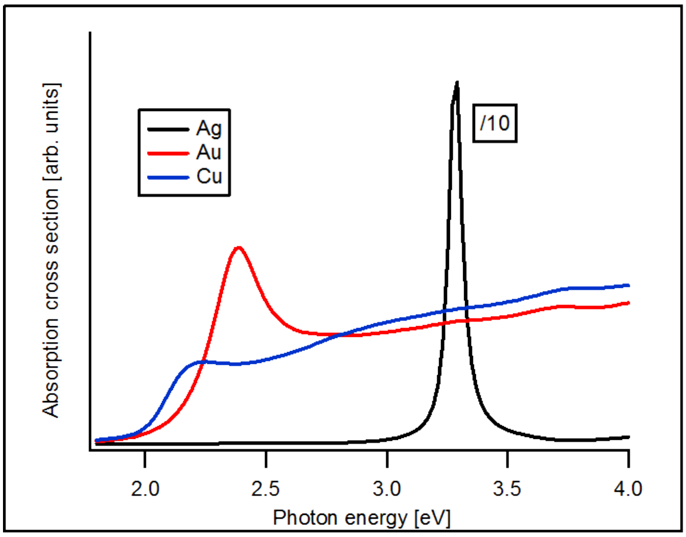

Fig. 8-*04*. Calculated absorption spectra of Ag, Au and Cu nano-particles using Mie theory for particles that are small compared to the wavelength of the laser light. Each metal cluster shows a characteristic plasmonic excitation band.

In figure 8-*04*, the resulting calculated absorption spectra for the metals Au, Ag, and Cu are shown. For a better comparability of the presented cluster spectra with spectra found in the literature, the energy unit of eV for the photon energy will be utilized throughout this chapter. All three metals show a characteristic plasmon absorption band. For gold clusters the plasmon excitation is located around 2.37 eV and for copper a very broad peak is located at 3.1 eV which is almost not visible. The reason for the small plasmon peak in copper clusters is the strong interband absorption in this frequency range (see chapter 3.1.2). The most pronounced plasmon peak can be found for silver clusters (at 3.3 eV), which is about 20 times higher in intensity than that of gold. Since in s-SHG spectroscopy resonances at the fundamental as well as at the second harmonic frequency can be probed (measurable range: fundamental, 1.38 eV - 2.76 eV → SH, 2.76 eV - 5.52 eV), all three plasmon resonances lie within the applicable range of the spectrometer. Consequently, all three samples should show a peak in their s-SHG spectra.

8.2.1 Data Treatment for s-SHG Measurements

In order to perform the correct data treatment of the s-SHG measurements of supported metal clusters, some theoretical considerations must first be made. As shown in chapter 6.5.2, the s-SHG spectrum of the bare BK7 glass substrate can be described by the superposition of the SH contributions of the two surfaces (in the wavelength range where the substrate is transparent to the second harmonic frequency). In the case of a substrate with deposited clusters, a third SH contribution coming from the metal particles must be introduced in the equations. Following the nomenclature in chapter 6.5.2, the intensity, ${I_{(\lambda)}}^{(SHG)}$, of the generated SH beam can be expressed as follows:

$$
\begin{aligned}
{I_{(\lambda)}}^{(SHG)} = Y_{(\lambda)} \cdot [A_{(\lambda)} \cdot e^{i2\omega t} + T_{(\lambda)} \cdot A_{(\lambda)} \cdot e^{i2\omega(t+\zeta)} + B_{(\lambda)} \cdot e^{i(2\omega t+\varphi_{(\lambda)})}] \cdot \\
[A_{(\lambda)} \cdot e^{-i2\omega t} + T_{(\lambda)} \cdot A_{(\lambda)} \cdot e^{-i2\omega(t+\zeta)} + B_{(\lambda)} \cdot e^{-i(2\omega t+\varphi_{(\lambda)})}]
\end{aligned}
$$

$$
\begin{aligned}
\Rightarrow {I_{(\lambda)}}^{(SHG)} = Y_{(\lambda)} \cdot \{ {A^2}_{(\lambda)}[1 + {T^2}_{(\lambda)} + 2T_{(\lambda)} \cdot \cos(2\omega \cdot \zeta)] + {B^2}_{(\lambda)} \\
+2A_{(\lambda)}B_{(\lambda)} \cdot [\cos\varphi_{(\lambda)} + T_{(\lambda)} \cdot \cos(2\omega \cdot \zeta - \varphi_{(\lambda)})]\} \qquad \textit{(eq.8-02)}
\end{aligned}
$$

where, $Y_{(\lambda)}$, describes the spectrometer function, ${T^2}_{(\lambda)}$, is the transmittance of the sample, and ζ, the time delay between the SH beam from the first surface and the fundamental beam when they arrive at the second surface. $A^2_{(\lambda)}$ and $B^2_{(\lambda)}$, are the SH conversion efficiencies of the substrate and the metal clusters, respectively, and are proportional to the second order susceptibilities. The phase angle, $\varphi_{(\lambda)}$, describes a possible phase shift between the fundamental beam and the SH beam generated from the clusters and is wavelength dependent. The value of interest in the s-SHG measurements of deposited metal clusters is $B^2_{(\lambda)}$, because it describes the nonlinear response of the particles. In order to extract this value from equation 8-02, the pure substrate contribution must be removed. This can be done by subtracting the measured curve, $I_{(\lambda)}^{(SHG,\,\text{reference})}$, of a reference point without clusters, giving:

$$I_{(\lambda)}^{(SHG)} - I_{(\lambda)}^{(SHG,\,\text{reference})} = Y_{(\lambda)} \cdot \{B^2_{(\lambda)} + 2A_{(\lambda)}B_{(\lambda)} \cdot [\cos\varphi_{(\lambda)} + T_{(\lambda)} \cdot \cos(2\omega\cdot\zeta - \varphi_{(\lambda)})]\} \quad \textit{(eq.8-03)}$$

From the reference spectrum, the spectrometer function, $Y_{(\lambda)}$, can be derived (see chapter 6.5.2). Dividing equation 8-03 by $Y_{(\lambda)}$ and removing the oscillating part, $\cos(2\omega\cdot\zeta - \varphi_{(\lambda)})$, by applying a smoothing procedure yields:

$$\left\{\frac{I_{(\lambda)}^{(SHG)} - I_{(\lambda)}^{(SHG,\,\text{reference})}}{Y_{(\lambda)}}\right\}_{\text{smooth}} = B^2_{(\lambda)} + 2A_{(\lambda)}B_{(\lambda)} \cdot \cos\varphi_{(\lambda)} \quad \textit{(eq.8-04)}$$

In most of the cases shown later in this chapter, the SH contributions of the metal particles is one or more orders of magnitude larger than that of the substrate. Consequently, it can be written:

$$\left\{\frac{I_{(\lambda)}^{(SHG)} - I_{(\lambda)}^{(SHG,\,\text{reference})}}{Y_{(\lambda)}}\right\}_{\text{smooth}} \approx B^2_{(\lambda)} \ \text{ for } B_{(\lambda)} \gg A_{(\lambda)} \quad \textit{(eq.8-05)}$$

The subsequently derived spectrum gives the nonlinear response function of the clusters. The data treatment procedure shown here is applied to all s-SHG measurements throughout this chapter. Consequently, one s-SHG experiment always consists of the measurement of two different positions on the sample, one at the cluster spot position and one at a reference point which is far from the deposited metal particles. Here it should be mentioned that due to the wavelength dependency of the laser power all measured SH intensities must be corrected by the square of the fundamental pulse energy, which is measured simultaneously using a photo diode (see chapter 5.2). The absolute values for $B^2_{(\lambda)}$ which are plotted in the s-SHG spectra in this chapter are relative SH intensities, giving the number of SH photons generated by the clusters per SH photon coming from the second surface of the bare substrate. In order to derive absolute values for the intensity, the spectrometer function would have to be known, however, because the latter is calculated on basis of the spectrum of the reference point (see chapter 6.5.2) only the product $Y_{(\lambda)} \cdot A^2_{(\lambda)}$ is determined. Consequently, the function which is used in the data treatment for $Y_{(\lambda)}$ is only proportional to the real spectrometer function. The factor of proportionality is $A^2_{(\lambda)}$, which could be shown to be approximately constant over the applied wavelength range (chapter 6.5.2) and can thus be taken as constant. Because throughout this chapter all experiments are carried out using the BK7 glass substrate the absolute values of the relative SH intensities can be used to directly compare different spectra. One important result of the calculations above is that the measured s-SHG spectra using such a thin substrate contain phase information of the oscillating nonlinear dipole in the cluster with respect to the oscillation at the surface of the substrate. This means that the nonlinear spectrum and the phase of the nonlinear oscillation can be measured in one single experiment. However, to precisely determine the phase shift, it must be ensured that the two measured spots on the substrate have exactly the same nonlinear properties, especially the same substrate thickness, and finally the azimuth substrate angle must be equal for both positions. Here, temperature gradients on the sample can already lead to huge differences in the measured phase shift. In equation 8-02, only the superposition of the three different contributions to the SH signal induced by the fundamental laser radiation is considered, and not the interaction between the local fields of the metal particles and the surface. The excitation of a plasmon in a metal can lead to a strong enhancement of the local field, known as Plasmon Field Enhancement (PFE).[120-125] However, for the measurements of silver clusters presented later, small coverages are used which should minimize this contribution. For all other experiments the approximation shown above is sufficient to describe the main features of the spectra as shown in the remainder of this chapter.

8.2.2 s-SHG Measurements of Supported Coinage-Metal Clusters

For the measurement of the s-SHG spectra of supported coinage metal clusters, the metal particles are deposited under UHV conditions onto the backside of a BK7 substrate. Again, the RF-only mode of the quadrupole mass filter set at 2000 amu is used to prepare the non-size-selected cluster sample. The coverage of the particles on the BK7 substrate amounts to approximately one monolayer. In a second step, s-SHG measurements on both, the position where the clusters are deposited and on a reference position on the substrate are carried out for each experiment, with the substrate positioned at Brewster's angle. The resulting spectra are shown in figures 8-*05* to 8-*07*. In all three spectra (Cu, Ag and Au), a clear peak is observed, which can be attributed to the plasmon excitations of the different metals. In figure 8-*05*, the plasmon excitation of copper nano-particles is measured at a fundamental photon energy of 2.01 eV. Compared to the calculated value (see section 8.2) of 3.1 eV, however, its resonance position is shifted by approximately 1 eV. A reason for this large shift could not be found. The measurement shows that a plasmon resonance is excited at either 2.01 eV (corresponding to a SHG enhancement via resonance at the fundamental frequency) or at 4.02 eV (corresponding to a SHG enhancement via resonance at the SH frequency). However, the sample proved to be highly instable which could be observed by repeating the measurement. The relative SH intensity highly decreases for each additional scan. Possible reasons for the instability are photo damage of the sample by the laser radiation, or oxidation processes of the copper clusters. Due to this instability further s-SHG experiments with supported copper clusters were not carried out.

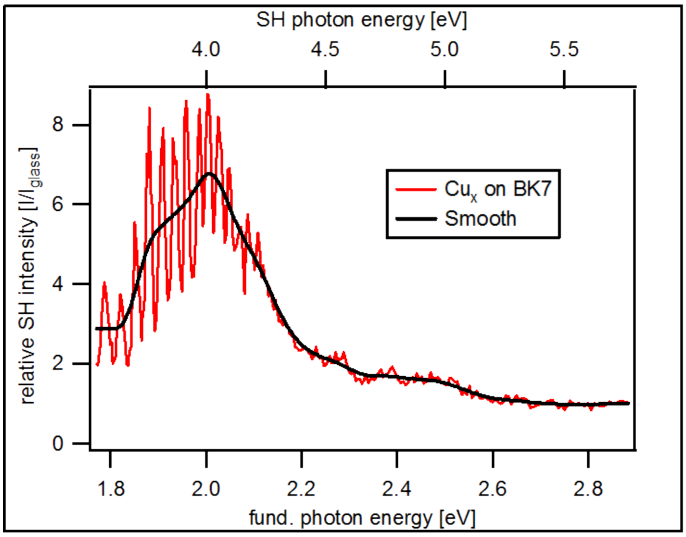

Fig. 8-*05*. s-SHG spectrum of Cu nano-particles on BK7.The surface coverage is approximately one monolayer. Particle size: between 1 and 3nm.

The oscillation of the SH signal on the low energy side of the spectrum (<2.1 eV) is the interference pattern which is predicted by equation 8-03. It is the interference between the SH-signal of the first surface of the substrate and the SH contribution of the clusters; it is described by the expression $\cos(2\omega\cdot\zeta-\varphi_{(\lambda)})$.

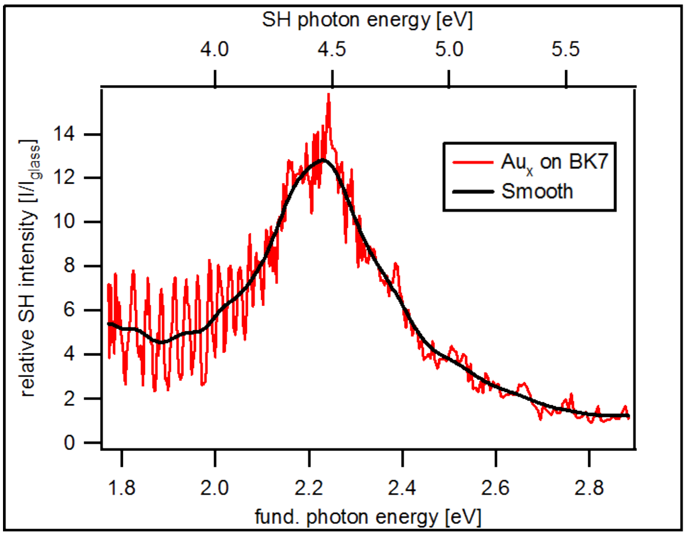

Fig. 8-*06*. s-SHG spectrum of Au nano-particles on BK7. The surface coverage is approximately one monolayer. Particle size: between 1 and 3nm. The SH intensity maximum at 2.23 eV is induced by the plasmon resonance in the supported Au particles at the fundamental frequency.

Figure 8-*06* shows the s-SHG spectrum of gold nano-particles on BK7. The plasmon excitation is measured at a fundamental photon energy of 2.23 eV. The comparison to the calculated value of 2.37 eV shows that this SH enhancement originates from a resonance at the fundamental laser frequency. The sample with the gold clusters shows a much higher stability than the copper sample, a photo damage could, however, be observed in the s-SHG intensity surface mapping in figure 8-*03*. Compared to the calculated value of the plasmon resonance position for supported Au clusters, the measured value is red shifted by 0.14 eV. As discussed in chapter 3, the position of the plasmon peak in metal particles depends on size, shape, and electrical environment of the metal particle. In the present calculation the dielectric influence of the substrate is approximated by taking the mean value $\varepsilon_m = 1.63$ (see chapter 8.2). The validity of this approximation is the first possible source for the observed discrepancy. Red shifts of the plasmon resonances can also be observed for clusters which are either larger than ca. 20 nm in diameter or for small clusters that are smaller than 10 nm. In the first case retardation effects occur and the excitation of electrical multipoles comes into play. The dipole approximation (eq. 8-01) is consequently not valid, and an increasing red shift of the resonance with growing particle size is the result. In the case of very small clusters, the plasmon resonance is red shifted if the size is smaller than the free mean path of the conducting electrons in the bulk metal (free mean path effect, see chapter 3.1.5). Here equation 8-01 remains valid but the dielectric function of the cluster changes. This effect leads

to an increasing red shift and a broadening of the plasmon peak with decreasing cluster size. The Au and Cu clusters deposited with an average size of about 1.6 nm are highly influenced by the free mean path effect and consequently, this effect may indeed explain the observed red shift of the plasmon peak. The second possibility to explain the red shift (the formation of larger Au clusters via agglomeration), however, seems improbable because final cluster sizes of several tens of nanometers would therefore be necessary. A mathematical correction of the dielectric function of the clusters in order to account for the free mean path effect, meanwhile, is rather challenging for gold and copper clusters because their dielectric functions are highly influenced by interband absorptions in the frequency region of the plasmon excitation. Such a correction is consequently not carried out in the framework of this thesis. In figure 8-*07*, the s-SHG spectrum of Ag nano-particles on BK7 is depicted. Here, the plasmon excitation is measured at a photon energy of 1.85 eV. The calculated energy of 3.3 eV is far from the measured value, however, by taking the SH photon energy axis the former is close to the measured resonance position with a value of 3.7 eV. This indicates that the SHG enhancement for Ag clusters is induced by a plasmon resonance at the second harmonic frequency rather than at the fundamental. Here, the measured energy is blue shifted by 0.4 eV with respect to the calculation. For silver clusters, shape effects have an enormous influence on the position of the plasmon frequency which can explain this shift. These considerations are shown in the following sections.

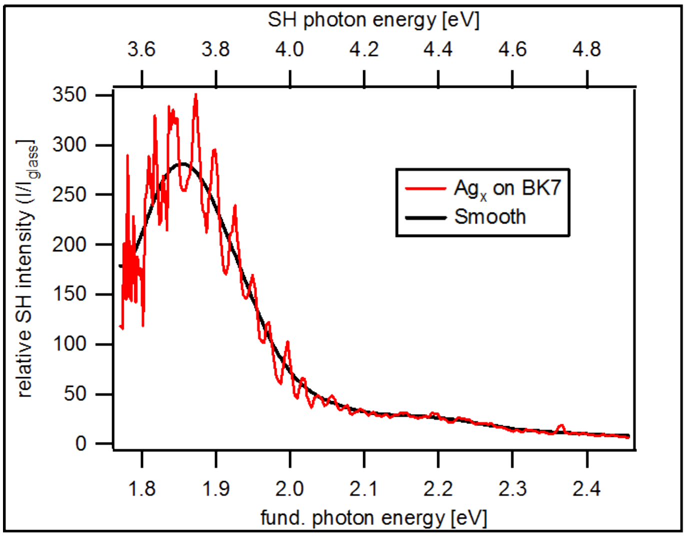

Fig. 8-*07*. s-SHG spectrum of Ag nano-particles on BK7. The surface coverage is approximately one monolayer. Particle size :between 1 and 3nm. The SH intensity maximum at 1.85 eV is induced by the plasmon resonance in the supported Au particles at the SH frequency. The plasmon excitation resonance of the supported Ag particles is consequently located at 3.7 eV.

In figure 8-*08*, the smoothed spectra of all three metal clusters are plotted for comparison. One remarkable observation is that the ratios of the peak heights of the plasmon excitations in the s-SHG spectra closely match the ratios of the peak heights in the calculated linear spectra in figure 8-*04* (notice, that the SH signal intensity for Ag is more than one order of magnitude greater than for Cu or Ag in the calculation as well as in the s-SHG measurement). Also, the plasmon peak of silver clusters has the highest intensity and the lowest width at half maximum. Furthermore, the silver plasmon excitation in the s-SHG spectrum originates from the resonance at the second harmonic frequency, whereas the absorption of the clusters at the fundamental frequency (1.85 eV) is expected to be nearly zero (see calculated spectrum in figure 8-*04*). This minimizes the risk of photo damage (induced desorption) of the clusters because the energy transfer from the highly intense laser beam into the clusters is small. These properties of supported silver clusters are crucial advantages for the use in s-SHG experiments. Furthermore, the mathematical description of the size and shape effects on the optical properties of silver clusters is well developed, which makes the further investigation of supported silver clusters using s-SHG spectroscopy initially the most promising of the coinage metals. Further investigations on the influence of the size and shape of clusters on the linear and nonlinear optical properties focus therefore on silver particles and are described in the following sections.

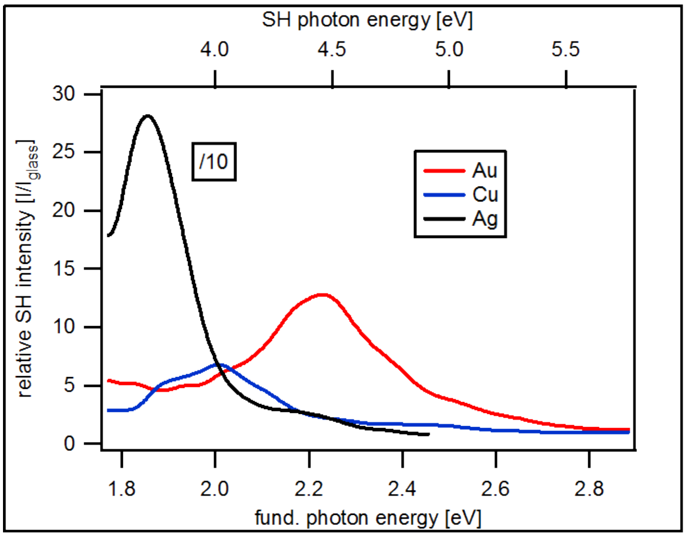

Fig. 8-*08*. Comparison of the smoothed s-SHG spectra of Cu, Ag and Au nano-particles. The ratios of the peak maxima (maxima of the SH intensities) between the different metals closely match the ratios obtained by the calculated linear spectra in figure 8-*04*.

8.3 Origin of the SH Contribution of Supported Metal Clusters

From theoretical considerations it can be learned that the only SHG active contribution of supported metal clusters originates from the oscillation that is perpendicular to the surface (see chapter 3.3). This can be verified by measuring the angular dependency of the SH intensity generated by the supported particles, and comparing the resulting data points with a curve which is calculated on basis of this assumption. The calculation is very similar to that of the angular dependency of the SH intensity for the bare BK7 substrate (see chapter 6.5.1) because there also the only SH active oscillation was assumed to be the oscillation which is parallel to the surface normal. In chapter 6.5.1, the following equation was derived (eq.6-18):

$$I_{(2\omega)} \sim (1-R_{(2\omega)}) \cdot I^2_{(\omega)} \cdot \sin^4 \alpha \quad \textit{(eq.8-06)}$$

where, $I_{(\omega)}$, is the intensity of the fundamental beam, α, the azimuth substrate angle, and $R_{(2\omega)}$, the reflectivity of the SH beam at the surface (for the SH beam coming from the inside of the substrate). In the case of clusters deposited on the backside of the sample, the only difference is that no reflections of the SH beam occur at the surface because it is generated outside the substrate (by the cluster). Considering that, equation 8-06 is simplified to give:

$$I_{(2\omega)} \sim I^2_{(\omega)} \cdot \sin^4 \alpha \quad \textit{(eq.8-07)}$$

In chapter 6.5.1, the calculation of the Intensity, $I_{(\omega)}$, of the fundamental beam is done for the position inside the substrate, P$_1$, giving:

$$I_{(P1)} = (1-R_p^{\,*}) \cdot A^2 \cdot \left[\sum_{n=0}^{m} R_p{}^n e^{i\omega[t+(m-n)\delta+n\Delta]}\right] \cdot \left[\sum_{n=0}^{m} R_p{}^n e^{-i\omega[t+(m-n)\delta+n\Delta]}\right] \quad \textit{(eq.8-08)}$$

However, for the cluster sample the intensity, $I_{(\omega)}$, must be derived for a position behind the substrate. Consequently, an additional transmission process at the second surface must be included in equation 8-08. Following the notation which is used in chapter 6.5.1, this can be done by multiplying equation 8-08 with the transmittance factor $(1-R_p)$, resulting in:

$$I_{(\omega)} = (1-R_p) \cdot (1-R_p^{\,*}) \cdot A^2 \cdot \left[\sum_{n=0}^{m} R_p{}^n e^{i\omega[t+(m-n)\delta+n\Delta]}\right] \cdot \left[\sum_{n=0}^{m} R_p{}^n e^{-i\omega[t+(m-n)\delta+n\Delta]}\right] \quad \textit{(eq.8-09)}$$

Combining equations 8-09 and 8-07, the angular dependency can be subsequently calculated.

For the measurement of the angular dependency of the SH intensity generated by supported metal clusters, approximately one monolayer of Pd nano-particles is deposited onto the backside of a BK7 glass substrate using the RF-only mode of the quadrupole mass filter set at 2000 amu. The SH intensity of the sample is subsequently recorded as function of the azimuth substrate angle at a wavelength of the fundamental laser beam of 560 nm. At this wavelength the measured relative SH intensity at the cluster spot is approximately 50, which means that the contribution of the substrate to the SH intensity is negligible. The results of the s-SHG measurement and the calculated curve are depicted in figure 8-*09*. The calculation is in a good agreement with the measured data points, indicating that the assumptions which the calculation is based on are correct. In particular, the assumption that the only SHG active oscillation mode inside a supported metal particle is the mode that is perpendicular to the substrate surface is clearly confirmed.

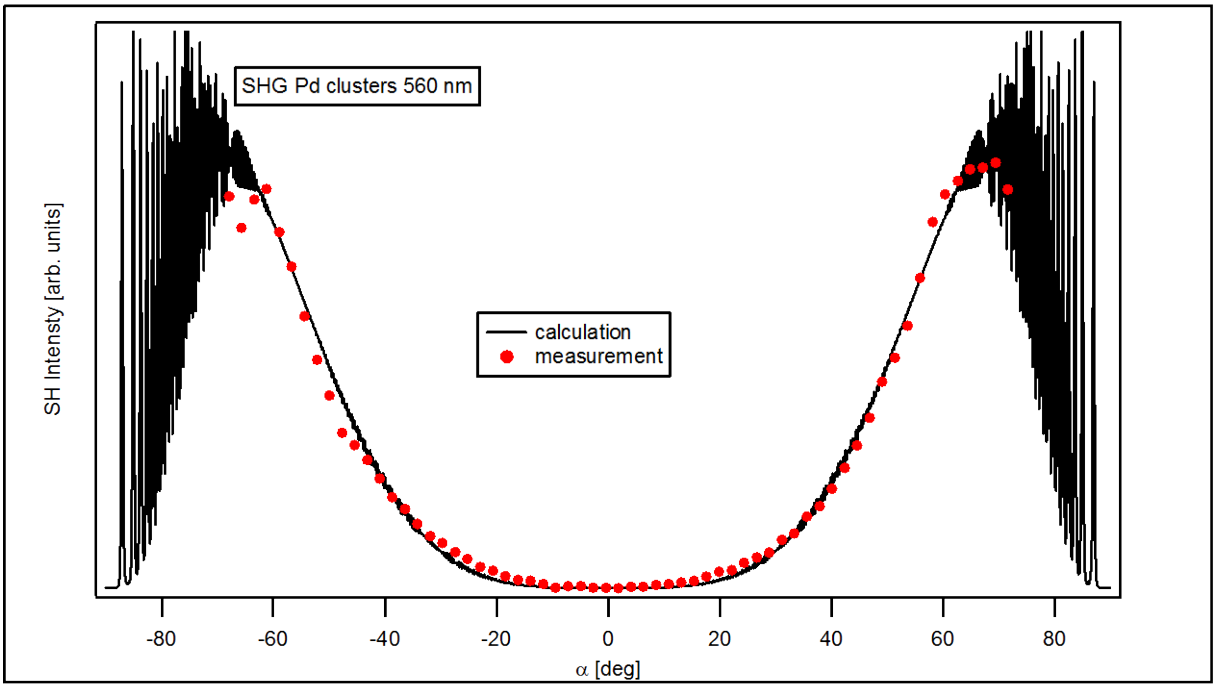

Fig. 8-*09*. Angular dependency of the SH intensity generated by Pd nano-particles (red dots) and calculation (black line). Note that the calculated curve consists of a limited number of data points leading to a not sufficient sampling. Fit parameters used for the calculation: substrate thickness d = 130 µm, $n_\omega = 1.518$, $\lambda = 560$ nm. The calculated curve is in a good agreement with the measured data points. Consequently, the assumption that the only SHG active oscillation inside the metal particles is the oscillation mode that is perpendicular to the substrate surface is clearly confirmed.

8.4 Shape Effects in the Plasmon Resonance of Silver Nano-Particles

In order to further investigate the linear and nonlinear optical properties of supported silver nano-particles, non-size-selected (RF-only mode) Ag clusters are deposited onto the backside of a BK7 substrate under UHV conditions. The sample is cooled to approximately 120 K during the deposition and the measurements to avoid an agglomeration of the clusters. The total number of deposited clusters is approximately $4.28 \cdot 10^{12}$. In a first experiment, the cluster coverage is determined by measuring the spatial distribution of the particles on the surface. In the following, s-Vis-CRD and s-SHG spectra of the sample are recorded and discussed. Furthermore, the stability of the clusters on the substrate is investigated using s-SHG spectroscopy.

8.4.1 Determination of the Cluster Coverage

For the calculation of the cluster coverage on the surface, the spatial distribution of the particles must be determined. This can be done (as seen in chapter 8.1) by performing a surface mapping at a fixed wavelength using either s-CRD or s-SHG spectroscopy.

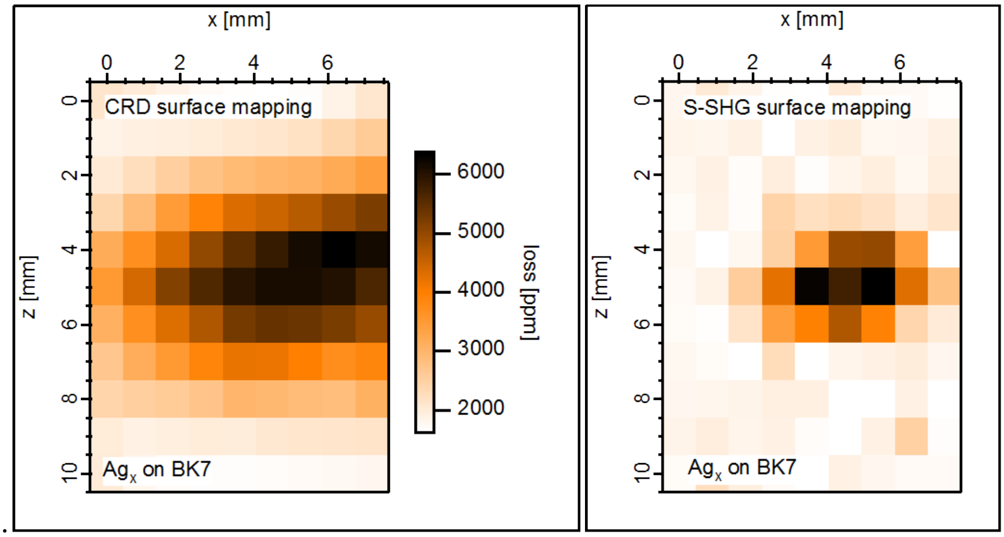

Fig. 8-*10*. Measurement of the spatial distribution of the Ag cluster on the BK7 surface . Left image: using s-Vis-CRD surface loss mapping at a wavelength of 450 nm; right image: s-SHG intensity surface mapping at a fund. wavelength of 680 nm. In both images the cluster spot is well resolved.

In figure 8-*10*, the images using both techniques on the same sample are depicted. The s-Vis-CRD surface loss mapping is carried out at a wavelength of 450 nm and the s-SHG intensity surface mapping at a fundamental wavelength of 680 nm (this is the wavelength where the maximum of the SH intensity in the s-SHG spectrum of Ag nano-particles is located, see fig. 8-*07*). For each of the two experiments the substrate is positioned at the Brewster's angle. In both images the cluster spot is well resolved and the maxima are at the same position of the sample (pos. x = 5, z = 5). However, the spot size seems to be much smaller in the s-SHG than in the s-Vis-CRD surface mapping. A possible reason is the field enhancement effect of the metal particles. Due to the strong oscillations of the conducting electrons in the cluster, the local field is strongly enhanced in the surrounding of the particle. Since the generated SH field scales with the square of the fundamental field, the SH intensity is very sensitive to such effects. As a result, the generated SH intensity does not grow linearly with increasing cluster coverage but rather with the power of three or even more. A more detailed description of this effect can be found in the literature.[143, 144] Consequently, the spot size might be underestimated in the s-SHG experiment and the linear surface mapping should be used to calculate the coverage of Ag clusters on the surface. The loss of the sample at a position (x,z), $\Lambda_{(x,z)}$, is therefore assumed to be proportional to the cluster coverage, ρ, at that point neglecting local field effects for the linear case, and is given by:

$$\Lambda_{(x,z)} = \rho_{(x,z)} \cdot \sigma_{abs} \quad (eq.8\text{-}10)$$

where, σ_{abs}, is the absorption cross section of one cluster. The function of interest is here $\rho_{(x,z)}$ because it describes the spatial distribution of the cluster coverage on the surface. In order to calculate its values, the absorption cross section must be determined (because the experiment is carried out at one fixed wavelength, σ_{abs} is a constant). This can be done using the relation:

$$\iint_{x,z} \rho_{(x,z)} dxdz = N_{particle} \quad (eq.8\text{-}11)$$

where, $N_{particle}$, is the total number of particles. Following that, equation 8-11 turns into:

$$\iint_{x,z} \Lambda_{(x,z)} dxdz = \sigma_{abs} \cdot \iint_{x,z} \rho_{(x,z)} dxdz = \sigma_{abs} \cdot N_{particle} \quad (eq.8\text{-}12)$$

Since the number of deposited particles is known, $\rho_{(x,z)}$ can be derived from equation 8-13:

$$\rho_{(x,z)} = \frac{\Lambda_{(x,z)} \cdot N_{particle}}{\iint_{x,z} \Lambda_{(x,z)} dxdz} \quad (eq.8-13)$$

In order to get a better resolution for $\rho_{(x,z)}$, a two dimensional Gauss fit is performed on the data of $\Lambda_{(x,z)}$. This method is justified because the deposition should lead to a cluster spot with approximately Gaussian distribution. The resulting coverage distribution derived from the s-Vis-CRD surface loss mapping (figure 8-*10*) is shown in figure 8-*11*.

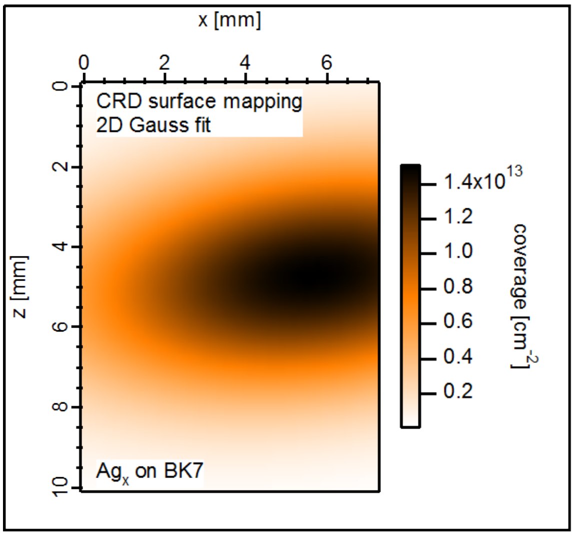

Fig. 8-*11*. Spatial distribution of the cluster coverage (Ag nano-particles) on BK7.

From the image, it can be extracted that maximal coverage is nearly $1.5 \cdot 10^{13}\,\mathrm{cm}^{-2}$. With a calculated mean cluster diameter of 1.4 nm (see next section), this corresponds to about 23% of a monolayer. The number of clusters per unit area, A, in a monolayer is approximated by:

$$N_{\mathrm{monolayer}} = A / (\pi \cdot r^2_{\mathrm{cluster}}) \quad (eq.8-14)$$

where, r_{cluster}, is the cluster radius.

8.4.2 Linear and Nonlinear Spectra of Supported Silver Nano-Particles

In a next experiment, the linear absorption spectrum of the Ag cluster sample is measured using s-Vis-CRD spectroscopy with the substrate positioned at Brewster's angle at a substrate temperature of ~120 K. In order to correct for substrate losses and changes in the resonator losses when realigning the cavity, a reference spectrum is taken before the deposition of clusters. For the reference, two points on the sample are measured, one point in the middle P_m where the clusters are subsequently deposited and one point far from the middle P_r which is not affected by the cluster deposition. As vertical position z_r of the point P_r the value $z_r = z_m + 5$ mm is chosen. The resulting curves for the losses at the two positions, $\Lambda_{(\omega)}^{(m_1)}$ and $\Lambda_{(\omega)}^{(r_1)}$, can be expressed mathematically as follows:

$$\Lambda_{(\omega)}^{(m_1)} = \Lambda_{(\omega)}^{(P_m)} + \Lambda_{(\omega)}^{(\text{cavity1})}$$

$$\Lambda_{(\omega)}^{(r_1)} = \Lambda_{(\omega)}^{(P_r)} + \Lambda_{(\omega)}^{(\text{cavity1})} \qquad \textit{(eq.8-15)}$$

where, $\Lambda_{(\omega)}^{(P_m)}$ and $\Lambda_{(\omega)}^{(P_r)}$, are the scattering losses at the points P_m and P_r, respectively. Since $\Lambda_{(\omega)}^{(m)}$ and $\Lambda_{(\omega)}^{(r)}$ are measured one after another without touching the cavity and the fact that the optical beam path inside the cavity is equal for both points (due to the high homogeneity of the BK7 glass substrate, see chapter 6), it can be assumed that the curve of the resonator losses, $\Lambda_{(\omega)}^{(\text{cavity})}$, is the same for both measurements. After the deposition of the Ag clusters both points are measured again ($\Lambda_{(\omega)}^{(m_2)}, \Lambda_{(\omega)}^{(r_2)}$) yielding:

$$\Lambda_{(\omega)}^{(m_2)} = \Lambda_{(\omega)}^{(P_m)} + \Lambda_{(\omega)}^{(\text{cluster})} + \Lambda_{(\omega)}^{(\text{cavity2})}$$

$$\Lambda_{(\omega)}^{(r_2)} = \Lambda_{(\omega)}^{(P_r)} + \Lambda_{(\omega)}^{(\text{cavity2})} \qquad \textit{(eq.8-16)}$$

The cluster spectrum, $\Lambda_{(\omega)}^{(\text{cluster})}$, can then be derived from:

$$\Lambda_{(\omega)}^{(\text{cluster})} = \Lambda_{(\omega)}^{(m_2)} - \Lambda_{(\omega)}^{(r_2)} - \left(\Lambda_{(\omega)}^{(m_1)} - \Lambda_{(\omega)}^{(r_1)}\right) \qquad \textit{(eq.8-17)}$$

All s-Vis-CRD spectra of supported metal clusters in chapter 8 are derived using this method which gives highly precise values for $\Lambda_{(\omega)}^{(\text{cluster})}$.

The measured difference s-Vis-CRD spectrum of the Ag cluster sample is shown in figure 8-*12*. A strong increase in the loss towards higher photon energies indicates the onset of an absorption band of the silver nano-particles. This can be attributed to the excitation of a plasmon in the metal cluster. Unfortunately, the peak cannot be resolved entirely because the laser system is limited to the applied wavelength range towards the UV. However, using the s-SHG spectroscopy, the UV-range becomes accessible.

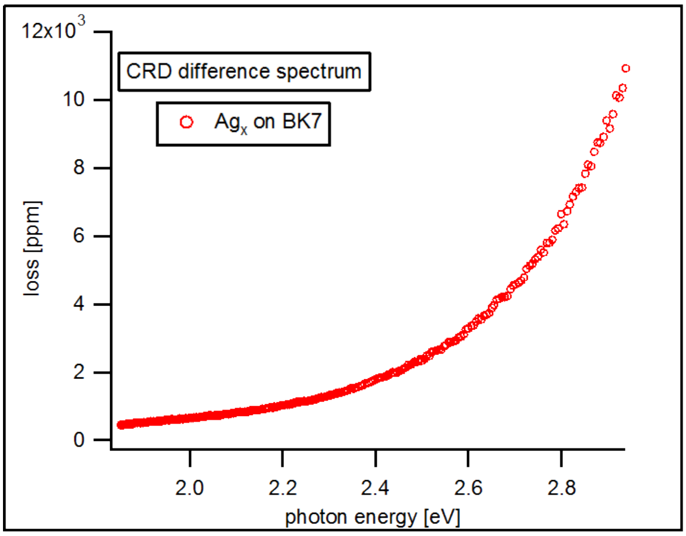

Fig. 8-*12*. Difference s-Vis-CRD spectrum of silver nano-particles on BK7. The strong increase in loss towards higher photon energies can be attributed to the onset of an absorption band of the Ag clusters.

In order to gain spectral information of the Ag cluster sample in the ultraviolet range, an s-SHG spectrum of the Ag sample, positioned at Brewster's angle at a substrate temperature of ~120 K is measured. The result of the measurement is depicted in figure 8-*13*. A peak in the spectrum can be observed at a photon energy of the fundamental beam of 1.85 eV (3.7 eV SH photon energy), which originates from the resonance of the silver plasmon at the SH frequency (see chapter 8.2.2). Consequently, this spectrum represents the optical response of the Ag clusters in the UV region (at the SH photon energy axis).

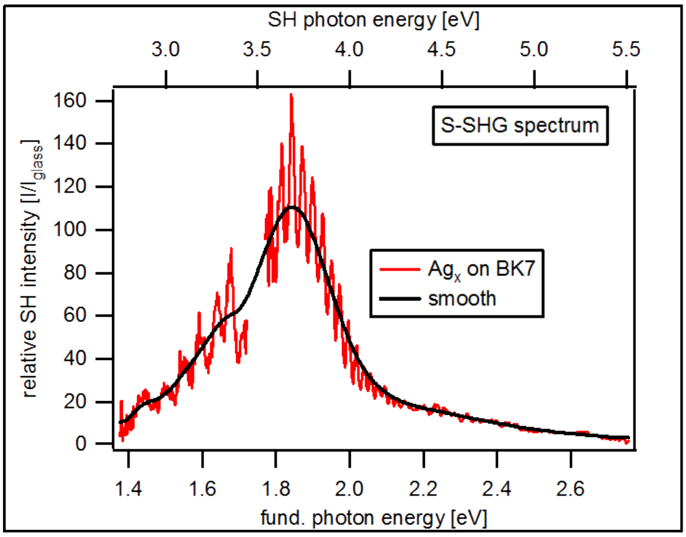

Fig. 8-*13*. s-SHG spectrum of Ag nano-particles on BK7. A resonance peak is present at an SH photon energy of 3.7 eV. The SHG enhancement originates from a resonance at the SH frequency.

The attribution of the resonances observed in both spectra to plasmonic oscillations of the conducting electrons inside the Ag clusters is justified by the observed spectral position and the extraordinarily large absorption/SH intensity. However, comparing the linear with the nonlinear spectrum (fig. 8-*12* and 8-*13*), one remarkable difference can be observed in the position of the onset of the plasmon peak. In the s-SHG spectrum, the relative SH intensity at 2.8 eV of SH photon energy is approximately one order of magnitude smaller than at the peak position, whereas the s-Vis-CRD spectrum already shows a strong absorption of ~6000 ppm at this photon energy. Furthermore, on the high energy side of the s-SHG spectrum, between 2 eV and 2.8 eV fundamental photon energy, there is no indication of an onset of an SHG enhancement induced by a resonance at the fundamental frequency, as is the case in the s-Vis-CRD spectrum. Instead, in the former the relative SH intensity decreases with increasing photon energy. This indicates that the onset of the plasmon peak in the s-Vis-CRD measurement is not part of the plasmon resonance observed in the nonlinear spectrum.

All these observations are strong evidence for the existence of two different modes of the plasmon, from which the one located at lower photon energy is not SHG active. Such a splitting of the plasmon resonance into two different modes is known from metal particles which have an oblate shape (see chapter 3.1.3). From the theory it could be learned that the resonance position of the plasmon mode parallel to the short axis in such particles is blue shifted, whereas the resonance position of the plasmon mode parallel to the long axis is red shifted. Due to the influence of the substrate on the metal particle it is most likely that the short axis of the Ag cluster is perpendicular to the substrate surface (this has also been observed by other groups[87, 88, 111]). The oscillation of the conducting electrons parallel to this axis is the only SHG active plasmon oscillation in a supported metal particle as shown in chapter 8.3. This explains the blue shifted position of the plasmon peak in the s-SHG spectrum as well as the lack of the second plasmon peak in the nonlinear spectrum. The results obtained in this chapter show clear evidence of a plasmon peak splitting into two plasmon modes, one perpendicular to the substrate surface which is blue shifted and SHG active, and the other parallel to the substrate surface which is not SHG active (this mode is observed in the s-Vis-CRD spectrum). However, further investigation is required in order to support this interpretation of the obtained spectra. One possibility is the verification of the existence of the plasmon mode parallel to the substrate surface. Since this plasmon mode cannot be fully resolved using s-Vis-CRD spectroscopy and it is not possible to measure this transition using s-SHG spectroscopy, its existence must be confirmed using a different method.

8.4.3 Stability of the Ag Clusters Illuminated by Strong Laser Pulses

In order to confirm that the strong increase in the loss towards higher photon energies in the s-Vis-CRD spectrum really originates from an absorption band of the particles corresponding to the excitation of a plasmon oscillation parallel to the substrate surface, an additional s-SHG experiment is carried out. Supposing this plasmon mode exists, the centro-symmetric electric potential in oscillation direction would not allow for the generation of SH photons; however, the strong linear absorption of fundamental photons could lead to photo induced desorption of the particles from the surface. Consequently, information about absorption bands may be obtained by measuring the stability of the supported clusters for different laser wavelengths, even if they do not belong to SHG active oscillations. Such an s-SHG stability measurement is carried out by recording the SH intensity of the sample as a function of time at different photon energies. For the measurement, the substrate is positioned at Brewster's angle and in the beginning, a fundamental photon energy of 1.82 eV (this is approximately the maximum of the plasmon peak in the s-SHG spectrum) is used. In a second step, the sample is irradiated with laser pulses at a photon energy of 2.76 (450 nm) for 20 minutes, followed again by measuring the SH intensity at 1.82 eV fundamental photon energy. The result of the experiment is shown in figure 8-*14*.

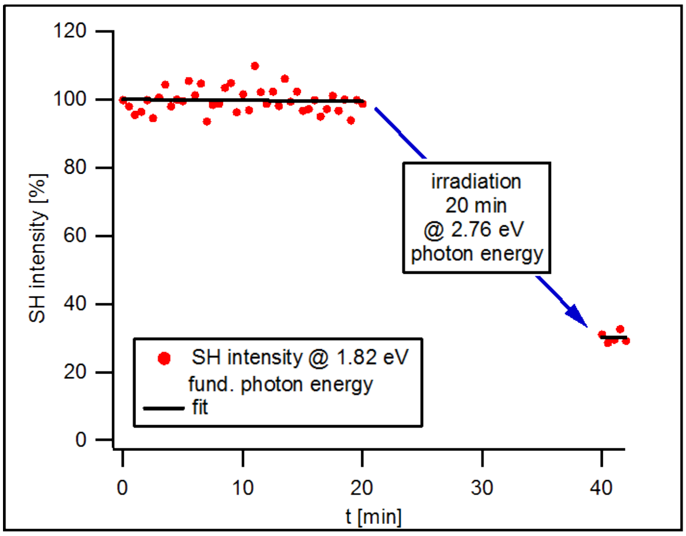

Fig. 8-*14*. Stability measurement of Ag clusters on BK7, irradiated with laser light of a fundamental photon energy of 1.82 eV (first 20 minutes) and 2.76 eV (second 20 minutes), respectively. The instability of the clusters when irradiated with laser light at a fundamental photon energy of 2.76 eV, is strong evidence for the existence of a linear absorption band close to this energy.

During the first 20 minutes, the SH intensity remains constant which shows that the clusters are stable when irradiated at 1.82 eV of fundamental photon energy even though the SH frequency is in resonance with the plasmon excitation. The reason for this is the low energy transfer from the laser beam into the clusters because the linear absorption cross section at 1.82 eV photon energy is small (see fig. 8-*12*). After the irradiation of the sample with laser light at 2.76 eV of fundamental photon energy for 20 minutes, the SH intensity at the peak position of the plasmon (measured again at 1.82 eV of fund. photon energy) has decreased to about 30 % of the initial value, indicating that the majority of the clusters are desorbed from the surface. This suggests that a strong absorption of fundamental photons takes place at 2.76 eV of fundamental photon energy even if the s-SHG spectrum does not show a strong enhancement of the SH intensity in this frequency region. This observation is in perfect agreement with the existence of the SHG inactive plasmon oscillation in the silver clusters that is parallel to the substrate surface and has a resonance frequency which is close to 2.76 eV of fundamental photon energy. Consequently, the correctness of the interpretation of the linear and nonlinear spectra of Ag clusters on BK7 from chapter 8.4.2 could be confirmed.

8.4.4 Interpretation of the Measured Spectra Using Mie-Theory

A theoretical description of the optical properties of small oblate shaped supported metal particles is given in detail in chapter 3. Here, the results are used to fit the measured data. Following equation 3-23, the absorption cross section, σ_i, of small oblate particles with the dielectric constant of the surrounding medium, ε_m, and the volume, V_0, is:

$$\sigma_i = \frac{\omega}{c_0}\varepsilon_m{}^{3/2}V_0 \frac{\varepsilon_2(\omega)}{\left[\left(\varepsilon_1(\omega)-\varepsilon_m\right)\left(L_i+\beta_i\right)+\varepsilon_m\right]^2+\varepsilon_2{}^2(\omega)\left(L_i+\beta_i\right)^2} \qquad \mathit{(eq.8\text{-}18)}$$

$\varepsilon(\omega)=\varepsilon_1(\omega)+i\cdot\varepsilon_2(\omega)$ is the complex dielectric function of the particle, L_i, the shape parameter, β_i, the interaction parameter, and c_0, the speed of light in vacuum. For an oblate particle there are two different values for L_i and consequently two absorption cross sections, one corresponding to the oscillation parallel to the short axis (s-mode), and one parallel to the long axis (p-mode), respectively. In the s-Vis-CRD experiment (schematic shown in figure 8-*15*) the total measured cross section, σ_{abs}, is:

$$\sigma_{abs} = \sigma_{\text{(p-mode)}}\cdot\cos^2\alpha+\sigma_{\text{(s-mode)}}\cdot\sin^2\alpha \qquad \mathit{(eq.8\text{-}19)}$$

where, α , is the azimuth substrate angle.

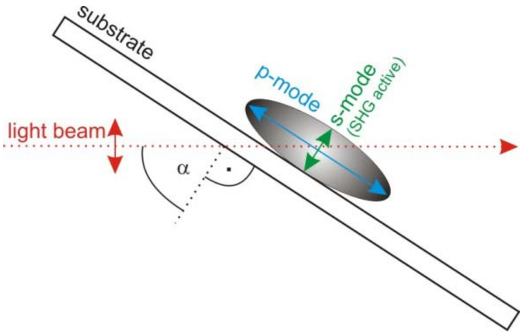

Fig. 8-*15*. Schematic of the s-Vis-CRD measurement of supported oblate silver clusters.

Since the performed s-Vis-CRD measurement only shows the part of the spectrum at small photon energies, the absorption is highly dominated by the red shifted p-mode oscillation. Consequently, in good approximation it can be written for the measured range in the s-Vis-CRD spectrum:

$$\sigma_{abs} = \sigma_{\text{(p-mode)}} \cdot \cos^2 \alpha \quad \textit{(eq.8-20)}$$

Using equation 8-10, the measured loss, $\Lambda_{(\omega)}$, is then:

$$\Lambda_{(\omega)} = \rho \cdot \sigma_{\text{(p-mode)}} \cdot \cos^2 \alpha \quad \textit{(eq.8-21)}$$

where, ρ, is the cluster coverage on the surface.

In order to derive the correct dielectric function for the silver clusters, the bulk data for $\varepsilon_1(\omega)$ and $\varepsilon_2(\omega)$ must be corrected to account for additional damping effects such as the free mean path effect in small particles and the chemical interface effect induced by the substrate (see chapter 3.1.5). This is done using equations 8-22 and 8-23.

$$\varepsilon_1(\omega) = \varepsilon_{1\text{(bulk)}}(\omega) + \omega_p{}^2 \cdot \left(\frac{1}{\omega^2 + \gamma^2{}_{\text{bulk}}} - \frac{1}{\omega^2 + \gamma^2{}_{(R)}} \right) \quad \textit{(eq.8-22)}$$

$$\varepsilon_2(\omega) = \varepsilon_{2\text{(bulk)}}(\omega) + \frac{\omega_p{}^2}{\omega} \cdot \left(\frac{\gamma_{(R)}}{\omega^2 + \gamma^2{}_{(R)}} - \frac{\gamma_{\text{bulk}}}{\omega^2 + \gamma^2{}_{\text{bulk}}} \right) \quad \textit{(eq.8-23)}$$

The dielectric functions, $\varepsilon_{1(\mathrm{bulk})}$ and $\varepsilon_{2(\mathrm{bulk})}$, can be derived from measurements of bulk silver[76] and, $\gamma_{(R)}$, is the size dependent damping constant. The latter can be expressed using the size independent parameter A as shown in chapter 3.1.5.

$$\gamma_{(R)} = \gamma_{\mathrm{bulk}} + A \cdot \frac{v_F}{r_{cluster}} \qquad \text{(eq.8-24)}$$

where, v_F, is the Fermi velocity of the electrons in bulk silver and, $r_{cluster}$, the radius of the cluster. The optical constants for bulk silver (plasma frequency ω_p, damping constant γ_{bulk} and Fermi velocity v_F) can be found in the literature[76] and are listed in table 8-*16*.

ω_p	9.08 eV
γ_{bulk}	0.018 eV
v_F	0.922 eVnm

Table 8-*16*. Optical constants for bulk silver.

The fit of the s-Vis-CRD spectrum of the silver clusters is carried out using equation 8-21 in combination with equations 8-18, 8-22, and 8-23. Furthermore, the fit parameters V_0, $(L_i + \beta_i)$, and $\gamma_{(R)}$ are used. For the dielectric constant of the surrounding medium ε_m, the value of 1.457 is used, corresponding to a particle which has a surface area of 70% exposed to vacuum $(\varepsilon_{(\mathrm{vacuum})} = 1)$ and 30% in contact with the BK7 substrate $(\varepsilon_{(\mathrm{BK7})} = 2.372)$. This ratio has also been observed for small silver clusters by other groups.[88, 91] The supported particle here is assumed to have approximated the shape of a hemisphere.

In chapter 2.2.5, it is shown by using the model of the anharmonic oscillator, that an s-SHG spectrum is in a first approximation similar to the linear absorption spectrum, if the enhancement of the SH signal originates from a resonance at the second harmonic frequency (this is for the s-SHG spectra of silver clusters the case). Even if the limited model of the anharmonic oscillator is used to describe the optical properties of metal clusters, it shows that the resonance frequencies and peak widths in the s-SHG spectra are comparable with those in the corresponding linear absorption spectra. Consequently, for the s-SHG spectrum of the supported silver nano-particles the fit function based on the calculation model for the linear case is used. In figure 8-*17*, the s-Vis-CRD and the s-SHG spectra are depicted including the two calculated spectra (Mie-fit). The fitted curves confirm the existence of a splitting of the plasmon peak into two resonances corresponding to the oscillation parallel to the long axis (p-mode) and parallel to the short axis (s-mode) of the particles as postulated above.

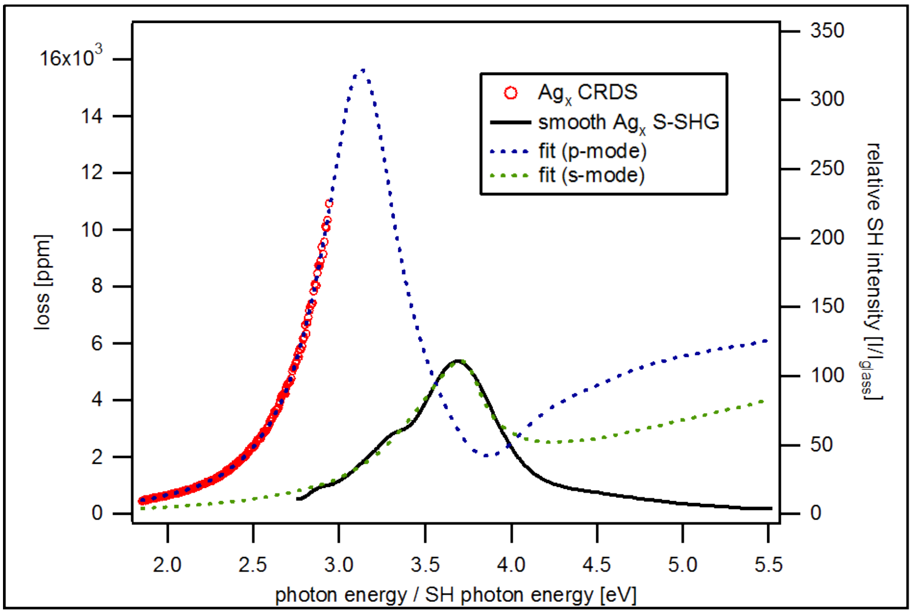

Fig. 8-*17*. s-Vis-CRD spectrum and s-SHG spectrum of Ag nano-particles supported on BK7. The dotted lines show the corresponding Mie-fits using equation 8-21. The calculated curves are in good agreement with the measured data and confirm the existence of the plasmon peak splitting.

The two calculated curves show a significant splitting of 0.58 eV between the maxima of the two peaks. The fit of the s-Vis-CRD spectrum shows very little deviations from the measured data points. This, in combination with the high precision of the s-CRD technique should guarantee that reliable fit parameters can be extracted, even if the peak maximum is outside the measured range. The Mie-fit of the s-SHG spectrum meanwhile is less accurate, however, the peak maximum is well reproduced by the calculated curve. On the high photon energy side (above 4.3 eV), the fit (green dotted line) strongly deviates from the measured spectrum (black line). The reason for the increase of the calculated curve is the onset of the interband absorption in silver at these photon energies (for bulk silver the edge of the interband absorption is located at around 3.8 eV).[77, 78] From the spectrum it can be concluded, that the interband absorption does not have an influence on the SH intensity, because the measured s-SHG spectrum does not follow the increase. In other words, the interband transition does not apparently represent an SHG active oscillation. The same effect could be observed in the s-SHG spectra of gold and copper nano-particles in chapter 8.2.2. There, the plasmon resonance is well resolved even if in linear absorption spectra of such small particles the plasmon peak vanishes due to the absorption of the interband transition.[80] From this observation it can concluded, that the s-SHG spectroscopy has a high potential for investigations of plasmon excitations in metal particles, which are not accessible with linear techniques.

resonance mode	**p-mode** (s-Vis-CRD spectrum)	**s-mode** (s-SHG spectrum)
V_0	1.5 nm^3	-
$(L_i + \beta_i)$	0.255	0.716
$\gamma_{(R)}$	0.62 eV	1.15 eV
$\hbar\omega_{\max}$	3.12 eV	3.7 eV

Table 8-*18*. Parameters extracted from the fit of the s-Vis-CRD- and the s-SHG spectrum of Ag nano-particles supported on BK7.

The parameters extracted from the two fits for the cluster coverage of $\rho = 1.5 \cdot 10^{13}\,\mathrm{cm}^{-2}$ (determined in chapter 8.4.1) and the azimuth substrate angle of $\alpha = 57°$ (Brewster's angle), are listed in table 8-*18*. From the Mie-fit of the s-Vis-CRD spectrum, the mean volume of the supported particles can be calculated to approximately 1.5 nm^3. This corresponds to a particle radius of 0.71 nm, assuming a spherical cluster shape. This value is in good agreement with the observed particle sizes in the AFM images in chapter 8.1 for the deposition of metal particles using the RF only mode of the mass filter, set at 2000 amu. However, the splitting of the plasmon peak shows that the particles have oblate shape. The axis ratio $R_{c/a} = \frac{\text{short axis}}{\text{long axis}}$ can be derived from the shape parameter, L_i. Using equations 3-16, 3-28, and 3-34 the two parameters, L_i and β_i, are calculated for the p-mode oscillation using the given cluster coverage and the measured values for V_0 and $(L_i + \beta_i)$. For the dielectric constant of the substrate the value for BK7 glass of $\varepsilon_s = 2.37$ is used. The resulting values and the corresponding axis ratio are listed in table 8-*19*.

$L_{\text{p-mode}}$	0.299
$\beta_{\text{p-mode}}$	-0.044
$R_{c/a}$	0.78

Table 8-*19*. Calculated shape and interaction parameter for supported Ag nano-particles on BK7. The axis ratio, $R_{c/a}$, is derived from the shape parameter, $L_{\text{p-mode}}$.

The derived value for the axis ratio of $R_{c/a} = 0.78$ is slightly smaller than the value found by Hövel[87, 88] with $R_{c/a} = 0.86$ (measured for silver clusters with a mean radius of 1 nm deposited on quartz glass). A possible reason for this discrepancy is the different cluster size. The volume of a cluster with a radius of 1nm is 2.8 times larger than the volume of the clusters investigated here. The smaller the clusters, the larger the influence of the substrate on the shape of the particle, because the fraction of cluster atoms which bind to the surface of the substrate increases with decreasing particle size. Consequently, a smaller value of $R_{c/a}$ for the measured silver particles seems reasonable. An influence on the particle shape could also be attributed to the different composition of the substrates (quartz glass, BK7 glass), leading to slightly different binding energies between the cluster and the surface.

Calculation of the A parameter

From the axis ratio and the particle volume, the radius of the short (c) and the long axis (a) of the oblate cluster may be calculated using equation 8-25:

$$V_{\text{oblate spheroid}} = \frac{4}{3}\pi \cdot c \cdot a^2 \quad (eq.8\text{-}25)$$

The resulting values are: c = 0.6 nm and a = 0.77 nm. These values are used as cluster radii for the p-mode (radius = a) and the s-mode oscillation (radius = c) in order to derive the A parameter from the measured damping constants, $\gamma_{(R)}$, using equation 8-24. The calculation yields: $A_{\text{p-mode}} = 0.5$ and $A_{\text{s-mode}} = 0.74$.

For particles on surfaces the parameter A can be split into two contributions, one for the cluster size, A_{size}, describing the additional damping induced by the free mean path effect, and a second one, $A_{\text{interface}}$, accounting for the chemical interface damping due to the presence of the substrate surface:

$$A = A_{\text{size}} + A_{\text{interface}} \quad \textit{(eq.8-26)}$$

From theoretical calculations, Persson found for A_{size} a constant value of 0.25 [99] which could be confirmed experimentally.[91, 101] Using this value, the size independent interface contribution to the damping for the measured p-mode plasmon is $A_{\text{interface}} = 0.25$, and for the s-mode $A_{\text{interface}} = 0.49$. Kreibig *et al.* determined $A_{\text{interface}}$ for the p-mode plasmon in silver clusters with a radius of 1 nm on a quartz glass substrate, and found a value of 0.35.[91, 101] The value measured here is ~30 % smaller. One possible reason for this deviation is the small cluster size which is studied in the presented experiment. Even if the A parameter should be independent of the cluster radius, it is likely that below a certain size limit additional quantum mechanical effects appear, and the classical formalism which predicts the size independency of A reaches its limits. More sophisticated quantum mechanical models could give an explanation for the observed deviation. Another reason could be the slightly different support material which definitely has an influence on the value of the $A_{\text{interface}}$ parameter. However, this contribution should be smaller than the observed discrepancy, because the main component of the substrate is in both cases the SiO_2 network. Finally, it should be mentioned that the accuracy of the $A_{\text{interface}}$ value determined here is limited because the plasmon peak for the p-mode oscillation is not fully resolved.

The calculated value of $A_{\text{interface}}$ corresponding to the s-mode plasmon peak $(A_{\text{interface}} = 0.49)$ is almost twice as high as the value derived for the p-mode plasmon $(A_{\text{interface}} = 0.25)$. Despite all uncertainties this difference seems to be significant, indicating that the contribution of the chemical interface damping to the overall damping constant of the plasmon depends on the direction of the oscillation with respect to the substrate surface. Considering, that the process leading to the interface damping is the tunneling of electrons from the cluster into the substrate during the plasmon oscillation[100], it seems reasonable that this effect is stronger for an electron movement perpendicular to the substrate surface (s-mode). This observed anisotropy of the interface damping for supported metal clusters has also been proposed by theory (see chapter 3.1.5). However, for better understanding an exact theoretical description of the nonlinear processes at the interface between a substrate and small metal particles is necessary.

Position of the s-mode plasmon

From the derived spectral position of the p-mode plasmon peak and the extracted parameters, the theoretical position of the s-mode plasmon peak can be calculated. The obtained value is subsequently compared to the peak position measured in the s-SHG spectrum in order to verify the consistency of the theoretical model with the experimental data. In a first step, the shape parameter for the s-mode plasmon, $L_{\text{s-mode}}$, is calculated from the obtained shape parameter for the p-mode oscillation $(L_{\text{p-mode}} = 0.299)$ using equation 8-27 (valid for oblate particles):

$$2 \cdot L_{\text{p-mode}} + L_{\text{s-mode}} = 1 \quad \textit{(eq.8-27)}$$

yielding $L_{\text{s-mode}} = 0.402$. In a second step, the interaction parameter for the s-mode oscillation, $\beta_{\text{s-mode}}$, is calculated using equations 3-29 and 3-35, yielding $\beta_{\text{s-mode}} = 0.019$. Consequently, the theoretical value for the expression $(L_{\text{s-mode}} + \beta_{\text{s-mode}})$ which defines the resonance position of the plasmon, is $(L_{\text{s-mode}} + \beta_{\text{s-mode}}) = 0.421$. This is far from the measured value of $(L_{\text{s-mode}} + \beta_{\text{s-mode}}) = 0.716$, derived from the s-SHG spectrum (see table 8-*18*). As a consequence, the plasmon peak measured in the s-SHG experiment is blue shifted by $\Delta\hbar\omega_{\max} = 0.19$ eV with respect to its calculated position. In figure 8-*20*, the fit of the p-mode plasmon, the calculated s-mode plasmon resonance curve, and the measured s-SHG spectrum are shown. The different positions of the peak maxima of the calculated and the measured curve can be clearly observed. In general, shifts of the resonance positions of silver plasmons on surfaces have already been observed by other groups and are reported in the literature.[88, 91] They are often attributed to the inaccuracy of the bulk dielectric function for silver and deviations from its cluster size dependency from the standard model. A correction of the dielectric function using the Kramers-Kronig-analysis which connects the real and the imaginary part of the dielectric function[145, 146], can give more realistic values. In the presented case of the blue shifted plasmon resonance position in the s-SHG spectrum, an additional issue must be considered concerning the interaction parameter $\beta_{\text{s-mode}}$. This parameter accounts for the difference between the local field at the cluster position and the electric field in the laser beam (see chapter 3.1.4.2). This local field effect has two main contributions: firstly, the modulation of the local electric field by dipole- image dipole interactions between the particles and the substrate, and secondly, the modulation of the local electric field by dipole-dipole interactions between neighboring clusters. The latter has a positive contribution to β for the s-mode oscillation (local field enhancement) and consequently leads to a blue shift of the plasmon resonance position. This field enhancement via dipole-dipole interactions is known to have a much larger impact on nonlinear than on linear processes, which leads to a larger blue shift of the plasmon position for the nonlinear case. Consequently, it is likely that the value of the interaction parameter calculated in this chapter is highly underestimated in order to correctly treat the nonlinear local field enhancement effect (for the calculation of $\beta_{\text{s-mode}}$ a model based on linear processes is used). The different impact of the local field enhancement effect on linear and nonlinear processes could also be seen by comparing the surface mapping measurements using s-Vis-CRD and s-SHG spectroscopy (see chapter 8.4.1). This observation supports the presented idea that the underestimation of $\beta_{\text{s-mode}}$ for nonlinear processes (the s-SHG experiment) is the reason for the discrepancy between the calculated and measured spectrum. All of these results show the necessity of an exact mathematical description of the nonlinear spectra for small supported metal clusters. However, the main features of the measured spectra in this chapter could be explained by the classical linear theory and some parameters could be derived which are in rather good agreement with data from the literature.

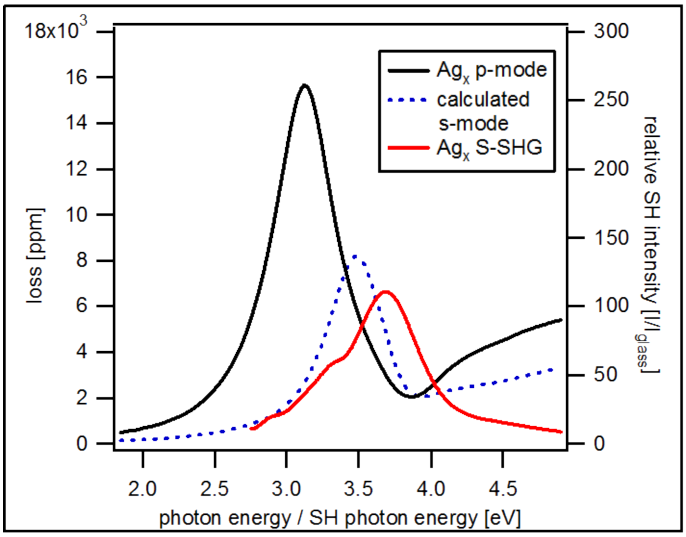

Fig. 8-*20*. Mie-Fit of the p-mode plasmon peak (black line), calculated s-mode plasmon peak using the parameters extracted from the p-mode Mie-fit (blue, dotted line) and s-SHG measurement (red line) of Ag nano-particles supported on BK7. The discrepancy between theory and measurement can be clearly observed.

8.5 Linear and Nonlinear Spectra of Size Selected Ag Clusters

In the previous chapter, the linear and nonlinear optical properties of small supported silver nano-particles were investigated and compared to theoretic calculations. Furthermore, by comparing the results to measurements of larger silver nano-particles performed by other groups, it could be shown that all main optical features which are described in the literature are also present in the spectra shown here. However, some deviations from the theory could be observed (especially in the nonlinear spectrum), indicating the existence of additional effects (beyond the used classical models) which appear for small clusters with radii of less than 1 nm. In order to investigate the evolution of these non-classical properties with cluster size towards very small clusters (1-50 atoms), experiments with size selected silver particles are presented in this chapter. Size selected means that all clusters deposited onto the substrate are composed of an exactly defined number of atoms. The cluster sizes investigated in the following are in order of decreasing cluster size: Ag_{42}, Ag_{21}, Ag_9 and Ag atoms.

8.5.1 Ag_{42} Clusters on BK7

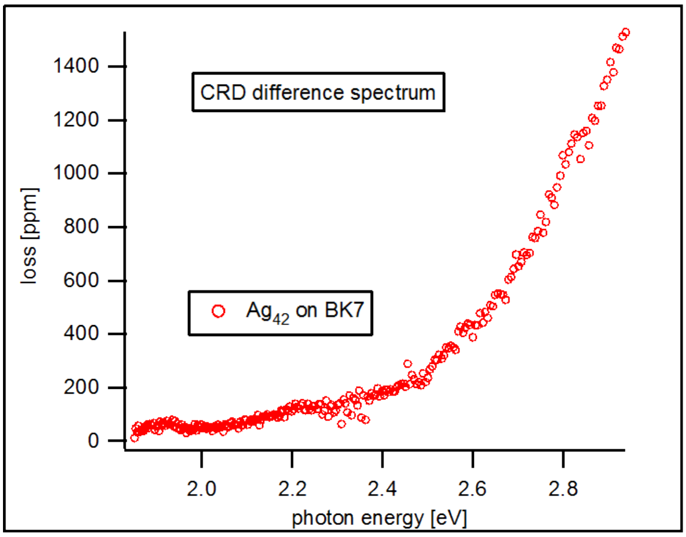

Fig. 8-*21*. Difference s-Vis-CRD spectrum of Ag_{42} clusters on BK7. The increase in loss towards larger photon energies indicates the onset of the p-mode plasmon absorption band.

In a first experiment with single sized particles, Ag_{42} clusters are deposited on the backside of a cooled BK7 glass substrate (120K) under UHV conditions. The total number of clusters amounts to $1.18 \cdot 10^{12}$. Assuming a cluster spot size which is similar to that measured in chapter 8.4.1, this corresponds to a surface coverage of $4 \cdot 10^{12} \mathrm{cm}^{-2}$ .Subsequently, s-Vis-CRD and s-SHG spectra of the cooled sample are measured, the results are shown in figure 8-*21* and 8-*22*, respectively.

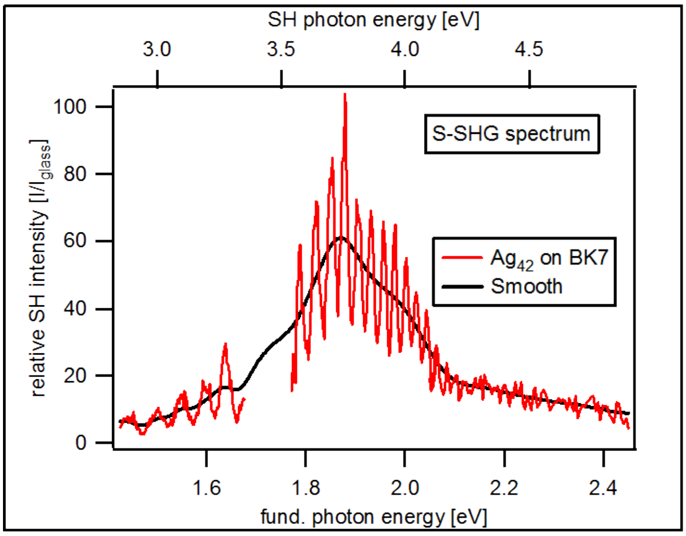

Fig. 8-*22*. s-SHG spectrum of Ag_{42} clusters on BK7. A plasmon resonance peak can be observed at an SH photon energy of 3.74 eV.

The linear s-Vis-CRD spectrum shows the onset of the p-mode plasmon absorption band as already seen for the silver nano-particles in chapter 8.4. The main difference to the spectrum in figure 8-*12* shown previously, is the reduced absorption loss. Since the height of the plasmon peak scales with the particle volume (see equation 8-18), this observation can be attributed to the smaller size of the Ag_{42} cluster compared to the nano-particles investigated in the previous chapter. The s-SHG spectrum in figure 8-*22*, shows the s-mode plasmon peak at an SH photon energy of 3.74 eV. In comparison to the measurement of silver nano-particles (fig. 8-*13*), the resonance is blue shifted and shows an additional shoulder at an SH photon energy of approximately 3.97 eV. The mean relative SH intensity of approximately 60 at the peak position, is a factor of two smaller than for the unselected silver particles.

The obtained spectra are fitted using the equations presented in the previous chapter. The results are depicted in figure 8-*23*. The calculated curves match the measured spectra well and again, the splitting of the plasmon peak into the p-mode and the s-mode oscillation band which was found for the larger silver nano-particles can be observed. The parameters extracted from the two fits are listed in table 8-*24*.

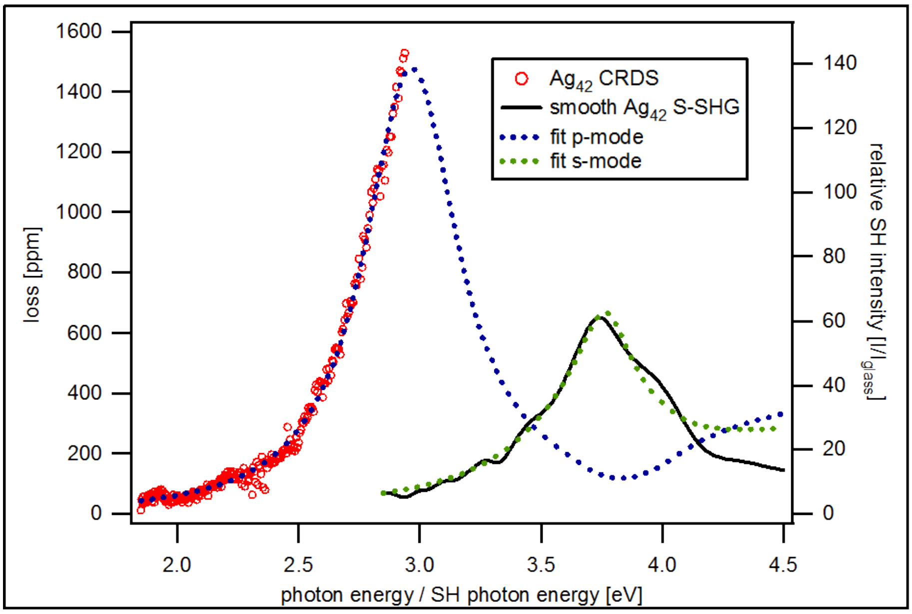

Fig. 8-*23*. s-Vis-CRD spectrum and s-SHG spectrum of Ag_{42} clusters on BK7. The dotted lines show the corresponding Mie-fits. The splitting of the plasmon resonance peak is larger than for the silver nano-particles investigated in the previous chapter.

resonance mode	**p-mode** (s-Vis-CRD spectrum)	**s-mode** (s-SHG spectrum)
V_0	0.37 nm^3	-
$(L_i + \beta_i)$	0.213	0.969
$\gamma_{(R)}$	0.5 eV	0.97 eV
$\hbar\omega_{\max}$	2.97 eV	3.74 eV

Table 8-*24*. Parameters extracted from the fit of the s-Vis-CRD- and the s-SHG spectrum of Ag_{42} clusters supported on BK7.

The splitting of the plasmon resonance peak leads to a difference between the resonance positions of the p-mode and the s-mode plasmon peak of 0.77 eV, and is thus larger than for the silver nano-particles investigated in the previous chapter. This suggests a stronger flattening of the clusters. From the value for $(L_i + \beta_i)$ extracted from the Mie-fit of the p-mode plasmon, the coverage of Ag_{42} clusters of $\rho = 4 \cdot 10^{12}\,\mathrm{cm}^{-2}$, and the calculated cluster volume of $V_0 = 0.37\mathrm{nm}^3$, the shape and the interaction parameter (L_i and β_i) can be calculated, as was shown in the previous section. The results are listed in table 8-*25*.

$L_{\text{p-mode}}$	0.262
$\beta_{\text{p-mode}}$	-0.048
$R_{c/a}$	0.6

Table 8-*25*. Calculated shape and interaction parameter for supported Ag_{42} clusters on BK7. The axis ratio, $R_{c/a}$, is derived from the shape parameter, $L_{\text{p-mode}}$.

The obtained axis ratio of $R_{c/a} = 0.6$ is smaller than the value derived for the silver nano-particles (0.78). This observation supports the suggested tendency that the smaller the silver particles are, the flatter their structure is on the substrate surface. Taking the derived particle volume of 0.37 nm^3, the calculation of the two different cluster radii for the oblate particle yields for the short axis c = 0.32 nm and for the long axis a = 0.53 nm.

The measured peak position of the s-mode plasmon (s-SHG spectrum) is again blue shifted with respect to the calculation of its position (the calculation is based on the resonance position obtained for the p-mode plasmon). The calculated interaction parameter is $\beta_{\text{s-mode}} = -0.09$ and from the fit of the s-SHG spectrum a value of $\beta_{\text{s-mode}} = 0.49$ can be extracted which is far from the calculated value. A possible explanation for this is given in chapter 8.4.4. Using the radii obtained for the short and the long axis of the particles, the A parameter can be calculated from the damping constants derived from the two fits using equation 8-24. The resulting values are $A_{\text{p-mode}} = 0.28$ and $A_{\text{s-mode}} = 0.33$. These values are much smaller than those derived from the measurements of the silver nano-particles. A discussion of the A parameters for the selected clusters is presented in chapter 8.6.

From theoretical calculations of the most stable geometries of silver clusters in vacuum, the distances between the nearest neighbors inside the cluster are found to be between 0.25 and 0.295 nm, with the latter being the value of the bulk and the former of the dimer.[147] For Ag_{42}, a value of approximately 0.285 nm is found. The radius of the short axis was determined above to be c = 0.32 nm which corresponds to a particle height of h = 0.64 nm. If close packing of silver atoms in the cluster is assumed, this height consequently corresponds to a mean thickness of the particle of approximately three atomic layers.

8.5.2 Ag_{21} Clusters on BK7

In a next experiment, Ag_{21} clusters are deposited on the backside of a cooled BK7 glass substrate under UHV conditions, followed by an s-Vis-CRD and s-SHG measurement. The total amount of clusters on the substrate is $1.35 \cdot 10^{12}$, corresponding to a coverage of $\sim 4.6 \cdot 10^{12}\,\mathrm{cm}^{-2}$. The resulting spectra and the Mie-fit of the measured s-Vis-CRD data are depicted in figure 8-*26*. The s-Vis-CRD spectrum shows the onset of the plasmon peak originating from the p-mode oscillation as already seen in the previous s-Vis-CRD experiments. However, the absorption losses are smaller than in the cases of larger clusters, which is in agreement with the theoretical considerations (see chapter 8.5.1). A remarkable observation is that the plasmon peak of the s-mode oscillation in the s-SHG spectrum has completely vanished. In figure 8-*27*, a more detailed plot of the s-SHG spectrum is shown. Apart from the interference patterns, there is only a small broadened peak centered around 4.5 eV of SH photon energy. However, the relative intensity of the peak of 0.5 is too small to be able to exclude the possibility that it is the product of a systematic error introduced by the extensive correction of the measured data. A Mie-fit of this spectrum is therefore not justified. These results indicate that the supported Ag_{21} clusters consist in height of such a low number of atomic layers that a free oscillation of the electrons along the short axis of the clusters is suppressed. However, the p-mode plasmon oscillation is still active which can be deduced from the measured s-Vis-CRD data.

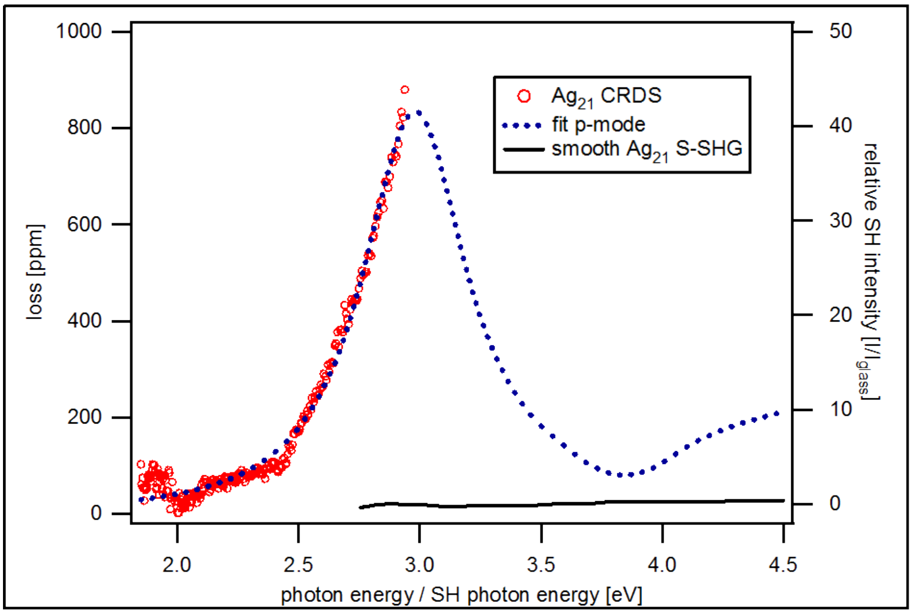

Fig. 8-*26*. s-Vis-CRD spectrum and s-SHG spectrum of Ag_{21} clusters on BK7. The dotted line shows the corresponding Mie-fit. The s-mode plasmon peak has vanished, whereas the p-mode oscillation still shows a clear plasmon resonance peak.

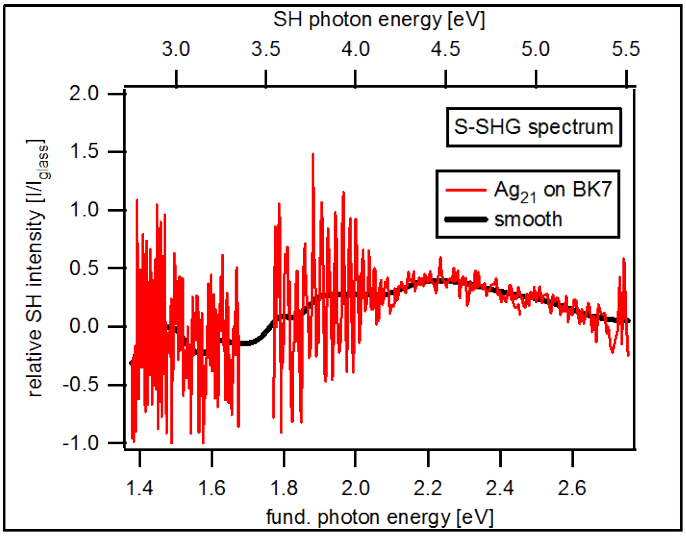

Fig. 8-*27*. Enlarged s-SHG spectrum of Ag_{21} clusters on BK7. No plasmon resonance peak is present, the small broadened peak centered around 4.5 eV of SH photon energy is too small to be significant.

V_0	0.21 nm^3
$(L_i + \beta_i)$	0.217
$\gamma_{(R)}$	0.57 eV
$\hbar\omega_{\text{max}}$	2.98 eV
$L_{\text{p-mode}}$	0.264
$\beta_{\text{p-mode}}$	-0.046
$R_{c/a}$	0.61

Table 8-*28*. Parameters extracted from the fit of the s-Vis-CRD spectrum of Ag_{21} clusters supported on BK7.

The parameters derived from the Mie-fit of the p-mode plasmon peak are listed in table 8-*28*. From the shape parameter the axis ratio is calculated yielding a value of 0.61, which is comparable to the value obtained for the Ag_{42} clusters. The radii of the short and the long axis of the Ag_{21} clusters are consequently $a = 0.43$ nm and $c = 0.265$ nm. The resulting mean height with $h = 0.53$ nm corresponds to approximately two atomic layers. The A parameter for the p-mode plasmon is $A_{\text{p-mode}} = 0.26$. This is even smaller than the value obtained for the Ag_{42} clusters and is close to the theoretical value for $A_{\text{size}} = 0.25$. From this result it can be suggested that the contribution of the chemical interface damping to the damping constant of the plasmon excitation is almost negligible for this cluster size.

8.5.3 Ag_9 Clusters on BK7

A similar experiment is carried out with Ag_9 clusters supported on a cooled BK7 glass substrate. The coverage here is approximately $\rho = 4.7 \cdot 10^{12} \mathrm{cm}^{-2}$. The measured s-Vis-CRD and s-SHG spectra with the corresponding Mie-fit of the p-mode plasmon peak are shown in figure 8-*29*.

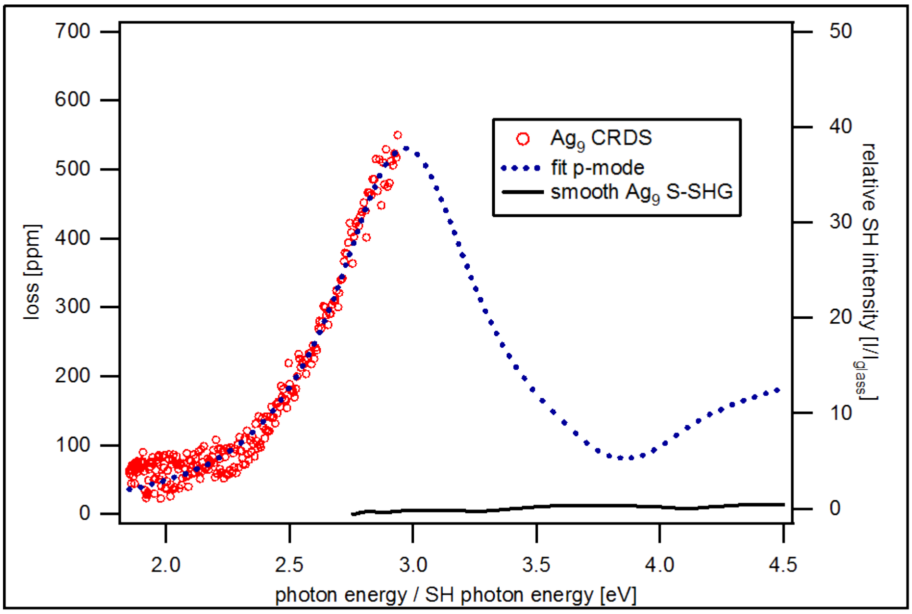

Fig. 8-*29*. s-Vis-CRD spectrum and s-SHG spectrum of Ag_9 clusters on BK7. The dotted line shows the Mie-fit of the p-mode plasmon peak. There is no s-mode plasmon resonance peak in the s-SHG spectrum.

In the spectra of Ag_9 clusters, there is a plasmon peak for the p-mode oscillation but not for the oscillation perpendicular to the surface (s-mode), as was observed for the Ag_{21} clusters. The main difference to the spectra of Ag_{21} clusters is the s-Vis-CRD absorption loss which is smaller in the case of Ag_9 clusters. The parameters extracted from the Mie-fit of the p-mode plasmon peak are listed in table 8-*30*. The calculated axis ratio is 0.6, which is approximately the same value as obtained for Ag_{42} and Ag_{21} clusters. From the theoretical calculation of the cluster geometries, the most stable configuration for Ag_9 clusters in the gas phase is found to be a planar structure.[147] On a surface, this structure should be even more stabilized due to the cluster-substrate interactions. Consequently, it can be assumed that Ag_9 forms a planar island of a height of one atomic layer on the BK7 substrate. By considering that the electrons in a planar cluster are confined in this single atomic layer, the absence of the s-mode plasmon is perhaps not surprising. On the other hand, there are three atomic layers parallel to the plane of the cluster/substrate in which the electrons can oscillate freely, resulting in a p-mode plasmon absorption. A sketch of the gas phase structure of Ag_9 clusters is shown in figure 8-*31*. The damping constant of the p-mode plasmon is again increased compared to the larger clusters, confirming its dependency on the cluster radius. The A parameter for the horizontal plasmon peak is $A_{\text{p-mode}} = 0.34$.

V_0	0.17 nm^3
$(L_i + \beta_i)$	0.216
$\gamma_{(R)}$	0.79 eV
$\hbar\omega_{\max}$	2.97 eV
$L_{\text{p-mode}}$	0.263
$\beta_{\text{p-mode}}$	-0.047
$R_{c/a}$	0.6

Fig. 8-*30*. Parameters extracted from the Mie-fit of the s-Vis-CRD spectrum of Ag_9 clusters supported on BK7.

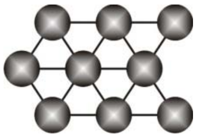

Fig. 8-*31*. Sketch of the gas phase structure of Ag_9 clusters.

8.5.4 Ag Atoms on BK7

In a last experiment, silver atoms are deposited on the backside of a cooled BK7 substrate and investigated using s-Vis-CRD and s-SHG spectroscopy. The coverage of atoms on the surface here is approximately $1 \cdot 10^{13}\,\text{cm}^{-2}$. The obtained spectra are depicted in figure 8-*32*. No spectral features can be observed in the s-Vis-CRD spectrum and neither in the s-SHG spectrum. Spectroscopic absorption measurements of silver atoms can be found in the literature.[148] There, experiments were carried out measuring linear spectra of silver atoms deposited in rare gas matrices at a temperature of 12 K. The spectra show several sharp absorption peaks around a photon energy of 4.1 eV. The s-SHG spectrum of the deposited silver atoms measured in this work (figure 8-*32*) does not show any enhancement of the relative SH intensity in this frequency region, which means that the transitions observed by other groups are either not SHG active (due to the special selection rules of the nonlinear technique), or the signals are under the detection limit of the present spectroscopic setup. In the latter case, the sensitivity of the setup must be improved in order to detect much smaller signals. This can be done e.g. by decreasing the noise level of the s-SHG apparatus. A more detailed discussion of these possibilities is given in the outlook (chapter 10). However, one important information can be gained from the absence of any plasmon absorption band. It shows that the silver atoms do not aggregate to larger clusters under the experimental conditions used for these measurements. This stability of the produced cluster samples is obviously one of the most important requirements for a successful spectroscopic characterization of supported size selected metal clusters which is the aim of this thesis.

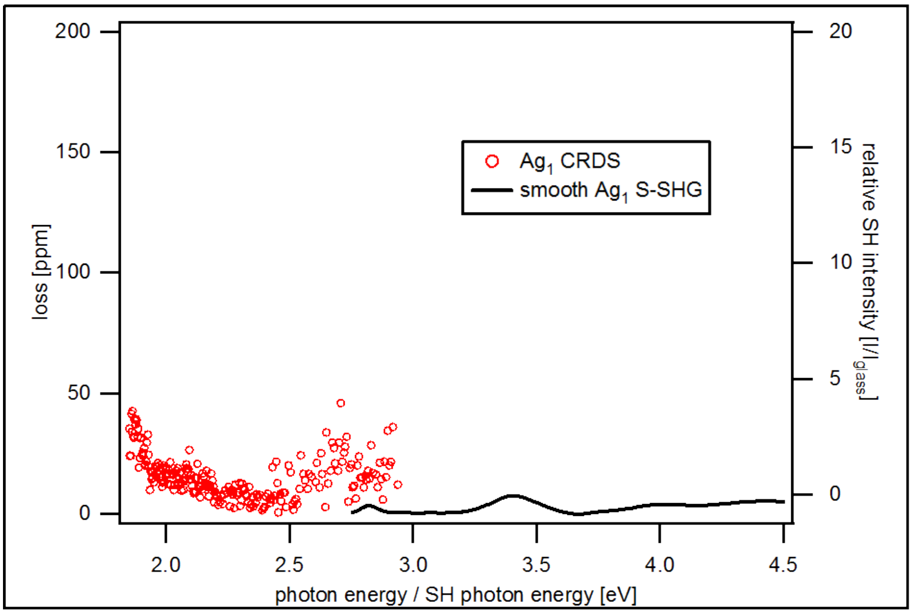

Fig. 8-*32*. s-Vis-CRD and s-SHG spectrum of Ag atoms on BK7. No spectral features from the cluster sample are resolved.

8.6 Conclusion

In chapter 8, it could be shown that coinage metal clusters can be successfully deposited on BK7 glass substrates using the experimental setup presented in chapter 4, and characterized using s-Vis-CRD- and s-SHG spectroscopy, respectively. A detailed investigation of the linear and nonlinear spectroscopic properties was carried out with samples containing supported silver clusters. In the spectra of supported silver nano-particles with an average size of 1.4 nm in diameter, the splitting of the plasmon resonance peak into two peaks, representing the plasmon oscillation parallel to the substrate surface (p-mode) and perpendicular to the substrate surface (s-mode) was observed. This effect could be attributed to a flattening of the particle on the BK7 substrate and described by a theoretical model based on Mie theory. Subsequently, the spectroscopic properties of size selected silver clusters of the sizes Ag_{42}, Ag_{21}, Ag_9, and silver atoms supported on BK7 glass substrates were investigated. The results obtained from these experiments are summarized and discussed in the following.

The most important values which could be extracted from the Mie-fits of the s-Vis-CRD and s-SHG spectra obtained for supported silver clusters of different cluster size are summarized in table 8-*33*.

	Ag_x	Ag_{42}	Ag_{21}	Ag_9	Ag_1	Ag_x(lit.)[91]
V_0 [nm^3]	1.5	0.37	0.21	0.17	-	4.2
$R_{c/a}$	0.78	0.6	0.61	0.6	-	0.86
$\gamma_{(R)[\text{p-mode}]}$ [eV]	0.62	0.5	0.57	0.79	-	0.48
$A_{\text{p-mode}}$	0.5	0.28	0.26	0.34	-	0.6
$\gamma_{(R)[\text{s-mode}]}$ [eV]	1.15	0.97	-	-	-	-
$A_{\text{s-mode}}$	0.74	0.33	-	-	-	-

Table 8-*33*. Summarized values extracted from the Mie-fits of the linear and nonlinear spectra obtained for supported Ag clusters of different cluster sizes. V_0, is the cluster volume, $R_{c/a}$, the axis ratio of the oblate cluster, $\gamma_{(R)}$, is the size dependent damping constant of the plasmon oscillation, and A, is the size independent parameter, describing the size dependency of the damping constant. The indices (p-mode and s-mode) show to which plasmonic oscillation the value is attributed. The caption Ag_x stands for non size selected Ag clusters.

In the column on the right side, there are data listed measured by Kreibig *et al.* for comparison.[87, 88, 91, 101] In their experiments, silver clusters with an average size of 2 nm in diameter supported on a quartz glass substrate were investigated. By comparing their results to the values obtained in this work for the unselected clusters (average cluster size of 1.4 nm in diameter), the values are found to be in rather good agreement. The axis ratio obtained in this work of 0.78 is slightly smaller than the literature value (0.86). A possible reason for that discrepancy is the small size of the silver nano-particles investigated here, which is with an average volume of 1.5 nm^3 almost by a factor of three smaller than the particles investigated by Kreibig *et al.* with a volume of 4.2 nm^3. The influence of the substrate on the particle increases with decreasing cluster size, because the fraction of cluster atoms which are located at the interface cluster-substrate raises. This can lead to a stronger flattening of small particles and thus to a smaller value of $R_{c/a}$. The axis ratio obtained for the Ag_{42} clusters which are smaller than the Ag_x clusters, follows this trend with a value of 0.6. For Ag_{21} and Ag_9 clusters the derived value remains constant at a value of approximately 0.6. However, the validity of computing the axis ratios for Ag_{21} and Ag_9 using the theoretical model based on the classical Mie theory is rather questionable, because for these cluster sizes only one plasmon peak (p-mode) is present. Consequently, such clusters do not have classical properties and more sophisticated quantum mechanical calculations are necessary for a realistic estimation of the cluster shape.

By comparing the damping constant derived from the p-mode plasmon peak of the non size selected cluster sample with the result from the literature, an increase from the literature value of 0.48 eV to the value for Ag_x measured in this work of 0.62 eV can be observed, confirming the cluster size dependency of the plasmon damping. However, the obtained A parameter which is supposed to be independent of cluster size shows a little deviation from 0.6 (lit.) to 0.5 in this work. About the reason for this one can only speculate, one possibility is the different contribution of the chemical interface damping to the value of A, originating from the slightly different compositions of the two substrates (quartz and BK7). A remarkable result of the experiments can be observed, studying the evolution of the derived values for the p-mode plasmon damping constant with cluster size. The trend of increasing damping constant with decreasing cluster size is present for the size selected Ag clusters, but from the larger unselected clusters Ag_x to the small Ag_{42} clusters the damping constant drops from 0.62 eV to 0.5 eV. This is the opposite of what could be expected. A reason for this effect could not be found in the framework of this thesis. The major difference between the Ag_x and the size selected clusters is that in the case of Ag_x, a large distribution of different cluster sizes is present on the substrate. Consequently, the resulting spectra represent the average over all deposited sizes. This could lead to effects which are not considered in the theoretical description. However, further investigation is necessary for clarification.

For Ag_{42} and Ag_{21}, the calculated values for A are close to the theoretically derived value for silver clusters in the gas phase with $A_{size} = 0.25$. The contribution of the chemical interface damping from the substrate would consequently be nearly zero which is in contradiction with the theory. Furthermore, by comparing the values of the A parameters for the s-mode and the p-mode plasmon, it can be observed that for the former larger values are obtained than for the latter (for the two cases, Ag_x and Ag_{42}, where an s-mode plasmon peak could be measured). This result is in good agreement with the theory of the anisotropy of the A parameter for supported metal particles proposed in the literature (see chapter 3.1.5). This anisotropy is introduced by the dependency of the chemical interface damping on the oscillation direction of the plasmon. A plasmon oscillation perpendicular to the substrate surface shows a larger chemical interface damping than the parallel oscillation.

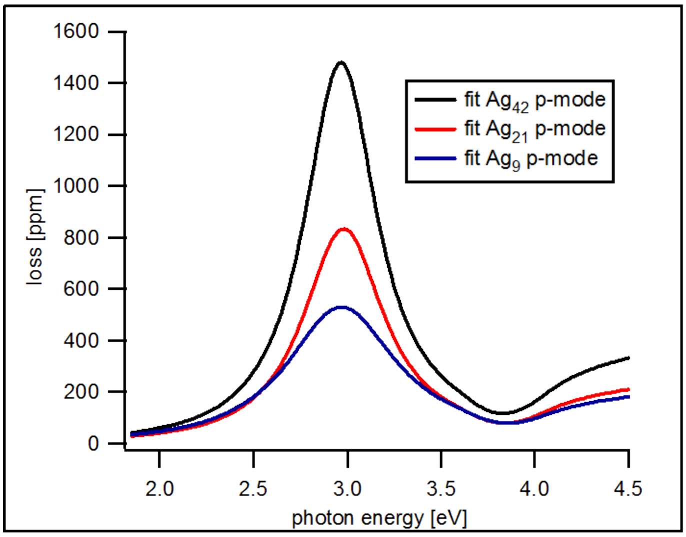

Fig. 8-*34*. Fitted curves of the p-mode plasmon peaks for Ag_{42}, Ag_{21} and Ag_9 clusters on BK7. The peak intensity decreases with decreasing cluster size, whereas the peak width increases.

The fitted curves of the p-mode plasmon peaks for the size selected silver clusters is shown in figure 8-*34*. For decreasing cluster size, the peak intensity decreases with an increasing peak width, as predicted by the theory. The resonance position of the s-mode plasmon peak (measured in the s-SHG spectrum) is blue shifted with respect to the p-mode plasmon peak due to the flattening of the particle (see chapter 3.1.3). Additional shifts of the peak positions originate from the cluster-substrate and the cluster-cluster interactions, leading to a modulation of the local electric field. These local field effects are described by the parameter β which can be calculated for the cluster samples investigated here. However, the theoretically obtained values for the s-mode plasmon peak show a large deviation from the experimentally derived values (from the s-SHG spectra). These deviations most likely originate from the underestimation of the calculated parameter. In general, changes in the local field have a much larger effect on nonlinear than on linear processes. Since the calculation is performed using a linear model and the measured s-SHG spectra are nonlinear spectra, the calculated value may be incorrect. The development of a theoretical model describing nonlinear local field effects is therefore required.

By comparing the spectra of the Ag_{42} and the Ag_{21} clusters, the observed disappearance of the s-mode plasmon peak in the s-SHG spectrum of supported Ag_{21} clusters is remarkable. The mean cluster height of the Ag_{42} on BK7 is calculated to be approximately 3 atomic layers, whereas for the Ag_{21} clusters a value corresponding to approximately two atomic layers is found. This observation indicates that the oscillator strength of the plasmon excitation does not grow linearly with the cluster size, but that there is a minimum size of approximately three atomic layers which is necessary in order to allow for a plasmonic oscillation. The result that the p-mode plasmon band is present down to the Ag_9 cluster (which is very likely to lie flat on the surface) supports this idea, showing that the existence of three atomic layers in the direction of the oscillation of the conducting electrons is sufficient for the excitation of a plasmon inside the cluster. The plasmon resonance is one of the main spectroscopic properties of metals. Consequently, the Ag_{21} cluster and the Ag_9 cluster on BK7 could be classified as two dimensional metals (even if they may have a 3D structure), whereas supported Ag_{42} clusters have metallic properties (plasmons) in all three dimensions. Following that, there should be at least two transitions of cluster types, one from a 3D to a 2D metal (located between Ag_{42} and Ag_{21}), and the other between a 2D metal and a cluster with only molecular properties ($<Ag_9$). The determination of these transitions is one of the main tasks for the future.

The discussion of the results obtained from the measured cluster samples presented in this chapter shows that a part of the investigated optical properties can be described using classical models, whereas other properties strongly deviate from these descriptions and show discontinuous behavior. This observation indicates that the investigated cluster sizes represent the transition from the classical to the semi-classical (quantum mechanical) size regime for supported silver clusters. More exact theoretical calculations based on quantum mechanics to determine cluster geometries on the surface and their linear and nonlinear optical properties could help to better understand the measured spectra and confirm the interpretations which are presented in this work.

9. Summary

In the framework of this thesis, the spectroscopic properties of small supported metal clusters and organic surface adsorbates were investigated under UHV conditions using different laser spectroscopic techniques. Therefore, two specific spectroscopic methods were employed, the highly sensitive surface Cavity Ringdown Spectroscopy (s-CRDS) and the surface Second Harmonic Generation Spectroscopy (s-SHG). The former is applied in the visible range as well as in the infrared range of the electromagnetic spectrum, whereas the latter covers the ultraviolet range. In the ultraviolet and the visible range, the electronic transitions in the clusters and the adsorbate molecules may be measured, whereas in the infrared range vibrational transitions in the organic adsorbates may be probed. In the following sections, the more crucial results that were obtained are summarized and discussed.

9.1. Spectroscopic Setup

A spectroscopic setup for measuring the optical properties of surface adsorbates in low coverage (< 10 % of a monolayer) was successfully installed. The setup was designed to allow for the fast switching between the different spectroscopic methods (s-Vis-CRD, s-IR-CRD, s-SHG) without any re-alignment of the setup, and was adapted for use in an ultrahigh vacuum chamber. Furthermore, the apparatus for the sample preparation was optimized (involving design of the sample holder, electron source etc.) for the application of the spectroscopic techniques. As a result of these improvements to the experimental apparatus, a unique state-of-the-art experimental setup was created which offers a large variety of experimental possibilities, such as the production and highly sensitive spectroscopic characterization of metal cluster samples over a wide wavelength range from the ultraviolet to the infrared.

9.2 Characterization of Substrate Materials

The requirements which must first be fulfilled by the substrates in order to be suitable for use with the afore-mentioned spectroscopic methods were defined and discussed in chapter 6. It was shown that only materials which have either a cubic or amorphous crystal structure are appropriate substrates because birefringence must be avoided. Furthermore, only thin substrate slides with very smooth surfaces can be used in order to guarantee a high sensitivity of the s-CRD spectroscopy. A surface analysis apparatus based on small angle laser reflection, which allows the detection of surface deformations in the sub-µm range was designed and successfully used in order to test different substrates for their adequacy. The substrate with the highest optical quality among the tested materials was found to be a 130 µm thin Borosilicate glass slide (BK7) which was then almost exclusively used as sample substrate for the investigation of supported clusters and adsorbed organic molecules. A special cleaning procedure for these substrates consisting of two steps was presented. The first step involved the removal of dust and other impurities under ambient conditions, whereas the second was carried out after transferring the substrate into the UHV camber, and had the purpose of cleaning the surface on the atomic scale by sputtering it with Ar ions. The sputtering process was characterized using the s-CRD spectroscopy where the roughening of the surface could be followed by the induced increase in light scattering. From such measurements the optimal sputtering conditions for adequate cleaning of the BK7 substrate were extracted. Furthermore, the linear and nonlinear optical properties of the substrates were investigated. A theoretical description of the nonlinear substrate properties was also presented and the comparison of the calculated spectrum with the measured nonlinear spectrum (s-SHG spectrum) showed good agreement. The challenge which had to be overcome here was the description of the interferences of the two second harmonic beams generated at both surfaces of the substrate. On the basis of this theoretical description, a data treatment procedure was developed allowing for the use of the measurement of the bare substrate as reference for the correction of the nonlinear spectra obtained from a sample with any surface adsorbate (e.g. metal clusters or organic molecules). The successful mathematical description (see chapter 6) of the nonlinear spectrum of the substrate is a crucial step, necessary for the extraction of the nonlinear spectra from the measured raw data and was subsequently used throughout this thesis.

9.3 Surface Spectroscopy of Organic Molecules

In order to test the reliability and to determine the sensitivity of the spectroscopic setup, a reference sample with well known optical properties was investigated, consisting of the laser dye Rhodamine 110 coated onto a BK7 glass substrate. s-Vis-CRD, s-IR-CRD, and s-SHG spectra were recorded and compared to spectra obtained from the dye dissolved in ethanol using commercial UV-Vis and FT-IR spectrometers (for the FT-IR measurement the dye was coated onto a KBr window). The comparison showed good agreement between the spectra obtained from the different methods and confirmed the reliability of the s-CRD/s-SHG spectroscopic setup. Small but significant differences between the measured spectra and the spectra obtained from the standard spectroscopic methods could be attributed to surface effects which occur for low coverages, such as those of the coated samples. From the experiments, the sensitivities of the different spectroscopic methods in the presented setup were extracted. The highest sensitivity was achieved by the s-Vis-CRD method, which was shown to be capable of detecting surface coverages of Rhodamine 110 of less than 0.1 % of a monolayer (approximately 10^{11} molecules per cm^2). The s-IR-CRD method meanwhile was capable of detecting coverages of Rhodamine 110 down to approximately 1 % of a monolayer. The reduced sensitivity of the s-IR-CRD technique originated from the small absorption cross sections of organic molecules in the infrared range compared to those in the UV-Vis range. The sensitivity of the s-SHG setup was not determined in the framework of this thesis; however, since the s-SHG shows a maximum in its signal for exactly one monolayer of molecules (because of the special selection rules) it was deduced to be sub-monolayer sensitive which is confirmed by measurements present in the literature. All of these results showed that all applied spectroscopic methods (in the presented setup) possess a sensitivity which is high enough to detect adsorbate coverages which are far below one monolayer. Furthermore, this enabled the investigation of the impact of the surface on the properties of the coated molecules.

The potential of the presented setup in surface science was demonstrated by measurements of a sample coated with 1,1'-Bi-2-naphthol (Binol). This molecule slowly evaporates from the surface under UHV conditions at room temperature, a process that could be followed using s-IR-CRD spectroscopy. From the evaporation speed measured at different temperatures, the binding energy of the bond between the molecule and the surface was calculated (in rough approximation) to be a value of approximately 6.5 kJ/mol. In principle, the sub-monolayer sensitivity of the s-IR-CRD setup allows the study of evaporation processes of adsorbed molecules as function of the coverage down to about 1 % of a monolayer, therefore yielding important information about the kinetics of surface processes. The promising results obtained encourage further investigations in this field.

s-SHG measurements were found to provide information about the molecular orientation of adsorbates on a surface. This was demonstrated using recorded nonlinear spectra of samples coated with {5}Helicene molecules and 4,4'''-Bis-(2-butyloctyloxi)-p-quaterphenyl (BiBuQ), respectively. Even from the existence or absence of SHG activity in combination with the geometry of the molecule, some general statements about their orientations could be made, as shown in chapter 7. The results obtained in this section showed that the combination of linear and nonlinear spectroscopic techniques over this broad wavelength range provides a powerful tool for the investigation of surface adsorbates.

9.4 Supported Metal Clusters

Metal clusters were successfully deposited on BK7 glass substrates. The deposition was confirmed by images measured by Atomic Force Microscopy (AFM) under ambient conditions (this work was carried out in Marseille in the group of Prof. C. Henry at the CINaM-CNRS in the framework of the "Deutsch Französische Hochschule"). The spatial distribution of the clusters was determined by a surface loss mapping technique using s-CRD spectroscopy. Here, the photon loss was recorded as function of the substrate position at a fixed wavelength. The measured raw data were transformed into a two dimensional image showing the cluster spot as approximately Gaussian shaped. It was also demonstrated that the sputtering of the surface completely removes the deposited clusters and leaves a blank substrate. A similar surface mapping was subsequently carried out using the s-SHG spectroscopy, showing a well resolved cluster spot. Both spectroscopic methods confirmed the successful deposition of the metal particles. The determination of the spatial distribution of the clusters was crucial for the calculation of the cluster coverage on the surface. This calculation was performed for a sample with supported silver clusters.

The nonlinear s-SHG spectra of supported coinage metal nano-particles were recorded. The sizes of the particles ranged between 1 and 3 nm in diameter. In the spectra of each sample a broad peak was observed which could be attributed to a plasmonic excitation of the conducting electrons inside the particles. These results showed that plasmonic oscillations in a small supported metal particle can give rise to a signal at the second harmonic frequency. Due to the selection rules of the SHG process, such a SH signal must exclusively originate from an oscillation inside an asymmetric electric potential (this was shown in chapter 2). In supported nano-particles this is the case for a plasmonic oscillation perpendicular to the substrate surface. A comparison between a measurement of the angular dependency of the SH signal for supported Pd nano-particles and its calculation for the perpendicular oscillation mode confirmed this origin of the second harmonic radiation. Consequently, it was shown that the s-SHG spectroscopy only probes the plasmonic properties of these small supported metal particles along the particle height (perpendicular to the substrate surface).

In the next part of the thesis, the optical properties of small supported silver clusters were investigated in greater detail. The average size of the non-size selected particles produced by the cluster source and deposited onto the substrate was found to be around 1.4 nm in diameter. The s-Vis-CRD spectrum of the sample showed the onset of an absorption peak towards higher photon energies (the measured spectrum ranged from 1.8 e V to 2.9 e V). Using a theoretical description based on Mie theory (presented in chapter 3), the raw data were fitted, identifying the measured spectrum as the onset of a plasmon absorption peak of the particle with its maximum located at 3.12 eV. The high accuracy of the measured raw data using s-CRD spectroscopy in combination with the small deviation of the fit from the measured curve made the fit trustworthy. The s-SHG spectrum of the same sample showed a broad peak with a maximum at 3.7 eV which could be attributed to a plasmonic excitation. Obviously, the positions of the plasmon peak determined from the spectra of the two different spectroscopic methods differ from each other. Using an extension of the classical mathematical description of the optical properties of small metal particles towards non-spherical geometries (presented in chapter 3), this effect was identified as a splitting of the plasmon peak into two resonances for oblate shaped particles. According to the calculation, the peak observed in the s-Vis-CRD measurement originated from the plasmonic oscillation parallel to the surface of the substrate, whereas the peak observed in the s-SHG spectrum belonged to the oscillation perpendicular to it. It could be shown that this interpretation is in full agreement with the selection rules of the s-SHG spectroscopy. The existence of two plasmonic modes inside the silver particles on the surface, from which one is SHG inactive was additionally confirmed by stability measurements using s-SHG spectroscopy. By irradiating the sample with laser light of a photon energy close to 3.12 e V the silver particles were evaporated from the surface indicating a strong absorption of the fundamental light, although no enhanced SH signal could be observed in this region (for more details see chapter 8).

From the position of the plasmon peak obtained from the s-Vis-CRD spectrum, the mean axis ratio of the oblate silver particles was derived to be a value of 0.78 which is slightly smaller than the value obtained by Hövel *et al.* for supported 2 nm silver clusters (0.86). A possible reason for this discrepancy could be given and justified, based on the idea that the reduced cluster size of the silver clusters investigated in this work leads to a stronger flattening of the particles due to an enlarged cluster-surface interaction. However, taking the values obtained from the s-Vis-CRD spectrum and subsequently calculating the position of the second SHG active plasmon mode, the result was found not to match exactly with the measured plasmon peak in the s-SHG spectrum. The measured peak was more blue shifted than predicted $(\Delta\hbar\omega_{\max} = 0.19 \text{ eV})$. This discrepancy was discussed in chapter 8 and was attributed to the underestimation of the local field parameter for nonlinear processes in the calculation. This attribution could be justified in a discussion about the impact of the plasmon field enhancement on nonlinear processes. Furthermore, the width of the plasmon peak was discussed on basis of the model of the "free mean path effect" for the oscillating electrons. The different damping constants derived for the two different oscillation modes suggested a different contribution of the so called "interface damping" to the overall damping constant (see chapter 8). This anisotropy of the interface damping has also been predicted theoretically; however, further measurements are needed to investigate this finding in more detail.

Following the investigation of non-size selected clusters using s-CRD and s-SHG spectroscopy, the focus was then shifted to the study of size selected Ag clusters. Here, the linear and nonlinear spectra of samples with the cluster sizes Ag_{42}, Ag_{21}, Ag_9 and silver atoms on BK7 were measured. In both, the s-SHG and the s-CRD spectra of the supported Ag_{42} clusters a plasmon resonance peak was observed, indicating the existence of a collective oscillation of the conducting electrons parallel and perpendicular to the surface. The spectra showed a larger splitting of the two resonances than it was the case for the non-size selected supported silver nano-particles, which suggested a stronger flattening of the Ag_{42} clusters to an axis ratio of approximately 0.6. In the s-SHG spectra of all other samples containing smaller silver clusters than Ag_{42}, there was no plasmonic resonance peak present, suggesting the breakdown of the collective electron oscillation perpendicular to the substrate surface between the cluster sizes Ag_{42} and Ag_{21}. The large difference between the nonlinear activities of the samples containing those two cluster sizes (factor of about 60) cannot be simply attributed to a scaling effect (which would lead to a factor of two) but instead indicates a drastic change in the excitation process. However, the s-CRD spectra of the Ag_{21} and Ag_9 clusters showed a plasmon peak at approximately the position where it was found in the s-CRD spectrum of the Ag_{42} clusters. These observations showed that supported Ag_{21} and Ag_9 clusters allow for a plasmonic oscillation parallel to the surface, whereas the perpendicular plasmon mode is inactive. Consequently, those clusters could be classified as two dimensional metals (even if they may have a 3D structure) since they possess clear metallic characteristics parallel to the surface but not along their height. The approximate calculations of the cluster mean heights yielded for Ag_{42} a value corresponding to about three atomic layers and for Ag_{21}

of two atomic layers. Based on these results, a three atomic layer model was proposed suggesting that three atomic layers are needed in supported silver clusters to allow for a collective oscillation of the conducting electrons. This model is in good agreement with the existence of a plasmon oscillation parallel to the surface for Ag_9 clusters since it is likely that those clusters form two dimensional islands on surfaces (confirmed by theory). Furthermore, the s-CRD spectra of Ag_{42}, Ag_{21}, and Ag_9 showed an increasing peak width with decreasing cluster size, which can be attributed to the increased damping of the plasmon oscillation originating from the mean free path effect of the conducting electrons.

The spectra of the single supported silver atoms did not show any spectroscopic features. The electronic transitions of silver atoms could be expected at a photon energy of about 4 eV thus in the range which is measured with the s-SHG spectroscopy. However, in this region nothing could be observed in the nonlinear spectra, indicating that either those transitions are not SHG active or their spectroscopic signal is under the detection limit of the s-SHG setup. The same observation was made in the s-SHG spectra of Ag_9 and Ag_{21}. These results suggested that only collective electron oscillations (plasmons) give rise to a significant signal at the second harmonic frequency. The reason for this is still to be found. So far, using the setup presented in this thesis, the transition from metallic clusters to particles with "molecule like" character must be determined by the disappearance of the plasmon peak in the spectra. However, from the results in this work, it can be concluded that this transition seems to take place at cluster sizes between 42 and 21 atoms for silver. Further measurements should give more precise answers to the questions which remain partly unanswered in this thesis.

10. Outlook

In this chapter, several suggestions for further investigations into the electronic properties of supported metal clusters are proposed. The ideas are based on the results that have been obtained within the work of this thesis and represent possible further characterization steps which could be carried out using the presented apparatus. Additionally, some small modifications to the spectroscopic setup are proposed, which would enlarge the experimental possibilities and increase the sensitivity of the spectroscopic methods.

10.1 Cluster Size Dependency of the Nonlinear Plasmon Excitation

The observed disappearance of the SHG activity for small silver clusters (Ag_N, $N \leq 21$) suggests a breakdown of the plasmon oscillation perpendicular to the surface for such small particles. So far, the exact cluster size where this transition takes place is not determined, however, it is probably located between the sizes Ag_{42} and Ag_{21}. A systematic investigation of the nonlinear properties of small size selected silver clusters between these two measured sizes should enable the exact size where this transition takes place to be determined. Furthermore, the investigation of the SHG activity as function of the cluster size in this size range could yield interesting information because it is likely that the cluster geometry plays an important role. By comparing these results to theoretical calculations, changes in the cluster geometry for different cluster sizes could consequently be identified. Investigating the cluster size dependency of the position of the plasmon resonance in the s-SHG spectrum and the size dependency of the width of the plasmon peak will yield additional information about the geometry and electronic structure of the particles, as well as the interaction between the clusters and the surface. Here, the observed anisotropy of the chemical interface damping is an especially promising field of investigation because this effect is directly related to the cluster-surface interaction. However, a detailed theoretical description of the nonlinear properties of these small supported clusters will be essential for an unambiguous interpretation of the obtained data.

10.2 Nonlinear Characterization of the Parallel Plasmon Mode

Due to the selection rules of the s-SHG spectroscopy, the plasmon oscillation mode parallel to the substrate surface is not SHG active and can thus not be directly probed by the second order nonlinear spectroscopy. Furthermore, the limited range of the s-CRD spectroscopy does not allow for the measurement of the entire plasmon peak for silver clusters using the linear technique. However, it is possible to determine its exact position using a destructive technique. In chapter 8.4.3, it could be shown that the irradiation of the cluster sample with strong light pulses at a fundamental photon energy which is close to the transition energy of this plasmon mode leads to the evaporation of the clusters from the surface. The decreasing number of clusters can be followed by detecting the second harmonic signal at the peak position of the SHG active plasmon mode perpendicular to the substrate surface, as was done in the stability measurement in chapter 8.4.3. The evaporation speed of the clusters is determined by the quantity of energy transfer from the fundamental light beam into the clusters and thus by the linear absorption coefficient. Measuring the evaporation speed as a function of the photon energy at a constant laser pulse energy should yield the linear absorption spectrum. In this way, the indirect measurement of this SHG inactive oscillation using s-SHG spectroscopy is possible.

A second possibility for the measurement of the plasmon mode parallel to the substrate surface, is the use of a third order nonlinear spectroscopy, such as Third Harmonic Generation Spectroscopy (THG)[149, 150] or Four Wave Mixing Spectroscopy (FWM).[151, 152] Third order nonlinear processes are not restricted to media with non-centro-symmetric electric potentials which makes the parallel plasmon active to a third order nonlinear oscillation. The drawback of the third order spectroscopic techniques is, however, the reduced conversion efficiency compared to second order processes and the loss of the surface sensitivity due to the different selection rules. Consequently, bulk contributions from the substrate would complicate the identification of the signal originating from the clusters. On the other hand, the implementation of a third order spectroscopic technique in the existing spectroscopic setup should be possible without significant modifications because the major parts of the setup can be used for most of the nonlinear spectroscopic techniques.

10.3 Pico-Second Laser System

As shown in chapter 2.2.1, the intensity of the generated second harmonic beam in an s-SHG experiment is proportional to the square of the intensity of the fundamental beam. Since the intensity of an electromagnetic wave is defined as energy per time and area, it is possible to increase the intensity of the fundamental laser beam by using short laser pulses. The present OPO laser system supplies laser pulses of 7 ns pulse length at a maximal pulse energy of 10 mJ (see chapter 5.1.1). Typical tunable picosecond laser systems (e.g. optical parametric generators OPG) generate laser pulses of 30 ps pulse length at a maximal pulse energy of 1 mJ. The intensity of the generated second harmonic radiation in an s-SHG experiment is consequently increased by a factor of 544 for the OPG laser source compared to the OPO. Since the number of photons in a laser pulse is proportional to the pulse energy and thus to the intensity multiplied with the pulse length, the number of SH photons generated per laser pulse using the OPG system is increased by a factor of approximately 2.3 in comparison to the nanosecond laser system. At the same time, the fundamental beam energy per pulse for the picosecond laser system is a factor of 10 smaller (1 mJ) than for the OPO system (10 mJ), which minimizes the total energy transfer into the measured sample, and thus reduces the risk of photo damage. These considerations show that using picosecond laser pulses, the intensity of the second harmonic beam generated, as well as the total number of generated SH photons per pulse, can be raised whereas the destructive potential of the fundamental beam is simultaneously reduced. The former would lead to larger SH signals in the s-SHG measurement and would thus facilitate the increase in the detection limit. Consequently, using such a laser system, the sensitivity and reliability of the s-SHG experiments could essentially be improved. This could help to investigate the molecule-like transitions of very small supported metal clusters which are predicted by theory.

10.4 Ligand Stabilized Clusters

UV-Vis measurements of silver nano-particles that are protected by thiol-ligands show the existence of plasmonic excitations in the metal core.[153-155] The plasmon resonance frequency is red shifted to 400 nm - 480 nm (2.57 eV - 3.1 eV photon energy), which is in agreement with the theoretical prediction (se chapter 3.2) because the electron density in the clusters is reduced by the chemical bond to the ligands. This makes such samples rather suitable for investigations using the s-Vis-CRD spectroscopy, because the transition lies within the applicable range of the spectroscopic technique. The experimental setup is equipped with an evaporator for organic molecules which allows organic ligands to be supplied to the cluster samples under UHV conditions. From the investigation of supported ligand stabilized clusters (LSC), information about the cluster reactivity as a function of the cluster size can be gained which would be an important step towards understanding the catalytic properties of supported metal clusters. The preparation of the supported LSC's using the presented experimental setup has the advantage, compared to the standard preparation method in liquid phase, that the sample can be produced step by step and the cluster size can be precisely defined. Measurements of the plasmonic transitions in such samples will yield information about the character of the metal ligand bond which is expressed by the quantity of the red shift of the peak and its width, which is influenced by the chemical interface damping. Furthermore, the impact of the cluster on the electronic properties of the ligands can be probed using s-Vis-CRD and s-SHG spectroscopy. Finally, changes in the vibrational transition frequencies in the organic adsorbates studied by s-IR-CRD spectroscopy give additional information about the cluster-ligand interaction. Combining all these measurements from a single sample will allow for a detailed characterization of the prepared cluster systems. The results obtained could then be compared to the results from measurements of LSC's prepared in liquid phase and should provide answers to many questions about the reactivity of metal clusters which still remain open.

10.5 Measurement of Chiral Cluster Samples

One of the important future projects will be the investigation of chiral cluster samples. The aim here is to perform enantioselective cluster catalysis representing the ultimate form of organic catalysis. A spectroscopic detection of chirality will be crucial in order to characterize the prepared samples. One possibility to investigate the chirality of a molecule (cluster) is the measurement of its circular dichroism. Chiral substances show different absorptions cross sections for right handed and left handed circularly polarized light. These effects are enhanced for nonlinear processes, such as the generation of the second harmonic.[156] In order to perform measurements of the nonlinear circular dichroism, the existing s-SHG setup could be modified by introducing a quarter wave plate or a Pockels cell, generating circularly polarized light. In such experiments, the different intensities of the SH radiation from a chiral sample for the two circular directions would be measured as a function of the fundamental photon energy, yielding the spectrum of the nonlinear circular dichroism. This technique (Circular

Dichroism surface Second Harmonic Generation spectroscopy, CD-s-SHG) has been successfully used by other groups and is described in the literature.[157] As a starting point, the measurement of (R)- and (S)-Binol coated onto a substrate seems suitable. These enantiomers of the Binol molecule were already used for CD-s-SHG measurements[141] and the coated racemic mixture has been successfully used for s-SHG measurements using the setup presented in this thesis (see chapter 7.2.2). Since the modifications of the spectroscopic setup for these purposes are not drastic, the installation of the CD-s-SHG spectroscopy is a promising project.

A second possibility to identify chirality is the property of chiral substances to turn the polarization plane of transmitting linearly polarized light if only one enantiomer is present.[158] Small changes of the polarization can already be detected by s-CRD spectroscopy. The reason for this is that the substrate is placed at Brewster's angle inside the optical cavity. The Brewster's angle, where the reflection of the light beam at the surface of a substrate is zero only exists for p-polarized light. The s-polarized component of a light beam for the substrate at this angle leads to the reflection of about 30 % of its intensity at the substrate surfaces (for BK7 glass). This reflected fraction of the light is removed from the oscillating beam in the resonator which increases the cavity loss. Turning the polarization plane of p-polarized light, the resulting beam can be described as superposition of the p-polarized and the s-polarized component. This process consequently leads to an increased cavity loss and can be detected by s-CRD spectroscopy. The high sensitivity of the s-CRD technique allows for the detection of polarization changes in the range of 10^{-5} degrees, corresponding to an increased cavity loss between 3 ppm and 30 ppm. This extraordinarily high sensitivity to detect changes in the polarization of the laser beam could be sufficient to detect the polarization effects induced by enantiopure chiral surface adsorbates.

The spectroscopic investigation of chiral cluster samples will remain a great challenge, however, the modifications of the existing spectroscopic setup proposed here, in combination with the use of the s-CRD technique as mentioned above, are promising methods for the characterization of these chiral samples.

Acknowledgement / Danksagung

Abschließend möchte ich mich bei den Personen bedanken, die dazu beigetragen haben, dass diese Arbeit entstehen konnte.

Meinen besonderen Dank möchte ich dabei an meinen Doktorvater Prof. Dr. Ueli Heiz richten, der es mir ermöglicht hat, dass ich an diesem interessanten Projekt zu arbeiten. Des Weiteren möchte ich ihm für die stetige Unterstützung während meiner Arbeit und den außerordentlich freundschaftlichen Umgang danken, die das Arbeiten an dem Projekt sehr angenehm gemacht haben.

Großer Dank geht auch an Prof. Dr. Ulrich Boesl für viele sehr hilfreiche wissenschaftliche Diskussionen und manche entscheidende Tipps beim Aufbau der spektroskopischen Methoden, ohne die eine Realisierung der Messungen nicht möglich gewesen wäre. Danken möchte ich auch PD Dr. F. Esch für die immer sehr motivierenden Gespräche und seine zahlreichen Hilfestellungen während meiner Arbeit.

Sehr großen Anteil an dem Erfolg der Messungen hat Dr. Aras Kartouzian, der mit mir zusammen praktisch über die gesamte Zeit an dem Aufbau und der Charakterisierung der spektroskopischen Methoden gearbeitet hat. Besonders der Aufbau der s-SHG Spektroskopie wäre ohne ihn kaum möglich gewesen. Dabei hat die sehr gute Zusammenarbeit einen großen Beitrag dazu geleistet, dass ich mich bei der Arbeit sehr wohl gefühlt und die Zeit als wissenschaftlich überaus spannend empfunden habe. Dasselbe gilt auch für meinen Arbeitskollegen Philipp Heister, dem ich darüber hinaus für die wichtigen Verbesserungen an dem experimentellen Aufbau und die überaus entspannte Atmosphäre in unserem Labor danken möchte.

Meinen herzlichen Dank richte ich an Sabine Gerlach und Constantin Walenta, die bei den Messungen eine sehr große Hilfe waren. Des Weiteren danke ich allen Forschungspraktikanten, die ich während meiner Doktorarbeit betreut habe, für ihre Beiträge.

Zu besonderem Dank bin ich vor allem den Mitarbeitern der Werkstätten verpflichtet, die in sehr professioneller Arbeit die technische und apparative Umsetzung des Projekts ermöglicht haben.

Besonders hervorgehoben werden muss der Beitrag von Dr. Sean Ashton, der mir in mühsamer Kleinarbeit geholfen hat, diese Arbeit auf ein akzeptables sprachliches Niveau zu bringen, wofür ich ihm überaus dankbar bin.

Gerne möchte ich mich auch bei den restlichen Mitarbeitern der Arbeitsgruppen Heiz und Boesl für deren Unterstützung und die nette Arbeitsatmosphäre danken.

Meinen Eltern danke für die jahrelange Unterstützung und meiner Mutter für die Hilfe beim Auffinden von letzten Fehlern in der Arbeit.

References

1. C. N. R. Rao, G. U. Kulkarni, P. J. Thomas and P. P. Edwards, Chemistry – A European Journal **8** (1), 28-35 (2002).
2. P. K. Jain, X. Huang, I. H. El-Sayed and M. A. El-Sayed, Accounts of Chemical Research **41** (12), 1578-1586 (2008).
3. H. Ditlbacher, B. Lamprecht, A. Leitner and F. R. Aussenegg, Opt. Lett. **25** (8), 563-565 (2000).
4. J. Caldwell, The Journal of Clinical Pharmacology **32** (10), 925-929 (1992).
5. A. Kaldor, D. M. Cox, R. O. Brickman and P. Fayet, Abstr Pap Am Chem S **196**, 52-Phys (1988).
6. R. L. Whetten, D. M. Cox, D. J. Trevor and A. Kaldor, Phys Rev Lett **54** (14), 1494-1497 (1985).
7. L. Holmgren, M. Andersson and A. Rosen, Surf Sci **331**, 231-236 (1995).
8. A. Berces, P. A. Hackett, L. Lian, S. A. Mitchell and D. M. Rayner, J Chem Phys **108** (13), 5476-5490 (1998).
9. E. K. Parks, G. C. Nieman, K. P. Kerns and S. J. Riley, J Chem Phys **108** (9), 3731-3739 (1998).
10. G. S. IckingKonert, H. Handschuh, G. Gantefor and W. Eberhardt, Phys Rev Lett **76** (7), 1047-1050 (1996).
11. Y. Shi and K. M. Ervin, J Chem Phys **108** (5), 1757-1760 (1998).
12. Z. Xu, F. S. Xiao, S. K. Purnell, O. Alexeev, S. Kawi, S. E. Deutsch and B. C. Gates, Nature **372** (6504), 346-348 (1994).
13. U. Heiz, F. Vanolli, A. Sanchez and W. D. Schneider, J Am Chem Soc **120** (37), 9668-9671 (1998).
14. S. Abbet, A. Sanchez, U. Heiz, W. D. Schneider, A. M. Ferrari, G. Pacchioni and N. Rösch, Surf Sci **454–456** (0), 984-989 (2000).
15. T. Mallat, E. Orglmeister and A. Baiker, Chem Rev **107** (11), 4863-4890 (2007).
16. W. P. Halperin, Reviews of Modern Physics **58** (3), 533-606 (1986).
17. M.-C. Daniel and D. Astruc, Chem Rev **104** (1), 293-346 (2003).
18. D. A. Evans, M. Alonso, R. Cimino and K. Horn, Phys Rev Lett **70** (22), 3483-3486 (1993).
19. O. Cheshnovsky, S. H. Yang, C. L. Pettiette, M. J. Craycraft and R. E. Smalley, Rev Sci Instrum **58** (11), 2131-2137 (1987).
20. G. Gantefor, M. Gausa, K. H. Meiwesbroer and H. O. Lutz, J Chem Soc Faraday T **86** (13), 2483-2488 (1990).
21. M. L. Polak, G. Gerber, J. Ho and W. C. Lineberger, J Chem Phys **97** (12), 8990-9000 (1992).
22. M. H. Schaffner, F. Patthey, W. D. Schneider and L. G. M. Pettersson, Surf Sci **402** (1-3), 450-453 (1998).
23. L. H. Dubois, P. K. Hansma and G. A. Somorjai, Applications of Surface Science **6** (2), 173-184 (1980).
24. W. Mahoney, D. M. Schaefer, A. Patil, R. P. Andres and R. Reifenberger, Surf Sci **316** (3), 383-390 (1994).
25. N. Nilius, T. M. Wallis and W. Ho, Phys Rev Lett **90** (18) (2003).
26. A. Piednoir, E. Perrot, S. Granjeaud, A. Humbert, C. Chapon and C. R. Henry, Surf Sci **391** (1-3), 19-26 (1997).
27. U. Heiz, F. Vanolli, L. Trento and W. D. Schneider, Rev Sci Instrum **68** (5), 1986-1994 (1997).
28. K. Christmann, *Introduction to Surface Physical Chemistry*. (Springer, 1991).

29. J. A. Creighton and D. G. Eadon, Journal of the Chemical Society, Faraday Transactions **87** (24) (1991).
30. M. J. Hostetler, C.-J. Zhong, B. K. H. Yen, J. Anderegg, S. M. Gross, N. D. Evans, M. Porter and R. W. Murray, J Am Chem Soc **120** (36), 9396-9397 (1998).
31. M. J. Hostetler, J. J. Stokes and R. W. Murray, Langmuir **12** (15), 3604-3612 (1996).
32. A. C. Templeton, M. J. Hostetler, C. T. Kraft and R. W. Murray, J Am Chem Soc **120** (8), 1906-1911 (1998).
33. A. Herrmann, M. Hofmann, S. Leutwyler, E. Schumacher and L. Wöste, Chem Phys Lett **62** (2), 216-222 (1979).
34. D. E. Powers, S. G. Hansen, M. E. Geusic, A. C. Puiu, J. B. Hopkins, T. G. Dietz, M. A. Duncan, P. R. R. Langridge-Smith and R. E. Smalley, The Journal of Physical Chemistry **86** (14), 2556-2560 (1982).
35. M. F. Jarrold and K. M. Creegan, Chem Phys Lett **166** (2), 116-122 (1990).
36. W. Harbich, S. Fedrigo and J. Buttet, Chem Phys Lett **195** (5-6), 613-617 (1992).
37. S. Fedrigo, W. Harbich and J. Buttet, Phys Rev B **47** (16), 10706-10715 (1993).
38. F. Conus, J. T. Lau, V. Rodrigues and C. Felix, Rev Sci Instrum **77** (11), 113103-113106 (2006).
39. W. Harbich, S. Fedrigo and J. Buttet, Zeitschrift für Physik D Atoms, Molecules and Clusters **26** (1), 138-140 (1993).
40. J. J. Scherer, J. B. Paul, A. OKeefe and R. J. Saykally, Chem Rev **97** (1), 25-51 (1997).
41. G. Berden, R. Peeters and G. Meijer, Int Rev Phys Chem **19** (4), 565-607 (2000).
42. M. D. Wheeler, S. M. Newman, A. J. Orr-Ewing and M. N. R. Ashfold, Journal of the Chemical Society, Faraday Transactions **94** (3), 337-351 (1998).
43. S. Wu, P. Dupre, P. Rupper and T. A. Miller, The Journal of Chemical Physics **127** (22), 224305-224310 (2007).
44. S. N. Mikhailenko, W. Le, S. Kassi and A. Campargue, Journal of Molecular Spectroscopy **244** (2), 170-178 (2007).
45. C.-Y. Chung, J. F. Ogilvie and Y.-P. Lee, The Journal of Physical Chemistry A **109** (35), 7854-7858 (2005).
46. N. R. Pillsbury, J. Choo, J. Laane and S. Drucker, The Journal of Physical Chemistry A **107** (49), 10648-10654 (2003).
47. A. O'Keefe and D. A. G. Deacon, Rev Sci Instrum **59** (12), 2544-2551 (1988).
48. J. M. Antonietti, M. Michalski, U. Heiz, H. Jones, K. H. Lim, N. Rosch, A. Del Vitto and G. Pacchioni, Phys Rev Lett **94** (21) (2005).
49. R. Engeln, G. von Helden, A. J. A. van Roij and G. Meijer, J Chem Phys **110** (5), 2732-2733 (1999).
50. S. Gilb, K. Hartl, A. Kartouzian, J. Peter, U. Heiz, H. G. Boyen and P. Ziemann, Eur Phys J D **45** (3), 501-506 (2007).
51. A. Kartouzian, M. Thamer, T. Soini, J. Peter, P. Pitschi, S. Gilb and U. Heiz, J Appl Phys **104** (12) (2008).
52. A. C. R. Pipino, J. P. M. Hoefnagels and N. Watanabe, J Chem Phys **120** (6), 2879-2888 (2004).
53. I. M. P. Aarts, B. Hoex, A. H. M. Smets, R. Engeln, W. M. M. Kessels and M. C. M. van de Sanden, Appl Phys Lett **84** (16), 3079-3081 (2004).
54. K. Egashira, A. Terasaki, T. Kondow, A. Terasaki and T. Kondow, J Chem Phys **126** (22) (2007).
55. M. A. Everest, V. M. Black, A. S. Haehlen, G. A. Haveman, C. J. Kliewer and H. A. Neill, J Phys Chem B **110** (39), 19461-19468 (2006).
56. R. N. Muir and A. J. Alexander, Phys Chem Chem Phys **5** (6), 1279-1283 (2003).

57. J. M. Herbelin, J. A. McKay, M. A. Kwok, R. H. Ueunten, D. S. Urevig, D. J. Spencer and D. J. Benard, Appl. Opt. **19** (1), 144-147 (1980).
58. A. J. Ramponi, F. P. Milanovich, T. Kan and D. Deacon, Appl. Opt. **27** (22), 4606-4608 (1988).
59. A. Gerrard, *Introduction to Matrix Methods in Optics*. (Dover Pubn Inc, 1994).
60. A. Kartouzian, M. Thämer and U. Heiz, physica status solidi (b) **247** (5), 1147-1151 (2010).
61. A. Kartouzian, Dissertation, Technische Universität München, 2010.
62. Y. R. Shen, *The Principles of Nonlinear Optics*. (Wiley-Interscience, 2002).
63. Y. R. Shen, Annu Rev Phys Chem **40**, 327-350 (1989).
64. A. Bratz and G. Marowsky, Molecular Engineering **1** (1), 59-65 (1991).
65. T. Inoue, M. Moriguchi and T. Ogawa, Thin Solid Films **350** (1-2), 238-244 (1999).
66. G. J. Simpson, S. G. Westerbuhr and K. L. Rowlen, Anal Chem **72** (5), 887-898 (2000).
67. R. W. J. Hollering and W. J. O. V. Teesselink, Opt Commun **79** (3-4), 224-228 (1990).
68. P. Brevet, *Surface Second Harmonic Generation*. (Presses polytechniques et universitaires romandes, 1997).
69. M. Evans, *Modern Nonlinear Optics*. (John Wiley & Sons Inc, 1994).
70. J. T. Lin, Proc. SPIE - Int. Soc. Opt. Eng. **895**, 162-169169 (1988).
71. N. Mukherjee, R. A. Myers and S. R. J. Brueck, J. Opt. Soc. Am. B **11** (4), 665-668 (1994).
72. V. Mizrahi and J. E. Sipe, J. Opt. Soc. Am. B **5** (3), 660-667 (1988).
73. C. F. Bohren, *Absorption and Scattering of Light by Small Particles*. (Wiley-VCH, 2004).
74. T. Inagaki, L. C. Emerson, E. T. Arakawa and M. W. Williams, Phys Rev B **13** (6), 2305-2313 (1976).
75. W. Y. Ching and J. Callaway, Phys Rev B **11** (4), 1324-1329 (1975).
76. P. B. Johnson and R. W. Christy, Phys Rev B **6** (12), 4370-4379 (1972).
77. T. Pakizeh, The Journal of Physical Chemistry C **115** (44), 21826-21831 (2011).
78. M. A. Cazalilla, J. S. Dolado, A. Rubio and P. M. Echenique, Phys Rev B **61** (12), 8033-8042 (2000).
79. N. E. Christensen, physica status solidi (b) **54** (2), 551-563 (1972).
80. U. Kreibig, *Optical Properties of Metal Clusters*. (Springer, 1995).
81. G. F. Bassani, *Electronic states and optical transitions in solids, by F. Bassani and G. Pastori Parravicini. Edited by R. A. Ballinger*. (Pergamon Press, Oxford, New York, 1975).
82. G. Mie, Annalen der Physik **330** (3), 377-445 (1908).
83. R. Gans, Annalen der Physik **342** (5), 881-900 (1912).
84. R. Fuchs, Phys Rev B **11** (4), 1732-1740 (1975).
85. Schuerman, *Light Scattering by Irregularly Shaped Particles*. (Springer, 1980).
86. P. Royer, J. L. Bijeon, J. P. Goudonnet, T. Inagaki and E. T. Arakawa, Surf Sci **217** (1-2), 384-402 (1989).
87. H. Hovel, A. Hilger, I. Nusch and U. Kreibig, Z Phys D Atom Mol Cl **42** (3), 203-208 (1997).
88. A. Hilger, N. Cuppers, M. Tenfelde and U. Kreibig, Eur Phys J D **10** (1), 115-118 (2000).
89. E. David, Zeitschrift für Physik A Hadrons and Nuclei **114** (7), 389-406 (1939).
90. T. Yamaguchi, S. Yoshida and A. Kinbara, Thin Solid Films **21** (1), 173-187 (1974).
91. A. Hilger, Dissertation, RWTH Aachen, 2001.
92. U. Kreibig and C. v. Fragstein, Zeitschrift für Physik A Hadrons and Nuclei **224** (4), 307-323 (1969).
93. W. Hampe, Zeitschrift für Physik A Hadrons and Nuclei **152** (4), 476-494 (1958).
94. W. T. Doyle, Physical Review **111** (4), 1067-1072 (1958).
95. R. H. Doremus, The Journal of Chemical Physics **42** (1), 414-417 (1965).
96. D. C. Skillman and C. R. Berry, J. Opt. Soc. Am. **63** (6), 707-713 (1973).
97. S. P. Apell, J. Giraldo and S. Lundqvist, Phase Transitions **24-26** (2), 577-604 (1990).

98. B. N. J. Persson and A. Baratoff, Phys Rev Lett **68** (21), 3224-3227 (1992).
99. E. Zaremba and B. N. J. Persson, Phys Rev B **35** (2), 596-606 (1987).
100. B. Persson, Surf Sci **281** (1–2), 153-162 (1993).
101. U. Kreibig, G. Bour, A. Hilger and M. Gartz, Phys Status Solidi A **175** (1), 351-366 (1999).
102. K. J. Berg, A. Berger and H. Hofmeister, Z Phys D Atom Mol Cl **20** (1-4), 309-311 (1991).
103. B. von Issendorff and O. Cheshnovsky, Annu Rev Phys Chem **56**, 549-580 (2005).
104. G. Delacrétaz and L. Wöste, Surf Sci **156, Part 2** (0), 770-776 (1985).
105. H. Zhang, G. Schmid and U. Hartmann, Nano Lett **3** (3), 305-307 (2003).
106. M. Hermann, U. Kreibig and G. Schmid, Zeitschrift für Physik D Atoms, Molecules and Clusters **26** (0), 1-3 (1993).
107. G. Schön and U. Simon, Colloid & Polymer Science **273** (2), 101-117 (1995).
108. G. Schmid, S. Emde, V. Maihack, W. Meyer-Zaika and S. Peschel, Journal of Molecular Catalysis A: Chemical **107** (1–3), 95-104 (1996).
109. G. Schmid, M. Harms, J. O. Malm, J. O. Bovin, J. Van Ruitenbeck, H. W. Zandbergen and W. T. Fu, J Am Chem Soc **115** (5), 2046-2048 (1993).
110. T. Hayakawa, Y. Usui, S. Bharathi and M. Nogami, Adv Mater **16** (16), 1408-+ (2004).
111. T. Götz, M. Buck, C. Dressler, F. Eisert and F. Träger, Applied Physics A: Materials Science & Processing **60** (6), 607-612 (1995).
112. R. Antoine, M. Pellarin, B. Palpant, M. Broyer, B. Prevel, P. Galletto, P. F. Brevet and H. H. Girault, J Appl Phys **84** (8), 4532-4536 (1998).
113. A. M. Moran, J. H. Sung, E. M. Hicks, R. P. Van Duyne and K. G. Spears, J Phys Chem B **109** (10), 4501-4506 (2005).
114. R. Srinivasan, Y. Tian and I. I. Suni, Surf Sci **490** (3), 308-314 (2001).
115. F. R. Aussenegg, A. Leitner and H. Gold, Applied Physics A: Materials Science & Processing **60** (2), 97-101 (1995).
116. B. Lamprecht, A. Leitner and F. R. Aussenegg, Appl Phys B-Lasers O **68** (3), 419-423 (1999).
117. I. Russier-Antoine, E. Benichou, G. Bachelier, C. Jonin and P. F. Brevet, J Phys Chem C **111** (26), 9044-9048 (2007).
118. F. X. Wang, F. J. Rodriguez, W. M. Albers, R. Ahorinta, J. E. Sipe and M. Kauranen, Phys Rev B **80** (23) (2009).
119. M. Finazzi, P. Biagioni, M. Celebrano and L. Duo, Phys Rev B **76** (12) (2007).
120. S. Kim, J. H. Jin, Y. J. Kim, I. Y. Park, Y. Kim and S. W. Kim, Nature **453** (7196), 757-760 (2008).
121. P. Ghenuche, R. Quidant and G. Badenes, Opt Lett **30** (14), 1882-1884 (2005).
122. Y. Liu, S. Xu, X. Xuyang, B. Zhao and W. Xu, The Journal of Physical Chemistry Letters **2** (17), 2218-2222 (2011).
123. G. T. Boyd, T. Rasing, J. R. R. Leite and Y. R. Shen, Phys Rev B **30** (2), 519-526 (1984).
124. P. Genevet, J.-P. Tetienne, E. Gatzogiannis, R. Blanchard, M. A. Kats, M. O. Scully and F. Capasso, Nano Lett **10** (12), 4880-4883 (2010).
125. J. R. Sambles and R. A. Innes, Journal of Modern Optics **35** (5), 791-797 (1988).
126. U. Heiz, A. Vayloyan and E. Schumacher, Rev Sci Instrum **68** (10), 3718-3722 (1997).
127. B. Delley, D. E. Ellis, A. J. Freeman, E. J. Baerends and D. Post, Phys Rev B **27** (4), 2132-2144 (1983).
128. H. Häkkinen and U. Landman, Phys Rev B **62** (4), R2287-R2290 (2000).
129. S. E. Harris, Proceedings of the IEEE **57** (12), 2096-2113 (1969).
130. J. Eichler, *Laser: Bauformen, Strahlführung, Anwendungen.* (Springer, 2010).
131. G. A. Kumar, L. Jianren, A. A. Kaminskii, K. I. Ueda, H. Yagi, T. Yanagitani and N. V. Unnikrishnan, Quantum Electronics, IEEE Journal of **40** (6), 747-758 (2004).

132. K. Kuriki, S. Nishihara, Y. Nishizawa, A. Tagaya, Y. Koike and Y. Okamoto, J. Opt. Soc. Am. B **19** (8), 1844-1848 (2002).
133. K. Terashima, S. Tamura, S.-H. Kim and T. Yoko, Journal of the American Ceramic Society **80** (11), 2903-2909 (1997).
134. Y. R. Shen, Annu Rev Phys Chem **40** (1), 327-350 (1989).
135. H. Weininger, J. Schmidt and A. Penzkofer, Chem Phys **130** (1-3), 379-387 (1989).
136. T. F. Heinz, C. K. Chen, D. Ricard and Y. R. Shen, Phys Rev Lett **48** (7), 478-481 (1982).
137. M. Thämer, P. Heister, A. Kartouzian, S. Gerlach, M. Tschurl, U. Boesl and U. Heiz, Submitted to J. Phys. Chem. C (2012).
138. C. Gautier, R. Taras, S. Gladiali and T. Bürgi, Chirality **20** (3-4), 486-493 (2008).
139. S. Knoppe, A. C. Dharmaratne, E. Schreiner, A. Dass and T. Bürgi, J Am Chem Soc **132** (47), 16783-16789 (2010).
140. C. Gautier and T. rgi, CHIMIA International Journal for Chemistry **62** (6), 465-470 (2008).
141. J. Byers, J. Chem. Phys. **101** (7), 6233 (1994).
142. A. Brown, C. M. Kemp and S. F. Mason, Journal of the Chemical Society A: Inorganic, Physical, Theoretical, 751-755 (1971).
143. M. Meier, A. Wokaun and P. F. Liao, J. Opt. Soc. Am. B **2** (6), 931-949 (1985).
144. A. K. Sarychev and V. M. Shalaev, in *Optical Properties of Nanostructured Random Media*, edited by V. M. Shalaev (Springer-Verlag Berlin, Berlin, 2002), Vol. 82, pp. 169-184.
145. U. Kreibig, Zeitschrift für Physik A Hadrons and Nuclei **234** (4), 307-318 (1970).
146. R. K. Ahrenkiel, J. Opt. Soc. Am. **61** (12), 1651-1655 (1971).
147. M. Itoh, V. Kumar, T. Adschiri and Y. Kawazoe, J Chem Phys **131** (17) (2009).
148. S. A. Mitchell, J. Farrell, G. A. Kenneywallace and G. A. Ozin, J Am Chem Soc **102** (26), 7702-7709 (1980).
149. M. Lippitz, M. A. van Dijk and M. Orrit, Nano Lett **5** (4), 799-802 (2005).
150. H. Kishida, M. Ono, K. Miura, H. Okamoto, M. Izumi, T. Manako, M. Kawasaki, Y. Taguchi, Y. Tokura, T. Tohyama, K. Tsutsui and S. Maekawa, Phys Rev Lett **87** (17), 177401 (2001).
151. M. J. Bloemer, J. W. Haus and P. R. Ashley, J. Opt. Soc. Am. B **7** (5), 790-795 (1990).
152. L. Yang, K. Becker, F. M. Smith, R. H. Magruder Iii, J. R. F. Haglund, L. Yang, R. Dorsinville, R. R. Alfano and R. A. Zuhr, J. Opt. Soc. Am. B **11** (3), 457-461 (1994).
153. R. Farrag, M. Thämer, M. Tschurl, T. Bürgi and U. Heiz, submitted to J. Phys. Chem. C (2012).
154. D. E. Cliffel, F. P. Zamborini, S. M. Gross and R. W. Murray, Langmuir **16** (25), 9699-9702 (2000).
155. R. C. Doty, T. R. Tshikhudo, M. Brust and D. G. Fernig, Chem Mater **17** (18), 4630-4635 (2005).
156. G. J. Simpson, The Journal of Chemical Physics **117** (7), 3398-3410 (2002).
157. T. Petralli-Mallow, T. M. Wong, J. D. Byers, H. I. Yee and J. M. Hicks, The Journal of Physical Chemistry **97** (7), 1383-1388 (1993).
158. P. L. Polavarapu, Chirality **14** (10), 768-781 (2002).

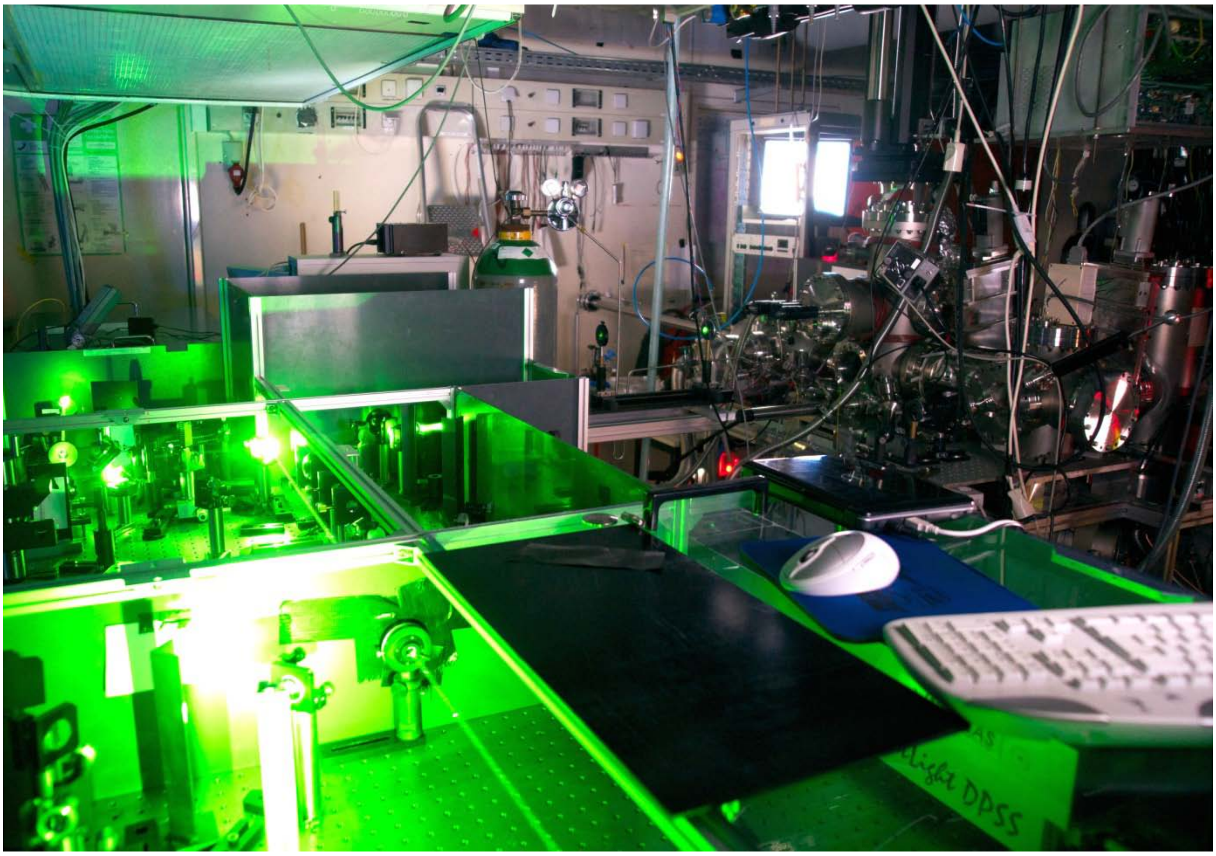

AS
light DPSS